Quantum walks and quantum search on graphene lattices

Iain Foulger

Thesis submitted to the University of Nottingham for the degree
of Doctor of Philosophy

December 2014

Abstract

This thesis details research I have carried out in the field of quantum walks, which are the quantum analogue of classical random walks. Quantum walks have been shown to offer a significant speed-up compared to classical random walks for certain tasks and for this reason there has been considerable interest in their use in algorithmic settings, as well as in experimental demonstrations of such phenomena.

One of the most interesting developments in quantum walk research is their application to spatial searches, where one searches for a particular site of some network or lattice structure. There has been much work done on the creation of discrete- and continuous-time quantum walk search algorithms on various lattice types. However, it has remained an issue that continuous-time searches on two-dimensional lattices have required the inclusion of additional memory in order to be effective, memory which takes the form of extra internal degrees of freedom for the walker.

In this work, we describe how the need for extra degrees of freedom can be negated by utilising a graphene lattice, demonstrating that a continuous-time quantum search in the experimentally relevant regime of two-dimensions is possible. This is achieved through alternative methods of marking a particular site to previous searches, creating a quantum search protocol at the Dirac point in graphene.

We demonstrate that this search mechanism can also be adapted to allow state transfer across the lattice. These two processes offer new methods for channelling information across lattices between specific sites and supports the possibility of graphene devices which operate at a single-atom level. Recent experiments on microwave analogues of

i

graphene that adapt these ideas, which we will detail, demonstrate the feasibility of realising the quantum search and transfer mechanisms on graphene.

Acknowledgements

Thank you to my supervisors, Gregor Tanner and Sven Gnutzmann, for their guidance and support over the past few years. Their help and advice has been invaluable to me throughout, and their enthusiasm for this work encouraged me to keep going through the difficult points of my research.

I would like to thank everybody in the Mathematical Sciences department for their help over the years and for making it such a pleasant and enjoyable place to work.

Throughout my studies I have had the opportunity to visit various conferences and universities where I was able to benefit from exposure to new ideas and interesting discussions which I would not have encountered otherwise. I would like to thank everyone who made this possible, in particular I would like to thank Hans-Jürgen Stöckmann and Klaus Richter for being so helpful and accommodating when visiting their respective groups.

I would also like to thank Ulrich Kuhl, Julian Böhm and Fabrice Mortessagne from the Université de Nice Sophie-Anitpolis for taking such an interest in this work, and for discussing and sending me their experimental results which provide the motivation for one of the chapters of this thesis.

Thank you to all the friends I've gained during my time in Nottingham. Our outings have helped keep me sane - I'll miss our 6 Nations and Christmas traditions.

Finally, thank you to my parents who have always provided me with so much love and support, and who kept me grounded at times when

I was struggling. I'm not sure how I would have made it through without their constant encouragement and belief in me.

Publications

Parts of this work have been presented in the following publication:

[1]: I. Foulger, S. Gnutzmann and G. Tanner. Quantum search on graphene lattices. *Phys. Rev. Lett.* **112** : 070504, February 2014.

Contents

1

Introduction

The success of quantum mechanics over the last century in describing our world is unparalleled but it took decades before the underlying principles were incorporated into an approach for information processing. Our increased understanding of matter which followed the development of quantum theory sparked the electronic age, leading to the creation of new technologies which allowed us to process information like never before. However, even though those developments lead to massive changes in society they were only a first effort to use quantum theory to advance technology and our information processing power. This initial approach can only take us so far though, because although improvements in electronic equipment have followed Moore's law so far, we are approaching the limit of how small and fast we can make devices. This unfortunate state of affairs has arisen as the devices have become so small that quantum effects have actually become an obstacle to further developments.

In the past decade or two, there has been a second, more direct approach of applying quantum theory to our view of information and computation. With the realisation that computation is ultimately a physical process and that these processes must fundamentally be quantum in nature, the theoretical framework in which one works is completely transformed, opening up new possibilities. By constructing a computer based on inherently quantum principles, whose bits can be placed in superpositions of off & on and can be entangled with one another, a whole new way of processing information develops.

From this seemingly simple idea of basing a computer on fundamental physi-

cal principles, several fruitful areas of research have opened up: the technological development of quantum computers themselves, new algorithms which run on them, cryptographic systems, and fundamental ideas on information theory including work on information channels and the transport of quantum states. Work in these fields has told us something new about the nature of quantum mechanics itself, not just about particular physical systems. The construction of quantum computers is a very interesting area from a technical perspective as the creation of these devices requires the control of single particles, not to mention the control of specific interactions between these particles themselves and also involves isolating them from the external environment. However, the development of these computers is pointless if we don't have the software to run on them.

Developing any software to run on these computers is a challenge but this is not the objective; the desire is to construct algorithms to run on quantum computers which are faster than those which run on classical computers. There have been several important advancements in this area. Deutsch was the first to construct a quantum algorithm [2]. This algorithm showed that for a quantum computer it was possible to check if a Boolean function with a single bit input is balanced or constant with only one evaluation of the function (this was later generalised to a function with an n-bit input [3, 4]). Although of little practical use these developments demonstrated that there were problems for which quantum computers could find solutions faster than a classical computer ever could and lead to the development of further quantum algorithms. Two of the most significant and well known algorithms are Shor's algorithm for finding prime factors [5] and Grover's algorithm for unstructured database search [6, 7]. Both are faster than their most efficient known classical counterparts where Shor's algorithm presents an exponential speedup and Grover's algorithm provides a polynomial speedup over the fastest classical algorithms.

The field of quantum walks offers a theoretical framework within which one can develop algorithms. Although quantum walks were first developed in a quantum optics setting [8], they later became established in a quantum information context, especially in the development of search algorithms on different data structures [9, 10]. Advances have been made using both models of quantum walks, discrete time-steps and continuous time-evolution, and work has been done on

not only developing algorithms but also in fundamental properties of walks such as traversal times across different structures. It has also been demonstrated that quantum walks on certain network configurations can create the universal set of gates needed for quantum computation [11, 12], offering possibilities of alternative architectures for quantum computers.

However, quantum walks are not restricted to purely theoretical considerations. They can also be directly represented in physical systems [13]. We can, therefore, potentially describe the transport properties of different systems using quantum walk descriptions. This direct equivalence of quantum information theory and physical systems is incredibly useful as one may find direct realisations of algorithms, but also properties of physical systems could lead the direction of theoretical research.

All this work has taken place against a backdrop of technological advances which has increased the number of systems which are relevant from a quantum walk point-of-view. Optical lattices [13], trapped ions [14], and waveguide lattices [15]; there is a wide range of systems for which quantum walks are suitable models. Even, potentially, the dynamics of systems involving Bose-Einstein condensates can be described by quantum walk models [16, 17]. However, an interesting omission from this list is one of the most discussed and researched materials in recent years, graphene. The exciting properties of graphene have made it potentially useful for several applications [18]. The ballistic transport properties of graphene make it an excellent conductor [19], and, when viewed in an quantum information context, is a promising system from an algorithmic viewpoint. It is also possible that a new theoretical perspective could open up other interesting behaviour and potential applications.

1.1 Thesis aims and structure

Our initial motivation for this work was to improve quantum walk searches on low-dimensional lattices. While there exist discrete-time searches on d-dimensional square lattices which are faster than classical searches for $d \geq 2$ [10] , effective continuous-time quantum searches only exist for $d \geq 4$ [20] or else they require additional memory in order to improve their search time in lower dimensions [21].

3

However, as we discuss in Chapter 3, we consider the possibility that the solution offered by the additional memory could be achieved in a simpler way which does not require extra degrees of freedom, and could, therefore, be viewed as more efficient. The solution we develop presents itself through the choice of a different lattice, specifically, a honeycomb lattice which is the underlying lattice structure of carbon atoms in the material graphene.

The association with graphene is important as, although we first study a purely theoretical problem in quantum information, the use of a graphene lattice also offers a potential physical realisation. Here, a quantum walk search algorithm on graphene would correspond to the propagation and localisation of electron probability amplitude on the lattice. From this correspondence of the abstract search problem and electron dynamics on graphene, we may use a quantum walk or quantum search algorithm framework to investigate the effect of perturbations on dynamics on various different carbon structures. This offers not only different possibilities for the demonstration of two-dimensional continuous-time quantum searches but also descriptions of novel effects and potentially useful behaviour on graphene.

Chapter 2 introduces the necessary preliminaries and definitions which will be needed throughout this thesis. This will cover Grover's algorithm, basic definitions of graph theory, and also descriptions of classical random walks. This is accompanied by introductions to the formalisms of quantum walks, both continuous- and discrete-time walks, and an overview of the various interests and results in the field. The chapter concludes with a review of graphene.

We present our main analytical result in Chapter 3, on quantum searches on graphene tori. Included here is a description of important continuous-time searches from [20, 21], where we explain the lack of improvement over classical searches in two dimensions and a solution to this issue using additional degrees of freedom or memory. In this chapter we offer an alternative solution requiring no additional degrees of freedom by performing a search on graphene. We provide an analysis of the running time and success probability, as well as further discussions on several subtleties of the search dynamics. It will also be demonstrated how the search mechanism can be utilised to construct a communication protocol.

In Chapter 4 we develop search and communication protocols using different

perturbation types. We also investigate numerically the application of various perturbations to several different carbon structures, namely, graphene tori, armchair nanotubes and graphene sheets.

Chapter 5 contains numerical modelling of a microwave analogue of a graphene sheet. In this chapter we model a particular set of experimental results demonstrating searching/switching dynamics and also some possible extensions to the previous experiment using the same apparatus.

The final chapter is a summary of the results of the earlier chapters, and a discussion of open questions and possible directions for further work.

1.2 Numerical methods

All of the numerical work in this thesis was carried out using the mathematical software Matlab. The code written to investigate the systems described in this thesis was written by myself alone, making use of the inbuilt features of Matlab.

The bulk of the numerical calculations involved the generation and diagonalisation of the adjacency matrices of various structures. To analyse the scaling of certain spectral properties, sparse matrix methods were utilised to ensure that the calculations could still be performed on a standard desktop or laptop computer in a reasonable time period.

2

Preliminaries

This chapter will start with an explanation of Grover's algorithm, which is the motivation for, and root of, the field of quantum walk searches. We will give an account of classical random walks [22] and the relation to their quantum analogs, starting with the relevant features of graph theory needed to describe the mechanics of the walks. This will be followed by a review of results discovered in the field including quantum walk implementations of the quantum (Grover) search algorithm, and finally we will review the relevant properties of graphene and introduce some necessary notation. Detailed introductions to quantum walks can be found in [23, 24, 25].

The first ideas of quantum walks can be traced back to Feynman when considering spatially discrete Dirac equations [26], however, the first proposal that can really be viewed as a quantum walk came from Aharonov, Davidovich and Zagury in a quantum optics setting [8]. They considered the propagation of a wave packet whose direction is dependent on a spin-degree of freedom, but with successive measurements after each step so it was not the coherent quantum walk considered today. Two models of quantum walks have developed since these early ideas. Discrete-time quantum walks were introduced in the form of quantum cellular automata by Meyer [27] but were more formally developed and analysed in [28] by Aharonov *et al.* and by Ambainis *et al.* in [29]. The other model, continuous-time quantum walks, were initially introduced by Farhi and Gutman [30] when studying the penetration of walks through decision trees. Both models, as we will see, display significant differences in behaviour to their classical

counterparts, and, in some cases, can accomplish certain algorithmic tasks, most notably searching, in a greatly reduced running time.

2.1 Grover's Algorithm

Grover's algorithm searches through an unstructured database of N states in time $\mathcal{O}\left(\sqrt{N}\right)$ [6, 7], which was proved by Bennett *et al.* [31] to be optimal for unstructured database search. This is a quadratic improvement over the classical search problem where merely searching through every item is optimal and so takes $\mathcal{O}\left(N\right)$ time.

The system is described by an N-dimensional Hilbert space spanned by the canonical basis states $\{|j\rangle : j \in \mathbb{Z}_N\}$. In [6, 7] the search problem is described in terms of a black-box oracle function which can recognise the solution and the problem is then to find a solution state using as few calls to the oracle function as possible. This oracle function is presented to us as a unitary operator U_f which acts on the basis states as

$$U_f |j\rangle = \begin{cases} - |j\rangle & \text{if } j \text{ is a solution} \\ |j\rangle & \text{if } j \text{ is not a solution.} \end{cases} \tag{2.1}$$

This is accompanied by another operator D, known as the diffusion transformation

$$D = 2 |s\rangle \langle s| - \mathbb{1}_N, \tag{2.2}$$

where $|s\rangle$ is the uniform superposition of all states $|s\rangle = \frac{1}{\sqrt{N}} \sum_{j=0}^{N-1} |j\rangle$. The diffusion transform is often known as the inversion-about-the-mean because of its effect on states. If a_j is the probability amplitude of the jth state and a is the average of the amplitudes of all basis states, then the action of D transforms a_j as $a_j \mapsto 2a - a_j$. The product of the two operators U_f and D form the Grover operator $G = DU_f$.

The algorithm then proceeds as follows:

1. The system is initialised in the uniform superposition $|s\rangle$

2. The Grover operator G is applied $\mathcal{O}\left(\sqrt{N}\right)$ times
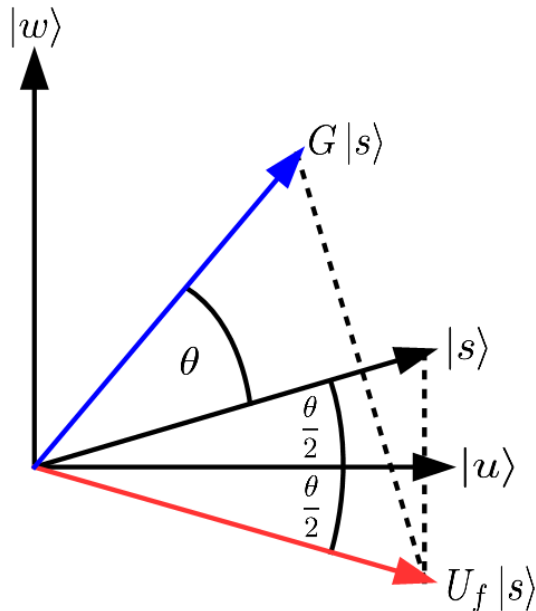
Figure 2.1: Geometric representation of one step of the Grover's algorithm. The oracle function U_f takes the uniform superposition $|s\rangle$ into red state. The application of the diffusion operator D then takes the system state into the blue state, completing one step.

3. The system is measured in the canonical basis

After these steps the measurement should result with the solution state with high probability. Boyer *et al.* [32] in their detailed analysis of the algorithm showed that the optimal time for measurement was after $T = \left[\frac{\pi}{4}\sqrt{N}\right]$ iterations, where the notation $[x]$ indicates that we round x to the nearest integer. After this number of iterations the probability of success is close to unity for large N.

Grover's algorithm can be simply described in a geometric picture. The original algorithm can be viewed as a rotation in a plane spanned by two states, a solution state $|w\rangle$ and the superposition over all other states $|u\rangle = \frac{1}{\sqrt{N-1}}\sum_{j\neq w}|j\rangle$. This enables the uniform superposition to be written as

$$|s\rangle = \sqrt{\frac{N-1}{N}}\,|u\rangle + \frac{1}{\sqrt{N}}\,|w\rangle \ . \tag{2.3}$$

Defining $\cos\left(\frac{\theta}{2}\right) = \sqrt{\frac{N-1}{N}}$ and $\sin\left(\frac{\theta}{2}\right) = \frac{1}{\sqrt{N}}$ we can rewrite $|s\rangle$ as

$$|s\rangle = \cos\left(\frac{\theta}{2}\right)|u\rangle + \sin\left(\frac{\theta}{2}\right)|w\rangle \,, \qquad (2.4)$$

and in the basis $\{|u\rangle, |w\rangle\}$ we may write the operators U_f and D as

$$U_f = \begin{pmatrix} 1 & 0 \\ 0 & -1 \end{pmatrix}, \quad D = \begin{pmatrix} \cos\theta & \sin\theta \\ \sin\theta & -\cos\theta \end{pmatrix}. \qquad (2.5)$$

It can be seen then that the operator U_f takes the uniform superposition $|s\rangle$ and performs a reflection about the state $|u\rangle$. This is then followed by the diffusion operator D which reflects the state about $|s\rangle$. It follows then that the Grover operator G performs a rotation through an angle θ and so the system's state remains in the plane spanned by $|u\rangle$ and $|w\rangle$. Figure 2.1 shows one step of the Grover search algorithm. As G is a rotation matrix, it is clear that $G(k\theta)\,G(\theta) = G((k+1)\theta)$. In this geometric picture it becomes apparent that the state of the system after T steps is

$$|\psi(T)\rangle = \cos\left(\frac{2T+1}{2}\theta\right)|u\rangle + \sin\left(\frac{2T+1}{2}\theta\right)|w\rangle\,. \qquad (2.6)$$

It is clear that the system rotates into the solution state $|w\rangle$ when $\frac{2T+1}{2}\theta = \frac{\pi}{2}$. Assuming that $N \gg 1$ so that $\frac{1}{\sqrt{N}} = \sin\left(\frac{\theta}{2}\right) \approx \frac{\theta}{2}$, we see that the measurement time which results in the solution state with maximum probability is $T = \left[\frac{\pi}{4}\sqrt{N}\right] = \mathcal{O}\left(\sqrt{N}\right)$. Viewing the search algorithm geometrically, it is also clear to see why there is an optimum time for measurement as, if the Grover operator continues to be applied, the system will rotate past the solution and back towards a uniform superposition.

2.2 Graph theory

To discuss the topic of quantum walks on discrete structures we will need to use some of the standard language of graph theory [33]. A graph is a network of sites or vertices connected by bonds or edges, an example is shown in Figure 2.2. More
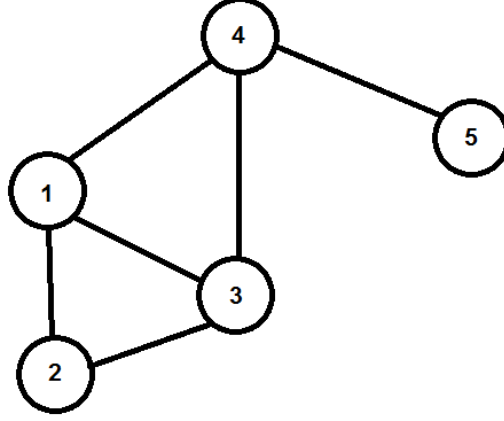
Figure 2.2: An example of a graph with 5 vertices and 6 edges.

formally, a graph, G, is an ordered pair of sets (V, E), where E is a 2-element subset of V. The set V is the set of vertices and E is the set of edges. An edge (x, y) connects the vertices x and y, and these vertices are described as adjacent. A graph where there is a sequence of adjacent edges between any two vertices is called a connected graph. We shall only discuss simple connected graphs, which are those with a single undirected edge between connected vertices (that is, the edge (x, y) is the same as (y, x)) and with no edges connecting a vertex to itself. The valency or degree of a vertex j, v_j, is the number of edges incident on the vertex. A graph where the valency of all vertices is the same is known as a d-regular graph, where d is the valency of the vertices of the graph.

The structure of a simple graph with N vertices can be described by its $N \times N$ adjacency matrix, A, defined as

$$A_{ij} = \begin{cases} 1 & \text{if } i \text{ and } j \text{ are adjacent} \\ 0 & \text{if } i \text{ and } j \text{ are not adjacent.} \end{cases} \tag{2.7}$$

One can also define the weighted adjacency matrix, although we will generally only consider graphs where the weights between vertices for all edges is constant. There is a related matrix to describe the connectivity of a graph, known as the

Laplacian matrix, which we will define as

$$L = A - D \,, \tag{2.8}$$

where $D_{jj} = v_j$ so that the diagonal entries of the matrix are the valencies of the vertices and all other entries are zero. The Laplacian of the graph shown in Figure 2.2 is given as,

$$L = \begin{pmatrix} -3 & 1 & 1 & 1 & 0 \\ 1 & -2 & 1 & 0 & 0 \\ 1 & 1 & -3 & 1 & 0 \\ 1 & 0 & 1 & -3 & 1 \\ 0 & 0 & 0 & 1 & -1 \end{pmatrix} \,. \tag{2.9}$$

If the graph we are considering is undirected, as we are restricting ourselves to, then L is a Hermitian and negative-semidefinite matrix.

The relation between graph theory and solid state physics can be seen when we consider the graph as an expression of the underlying lattice of the material, where the material's atomic sites are represented by the vertices and the edges correspond to the chemical bonds between atoms. If one only assumes chemical bonds exist between atoms which are nearest-neighbours, then such a graph is very closely related to the tight-binding model in solid state physics [34]. Alternatively, other physical systems, such as optical lattices or microwave resonators, can be reduced to a model on a graph in similar ways. These direct analogies allow for the realisation of several quantum walk results that we will encounter in later sections as physical systems or experiments.

2.3 Discrete-time walks

2.3.1 Classical walks

Before describing the quantum case it is perhaps helpful to discuss the classical walk, and to begin with the simplest and most well-known walk: the random walk on a line. In this case the direction of the walker with every time step is

dictated by the outcome of the flip of a coin. If the walker is placed at the origin then after one time step the walker will be at either $x = 1$ or $x = -1$, both with probability $p = \frac{1}{2}$. After t time steps, the probability of the walker being found at site x is

$$p(t, x) = \frac{1}{2^t} \binom{t}{\frac{t+|x|}{2}}, \tag{2.10}$$

which is only valid for $t + |x|$ even and $t \geq x$, for all other x, $p(t, x) = 0$. This probability distribution is shown in Figure 2.3 for a walker starting at the origin after $t = 100$ time steps. We can see from this symmetric probability distribution that the most probable position to find the walker is at the origin, $x = 0$. For large times, the probability distribution can be approximated by

$$p(t, n) \approx \frac{2}{\sqrt{2\pi t}} e^{-\frac{n^2}{2t}}, \tag{2.11}$$

with the use of Stirling's approximation. The expected distance of the walker from the origin for this particular walk is the standard deviation of the probability distribution

$$\left(\langle x^2 \rangle - \langle x \rangle^2\right)^{\frac{1}{2}} = \sqrt{t}, \tag{2.12}$$

indicating that the transport of walker across the line is diffusive.

This example of a random walk on a line can be extended to random walks on more complicated structures through Markov chains, which describe transitions of a system between some countable number of states. The evolution of the Markov chain at a particular time is determined by a probability distribution describing the probability to be in a particular state. In these processes the subsequent distribution of the chain depends only on the current state, and the previous evolution of the system is unimportant i.e. the Markov chain has no 'memory' of its past. A Markov chain can be viewed as a graph $G(V, E)$, where the vertices describe possible states and the edges represent possible transitions between states. The probability distribution is given by a column vector

$$p(t) = \Big(p_1(t), p_2(t), \ldots, p_N(t)\Big)^T, \tag{2.13}$$

where $p_j(t)$ is the probability of being found at vertex j at time t. The time

step of a discrete-time Markov chain is implemented with the use of a matrix M, known as the transition matrix. The probability at vertex j at time $t+1$ is given by

$$p_j(t+1) = \sum_{l=1}^{N} M_{jl} p_l(t) \ . \tag{2.14}$$

The entries of M describes the probability of transitioning between any two vertices and, therefore, has non-zero entries only where it is possible to make a transition from one vertex to another. To remain probability conserving M must satisfy the conditions $M_{ij} \geq 0$, $\sum_{j=1}^{N} M_{ij} = 1$ for all $i, j \in V$. The probability distribution after T steps is

$$p(T) = M^T p(0) \ . \tag{2.15}$$

If our Markov chain system is a walker moving across some graph, it is clear to see that the probability distribution describes the odds of the walker ending up at some particular vertex.

2.3.2   Quantum walks

The formalism of discrete-time Markov chains can be adapted into a quantum framework to create discrete-time quantum walks (DTQW) but with some differences which allow for some interesting alternative behaviour. Again it is perhaps simpler to begin with the walk on the line.

In our quantum walk on a line the position of the walker is described by a vector in the Hilbert space $\mathcal{H}_p$, where we use the canonical basis $\{|j\rangle : j \in \mathbb{Z}\}$. The aim is to construct a unitary operator on the Hilbert space $\mathcal{H}_p$ describing transitions of the walker, in a similar way to the classical walk transition matrix M, first encountered in Equation (2.14). In [27], it was shown (in the form of quantum cellular automata) that it is not possible for a unitary operator describing a discrete-time quantum walk on a line to be constructed which allows a state to evolve along both directions in superposition. Rather, the only unitary operators which can be constructed are the trivial r-step translation matrices T^r which simply move each component of a state r steps along one direction, i.e

$T^r |i\rangle = |i + r\rangle$.

To develop more interesting behaviour, while keeping the operator describing the time-evolution unitary, we add an extra internal degree of freedom for the walker. As a physical example, for our walk on a line we could assume that the walker is an electron and the internal degree of freedom is represented by spin. An additional constraint is then added to the time-evolution of the walk, that the direction taken by the walker at each time step is dependent on the internal degree of freedom. Thus, the walk takes place in the Hilbert space $\mathcal{H} = \mathcal{H}_p \otimes \mathcal{H}_c$, where $\mathcal{H}_c$ is spanned by the basis states $\{|c\rangle : |0\rangle, |1\rangle\}$, and a general state of the walker becomes the tensor product

$$|\psi\rangle = \sum_{j \in \mathbb{Z}} |j\rangle \otimes \left(\alpha_j^0 |0\rangle + \alpha_j^1 |1\rangle \right) , \tag{2.16}$$

so that we are no longer dealing with a probability distribution, but with probability amplitudes. In the previous classical example, the role of chance in the walk direction was represented by a coin flip. This is incorporated in DTQW by a rotation in $\mathcal{H}_c$, known as the 'coin' space. A rotation is performed by applying the unitary coin operator, C, to place the walker in a superposition of coin states. For the walk on a line, probably the most frequently used coin operator is the Hadamard coin

$$H_c = \frac{1}{\sqrt{2}} \begin{pmatrix} 1 & 1 \\ 1 & -1 \end{pmatrix} . \tag{2.17}$$

After the walker has been put in a superposition of coin states, a shift operator has to be applied to move the walker depending on the coin state. For the line this is normally taken to be

$$S = \sum_{j \in \mathbb{Z}} |j + 1\rangle \langle j| \otimes |0\rangle \langle 0| \ + \ \sum_{j \in \mathbb{Z}} |j - 1\rangle \langle j| \otimes |1\rangle \langle 1| , \tag{2.18}$$

where the walker moves one unit to the right if the walker is in the state $|j\rangle \otimes |0\rangle$ and to the left if in the state $|j\rangle \otimes |1\rangle$. The successive applications of the coin and shift operators form a single step and so we define the unitary evolution operator

$$U = S \left(I \otimes C \right) . \tag{2.19}$$
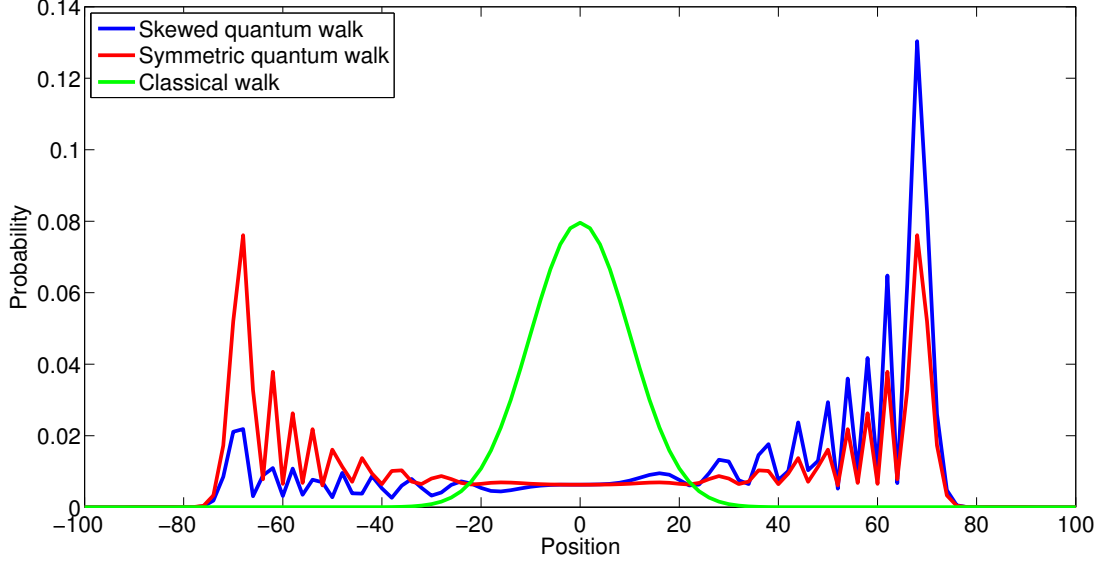
Figure 2.3: Probability distributions for classical random walk (green) and two quantum walks with different initial states (blue/red) on a line after 100 steps. The skewed quantum walk has initial state $|0\rangle \otimes |0\rangle$ and the symmetric walk starts with $|0\rangle \otimes \frac{1}{\sqrt{2}} (|0\rangle + i\,|1\rangle)$. Only the even sites are shown as odd positions are zero.

Thus, the state of the system after T steps is

$$|\psi(T)\rangle = U^T |\psi(0)\rangle \,, \tag{2.20}$$

and the probability of being found at a vertex j is

$$p_j(T) = \sum_{c=0}^{\dim\mathcal{H}_c} |\langle j, c|\psi(T)\rangle|^2 \,, \tag{2.21}$$

where $|j, c\rangle = |j\rangle \otimes |c\rangle$.

It is clear that the Hadamard coin treats both directions fairly as can be seen from the application of the evolution operator once,

$$U |0\rangle \otimes |0\rangle = S |0\rangle \otimes \frac{1}{\sqrt{2}} (|0\rangle + |1\rangle) \tag{2.22}$$

$$= \frac{1}{\sqrt{2}} (|1\rangle \otimes |0\rangle + |-1\rangle \otimes |0\rangle) \,. \tag{2.23}$$

15

The continued evolution of this state after $T = 100$ is shown as the blue curve in Figure 2.3. It clearly displays radically different behaviour from the classical walk, with a relatively low and uniform probability of the walker being found around the origin and a peak in probability to be found a significant distance away from the starting point. The shape of the probability distribution is strikingly different from the classical case, with an asymmetry appearing in the distribution. This asymmetry can be understood by the introduction of a phase difference between the coin states $|0\rangle$ and $|1\rangle$ when the Hadamard coin acts on $|1\rangle$, meaning that there is greater destructive interference between states in the negative direction.

This asymmetry can be removed either with the use of an alternative coin, by carefully setting a weighted superposition between coin-states, or by initialising the system in $|\psi(0)\rangle = |0\rangle \otimes \frac{1}{\sqrt{2}}(|0\rangle + i|1\rangle)$. As the Hadamard coin matrix only has real entries, the real and imaginary parts of the superposition will evolve independently. The probability distribution of this complex initial state is also shown in Figure 2.3 and is indeed symmetrical. The asymptotics of a DTQW on a line were investigated by Ambainis *et al.* in [29] where it was found that nearly all the probability distribution is contained in the region $\left[-\frac{T}{\sqrt{2}}, \frac{T}{\sqrt{2}}\right]$, implying that the expected distance grows linearly with T. This was calculated explicitly by Konno [35], thus confirming the ballistic behaviour of the walk, in stark contrast to the classical walk.

The DTQW on a line can be extended to walks over more complex graphs by modifying the coin matrix. To make the explanation simpler we will first consider only d-regular graphs. We have seen in the example on a line that a state in the coin space must be associated with each direction or each edge from a vertex. Thus, for each vertex we associate the connected edges with a particular coin state. So, our coin space $\mathcal{H}_C$ is spanned by the states $\{|c\rangle : c = 0, 1 \ldots d-1\}$. The coin matrix is now a d-dimensional unitary operator, which leaves many choices of possible coin matrices open. The action of different coins has been studied and they can result in different behaviour [36]. However, one very commonly used

coin matrix is the Grover coin,

$$
C_d = \begin{pmatrix} \frac{2}{d} - 1 & \frac{2}{d} & \cdots & \frac{2}{d} \\ \frac{2}{d} & \frac{2}{d} - 1 & \cdots & \frac{2}{d} \\ \vdots & \vdots & \ddots & \vdots \\ \frac{2}{d} & \frac{2}{d} & \cdots & \frac{2}{d} - 1 \end{pmatrix} ,
\tag{2.24}
$$

which is unbiased for all directions except back-scattering (apart from the special case $d = 4$ where it is fair). The change to the shift operator follows directly; as the coin state specifies a particular edge the application of the shift operator results in

$$
S \cdot |x\rangle \otimes |c\rangle = |y\rangle \otimes |c\rangle ,
\tag{2.25}
$$

where $(x, y) \in E$. For graphs that are not d-regular, there are two options for defining the coin and shift operators. One can either add self-loops to vertices with a valency lower than the maximum valency to force it to be a regular graph, or one can leave the graph unchanged and use a different coin operator for each vertex. However, the second option forces the coin operation to be dependent on the walker's position.

2.4 Continuous-time walks

2.4.1 Classical walks

In continuous-time Markov chains the system can transition between connected vertices at any time, such that as time goes on the probability of being found at a different vertex increases. Continuous-time Markov chains are defined in a similar manner to their discrete-time counterparts described in SubSection 2.3.1. A transition matrix, M, describes the probability to move between states and there is a vector $p(t)$ describing the probability distribution, the jth element of which describes the probability of the walker being found at vertex j at time t. Assuming a homogeneous transition rate between connected vertices, transitions occur with probability γ per unit time. For an infinitesimal time ϵ, the probability

of transition to a connected vertex is $\gamma\epsilon$, and this leads to the probability of not hopping of $1 - d\gamma\epsilon$ for a vertex with valency d. Thus, the infinitesimal transfer matrix is

$$
M_{ij}(\epsilon) = \begin{cases} \gamma\epsilon + \mathcal{O}(\epsilon^2) & \text{if } i \text{ and } j \text{ are adjacent} \\ 1 - d_i\gamma\epsilon + \mathcal{O}(\epsilon^2) & \text{if } i = j \\ 0 & \text{if } i \text{ and } j \text{ are not adjacent.} \end{cases} \tag{2.26}
$$

It can be seen that M satisfies the same probability conserving conditions $M_{ij} \geq 0$, $\sum_{j=1}^{N} M_{ij} = 1$ for all $i, j \in V$. Since the probability to transition only depends on the current state, and not previous states, this implies that the transition matrices can be multiplied,

$$
M_{ij}(t + \epsilon) = \sum_k M_{ik}(t) M_{kj}(\epsilon) . \tag{2.27}
$$

By substituting in the entries of $M(\epsilon)$ from Equation (2.26) and then appropriately taking the limit $\epsilon \to 0$, gives the matrix differential equation

$$
\frac{d}{dt} M_{ij}(t) = -\sum_k M_{ik}(t) H_{kj} , \tag{2.28}
$$

which governs the system evolution where the matrix H, known as the generator matrix, is given by

$$
H_{ij} = \begin{cases} -\gamma & \text{if } i \text{ and } j \text{ are adjacent} \\ d_i\gamma & \text{if } i = j \\ 0 & \text{if } i \text{ and } j \text{ are not adjacent.} \end{cases} \tag{2.29}
$$

(For more details of the derivation, see [22] or [24].) Using the initial condition $M(0) = \mathbb{1}$, the solution to Equation (2.28) is the evolution operator

$$
M(t) = e^{-Ht} , \tag{2.30}
$$

leading to a probability distribution at time T

$$p(T) = M(T)p(0) = e^{-HT}p(0) \ .$$ (2.31)

As an aside, we note the generator matrix describing the transition rates between states can be written in terms of the graph Laplacian, $H = -\gamma L$.

2.4.2 Quantum walks

Continuous-time quantum walks (CTQW) can be described in a very similar way to its classical counterpart, except that it must be formulated in such a way that the dynamics are described by states in a Hilbert space. In the same way as the DTQW, the position of the walker is described by a vector in the Hilbert space $\mathcal{H}_p$, where the canonical basis $\{|j\rangle : j \in V\}$ is used. The next step, initially proposed by Farhi & Gutmann [30], is to use the same generator matrix as in Equation (2.29) to describe the evolution of probability amplitudes. The evolution operator that this generator gives rise to in Equation (2.30) is not unitary as is required for quantum evolution, but this is easily remedied by substituting H for iH giving the unitary quantum evolution operator

$$U(t) = e^{-iHt} \ .$$ (2.32)

This implies that the amplitudes are governed by the Schrödinger equation

$$\frac{d}{dt}\alpha_j(t) = -i\sum_l H_{jl}\alpha_l(t) \ ,$$ (2.33)

where the generator in Equation (2.29) is now used as the Hamiltonian for the CTQW. We can now see that the state of the walker at time T, initialised in a state $|\psi(0)\rangle = \sum_j \alpha_j|j\rangle$, is

$$|\psi(T)\rangle = U(T)|\psi(0)\rangle = e^{-iHT}|\psi(0)\rangle \ ,$$ (2.34)

which is very similar to the classical evolution in Equation (2.31), except, again, we are now dealing with probability amplitudes rather than a probability distri-
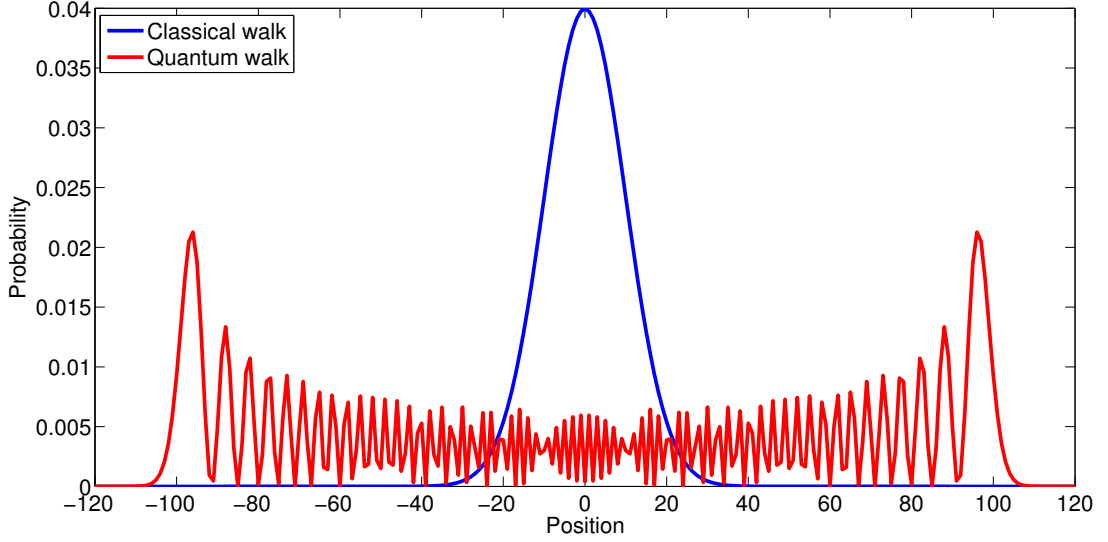
Figure 2.4: Probability distributions at time $T = 100$ for classical random walk (blue) and quantum walk (red) for a walker initially placed at the origin.

bution. Now, the probability to find the walker at a vertex j is given by

$$p_j (T) = |\langle j|\psi (T)\rangle|^2 . \tag{2.35}$$

As an example we again look at the walk on the line, reviewed for CTQW in [37]. We compare the distributions for both the classical and quantum cases, which were both initially centered at the origin. The generator matrix in Equation (2.29) is used for both walks, using the hopping rate $\gamma = \frac{1}{2}$. The transition probabilities from the origin to a vertex j at a time T for the classical and quantum walks are given by

$$p_j^C (T) = e^{-T} I_{|j|} (T) \tag{2.36}$$

$$p_j^Q (T) = |J_{|j|} (T)|^2 , \tag{2.37}$$

where $J_\alpha (x)$ and $I_\alpha (x)$ are the Bessel functions of the first kind and the modified first kind. The evolution of both walks for $T = 100$ is shown in Figure 2.4. Much like the discrete-time case we see that the classical walker is most likely to be found at the origin while the quantum case clearly spreads throughout the lattice

more rapidly.

We note that since Hamiltonian for the quantum walk is not subject to the same restrictions as the generator matrix in Equation (2.29), namely that $\sum_{j=1}^{N} H_{ij} = 0$ for the Markov process to be probability conserving. Instead, the quantum walk Hamiltonian is only required to be Hermitian. For example, one is not restricted to using the Laplacian, the adjacency matrix could be used instead. It should also be noted that, unlike the DTQW, no additional coin space is required, the walk takes place directly on the vertices of the graph and the Hilbert space does not need to be augmented.

2.5 Properties and applications of quantum walks

2.5.1 General results

In this section we will review some important results on the behaviour of quantum walks compared to their classical versions, and also their application in solving several algorithmic problems.

We have already seen that quantum walks on a line display very different behaviour to their classical counterparts, in terms of the propagation rate and how starting states can affect the shape of probability distributions. Kendon and Tregenna [38, 39] showed that the introduction of decoherence into the walks can reduce the rate of propagation, returning to classical behaviour for the correct decoherence rates. They also showed that the distribution can be manipulated by the rate of decoherence to one's advantage, for example creating a 'top-hat' distribution for uniform sampling, or trapping a particle via the quantum Zeno effect in continuous-time walks.

To explore the potential speed-up of algorithms based on quantum walks, various measures of their dispersion across graphs found in classical walks have been defined for the quantum case, namely mixing and hitting times. These measures are important when analysing the efficiency of algorithmic applications.

Classical walks on connected, non-bipartite graphs converge to some stationary state as $T \to \infty$ but, due to the unitary evolution of quantum walks, this is not true for the quantum case. However, although quantum walks do not con-

verge to a stationary state, Aharanov *et al.* [28] showed that alternative concepts for DTQW can be defined which do converge. The first is the average probability distribution over time. Using the definition of the probability to be found at a vertex j from Equation 2.21, this quantity, for an initial state $|\psi\rangle$, is defined as

$$\overline{P}_T \left(j \mid |\psi\rangle \right) = \frac{1}{T} \sum_{t=0}^{T-1} p_j \left(t \right) . \tag{2.38}$$

By taking T to infinity, one can use this quantity to define an analogous concept to stationary states in classical walks, $\pi \left(j \mid |\psi\rangle \right)$. As stated in [28], $\pi \left(j \mid |\psi\rangle \right)$ can be thought of as describing how often a given vertex is visited throughout the time-evolution of a quantum walk. If we express the walk's initial state in terms of the eigenstates of the evolution operator, i.e. as $|\psi\rangle = a_k |\phi_k\rangle$, then the quantity $\pi \left(j \mid |\psi\rangle \right)$ is explicitly defined as

$$\pi \left(j \mid |\psi\rangle \right) = \lim_{T \to \infty} \overline{P}_T \left(j \mid |\psi\rangle \right) = \sum_{k,l,c} a_k a_l^* \langle j, c \mid \phi_k \rangle \langle \phi_l \mid j, c \rangle , \tag{2.39}$$

where the index c indicates the coin degree of freedom and we sum over only those k, l where $|\phi_{k/l}\rangle$ have equal eigenvalues.

By using these two previously defined concepts, Aharonov *et al.* [28] were then able to define the ϵ-mixing time as

$$M_\epsilon = \min\{T | \forall t \geq T, |\psi\rangle : \left\| \pi \left(j \mid |\psi\rangle \right) - \overline{P}_T \left(j \mid |\psi\rangle \right) \right\| \leq \epsilon \} , \tag{2.40}$$

where $\|d_1 - d_2\| = \sum_i |d_1 \left(i \right) - d_2 \left(i \right)|$. This gives the minimum time needed for the probability distribution to remain an ϵ-distance away from its 'steady state' distribution $\pi \left(j \mid |\psi\rangle \right)$.

As an example, for classical walks on a cycle (essentially a walk on a line with periodic boundary conditions) of length N the ϵ-mixing time is $M_\epsilon \sim \mathcal{O} \left(N^2 \log \left(1/\epsilon \right) \right)$. That is, after a time $\mathcal{O} \left(N^2 \right)$ the walk is equally likely to be found anywhere on the cycle. For quantum walks it is possible to show that the mixing time on a cycle is bounded by $M_\epsilon \leq \mathcal{O} \left(\frac{N \log N}{\epsilon^3} \right)$ [28], which is almost a quadratic improvement over the classical case. Similar results of close to quadratic improvements (with logarithmic corrections) can be found for DTQW

on the two-dimensional square lattice [40], and the hypercube for both DTQW and CTQW [41]. In fact, it was shown by Aharanov *et al.* [28] that the improvement in mixing times, compared to the classical case, for quantum walks on graphs of bounded valency could be at most quadratic.

The hitting time, which can be defined as the time taken to reach a particular vertex with sufficiently high probability, also displays very different behaviour than the classical case. The running time of certain algorithms (e.g. tests of connectivity between vertices) can be estimated using the hitting time. As an example of the improvement over the classical case, Kempe [42] showed that the hitting time between opposite corners on the hypercube, for both DTQW and CTQW, is exponentially faster than the classical walk. Quadratic improvements can be found for DTQW on the two-dimensional lattice [43] and the complete graph [44]. For CTQW, Farhi and Gutmann [30] showed that for certain families of tree graphs the walk can penetrate from the root to the deepest vertex in polynomial time, in contrast to the exponential time taken by the classical walk. Childs *et al.* [45] found a similar result, when they demonstrated that there is an exponential difference in time for transport between the roots of two glued binary trees. In contrast to these other results, it was demonstrated by Krovi and Brun [46] that for certain graphs where the walk evolution operator has sufficiently degenerate eigenvalues, some of the degenerate eigenvectors will span a subspace with zero overlap on certain vertices. Thus, for some initial states that start and remain in this subspace, there are vertices that the walk will never reach and for which the hitting time is infinite, radically different from the classical case where the hitting time will always be finite and the walk will reach every connected vertex.

The improvement in hitting time was used in an algorithmic context by Childs *et al.* [47] to travel between the roots of two glued trees, where the edges connecting the two trees were randomised. Various other algorithms based on quantum walks (or using them as a subroutine) have been found, such as those for testing element distinctness [48], triangle finding [49], matrix product verification [50], and group commutativity testing [51]. However, many of these algorithms can be viewed as a search problem in some state space, and the spatial search problem is an interesting problem in its own right, so we review quantum walk searches

in the next subsection.

2.5.2 Spatial search algorithms

While Grover's algorithm, described in Section 2.1 was a major development in the field it was not designed to search a physical system. In the original algorithm it is assumed that one can act on all the elements of the database, whereas for a physical network connections between nodes of the network may be restricted in some way and so only local interactions are possible. Taking inspiration from classical models of computation, various people began to investigate whether a search could be implemented using quantum walks, employing their speed in traversing graphs to improve search times.

It has been shown that both types of walk can be successfully used to carry out searches on various topologies, but there are differences in how the search is implemented and in the order of the running times. However, the main idea of both models of quantum walk searches is the same; the search is initialised in some delocalised state (normally the uniform distribution), allowed to evolve for a certain time T and then measured in the canonical basis. With high probability, the result of the measurement should be the marked vertex, and the aim is to set the search parameters in such a way as to minimise the time taken to reach a high success probability.

The main difference between searches using the two types of quantum walks is how the oracle function of the Grover search is modelled, or, put more explicitly, how a particular vertex of the graph being searched is marked. A vertex is marked by introducing a perturbation to the quantum walk in such a way that the walk localises on the perturbed site. For DTQWs, a marked vertex is introduced by choosing an alternative coin-flip matrix to be used at that site, the most common choice of marking being

$$C' = -\mathbb{1}_C \,, \tag{2.41}$$

that is, the probability amplitude is reflected back from the marked vertex with a π-phase change. This type of marking was used in the first quantum walk search developed by Shenvi, Kempe & Whaley [9], where they used a discrete-time walk to search for a marked vertex of a n-dimensional hypercube with $N = 2^n$ vertices.

They showed that the system localises on the marked vertex in the optimal time of $T = \mathcal{O}\left(\sqrt{N}\right)$ time steps with probability $\frac{1}{2} - \mathcal{O}\left(\frac{1}{n}\right)$. However, by repeating the algorithm one can find the marked vertex with negligible error and increase the running time by only a constant factor, a common additional step to improve the success probability of search algorithms. After this result, algorithms were developed to search d-dimensional square lattices, though not quite using the quantum walk formalism. The first was developed by Benioff [52]. His algorithm was based on a quantum robot moving in superposition with each time step over the lattice, reaching the optimal search time only for large d but offering no speed-up for $d = 2$. Aaronson and Ambainis [53] used a similar model to Bennioff and employed a 'divide and conquer' approach to create a search which is optimal for $d \geq 3$ and for $d = 2$ runs with a search time $\mathcal{O}\left(\sqrt{N} \ln^{\frac{3}{2}} N\right)$.

Later spatial searches returned to the DTQW search model introduced by Shenvi, Kempe & Whaley [9]. Ambainis, Kempe & Rivosh [10] were the first to return to the problem of searching d-dimensional square lattices with N vertices [10]. They found that for lattices of dimensions $d \geq 3$ the marked vertex is found in $\mathcal{O}\left(\sqrt{N}\right)$ time steps but for $d = 2$ the search succeeds with probability $\mathcal{O}\left(1/\ln N\right)$ in $\mathcal{O}\left(\sqrt{N \ln N}\right)$ time steps. Thus, to increase the probability to $\mathcal{O}\left(1\right)$ one has to repeat the search $\mathcal{O}\left(\sqrt{\ln N}\right)$ times, increasing the total run time to $\mathcal{O}\left(\sqrt{N} \ln^{\frac{3}{2}} N\right)$ or employ amplitude amplification methods to achieve a running time $\mathcal{O}\left(\sqrt{N} \ln N\right)$ [54, 55].

In both of the original DTQW searches [9, 10] it was shown that by constructing two approximate eigenvectors of the evolution operator (one which is the uniform superposition and the other a very close approximation to the target state) the walk remains approximately in the two-dimensional subspace spanned by these two states, similar to the original Grover algorithm. Hein and Tanner [56, 57] gave improved approximations for the search times for both the d-dimensional lattice and the hypercube. They also showed that the two-dimensional subspaces where the search takes place are introduced through avoided crossings in the spectra of the walk's evolution operators between an eigenstate of the unperturbed walk and a perturber state localised on the marked vertex.

Work has continued on improving DTQW searches on these lattices, mainly

for the case of the two-dimensional square lattice, but also for the hypercube where to increase the success probability some additional amplitude amplification steps are required. It was realised by Potoček *et al.* [58] that by adding a self-loop to every vertex of a hypercube (thereby increasing the dimension of the coin space) and alternating between two evolution operators with different coins boosts the success probability of a single run to almost 1, removing the need to repeat the search. They also found that the final state of the Shenvi, Kempe & Whaley hypercube search [9] exists not only on the target vertex but also has a significant overlap with the nearest neighbours. Therefore, if the measured final state is not the target vertex then a classical search of the nearest neighbours will yield the target site, reducing the running time by more than simply repeating the search. A similar approach using localisation on the nearest neighbours of the target site was employed by Ambainis *et al.* [59] for searches on the two-dimensional square lattice, removing the need for the amplification step and reducing the running time to $\mathcal{O}\left(\sqrt{N \ln N}\right)$. The same running time was achieved by Tulsi [60] where an ancilla qubit is used to modify the walk so that the final state has constant overlap with the target state and does not scale with the size of the lattice. In an effort to try to reduce the search running time for two-dimensional lattices a DTQW walk based search has also been investigated on the honeycomb lattice [61]. Using the same methods found in [10, 60] it was found that there is no difference in the behaviour of searches on the honeycomb and two-dimensional square lattices.

The first CTQW based search was developed by Childs & Goldstone [20]. They used the Laplacian of a graph as the walk Hamiltonian and marked a vertex by introducing a projector that effectively alters its on-site energy, giving the search Hamiltonian H_w

$$H_w = -\gamma L - |w\rangle \langle w| \, , \tag{2.42}$$

where γ is the transition rate between vertices. They applied this search to various graphs including the hypercube where they found similar results to Shenvi, Kempe & Whaley [9], and also the complete graph where they found the search time $\mathcal{O}\left(\sqrt{N}\right)$ as expected (the results for the complete graph had been found ear-

lier by Farhi & Gutmann [62] and can, retrospectively, be viewed as a continuous-time walk). For the d-dimensional square lattice they found that for lattices with dimension $d > 4$ the search time is optimal and for $d = 4$ the total search time is $\mathcal{O}\left(\sqrt{N}\ln^{\frac{3}{2}}N\right)$. The $d = 4$ case has a similar success probability scaling found by Ambainis *et al.* [10] for DTQW, where the success probability is a decreasing function of N, and requires $\mathcal{O}\left(\ln N\right)$ repetitions giving rise to the extra $\mathcal{O}\left(\ln^{\frac{3}{2}}N\right)$ factor in the search time. However, they found that for $d = 2, 3$ the algorithm provided no speed-up over the classical search.

The failure of the algorithm to provide a speed-up for $d \leq 4$ results from the quadratic dispersion relation of the Laplacian operator (more details will be given in the next chapter in Section 3.1). To solve this problem Childs & Goldstone replaced the Laplacian operator with a discretized Dirac operator [21], thereby replacing the quadratic dispersion with a linear dispersion relation. Use of the Dirac operator introduces an additional spin degree of freedom and, therefore, this solution is similar to the ideas proposed by Tulsi and Potoček *et al.* [58, 60] where the Hilbert space of the DTQW was augmented by additional degrees of freedom. The use of the Dirac operator gives optimum search times for lattices with dimension $d \geq 3$ and a search time of $\mathcal{O}\left(\sqrt{N}\ln N\right)$ for two-dimensional lattices.

Quantum walk searches have been implemented on other types of lattices such as fractal lattices [63, 64]. A more general formulation of quantum walk searches was constructed by Krovi *et al.* [65] where they were able to develop searches which run in a time quadratically faster than the corresponding classical walk's hitting time. Lovett *et al.* [66] investigated the running time of searches on various two-dimensional lattices. Their findings, along with other results on mixing and hitting times previously mentioned, indicate that the logarithmic factor in the search times for two-dimensional lattices, for both DTQW and CTQW, cannot be removed and that the optimal search time of $\mathcal{O}\left(\sqrt{N}\right)$ may be out of reach for two-dimensional lattices.

2.5.3 Experimental implementations

The experimental implementation of quantum walks has been successfully achieved in various types of systems. The first experiment that can be viewed as a DTQW was reported as early as 1999 by Bouwmeester *et al.* [67], where they created an optical Galton board (a Galton board is a sloped board with an interlaced grid of pins, used to demonstrate classical random walks). Here the walk was simulated using a linear optical cavity, occupied with birefringent crystals to carryout the coin-flip and shift operations by manipulating the phase of photons, to induce spectral diffusion. Photonic experiments that followed improved on the ability to manipulate single photons and utilised different apparatus and setups, for example using interferometers and displacing photons spatially [68, 69] or employing fibre optic networks and translating the walk position of the photons into detector arrival times [70].

Alternative DTQW implementations generally consist of manipulating systems of single atoms. Schmitz *et al.* [14] used a trapped ion to perform a three-step quantum walk in phase space, using the long-lived excited states of the ion as the basis for the coin states. This approach was improved to perform walks of 23 steps and also walks with two ions by Zähringer *et al.* [71]. Atomic walks in position space on spin-dependent optical lattices have been demonstrated by Karski *et al.* [13].

All these experiments focused on discrete-time walks on a one-dimensional line and are limited to the number of steps that they can perform, typically the number of steps achieved is $T \sim 20$. Problems when trying to scale up the walks are encountered in all the experimental models. For example, in trapped-ion experiments there is a difficulty in achieving necessary control and isolating the system from the environment, and in interferometer experiments the apparatus needed increases rapidly with each time step of the walk. However, despite these issues this has not prevented new and interesting effects being investigated in these systems, such as demonstrations of Anderson localisation in quantum walks or different particle statistics being introduced [72].

Experimental realisations of CTQW are not as common as for their discrete-time counterparts. The first demonstration by Du *et al.* [73] involved mapping a

four-site walk onto a two-qubit NMR quantum computer. However, later experiments almost exclusively involved the propagation of photons through waveguide lattices, first investigated in the context of one-dimensional CTQW by Perets *et al.* [15]. They were also able to investigate Anderson localisation and the addition of reflecting boundaries on the walk's behaviour. Use of waveguides also allowed propagation of the walks over larger numbers of sites ($N \sim 100$). In the past couple of years these ideas have been expanded upon and walks using two correlated photons have been carried out [74, 75].

Recently the first demonstration of a two-dimensional DTQW was presented by Jeong *et al.* [76]. The team were able to simulate the Grover walk by employing the theoretical results of Franco *et al.* [77], where it was shown that a two-dimensional walk can be recreated by alternating between one-dimensional walks in the x- and y-directions with each time step. This result has opened the door towards the first demonstration of the Grover search algorithm on a two-dimensional lattice.
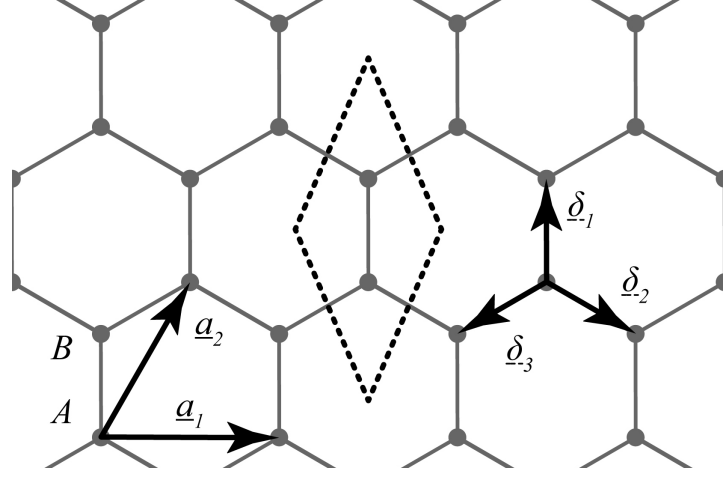
2.6 Graphene - Lattice and Spectrum Properties

As the remainder of this thesis will focus on quantum walks on graphene and related structures, we will now review the relevant properties of graphene and standardise the notation that will be used throughout. Detailed introductions to the properties of graphene and related carbon nanostructures can be found in [78, 79].

Graphene is a single layer of carbon atoms arranged in a honeycomb lattice. The honeycomb lattice is a bipartite lattice with two sublattices, labelled A and B, and the unit cell contains two carbon atoms. The spatial and reciprocal lattices are shown in Figures 2.5 & 2.6. The primitive vectors describing translations between unit cells and the nearest-neighbour vectors between A and B sublattices are given by

$$\underline{a}_1 = a\underline{\mathbf{i}}, \qquad \underline{a}_2 = \frac{a}{2}\underline{\mathbf{i}}, +\frac{\sqrt{3}}{2}a\underline{\mathbf{j}} \tag{2.43}$$

Figure 2.5: Graphene with lattice vectors $\underline{a}_{1/2}$, nearest-neigbour vectors $\underline{\delta}_i$ and unit cell (dashed lines).

$$\underline{\delta}_1 = \frac{a}{\sqrt{3}}\mathbf{j}, \qquad \underline{\delta}_2 = \frac{a}{2}\mathbf{i} - \frac{a}{2\sqrt{3}}\mathbf{j}, \qquad \underline{\delta}_3 = -\frac{a}{2}\mathbf{i} - \frac{a}{2\sqrt{3}}\mathbf{j}, \tag{2.44}$$

where $a = 0.246$nm is the lattice constant for carbon. The unit vectors of the reciprocal lattice are

$$\underline{b}_1 = \frac{2\pi}{a}\mathbf{i} - \frac{2\pi}{\sqrt{3}a}\mathbf{j}, \qquad \underline{b}_2 = \frac{4\pi}{\sqrt{3}a}\mathbf{j}. \tag{2.45}$$

The first Brillouin zone is also a hexagon with the important symmetry points of the reciprocal lattice

$$\underline{K} = \frac{2\pi}{3a}\underline{i} + \frac{2\pi}{\sqrt{3}a}\underline{j}, \qquad \underline{K}' = \frac{4\pi}{3a}\underline{i}, \qquad \underline{M} = \frac{2\pi}{\sqrt{3}a}\underline{j}. \tag{2.46}$$

As will soon become clear, the two inequivalent corners of the Brillouin zone, $\underline{K}$ and $\underline{K}'$, are of particular importance.

The energy spectrum of electrons in graphene was first derived by Wallace [80] when considering the band theory of graphite using a tight-binding Hamiltonian. When constructing the tight-binding Hamiltonian we use the orthonormal basis states $\{|\alpha, \beta\rangle^A, |\alpha, \beta\rangle^B\}$ to denote states on either the A or B sublattice in the cell at position $\underline{R}(\alpha, \beta) = \alpha\underline{a}_1 + \beta\underline{a}_2 = \left(\alpha + \frac{1}{2}\beta\right)a\underline{i} + \frac{\sqrt{3}}{2}\beta a\underline{j}$. We construct our lattice in such a way that the A sublattice is generated by the translation vector
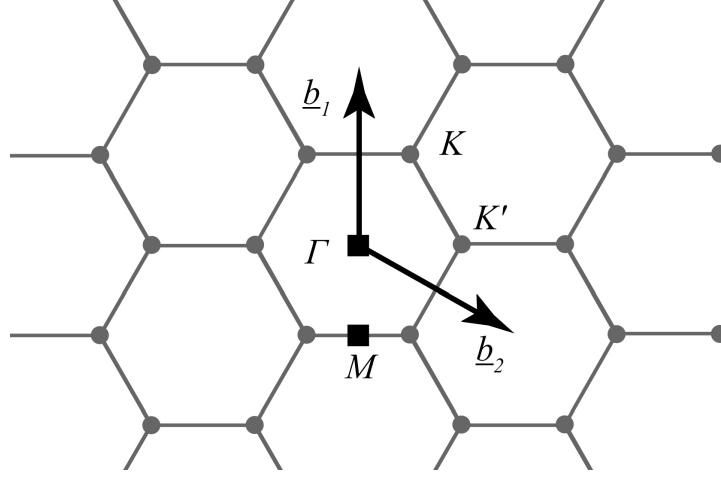
Figure 2.6: Reciprocal lattice with basis vectors $\underline{b}_{1/2}$, symmetry points $\underline{\Gamma}$, $\underline{K}$, $\underline{K}'$, $\underline{M}$ and first Brillouin zone (hexagon).

$\underline{R}(\alpha, \beta)$. That is, the position of $(\alpha, \beta)^A$ is given by $\underline{R}(\alpha, \beta)$ and the position of $(\alpha, \beta)^B$ is given by $\underline{R}(\alpha, \beta) + \underline{\delta}_1$, as is illustrated in Figure 2.5.

For graphene, the tight-binding Hamiltonian is

$$
\begin{aligned}
H = \sum_{(\alpha, \beta)} \sum_{(\alpha', \beta')} \Big[& \delta_{\alpha, \alpha'} \delta_{\beta, \beta'} \epsilon_D \left(|\alpha, \beta\rangle^A \langle\alpha', \beta'|^A + |\alpha, \beta\rangle^B \langle\alpha', \beta'|^B \right) \\
& + t_{(\alpha', \beta')}^{(\alpha, \beta)} \left(|\alpha, \beta\rangle^A \langle\alpha', \beta'|^B + |\alpha', \beta'\rangle^B \langle\alpha, \beta|^A \right) \Big],
\end{aligned}
\tag{2.47}
$$

where ϵ_D is the on-site carbon energy and the hopping potential $t_{(\alpha', \beta')}^{(\alpha, \beta)}$ is described by

$$
t_{(\alpha', \beta')}^{(\alpha, \beta)} = \begin{cases} t & \text{if } (\alpha', \beta') \in \{(\alpha, \beta), (\alpha, \beta - 1), (\alpha + 1, \beta - 1)\} \\ 0 & \text{for all other values of } (\alpha', \beta'). \end{cases}
\tag{2.48}
$$

We note that this Hamiltonian can be rewritten, in terms of the adjacency matrix of the underlying lattice, as $H = \epsilon_D \mathbb{1} + tA$.

As the lattice possesses a translational symmetry the Hamiltonian can be solved using linear superpositions of Bloch functions over both sublattices. We will focus on finite-sized lattices and assume periodic boundary conditions along the axes of both primitive vectors (i.e. $|\psi\rangle = \sum_{\alpha=1}^{m} \sum_{\beta=1}^{n} \left(\psi_{\alpha, \beta}^A |\alpha, \beta\rangle^A + \psi_{\alpha, \beta}^B |\alpha, \beta\rangle^B \right)$

with $\psi_{\alpha,\beta}^{A(B)} = \psi_{\alpha+m,\beta}^{A(B)} = \psi_{\alpha,\beta+n}^{A(B)}$), so that the topology of our lattice is a torus. Thus, our wavefunctions on the torus take the Bloch function form

$$|\psi\rangle = C_A(\underline{k})|\phi_A\rangle + C_B(\underline{k})|\phi_B\rangle \tag{2.49}$$

$$= \sum_{(\alpha,\beta)} \left[\frac{C_A(\underline{k})}{\sqrt{M}} e^{i\underline{k}\cdot\underline{R}(\alpha,\beta)}|\alpha,\beta\rangle^A + \frac{C_B(\underline{k})}{\sqrt{M}} e^{i\underline{k}\cdot(\underline{R}(\alpha,\beta)+\underline{\delta}_1)}|\alpha,\beta\rangle^B \right], \tag{2.50}$$

with M being the number of unit cells and $\underline{k}$ the momenta. Applying the periodic boundary conditions we obtain the following quantised momenta

$$k_x = \frac{2\pi p}{ma}, \qquad k_y = \frac{1}{\sqrt{3}} \left(\frac{4\pi q}{na} - k_x \right), \tag{2.51}$$

where $p \in \{0, 1, \ldots m-1\}$ and $q \in \{0, 1, \ldots n-1\}$. Using the Bloch functions $|\phi_A\rangle$ and $|\phi_B\rangle$ for each sublattice, the tight-binding Hamiltonian can be reduced to a simple 2×2 matrix eigenvalue problem. We note that all the atoms in the lattice are carbon $\langle\phi_A|H|\phi_A\rangle = \langle\phi_B|H|\phi_B\rangle$ and the Hamiltonian must remain Hermitian. Using these facts we find

$$\begin{aligned} C_A(\underline{k}) H_{AA} + C_B(\underline{k}) H_{AB} &= EC_A(\underline{k}) \\ C_A(\underline{k}) H_{AB}^* + C_B(\underline{k}) H_{AA} &= EC_B(\underline{k}) \ . \end{aligned} \tag{2.52}$$

The determinant gives the energy relation $E(\underline{k}) = \epsilon_D \pm \sqrt{H_{AB}(\underline{k}) H_{AB}^*(\underline{k})}$, where $\epsilon_D = H_{AA}$. The explicit form of the matrix element H_{AB} is
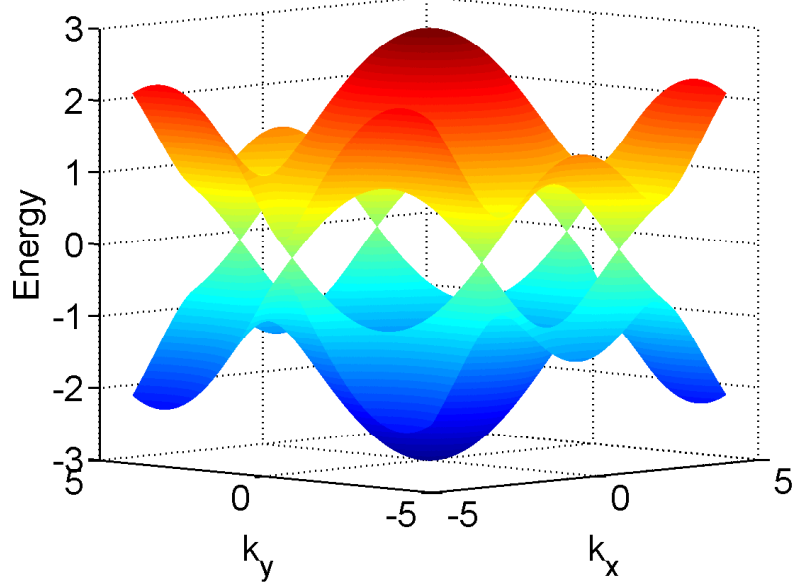
$$H_{AB} = \langle\phi_A|H|\phi_B\rangle \tag{2.53}$$

$$= \frac{1}{M} \sum_{(\alpha,\beta)} \sum_{(\alpha',\beta')} e^{-i\underline{k}\cdot(\underline{R}(\alpha,\beta)-\underline{R}(\alpha',\beta')-\underline{\delta}_1)} \langle\alpha,\beta|^A H |\alpha',\beta'\rangle^B \tag{2.54}$$

$$= t \left(e^{\frac{ik_y a}{\sqrt{3}}} + 2e^{\frac{-ik_y a}{2\sqrt{3}}} \cos\left(\frac{k_x a}{2}\right) \right), \tag{2.55}$$

leading to the energy relation

$$E = \epsilon_D \pm t \sqrt{1 + 4\cos^2\left(\frac{k_x a}{2}\right) + 4\cos\left(\frac{k_x a}{2}\right)\cos\left(\frac{\sqrt{3}k_y a}{2}\right)}. \tag{2.56}$$

Figure 2.7: Energy dispersion relation for infinite graphene sheet, only the first Brillouin zone is shown. ($\epsilon_D = 0$)

The coefficients $C_A(\underline{k})$, $C_B(\underline{k})$ are found from the eigenvalue equations (2.52) and the normalisation condition $|C_A(\underline{k})|^2 + |C_B(\underline{k})|^2 = 1$, that is,

$$C_A(\underline{k}) = \frac{1}{\sqrt{2}} \qquad C_B(\underline{k}) = \frac{1}{\sqrt{2}} \times \begin{cases} \frac{H_{AB}^*}{|H_{AB}|} & \text{for } E > \epsilon_D \\ \frac{-H_{AB}^*}{|H_{AB}|} & \text{for } E < \epsilon_D. \end{cases} \qquad (2.57)$$

Implied from the expressions for the coefficients C_A and C_B is the existence of an operator to transform states with energy greater than ϵ_D into states with energy less than ϵ_D. Remaining in the reduced basis $\{|\phi_A\rangle, |\phi_B\rangle\}$, this operator is simply the third Pauli matrix $\sigma_3 = \left(\begin{smallmatrix} 1 & 0 \\ 0 & -1 \end{smallmatrix}\right)$. Using σ_3, the chiral symmetry of the spectrum around ϵ_D can be expressed in the anti-commutation relation $\{H, \sigma_3\} = 2\epsilon_D \sigma_3$.

A plot of Equation (2.56) as a function of $\underline{k}$ is shown in Figure 2.7 for an infinite graphene sheet, where $\underline{k}$ becomes continuous. As there are two atoms per unit cell the spectrum has two branches, the upper branch being the conduction band and the lower the valence band, which meet at the corners of the Brillouin zone, the K-points. The energy at the K-points is ϵ_D which we name the Dirac

energy. Around these points the behaviour of the spectrum is conical, and, in fact, by performing a Taylor expansion of $H_{AB}(\underline{k})$ around either $\underline{K}$ point we find

$$H_{AB}(\underline{k}) = H_{AB}(\underline{K} + \delta\underline{k}) \tag{2.58}$$

$$\approx H_{AB}(\underline{K}) + (\underline{k} - \underline{K}) \left.\frac{\partial H_{AB}(\underline{k}')}{\partial \underline{k}'}\right|_{\underline{k}'=\underline{K}} \tag{2.59}$$

$$= \frac{\sqrt{3}}{2}t\left(\delta k_x e^{i\frac{2\pi}{3}} + \delta k_y e^{-i\frac{2\pi}{3}}\right), \tag{2.60}$$

which leads to

$$E(\underline{k}) \approx \epsilon_D \pm t\frac{\sqrt{3}}{2}\sqrt{\delta k_x^2 + \delta k_y^2} = \epsilon_D \pm t\frac{\sqrt{3}}{2}|\delta k| . \tag{2.61}$$

Thus, we see that around the $\underline{K}$-points the spectrum has a conic dispersion relation. It is this property that has lead to interesting electronic behaviour and large amounts of interest in graphene [78, 81]. For finite graphene lattices, the spectrum shown in Figure 2.7 will obviously become discrete with a finite number of states in the region described by the conic dispersion, and, potentially, exactly at the $\underline{K}$-points where the conduction and valence bands meet. In fact, using the quantised momenta in Equation (2.51) obtained for periodic boundary conditions, and the values for the $\underline{K}$-points in Equation (2.46), we find that there are four degenerate eigenenergies that coincide exactly with the Dirac energy when m and n are both multiples of 3. These four states, known as the Dirac states, are given by

$$|\psi_{\underline{K}\pm}\rangle = \sum_{(\alpha,\beta)} \left[\frac{1}{\sqrt{2M}}e^{i\frac{2\pi}{3}(\alpha+2\beta)}|\alpha,\beta\rangle^A \pm \frac{1}{\sqrt{2M}}e^{i\frac{2\pi}{3}(\alpha+2\beta+2)}|\alpha,\beta\rangle^B\right] \tag{2.62}$$

$$|\psi_{\underline{K}'\pm}\rangle = \sum_{(\alpha,\beta)} \left[\frac{1}{\sqrt{2M}}e^{i\frac{2\pi}{3}(2\alpha+\beta)}|\alpha,\beta\rangle^A \pm \frac{1}{\sqrt{2M}}e^{i\frac{2\pi}{3}(2\alpha+\beta)}|\alpha,\beta\rangle^B\right] \tag{2.63}$$

where the coefficients are $C_B(\underline{K}) = e^{i\frac{2\pi}{3}}$ and $C_B(\underline{K}') = 1$.

3

Quantum search on a graphene lattice

We will start this chapter with a review of how quantum search algorithms can be recast in terms of an avoided crossing problem. We will then discuss the Childs & Goldstone continuous-time search algorithm [20], and focus on issues that the search has in lower dimensional systems. The algorithm was designed to search a d-dimensional regular square lattice for a marked vertex but fails to improve on the classical search time for $d < 4$. We will explain how, in the framework of avoided crossings, this lack of speed-up can be traced back to the quadratic dispersion relation of the search Hamiltonian and the spectral gap at the avoided crossing.

This will be followed by an explanation of how graphene lattices can present a solution to the problem of a lack of speed-up for lower dimensions, and a short discussion on why, for DTQW searches, graphene lattices behave in the same way as square lattices, shown in [61]. However, it will be shown by investigating the dynamics in a reduced Hilbert space involving only critically important states, that by using alternative ways of marking a vertex, a CTQW quantum search can be constructed on a graphene lattice. Further analysis of the search running time and success probability using the full Hilbert space will also be given, using similar methods to those found in [20, 21].

We will complete this chapter by demonstrating that the search mechanism

described can be used to create a communication protocol across a graphene lattice, where probability amplitude is transferred from one perturbed site to another. It will be shown that the reduced model outlined can be used to describe the behaviour of certain state transfer setups, allowing one to construct a secure state transfer system or develop a method of switching.

3.1   Introduction

3.1.1   Searching using avoided crossings

In [56] it was shown that the quantum walk search problem can viewed in terms of an avoided crossing interaction between an eigenstate of the DTQW evolution operator and a perturber state which is a state localised on the marked vertex. This is also true in CTQW searches but in these cases the avoided crossing is in the spectrum of the search Hamiltonian. The interaction between an eigenstate of the unperturbed walk Hamiltonian and a perturber state gives rise to, at the minimal energy gap of the avoided crossing, two states which are linear superpositions of the two former ones. If the system is placed in the eigenstate of the unperturbed walk Hamiltonian and allowed to evolve in time, it will then rotate into the localised state.

As an example of the avoided crossing mechanism, we consider a Hamiltonian constructed using only two states $|a_1\rangle$ and $|a_2\rangle$, with energies ϵ_1 and ϵ_2 which are dependent on some parameter λ

$$H_o\left(\lambda\right) = \begin{pmatrix} \epsilon_1\left(\lambda\right) & 0 \\ 0 & \epsilon_2\left(\lambda\right) \end{pmatrix}.$$
(3.1)

For some particular value of λ, for example $\lambda = 0$, these energies cross and $\epsilon_1\left(0\right) = \epsilon_2\left(0\right) = \epsilon$, forming a doubly degenerate state. It is clear that if one adds an interaction between these states in the form of a perturbing potential term

$$H\left(\lambda\right) = H_o\left(\lambda\right) + V = \begin{pmatrix} \epsilon_1\left(\lambda\right) & v \\ v^* & \epsilon_2\left(\lambda\right) \end{pmatrix},$$
(3.2)

then the degeneracy in the eigenenergies for $\lambda = 0$ is lifted and the eigenenergies at this point become

$$\epsilon_{\pm} = \frac{\epsilon_1(0) + \epsilon_2(0)}{2} \pm \frac{1}{2}\sqrt{(\epsilon_2(0) - \epsilon_1(0))^2 + 4|v|^2} \tag{3.3}$$

$$= \epsilon \pm |v|, \tag{3.4}$$

with eigenstates

$$|b_+\rangle = \frac{1}{|v|\sqrt{2}}\begin{pmatrix} v \\ |v| \end{pmatrix}, \quad |b_-\rangle = \frac{1}{|v|\sqrt{2}}\begin{pmatrix} -v \\ |v| \end{pmatrix}. \tag{3.5}$$

Placing the system in one of the unperturbed states, $|a_1\rangle$, and allowing it to evolve in time

$$|\psi(t)\rangle = e^{-iHt}|a_1\rangle \tag{3.6}$$

$$= \frac{v^* e^{-i\epsilon t}}{|v|\sqrt{2}}\left(e^{-i|v|t}|b_+\rangle - e^{i|v|t}|b_-\rangle\right) \tag{3.7}$$

$$= e^{-i\epsilon t}\left(\cos(|v|t)|a_1\rangle - \frac{v^*}{|v|}\sin(|v|t)|a_2\rangle\right), \tag{3.8}$$

we find that (up to an arbitrary phase) the system rotates between the two states in a time $T = \frac{\pi}{2|v|}$, inversely proportional to the energy gap at the crossing. It should now be clear, if one can create an interaction between an eigenstate of the unperturbed walk Hamiltonian and a localised perturber state that can be well approximated in this avoided crossing picture, one can create a quantum walk search algorithm.

3.1.2 Continuous-time searches

Childs & Goldstone's search algorithm [20] was the first continuous-time algorithm for searches on a lattice and although their analysis in [20] takes a different viewpoint the algorithm can be understood in terms of an avoided crossing picture. Their algorithm takes place on a d-dimensional square lattice, G, with N vertices and is periodic along each axis with period $N^{\frac{1}{d}}$. The Hilbert space de-

scribing the walk is spanned by the states $|\underline{j}\rangle$, where $\underline{j}$ is a vertex in G and the labelling is a d-component vector with components $j_i \in \{0, 1 \ldots N^{\frac{1}{d}} - 1\}$. To create a quantum walk search over the lattice they perturbed the system using (what they called) the oracle Hamiltonian

$$H_{\underline{w}} = - |\underline{w}\rangle \langle \underline{w}| \ , \tag{3.9}$$

marking the single vertex $\underline{w}$. This Hamiltonian has the ground state $|\underline{w}\rangle$ with energy -1 and all other states have energy zero. As Childs & Goldstone explain in their first search paper [20], the Grover search problem is essentially finding the ground state of the oracle Hamiltonian.

The search Hamiltonian for the graph G follows as

$$H = -\gamma L + H_{\underline{w}} = -\gamma L - |\underline{w}\rangle \langle \underline{w}| \ , \tag{3.10}$$

where L is the Laplacian of the graph and γ is a free parameter. The first term, $-\gamma L$, can be viewed as the basic walk Hamiltonian, which is then perturbed by the second term, $- |\underline{w}\rangle \langle \underline{w}|$. It is assumed in the search problem that the oracle Hamiltonian is given but that the state involved remains unknown. Another important conceptual point is that the free parameter γ is placed in front of the Laplacian rather than the oracle Hamiltonian, implying control over the interactions in the lattice and not control over the strength of the perturbation itself. Otherwise, control over the oracle Hamiltonian term implies knowledge of the marked vertex, rendering the search problem moot.

In the search Hamiltonian given in Equation (3.10) the oracle Hamiltonian fulfils the role of the interaction between the localised state, $|\underline{w}\rangle$, and the unperturbed eigenstates. The search algorithm is then created by inducing an avoided crossing, by judicious choice of the free parameter γ, with a particular eigenstate, typically the ground state of the walk Hamiltonian. For the Laplacian this is the uniform superposition

$$|s\rangle = \frac{1}{\sqrt{N}} \sum_{\underline{j}} |\underline{j}\rangle \ . \tag{3.11}$$

The search problem then attempts to maximise the success amplitude

$$\langle \underline{w} | \, e^{-iHt} \, | s \rangle = \sum_a \langle \underline{w} | \psi_a \rangle \, \langle \psi_a | s \rangle \, e^{-iE_a t} \, , \tag{3.12}$$

while evolving the system for as short a time as possible, where $|\psi_a\rangle$ and E_a are the eigenstates and eigenenergies of the search Hamiltonian.

For an explanation of the search Hamiltonian behaviour, knowledge of the spectrum and eigenstates of Laplacian is helpful. The eigenstates of $-L$ are simply the Bloch states

$$|\psi_{\underline{k}}\rangle = \frac{1}{\sqrt{N}} \sum_{\underline{j}} e^{i\underline{k} \cdot \underline{j}} \, |\underline{j}\rangle \, , \tag{3.13}$$

with eigenenergies

$$\epsilon\left(\underline{k}\right) = 2d - 2 \sum_{l=1}^{d} \cos\left(k_l\right) \, , \tag{3.14}$$

where

$$k_l = \frac{2\pi m_l}{N^{\frac{1}{d}}} \tag{3.15}$$

with $m_l \in \{0, 1 \ldots N^{\frac{1}{d}} - 1\}$, for each $l = 1, \ldots d$.

By considering the spectrum around the ground state energy we can see why the algorithm struggles in lower dimensions. It can be easily seen from Equation (3.14) that for small momenta the eigenenergies can be well-approximated by

$$\epsilon\left(\underline{k}\right) \approx k^2 = \sum_{j=1}^{d} \left(\frac{2\pi m_j}{N^{\frac{1}{d}}} \right)^2 \, , \tag{3.16}$$

where the notation $k^2 = k_1^2 + \ldots + k_d^2$ has been used. It is clear that the first excited state has energy

$$E_1 = \mathcal{O}\left(N^{-\frac{2}{d}} \right) \, . \tag{3.17}$$

As we have already seen in the earlier avoided crossing example, the width of the avoided crossing is directly proportional to the interaction between the

eigenstate and the localised state, which is

$$\Delta \sim \langle s | H | \underline{w} \rangle \tag{3.18}$$

$$= \langle s | \left(-\gamma L - | \underline{w} \rangle \langle \underline{w} | \right) | \underline{w} \rangle \tag{3.19}$$

$$= \mathcal{O}\left(N^{-\frac{1}{2}} \right), \tag{3.20}$$

where the final equality follows from $\langle s | \underline{w} \rangle = \frac{1}{\sqrt{N}}$. It should be noted that the scaling of the gap does not depend on the dimension of the lattice, only on the number of sites.

The avoided crossing remains isolated in the spectrum provided that other states do not intrude, that is, if $E_1 \geq \Delta$ for all N. It can be seen on comparison that the inequality is true for $d > 4$ and that $d = 4$ is a critical case where the two energy scales scale the same way. Thus, it can be inferred that other states do not interact with the crossing and that the two-state approximation remains valid for $d \geq 4$. However, for $d < 4$, as the system size increases, the first excited energy E_1 becomes smaller than the gap at the avoided crossing involving the ground state and other states in the spectrum necessarily start to interact with the crossing. This destroys the search mechanism, as the probability of rotating into the localised state $| \underline{w} \rangle$ is reduced as the probability of evolving into other interacting states increases.

In Section 2.6 we reviewed the properties of graphene that would be relevant for the rest of this thesis. The tight-binding model described in that section is equivalent to the Laplacian walk Hamiltonian used by Childs & Goldstone, if the on-site energy is set equal to the valency of the vertices and the potential is set to $t = -1$. Therefore, the spectrum and eigenstates calculated there are directly relevant to this search model. It was shown that around the $\underline{K}$-points in momentum space that the spectrum has a conical, rather than quadratic, dispersion relation. In fact, using Equations (2.51) & (2.61), we see that in this region of the spectrum the eigenenergies scale as

$$E \sim |\delta k| = \mathcal{O}\left(N^{-\frac{1}{2}} \right), \tag{3.21}$$

for a rectangular graphene lattice with approximately equal numbers of cells

along each axis. The behaviour of the gap remains the same as in Equation (3.20), regardless of which eigenstate we choose to induce the avoided crossing with, since the inner product of any Bloch state and $|\underline{w}\rangle$ is of order $\mathcal{O}\left(N^{-\frac{1}{2}}\right)$. On comparison with the scaling of the avoided crossing gap, we have a critical case where the avoided crossing gap and the difference between successive eigenenergies scale in the same way, but now the critical case occurs naturally for a two-dimensional graphene lattice rather than a four-dimensional square lattice. The implication is then, if one can form an avoided crossing with states in the conical region of the spectrum, a search can successfully be created.

3.1.3   Discrete-time searches

Given the number of discrete-time search algorithms (see SubSection 2.5.2), one may wonder if the use of a graphene lattice can improve the running time of a discrete-time search algorithm. Unfortunately this is not the case, and the search behaviour is the same as on a square lattice. This is due to walk dynamics being implemented by the repeated application of the unitary evolution operator in discrete-time searches. Rather than the avoided crossing taking place in the spectrum of the Hamiltonian, as in the CTQW, the avoided crossing takes place in the eigenphases of the evolution operator. DTQW searches for the square and graphene lattices were first analysed in [10, 61]. In both papers, periodic boundary conditions are assumed so the spatial component (excluding the coin state component) of the eigenstates are simply Bloch states, which have the general form

$$|\phi_{\underline{k}}\rangle = \frac{1}{\sqrt{N}} \bigotimes_{j=1}^{d} \left[\sum_{l=0}^{N^{\frac{1}{d}}-1} e^{i\frac{2\pi k_j}{N^{1/d}}} |l\rangle \right] , \tag{3.22}$$

the important aspect of the eigenstates to note being the normalisation factor of $\frac{1}{\sqrt{N}}$. Again, the chosen starting state is the uniform superposition $|s\rangle$ with $\underline{k} = \underline{0}$, which is an eigenstate of the unperturbed walk operator with eigenvalue 1. Thus, the interaction between the uniform superposition and the localised state $|\underline{w}\rangle$, and so the avoided crossing gap, scales as

$$\Delta = \langle s| U |\underline{w}\rangle = \mathcal{O}\left(N^{-\frac{1}{2}}\right) , \tag{3.23}$$

where U is the search evolution operator.

One must then compare this scaling with the eigenphases associated with states nearest the uniform superposition. As the evolution operator is unitary the eigenvalues take the form $e^{i\theta_{\underline{k}}}$, and for a translationally invariant lattice with periodic boundary conditions the eigenphases satisfy the general form

$$\cos\theta_{\underline{k}} = \sum_{j=1}^{d} a_j^c \cos\left(\frac{2\pi k_j}{N^{\frac{1}{d}}}\right) + b \tag{3.24}$$

$$\sin\theta_{\underline{k}} = \sum_{j=1}^{d} a_j^s \sin\left(\frac{2\pi k_j}{N^{\frac{1}{d}}}\right) , \tag{3.25}$$

where $k_j \in \{0, 1, \ldots N^{1/d} - 1\}$ and b is a constant (the exact expressions can be found in [10, 61] but a generalisation will suffice for the explanation here). Taylor expanding around the relevant point $\theta_{\underline{0}} = \underline{0}$, one finds

$$e^{i\theta_{\underline{k}}} \approx 1 + i \sum_{j=1}^{d} a_j^s \theta_{\underline{k}} + \mathcal{O}\left(\theta_{\underline{k}}^2\right) . \tag{3.26}$$

That is, the distance between eigenphases scales as $\mathcal{O}\left(N^{-1/d}\right)$ since $\theta_{\underline{k}} = \mathcal{O}\left(N^{-1/d}\right)$. For $d = 2$, we find the critical case where the scaling of the avoided crossing gap and the spacing between successive eigenphases scales the same. Here we have only used that the lattice is periodic and two-dimensional, the exact nature of the lattice has not been required, so we see that the square and graphene lattices have the same avoided crossing/spectrum interaction behaviour.

It is clear then that the advantageous properties of a graphene lattice only become apparent in the continuous-time model, and not the discrete-time case. Due to the unitary evolution operator used in the discrete-time walk, walks on both lattices have a conical dispersion relation in their spectra around $e^{i\theta_{\underline{k}}} = 1$ since they are linear in $\theta_{\underline{k}}$ (to first order), as can be seen from Equation (3.26). This is in contrast to the continuous-time searches where a conical dispersion relation only appears in the spectrum of the search Hamiltonian for the graphene lattice and not the square lattice.
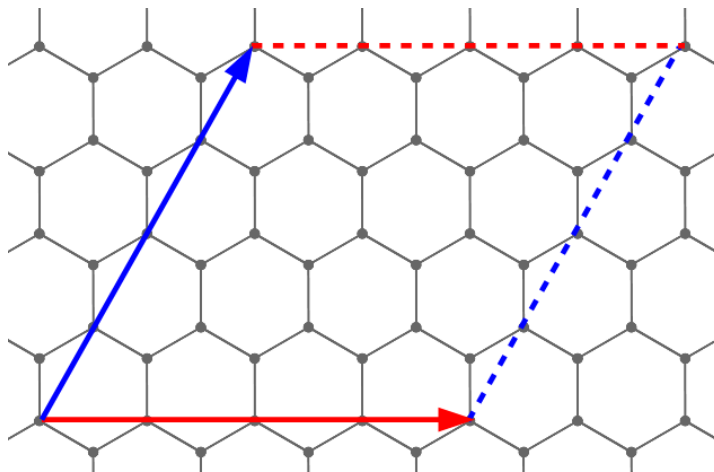
Figure 3.1: An example of the torus cell with $m = n = 4$. Border lines with the same colour are equivalent.

3.2 Creating a search

As we have seen, the key to creating a successful search in two-dimensions is creating an avoided crossing in a region of the spectrum which has a conical dispersion relation. In order to achieve this, we now change the search topology from a square lattice to a graphene lattice, the relevant details of which can be found in Section 2.6. We apply periodic boundary conditions on the lattice along the axes described by the basis vectors so that the walk takes place on a torus, an example of the torus cell is shown in Figure 3.1. For simplicity, we will also set the lattice constant to $a = 1$. We will in general only focus on tori where the number of primitive cells in each direction are equal and those with states whose eigenenergy coincides with the Dirac energy. As the Dirac states lie directly in the conical dispersion region it is with these states that we want to create an avoided crossing, rather than the uniform superposition at the ground state.

Rather than using the Laplacian $H_o = -\gamma L$ as the unperturbed walk Hamiltonian, we will use the adjacency matrix

$$H_o = -\gamma A \,, \tag{3.27}$$

as the unperturbed walk Hamiltonian to simplify later calculations. As the graphene lattice is a regular lattice, the Laplacian can be written as $-L = 3\mathbb{1} - A$,

where the factor of three arises because the graphene lattice is 3-regular. Since the adjacency and identity matrices commute, the unperturbed walk evolution operator using $H_o = -\gamma L$ can be expressed as

$$U\left(t\right) = e^{i\gamma Lt} = e^{i\gamma 3t}e^{-i\gamma At} .$$ (3.28)

Thus, for regular graphs, the diagonal entries of the Laplacian only introduce an overall phase to the system's evolution and so the walk dynamics under the Laplacian and the adjacency matrices are equivalent. The unperturbed walk Hamiltonian $H_o = -\gamma A$ is, in the tight-binding model described in Section 2.6, equivalent to setting $\epsilon_D = 0$ and $t = -\gamma$.

The next step is to introduce the perturbation marking a particular vertex in such a way that it interacts with the Dirac states. An initial thought would be to keep the same perturbation used by Childs & Goldstone [20], in Equation (3.9), and use the search Hamiltonian in Equation (3.10). It would then be necessary to modify the parameter γ until the perturber state interacts with the relevant states, occurring when they have comparable energies. However, it turns out that it is not possible to introduce an effective marking through the type of perturbation in Equation (3.9).

The inefficacy of the on-site energy perturbation is perhaps most easily seen by slightly changing the search Hamiltonian for the moment, so that the parameter γ is placed in front of the oracle Hamiltonian

$$H = -A - \gamma \left|\underline{w}\right\rangle \left\langle\underline{w}\right| .$$ (3.29)

This has the effect of keeping the bond strength (or hopping potential) between vertices across the whole lattice constant and continuously altering only the on-site energy of the marked vertex. This is in contrast to Equation (3.10) where the marked vertex has a fixed on-site energy which is different to all other vertices and the bond strength between *all* connected vertices is continuously changed. Figure 3.2 shows the spectrum of Equation (3.29) as a function of γ. It is clear that the perturbation only begins to interact with the Dirac states in the limit $\gamma \to 0$, that is, when the on-site energy of the marked vertex approaches the same
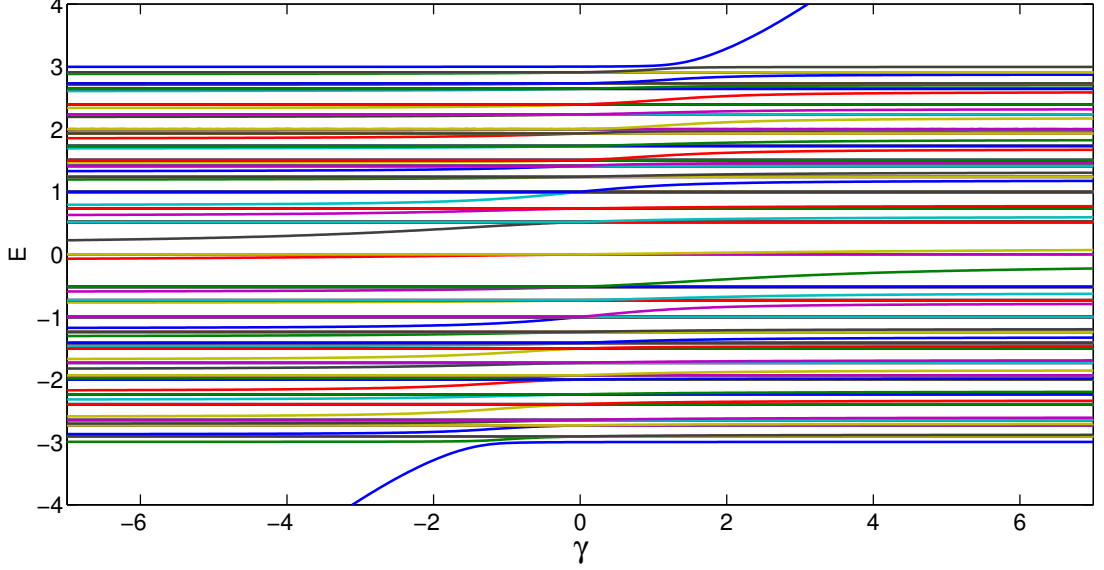
Figure 3.2: Spectrum of $H = -A - \gamma \left| \underline{w} \right\rangle \left\langle \underline{w} \right|$ as a function of γ for a 12×12 cell torus

on-site energy as all other vertices. In this limit we do not find an avoided crossing which can be utilised, but rather we find only the unperturbed Dirac states which are simply Bloch states. Consequently, no matter how long we evolve the system for, the probability of measuring the system and finding the correct site is $\frac{1}{N}$, which is no better than a random guess.

As marking a particular vertex by introducing a projector onto that vertex (effectively changing the on-site energy) does not lead to a successful search, an alternative method of marking a vertex is to alter the bond strength between the marked site and its nearest-neighbours. There are several ways of doing this, but we will choose to change the bond strength to all three nearest-neighbours equally (other perturbation types will be investigated in Chapter 4). The perturbation matrix W we use, for marking the vertex $(\alpha_0, \beta_0)^A$ on the A-sublattice, is

$$W = \left| \alpha_0, \beta_0 \right\rangle^A \left(\left\langle \alpha_0, \beta_0 \right|^B + \left\langle \alpha_0, \beta_0 - 1 \right|^B + \left\langle \alpha_0 + 1, \beta_0 - 1 \right|^B \right) + h.c. \ . \quad (3.30)$$

By defining the state

$$\left| \ell \right\rangle \equiv \frac{1}{\sqrt{3}} \left(\left| \alpha_0, \beta_0 \right\rangle^B + \left| \alpha_0, \beta_0 - 1 \right\rangle^B + \left| \alpha_0 + 1, \beta_0 - 1 \right\rangle^B \right) , \quad (3.31)$$

the perturbation matrix W can be rewritten in the slightly more illuminating form

$$W = \sqrt{3}\,|\alpha_0, \beta_0\rangle^A \langle \ell| + \sqrt{3}\,|\ell\rangle \langle \alpha_0, \beta_0|^A \ . \tag{3.32}$$

It is now clearer that our perturbation matrix is a rank-2 matrix involving two states, the basis state living on the marked vertex and a state localised on the nearest-neighbours of the marked site. As it is a rank-2 perturbation, one would expect two perturber states in the spectrum of the search Hamiltonian, not a single perturber state that arises from the rank-1 perturbation used by Childs & Goldstone [20]. We also note that the perturbation matrix in Equation (3.32) satisfies the same anti-commutation relation as the graphene tight-binding Hamiltonian, namely $\{W, \sigma_3\} = 0$, therefore obeying the same spectral symmetry around $\epsilon_D = 0$ as the graphene spectrum. This indicates that there will be one perturber state in both bands of the spectrum, as one state must have positive energy and the other negative energy. This means that the search Hamiltonian will obey the same spectral symmetry as the graphene tight-binding Hamiltonian.

In contrast, a search Hamiltonian using a rank-1 Childs & Goldstone type of perturbation from Equation (3.9) breaks this spectral symmetry. It is clearer that the perturber state created by such a perturbation only interacts with the Dirac states in the limit of vanishing perturbation, as this is the only point that the search Hamiltonian obeys the symmetry.

Returning to our earlier convention of placing the free parameter γ in front of the adjacency matrix A, our search Hamiltonian is then

$$H = -\gamma A + \sqrt{3}\,|\alpha_0, \beta_0\rangle^A \langle \ell| + \sqrt{3}\,|\ell\rangle \langle \alpha_0, \beta_0|^A \ . \tag{3.33}$$

Figure 3.3 shows the spectrum of the search Hamiltonian from Equation (3.33) as the parameter γ is varied for a torus with dimensions $m = n = 12$ and $N = 288$ sites. The eigenenergies of the search Hamiltonian have been scaled so that one can see how the perturbation interacts with the spectrum of the adjacency matrix. One can see clearly two perturber states entering the unperturbed spectrum from around $\gamma \approx 0.4$ onwards. The perturbers approach the Dirac states, from both negative and positive parts of the spectrum, towards an avoided crossing around $E = 0$ at $\gamma = 1$. It is this point that we will focus on in the following.
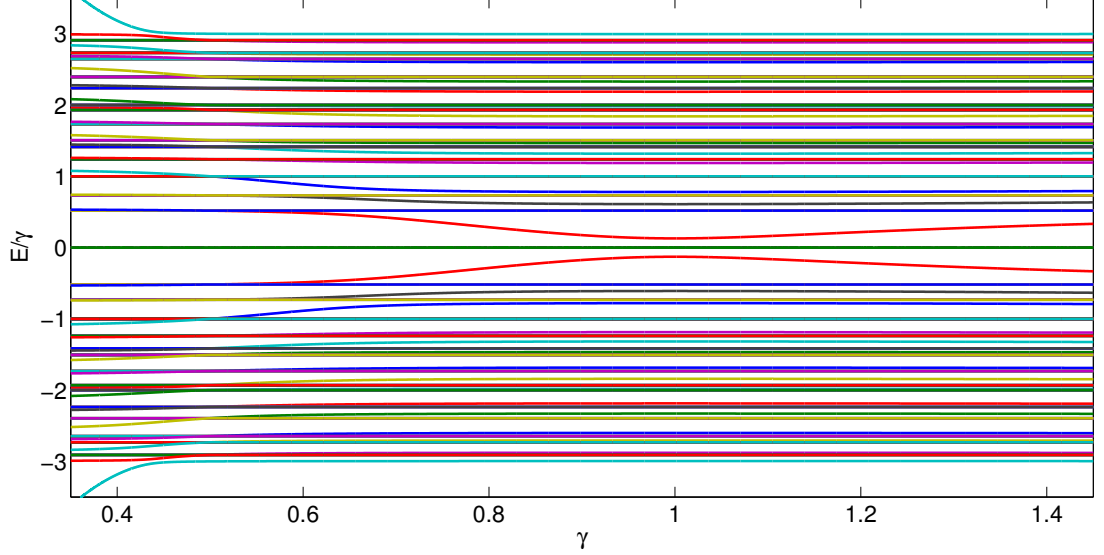
Figure 3.3: Numerically calculated spectrum of $H = -\gamma A + \sqrt{3}\, |\alpha_0, \beta_0\rangle^A \langle \ell| + \sqrt{3}\, |\ell\rangle \langle \alpha_0, \beta_0|^A$ as a function of γ for a 12×12 cell torus.

At the avoided crossing, there are altogether six states at or close to the Dirac energy: the four degenerate Dirac states and the two perturber states. As the two states that form the basis of the perturbation matrix lie exclusively on one sublattice or the other, we rewrite the Dirac states, given in Equation (2.63), in a similar manner

$$
\begin{aligned}
|\underline{K}\rangle^{A(B)} &= \sqrt{\frac{2}{N}} \sum_{\alpha,\beta} e^{i\frac{2\pi}{3}(\alpha + 2\beta + 2\sigma)} |\alpha, \beta\rangle^{A(B)} \\
|\underline{K'}\rangle^{A(B)} &= \sqrt{\frac{2}{N}} \sum_{\alpha,\beta} e^{i\frac{2\pi}{3}(2\alpha + \beta)} |\alpha, \beta\rangle^{A(B)} ,
\end{aligned}
\tag{3.34}
$$

where $\sigma = 1$ ($\sigma = 0$) for states on the B (A) lattice. We assert that the search mechanism involves a subset of the six states $\{|\underline{K}\rangle^A, |\underline{K'}\rangle^A, |\underline{K}\rangle^B, |\underline{K'}\rangle^B, |\ell\rangle, |\alpha_0, \beta_0\rangle^A\}$ and that the dynamics at the avoided crossing can be described by a reduced Hamiltonian using the subset of states as the basis.

We find by direct calculation that the B-type Dirac states do not interact

with a perturbation for a marked vertex on the A-sublattice

$$W \, |\underline{K}\rangle^B = \sqrt{3} \, \langle\ell|\underline{K}\rangle^B \, |\alpha_0, \beta_0\rangle^A + \sqrt{3} \, {}^A\langle\alpha_0, \beta_0|\underline{K}\rangle^B \, |\ell\rangle \tag{3.35}$$

$$= \sqrt{\frac{2}{N}} \, e^{i\frac{2\pi}{3}(\alpha_0 + 2\beta_o + 2)} \left(1 + e^{-i\frac{4\pi}{3}} + e^{-i\frac{2\pi}{3}}\right) |\alpha_0, \beta_0\rangle^A \tag{3.36}$$

$$= 0 \,, \tag{3.37}$$

and, similarly, it can be shown that $W \, |\underline{K'}\rangle^B = 0$. Also, we note that as the type of perturbation being used alters the bond strength between $(\alpha_0, \beta_0)^A$ and its nearest-neighbours, the effect of the perturbation when $\gamma = 1$ is to disconnect the vertex $(\alpha_0, \beta_0)^A$ from the rest of the lattice. Consequently, $|\alpha_0, \beta_0\rangle^A$ is an eigenvector of H with eigenvalue 0 and is, therefore, orthogonal to all other eigenvectors of the search Hamiltonian. Thus, the basis state $|\alpha_0, \beta_0\rangle^A$ does not interact with any other states and, as a result, does not play a role in the search mechanism. This may appear to be a problem, that the marked state does not interact in anyway, but as we will see a search can still be constructed.

This leaves only three states possibly involved in the crossing $\{|\underline{K}\rangle^A, |\underline{K'}\rangle^A, |\ell\rangle\}$, which we use to reduce the full Hamiltonian in Equation (3.33) to investigate the form of the eigenenergies and eigenvectors at the avoided crossing, and describe the local dynamics. Calculating the matrix elements of the search Hamiltonian using this basis, the reduced Hamiltonian is expressed as

$$\tilde{H} = \sqrt{\frac{6}{N}} \begin{bmatrix} 0 & 0 & e^{-i\frac{2\pi}{3}(\alpha_0 + 2\beta_o)} \\ 0 & 0 & e^{-i\frac{2\pi}{3}(2\alpha_o + \beta_0)} \\ e^{i\frac{2\pi}{3}(\alpha_0 + 2\beta_o)} & e^{i\frac{2\pi}{3}(2\alpha_o + \beta_0)} & 0 \end{bmatrix} . \tag{3.38}$$

It is clear then that the A-type Dirac states from both $\underline{K}$-points interact with the state localised on the nearest-neighbours of the marked vertex. The reduced Hamiltonian has eigenvalues $\tilde{E}_\pm = \pm 2\sqrt{\frac{3}{N}}, \tilde{E}_0 = 0$, and eigenvectors

$$|\tilde{\psi_\pm}\rangle = \frac{1}{2} \left(e^{-i\frac{2\pi}{3}(\alpha_0 + 2\beta_o)} \, |\underline{K}\rangle^A + e^{-i\frac{2\pi}{3}(2\alpha_o + \beta_0)} \, |\underline{K'}\rangle^A \pm \sqrt{2} \, |\ell\rangle \right) \tag{3.39}$$

$$|\tilde{\psi_0}\rangle = \frac{1}{\sqrt{2}} \left(e^{-i\frac{2\pi}{3}(\alpha_0 + 2\beta_o)} \, |\underline{K}\rangle^A - e^{-i\frac{2\pi}{3}(2\alpha_o + \beta_0)} \, |\underline{K'}\rangle^A \right) . \tag{3.40}$$

To perform a search for the marked vertex, we want to start the search in an eigenstate of the unperturbed walk Hamiltonian. The system is placed in a starting state which is a superposition of the Dirac states, formed by a superposition of the reduced Hamiltonian eigenvectors $|\tilde{\psi}_{\pm}\rangle$

$$|start\rangle = \frac{1}{\sqrt{2}} \left(|\tilde{\psi}_+\rangle + |\tilde{\psi}_-\rangle \right) \tag{3.41}$$

$$= \frac{e^{-i\frac{2\pi}{3}(\alpha_0+2\beta_0)}}{\sqrt{2}} \left(|\underline{K}\rangle^A + e^{-i\frac{2\pi}{3}(\alpha_0-\beta_0)} |\underline{K}'\rangle^A \right). \tag{3.42}$$

If the system is allowed to evolve under the reduced Hamiltonian

$$|\psi(t)\rangle = e^{-i\tilde{H}t} |start\rangle \tag{3.43}$$

$$= \frac{1}{\sqrt{2}} \left(e^{-i\tilde{E}_+ t} |\tilde{\psi}_+\rangle + e^{-i\tilde{E}_- t} |\tilde{\psi}_-\rangle \right) \tag{3.44}$$

$$= \cos\left(\tilde{E}_+ t\right) |start\rangle - i\sin\left(\tilde{E}_+ t\right) |\ell\rangle, \tag{3.45}$$

we find that it evolves from the superposition of Dirac states $|start\rangle$ into the state localised on the nearest-neighbours $|\ell\rangle$ in time $t = \frac{\pi}{4}\sqrt{\frac{N}{3}}$.

This differs from other searches, in that this system localises on the nearest-neighbours of the marked vertex, rather than on the marked site itself. However, the marked site can be found by an additional three classical steps. This only leads to a constant overhead in search time as the topology of the lattice does not change as N grows and remains 3-regular. In this simplified model, we find a quadratic speed-up over the classical search generated by the $N^{-1/2}$-scaling of the avoided crossing. It is this, combined with the $O\left(N^{-1/2}\right)$ eigenenergy spacing around the Dirac energy, which makes the search on this lattice one of the critical cases with respect to dimension and indicates that a search under the full Hamiltonian will be successful.

However, the states involved in the search are not completely isolated from the rest of the spectrum of the full search Hamiltonian, as the perturber state will interact with other eigenstates of the unperturbed walk Hamiltonian. Contributions from other states will be considered in the next section but the reduced Hamiltonian method is useful for demonstrating the underlying mechanism and

establishing those states which are most relevant. Since we have neglected the rest of the spectrum in this reduced model, it is not expected that, when the system is evolved under the full search Hamiltonian, all probability amplitude will localise on the nearest-neighbours as there will be some probability to measure the system in one of the other interacting eigenstates. Rather, the true localised state will have some tail that extends into the rest of the lattice.

The reduced model that has been described is for a marked vertex on the A-sublattice. However, the same results hold for perturbations to the B-sublattice, but using B-type Dirac states instead. This can be seen from the symmetry between the two sublattices.

As stated in the previous section, normally, the uniform superposition is chosen as the initial state because not only is it the ground state of the search Hamiltonian, but it also contains no information about the marked site. Our starting state for the search, given in Equation (3.42), does contain some information about the marked vertex in the relative phase between the Dirac states. However, this phase can only take three different values which implies three different optimal starting states. The same is true for searches on the B-sublattice so there are, in total, six unique optimal starting states. However, the number of unique starting states does not scale with N and so does not affect the scaling of the search time with system size, but rather just leads to a constant overhead.

Figure 3.4 shows a search on a 12×12 cell graphene torus that has been numerically calculated, where the system has been initialised in the optimal state $|start\rangle$ and allowed to evolve under the full search Hamiltonian. It confirms the expected search behaviour that was obtained from the reduced calculation. As suspected, the probability to be found on the nearest-neighbours does not reach 100% but reaches around 45% which is two orders of magnitude larger than the average probability of being found at any vertex $100/N$.

3.3 Detailed algorithm analysis

In this section we will justify the results of the previous reduced Hamiltonian calculation by showing that the dynamics of the algorithm take place mainly in a two-dimensional subspace of the full Hamiltonian spanned by a superposition of
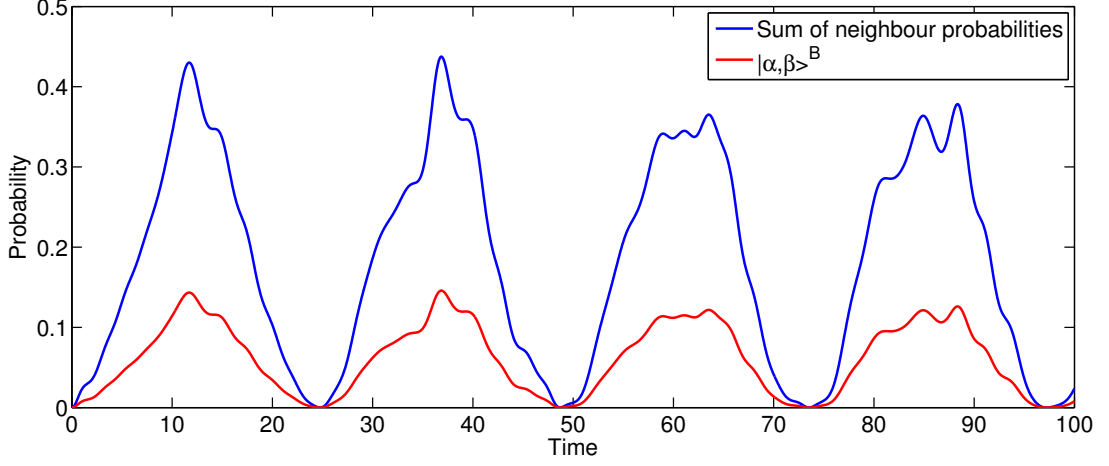
Figure 3.4: Numerically calculated search on a 12×12 cell graphene lattice using optimal starting state $|start\rangle$. The behaviour at each neighbour site is the same so only one has been shown.

Dirac states and the localised neighbour state $|\ell\rangle$. We will also provide further, detailed analysis of the search algorithm, specifically logarithmic corrections to the running time and success probability. Our analysis follows that found in [20, 21] but is modified to take into account the symmetry in the spectrum of the search Hamiltonian.

3.3.1 Preliminaries and setup

In particular we focus on the search running time and success amplitude. The graphene lattice and the boundary conditions we consider remain the same and we will continue to assume that the marked site is on the A-sublattice. We fix $\gamma = 1$ such that the search Hamiltonian is

$$H = -A + \sqrt{3}\, |\alpha_0, \beta_0\rangle^A \langle \ell| + \sqrt{3}\, |\ell\rangle \langle \alpha_0, \beta_0|^A \ . \tag{3.46}$$

We assume, without loss of generality, that the marked vertex is positioned so that the phase $e^{-i\frac{2\pi}{3}(\alpha_0 - \beta_0)} = 1$ and, therefore, the optimal starting state is

$$|start\rangle = \frac{1}{\sqrt{2}} \left(|\underline{K}\rangle^A + |\underline{K}'\rangle^A \right) \ . \tag{3.47}$$

51

We will derive the time T at which the probability to be found in $|\ell\rangle$ reaches a maximum, interpreted as the search running time and success probability, and also the scaling of this maximum probability with N, by evaluating

$$\langle\ell|\, e^{-iHT}\, |start\rangle = \sum_{|\psi_a\rangle} \langle\ell|\psi_a\rangle \langle\psi_a|start\rangle\, e^{-iE_a T}\,, \tag{3.48}$$

where $|\psi_a\rangle$ and E_a are the eigenstates and eigenenergies of the perturbed search Hamiltonian in Equation (3.46).

We can remove several states from the summation in Equation (3.48). As stated in the previous section, $|\alpha_0, \beta_0\rangle^A$ is an eigenvector of H with eigenenergy 0 but, by construction, $\langle\ell|\alpha_0, \beta_0\rangle^A = 0$, and so does not contribute to the time evolution at all. Also, states whose eigenenergies do not change after the introduction of the perturbation matrix, so that E_a is also in the spectrum of $-A$, have $\langle\ell|\psi_a\rangle = 0$ and are not relevant to the search behaviour.

This can be seen in the following way. We first consider an unperturbed eigenstate $|\psi_a^o\rangle$ such that $-A|\psi_a^o\rangle = E_a|\psi_a^o\rangle$. Let us assume that there is an eigenvector $|\psi_a\rangle$ of the search Hamiltonian with the same eigenenergy E_a, that is, $H|\psi_a\rangle = E_a|\psi_a\rangle$. Considering the matrix element $\langle\psi_a^o|\,H\,|\psi_a\rangle$, we find $\langle\psi_a^o|\ell\rangle \langle\alpha_o, \beta_o|\psi_a\rangle + \langle\psi_a^o|\alpha_o, \beta_o\rangle \langle\ell|\psi_a\rangle = 0$. As $|\alpha_o, \beta_o\rangle$ is an eigenvector of the search Hamiltonian we know that $\langle\alpha_o, \beta_o|\psi_a\rangle = 0$. This leaves us with $\langle\psi_a^o|\alpha_o, \beta_o\rangle \langle\ell|\psi_a\rangle = 0$. As the unperturbed eigenstate $|\psi_a^o\rangle$ is simply a Bloch state we know $\langle\psi_a^o|\alpha_o, \beta_o\rangle \neq 0$. Thus, we obtain $\langle\ell|\psi_a\rangle = 0$. It is then clear that eigenstates of the search Hamiltonian whose eigenenergies remain in the spectrum of $-A$ do not play a role in the time-evolution of the search, given by Equation (3.48).

Using Equation (3.46) we can rewrite the eigenstates $|\psi_a\rangle$ in the form

$$|\psi_a\rangle = \frac{\sqrt{3R_a}}{E_a + A}\, |\alpha_0, \beta_0\rangle^A\,, \tag{3.49}$$

where $\sqrt{R_a} = \langle\ell|\psi_a\rangle$ and the phase of $|\psi_a\rangle$ has been chosen such that $\langle\ell|\psi_a\rangle \geq 0$.

Equation (3.49) can be used to derive an eigenvalue condition for those E_a which are perturbed and do not remain in the spectrum of $-A$. Using the fact that $|\alpha_0, \beta_0\rangle^A$ is an eigenvector of H, by orthogonality of eigenvectors we have

$^A\langle\alpha_0,\beta_0|\psi_a\rangle = 0$, leading to

$$^A\langle\alpha_0,\beta_0|\frac{\sqrt{3R_a}}{(E_a+A)}\,|\alpha_0,\beta_0\rangle^A = 0\,. \tag{3.50}$$

By expanding the basis state $|\alpha_0,\beta_0\rangle^A$ in terms of the unperturbed eigenvectors of $-A$, which are the Bloch states, the condition for perturbed eigenvalues can be expressed as

$$F(E_a) = 0 \tag{3.51}$$

$$F(E) = \frac{\sqrt{3}}{N}\sum_{\underline{k}}\left[\frac{1}{E-\epsilon(\underline{k})} + \frac{1}{E+\epsilon(\underline{k})}\right]\,, \tag{3.52}$$

where N is the number of vertices in the lattice and $\epsilon(\underline{k})$ are the unperturbed *positive* eigenenergies of $-A$ given in Equation (2.56). We reiterate at this point that we are assuming periodic boundary conditions with equal numbers of cells in each direction, so that the momenta we are summing over (from Equation (2.51)) are explicitly given by

$$k_x = \frac{2\pi p}{\sqrt{N}}\,, \qquad k_y = \frac{1}{\sqrt{3}}\left(\frac{4\pi q}{\sqrt{N}} - k_x\right)\,, \tag{3.53}$$

where $p,q \in \{0,1,\ldots\sqrt{N}-1\}$.

By applying the normalisation condition $\langle\psi_a|\psi_a\rangle = 1$, the expression in Equation (3.49) gives

$$3R_a\,^A\langle\alpha_0,\beta_0|\,(E_a+A)^{-2}\,|\alpha_0,\beta_0\rangle^A = 1\,. \tag{3.54}$$

The matrix element in this last equation can be rewritten as the first derivative of the eigenvalue condition function $F(E)$, leading to the expression for R_a

$$R_a = \frac{1}{\sqrt{3}|F'(E_a)|}\,. \tag{3.55}$$

Now, Equations (3.49) & (3.55) allow the success amplitude in Equation (3.48)

to be rewritten as

$$\langle \ell | \, e^{-iHT} \, | start \rangle = \sum_{a:R_a \neq 0} \sqrt{R_a} \, \langle \psi_a | start \rangle \, e^{-iE_a T} \qquad (3.56)$$

$$= {}^{A}\langle \alpha_0, \beta_0 | start \rangle \sum_{a:R_a \neq 0} \frac{\sqrt{3}R_a}{E_a} e^{-iE_a T} \qquad (3.57)$$

$$= {}^{A}\langle \alpha_0, \beta_0 | start \rangle \sum_{a:R_a \neq 0} \frac{e^{-iE_a T}}{E_a |F'(E_a)|} \, . \qquad (3.58)$$

The reduced Hamiltonian calculation in the previous section implied that the relevant search dynamics take place at the Dirac point. Using the insight gained from that model, we focus here on the perturbed states closest to the Dirac energies, with a view to proving that these are the states with the dominant contributions to the time evolution. We label these states $|\psi_\pm\rangle$ and their eigenenergies $E_\pm$. We note that $E_+ = -E_- > 0$, and we write what follows in terms of E_+. As well as estimating E_+, we will derive an estimate of $F'(E_+)$ to leading-order.

We start from Equation (3.52), and separate out the contributions to the sum from the $\underline{K}$-points, where $\epsilon(\underline{K}) = \epsilon(\underline{K}') = 0$

$$F(E_+) = \frac{4\sqrt{3}}{NE_+} + \frac{\sqrt{3}}{N} \sum_{\underline{k} \neq \underline{K}, \underline{K}'} \left[\frac{1}{E_+ - \epsilon(\underline{k})} + \frac{1}{E_+ + \epsilon(\underline{k})} \right] , \qquad (3.59)$$

and then proceed by Taylor expanding the remaining summation around $E = 0$, leading to

$$F(E_+) = \frac{4\sqrt{3}}{NE_+} - \sum_{n=1}^{\infty} I_{2n} E_+^{2n-1} , \qquad (3.60)$$

where the sums I_{2n} are given by

$$I_{2n} = \frac{\sqrt{3}}{N} \sum_{\underline{k} \neq \underline{K}, \underline{K}'} \left[\frac{1}{[\epsilon(\underline{k})]^{2n}} + \frac{1}{[-\epsilon(\underline{k})]^{2n}} \right] . \qquad (3.61)$$

It is clear from the symmetry in the spectrum that for odd m then $I_m = 0$, so only the even I_m terms contribute to the sum in Equation (3.60).

By applying the eigenvalue condition $F\left(E_+\right) = 0$, we can obtain an estimate for E_+ by solving Equation (3.60), provided we have estimates on the sums I_{2n}.

3.3.2 Estimates of I_{2n} sums

As several terms in the search time-evolution in Equation (3.58) can be rewritten in terms of the I_{2n} sums, we devote this subsection to estimating these sums.

The dominant contributions to the sums come from the smallest magnitude energies around the Dirac energy. As described in Section (2.6), it is these energies that are well-described by the conical dispersion relation $\epsilon\left(\underline{k}\right) \approx \frac{\sqrt{3}}{2}\sqrt{\delta k_x^2 + \delta k_y^2}$, where $\delta k_{x/y} = k_{x/y} - K_{x/y}$ and the same is true around the $\underline{K}'$ point. Consequently, we approximate the sums I_{2n} as

$$I_{2n} = \frac{2\sqrt{3}}{N} \sum_{\underline{k}\neq\underline{K},\underline{K}'} \left[\frac{1}{\left[\frac{\sqrt{3}}{2}\left(\delta k_x^2 + \delta k_y^2\right)^{\frac{1}{2}}\right]^{2n}} + \frac{1}{\left[\frac{\sqrt{3}}{2}\left(\delta k_x'^2 + \delta k_y'^2\right)^{\frac{1}{2}}\right]^{2n}} \right] + \mathcal{O}\left(1\right),$$
(3.62)

where there is a sum from each $\underline{K}$-point and the pre-factor of 2 arises from the equal contributions from positive and negative energies. The conical dispersion relation becomes a worse approximation further away from the K-points, introducing an $\mathcal{O}\left(1\right)$ correction.

Rewriting this in terms of the momenta quantum numbers p, q we find

$$I_{2n} = \frac{2\sqrt{3}N^{n-1}}{\left(8\pi^2\right)^n} \left[\sum_{(p,q)\in L}' \frac{1}{\left(p^2 + q^2 - pq\right)^n} + \sum_{(p,q)\in L'}' \frac{1}{\left(p^2 + q^2 - pq\right)^n} \right] + \mathcal{O}\left(1\right),$$
(3.63)

where the prime on the summation indicates that the origin has been omitted. The momenta quantum numbers p and q, as described previously in reference to Equation (3.53), are normally in the set $p, q \in \{0, 1, \ldots \sqrt{N} - 1\}$ so that we sum over a square region with sides of length $\sqrt{N}$. We note that the two summations in Equation (3.63) are truncated Epstein zeta functions for real positive-definite quadratic forms [82].

In the summations in Equation (3.63), we sum over regions with the same area, but the origins of L and L' have been shifted to correspond to the relevant

$\underline{K}$-point. This leads to L being spanned by

$$
\begin{aligned}
p &\in \{-\frac{\sqrt{N}}{3}, -\frac{\sqrt{N}}{3} + 1, \dots \frac{2\sqrt{N}}{3} - 1\} \\
q &\in \{-\frac{2\sqrt{N}}{3}, -\frac{2\sqrt{N}}{3} + 1, \dots \frac{\sqrt{N}}{3} - 1\},
\end{aligned}
\tag{3.64}
$$

and L' by

$$
\begin{aligned}
p &\in \{-\frac{2\sqrt{N}}{3}, -\frac{2\sqrt{N}}{3} + 1, \dots \frac{\sqrt{N}}{3} - 1\} \\
q &\in \{-\frac{\sqrt{N}}{3}, -\frac{\sqrt{N}}{3} + 1, \dots \frac{2\sqrt{N}}{3} - 1\}.
\end{aligned}
\tag{3.65}
$$

For $n > 1$, the two individual sums in Equation (3.63) converge as the area being summed over tends to infinity [82, 83]. This can be seen by the fact that one can always find a constant λ such that $(p^2 + q^2 - pq) \geq \lambda (p^2 + q^2)$, placing an upper bound on the summation. Using bounds on binary quadratic forms, one can in fact find the correct value for λ [83], which for this case is $\lambda = \frac{1}{2}$. Considering the upper bound, it is known that the infinite sum $2^{-n} \sum_{p,q=-\infty}^{'\infty} (p^2 + q^2)^{-n}$ does converge. Thus, to leading-order, for $n > 1$, the finite sums I_{2n} are estimated as

$$
I_{2n} = \mathcal{O}\left(N^{n-1}\right).
\tag{3.66}
$$

For the case $n = 1$, we can bound I_2 from above and below, by deforming the regions of summation and placing bounds on the resultant sums. We first deform the sum to a square region $-c_s\sqrt{N} \leq p, q \leq c_s\sqrt{N}$, where $0 < c_s < \frac{1}{3}$ so that it is fully contained in L and L'. By restricting the sum to a smaller region, we have

$$
S_{small} = \sum_{p,q=-c_s\sqrt{N}}^{c_s\sqrt{N}} {}' \frac{1}{(p^2 + q^2 - pq)} < \sum_{(p,q)\in L} {}' \frac{1}{(p^2 + q^2 - pq)}.
\tag{3.67}
$$

By considering the symmetry of the problem, the sum over the square region can

be rewritten as

$$S_{small} = 4 \sum_{p=1}^{c_s \sqrt{N}} \frac{1}{p^2} + 2 \sum_{p,q=1}^{c_s \sqrt{N}} \frac{1}{p^2 + q^2 - pq} + 2 \sum_{p,q=1}^{c_s \sqrt{N}} \frac{1}{p^2 + q^2 + pq} , \qquad (3.68)$$

where the first sum arises from summing along each axis, the second term comes from the symmetry between the positive-positive & negative-negative quadrants and the third from the positive-negative quadrants. The first term in this expression is just a truncated Riemann zeta function $\zeta(s)$ with $s = 2$ which converges, so it is only the next two terms which require our attention. The region that we consider can be reduced further, by noticing the symmetry of each quadrant about $p = q$

$$S_{small} = 4 \sum_{p=1}^{c_s \sqrt{N}} \sum_{q=1}^{p} \frac{1}{p^2 + q^2 - pq} + 4 \sum_{p=1}^{c_s \sqrt{N}} \sum_{q=1}^{p} \frac{1}{p^2 + q^2 + pq} + \mathcal{O}(1) . \qquad (3.69)$$

For each p, there is a q_{max} such that the sums can be bound from below by

$$\sum_{q=1}^{p} \frac{1}{p^2 + q^2 \pm pq} > \frac{p}{p^2 + q_{max}^2 \pm pq_{max}} . \qquad (3.70)$$

We may fix $q_{max} = ap$ where $a > 0$, such that the above statement is true for all $1 \leq p \leq c_s \sqrt{N}$, which allows us to write

$$S_{small} > \frac{4}{a^2 - a + 1} \sum_{p=1}^{c_s \sqrt{N}} \frac{1}{p} + \frac{4}{a^2 + a + 1} \sum_{p=1}^{c_s \sqrt{N}} \frac{1}{p} , \qquad (3.71)$$

and both sums diverge as $\mathcal{O}(\ln N)$. This leads to a lower bound

$$\sum_{(p,q) \in L}' \frac{1}{(p^2 + q^2 - pq)} > C_s \ln N . \qquad (3.72)$$

An upper bound on I_2 can be found in a similar way by deforming the region we sum over again to a square region $-c_l \sqrt{N} \leq p, q \leq c_l \sqrt{N}$, where $c_l > \frac{2}{3}$ so that this time the region contains both L and L'. This allows us to place an upper

bound as

$$S_{large} = \sideset{}{'}\sum_{p,q=-c_l\sqrt{N}}^{c_l\sqrt{N}} \frac{1}{(p^2 + q^2 - pq)} > \sideset{}{'}\sum_{(p,q)\in L} \frac{1}{(p^2 + q^2 - pq)} \,. \tag{3.73}$$

As only the limits have been changed S_{large} can be reduced again to the same form as Equation (3.69). Similar to the lower bound, we can find q_{min} to bound the sums from above as

$$\sum_{q=1}^{p} \frac{1}{p^2 + q^2 \pm pq} < \frac{p}{p^2 + q_{min}^2 \pm pq_{min}} \,. \tag{3.74}$$

Again we can recast the sum purely in terms of p by establishing $q_{min} = ap$ where $a \geq 0$, this leads to an equation with exactly the same form as Equation (3.71) but with the inequality reversed, so that $S_{large} < \mathcal{O}(\ln N)$. This leads to the bounds on I_2

$$C_s \ln N < I_2 < C_l \ln N \,. \tag{3.75}$$

As these estimates for I_{2n} are important in what follows we will state them again, separately from their derivations. Our leading-order estimates for the sums I_2 and I_{2n} are

$$I_2 = \mathcal{O}(\ln N) \tag{3.76}$$

$$I_{2n} = \mathcal{O}\left(N^{n-1}\right) \,, \quad \text{for } n \geq 2 \,. \tag{3.77}$$

One can, with a more involved analysis give rough estimates for the prefactors of these leading-order estimates, shown in Appendix A.

3.3.3 Analysis of the search time-evolution and success probability

We now use these leading-order estimates from the previous subsection to obtain E_+ by considering the expansion of $F(E_+)$ in Equation (3.60). We note that each term in the sum $I_{2(n+1)}$ is smaller than the corresponding term in I_{2n}, so that $I_{2n} > I_{2(n+1)}$. This implies that the sum of higher order terms in the Taylor

expansion in Equation (3.60), for $n \geq 2$ is bound by

$$\sum_{n=2}^{\infty} I_{2n} E_+^{2n-1} < \frac{C}{NE_+} \sum_{n=2}^{\infty} \left(NE_+^2 \right)^n \,, \tag{3.78}$$

so that the continued sum of the Taylor expansion converges provided $E_+ < 1/\sqrt{N}$. This indicates that we can truncate the Taylor expansion at the $n = 1$ term

$$F\left(E_+\right) \approx \frac{4\sqrt{3}}{NE_+} - I_2 E_+ \,, \tag{3.79}$$

provided that the solution that we obtain for E_+ is within the radius of convergence of the sum of higher order terms. Applying the eigenvalue condition $F\left(E_+\right) = 0$ to the truncated expression of $F\left(E_+\right)$ in Equation (3.79), we find

$$E_+ \approx \left(\frac{4\sqrt{3}}{NI_2} \right)^{\frac{1}{2}} \,, \tag{3.80}$$

and, when we apply the behaviour of I_2, we find the leading-order estimate

$$E_+ = \mathcal{O} \left(\frac{1}{\sqrt{N \ln N}} \right) \,, \tag{3.81}$$

which is in the radius of convergence for sufficiently large N. This scaling of E_+ with N is borne out by the numerically calculated gap using the full search Hamiltonian, shown in Figure 3.5.

We will now show that the $n = 1$ term of the Taylor expansion is the only one necessary for the leading-order behaviour by evaluating the error on this estimate. All the I_{2n} sums are positive so that, given the sign of all the terms in the Taylor expansion in Equation (3.60), the true value of $E_+ > 0$ has to be smaller than the estimate we have obtained. Thus, we write the true value of E_+ as

$$E_+^2 = \frac{4\sqrt{3}}{NI_2} - \Delta \,, \tag{3.82}$$

where $\Delta > 0$. We rewrite the eigenvalue condition $F\left(E_+\right) = 0$, using the expan-
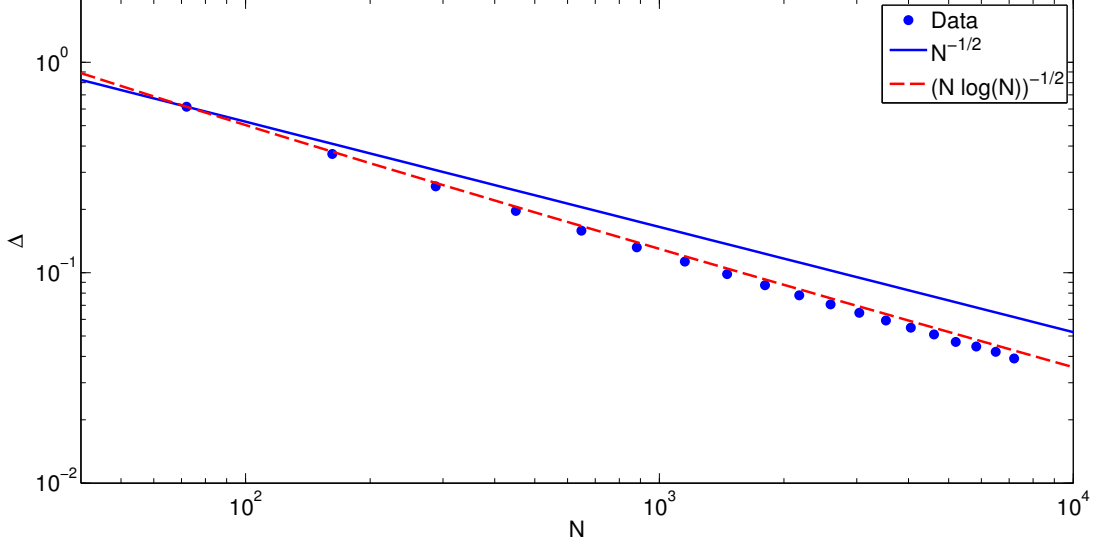
Figure 3.5: Numerically calculated avoided crossing gap $\Delta = E_+ - E_-$ (dots) and curves $c_1/\sqrt{N}$ & $c_2/\sqrt{N \ln N}$ for comparison, as a function of number vertices N

sion from Equation (3.60) and the true value of E_+, as

$$\frac{4\sqrt{3}}{N} - I_2 E_+^2 = \sum_{n=2}^{\infty} I_{2n} E_+^{2n} \,, \tag{3.83}$$

leading to

$$I_2 \Delta = \sum_{n=2}^{\infty} I_{2n} E_+^{2n} \,. \tag{3.84}$$

By applying our estimates for the I_{2n} sums we can bound Δ as

$$0 < N I_2 \Delta < C \sum_{n=2}^{\infty} (N E_+^2)^n \tag{3.85}$$

$$= \frac{C N^2 E_+^4}{1 - N E_+^2} \,. \tag{3.86}$$

We will assume a worst-case error, where we make the upper bound inequality an equality, and so the true error may actually be of a smaller order than is

calculated. Substituting in $E_+^2 = \frac{4\sqrt{3}}{NI_2} - \Delta$ and rearranging we find

$$I_2 N \Delta - C \frac{N^2 \left(\frac{4\sqrt{3}}{NI_2} - \Delta \right)^2}{1 - N \left(\frac{4\sqrt{3}}{NI_2} - \Delta \right)} = 0 \,, \tag{3.87}$$

$$\left(I_2 - C \right) N^2 \Delta^2 + \left(I_2 - 4\sqrt{3} + \frac{8\sqrt{3}C}{I_2} \right) N\Delta - \frac{48C}{I_2^2} = 0 \,. \tag{3.88}$$

By only keeping the leading order terms and defining $x \equiv N\Delta$, we reduce the above expression to the simple quadratic

$$I_2^3 x^2 + I_2^3 x - C = 0 \,, \tag{3.89}$$

where we have incorporated any additional constant factors into the constant C. Only the positive energy solution of the quadratic is of interest to us as $\Delta > 0$, and we find $x \approx C/I_2^3$. Inserting this behaviour into our expression for E_+^2 and the leading-order behaviour of I_2, we can estimate the error on our initial estimate in Equation (3.80)

$$E_+ = \left(\frac{4\sqrt{3}}{NI_2} - \Delta \right)^{\frac{1}{2}} \tag{3.90}$$

$$= \left(\frac{4\sqrt{3}}{NI_2} - \frac{x}{N} \right)^{\frac{1}{2}} \tag{3.91}$$

$$= \left(\frac{4\sqrt{3}}{NI_2} - \frac{C}{NI_2^3} \right)^{\frac{1}{2}} \tag{3.92}$$

$$\approx \left(\frac{4\sqrt{3}}{NI_2} \right)^{\frac{1}{2}} \left(1 + \mathcal{O} \left(\frac{1}{\ln^2 N} \right) \right) \,, \tag{3.93}$$

for large N, where for the last step we have used the approximation $(1 + x)^{-1/2} \approx 1 - \frac{1}{2}x$.

We now turn our attention to the other term necessary for calculating the time-evolution in Equation (3.48), $F'(E_+)$. By differentiating the truncated Tay-

lor expansion of $F(E)$ in Equation (3.79), we find

$$F'(E_+) \approx \frac{4\sqrt{3}}{NE_+^2} - I_2 \,. \tag{3.94}$$

As the derivative of a Taylor expansion has the same radius of convergence, we neglect the higher order terms here as well. Inserting the behaviour of E_+, with the corrective term Δ, gives us

$$F'(E_+) \approx -\frac{4\sqrt{3}}{N} \left(\frac{NI_2}{4\sqrt{3}}\right) \left(1 + \mathcal{O}\left(\frac{1}{\ln^2 N}\right)\right)^{-2} - I_2 \tag{3.95}$$

$$\approx -2I_2 + O\left(\frac{1}{\ln N}\right) \,, \tag{3.96}$$

where the approximation $(1 + x)^{-2} \approx 1 - 2x$, valid for small x, has been used.

Our estimates now allow us to demonstrate that the relevant states for the search time-evolution are the states $|\psi_\pm\rangle$, which we assumed in the reduced model. There we found that the initial state $|start\rangle$ was an equal superposition of the states $|\psi_\pm\rangle$, and so we look at the inner product of $|start\rangle$ with these states

$$|\langle start|\psi_\pm\rangle| = |\langle start| \frac{\sqrt{3R_\pm}}{E_\pm + A} |\alpha_0, \beta_0\rangle^A| \tag{3.97}$$

$$= |\frac{\sqrt{3R_\pm}}{E_\pm} \langle start|\alpha_0, \beta_0\rangle^A| \tag{3.98}$$

$$= \frac{2}{E_+} \sqrt{\frac{3R_+}{N}} \,. \tag{3.99}$$

We have used that $A|start\rangle = 0$, and that $R_+ = R_-$ and $E_+ = -E_-$. Using the definition $R_a = 1/\left(\sqrt{3}|F'(E_a)|\right)$, and the leading-order behaviour of E_+ and $F'(E_+)$ we find

$$|\langle start|\psi_\pm\rangle| = \frac{2}{E_+} \sqrt{\frac{3}{N}} \left(\frac{1}{\sqrt{3}|F'(E_+)|}\right)^{\frac{1}{2}} \tag{3.100}$$

$$= \frac{I_2^{\frac{1}{2}}}{1 + \mathcal{O}\left(\ln^2 N\right)} \left(\frac{1}{2I_2 + \mathcal{O}\left(\frac{1}{\ln N}\right)}\right)^{\frac{1}{2}} \tag{3.101}$$

$$\approx \frac{1}{\sqrt{2}} + \mathcal{O}\left(\frac{1}{\ln^2 N}\right), \tag{3.102}$$

where we have only kept the leading-order correction. This implies that when calculating the time-evolution beginning in $|start\rangle$, we only need to use the perturbed eigenstates $|\psi_\pm\rangle$ and all other states have a vanishing contribution as $N \to \infty$. Thus, looking at the time-evolution of the search described in Equation (3.58), and neglecting all states other than $|\psi_\pm\rangle$, we obtain

$$|\langle\ell|\, e^{-iHt}\,|start\rangle| \approx |\langle\ell|\, e^{-iHt} \frac{1}{\sqrt{2}}\left(|\psi_+\rangle - |\psi_-\rangle\right)| \tag{3.103}$$

$$= |\frac{1}{\sqrt{2}}\left(e^{-iE_+t}\,\langle\ell|\psi_+\rangle - e^{iE_+t}\,\langle\ell|\psi_-\rangle\right)| \tag{3.104}$$

$$= \sqrt{2R_+}|\sin\left(E_+t\right)| \tag{3.105}$$

$$= \frac{1}{\sqrt{3^{\frac{1}{2}}I_2}}|\sin\left(E_+t\right)|. \tag{3.106}$$

We then find that the maximum success amplitude is found when $T = \frac{\pi}{2E_+}$ and, using our results for E_+ and I_2, it is clear that the search time is $T = \mathcal{O}\left(\sqrt{N\ln N}\right)$ and succeeds with probability amplitude $\mathcal{O}\left(1/\sqrt{\ln N}\right)$. To boost the probability to $\mathcal{O}\left(1\right)$, then $\mathcal{O}\left(\ln N\right)$ repetitions are needed to guarantee success, leading to an overall time complexity of $T = \mathcal{O}\left(\sqrt{N}\ln^{3/2} N\right)$.

3.4 Non-optimal starting states & alternative torus configurations

3.4.1 Random starting states

We have seen that for a particular marked vertex there is an optimal starting state. So far we have assumed that the search is initialised in one of these states. One may, however, wonder about the time-evolution when the search starts in a non-optimised state. Indeed, this is what is most likely in an experimental setting, where constructing the optimal state with a particular phase difference between degenerate states is likely to be difficult. Rather, when exciting a system

to a degenerate energy one will end up with a superposition of the degenerate states with random phases and weights.

However, running the search with a random state only reduces the success probability, on average, by a factor of $\frac{1}{4}$. This can be seen by considering the probability of measuring a random superposition of Dirac states in the basis $\{|\underline{K}\rangle^A$, $|\underline{K'}\rangle^A, |\underline{K}\rangle^B, |\underline{K'}\rangle^B\}$, and finding the system in one of the particular states, for example $|\underline{K}\rangle^A$. On average, as all random superpositions are equally likely, one would measure the system in $|\underline{K}\rangle^A$ 25% of the time. As we are free to choose the basis as we wish, the same is true of any particular starting state. Thus, the contribution to the time-evolution, on average, from the starting state will be reduced by half, leading to a reduction of the success probability by a factor of $\frac{1}{4}$. Again, the number of repetitions to boost the success probability is only increased by a constant factor, independent of N.

3.4.2 Tori without eigenenergies at the Dirac point

We have so far restricted the setting of the search algorithm to only those tori with eigenenergies which coincide with the Dirac point, that is those with dimensions where m and n are multiples of 3. We now relax that restriction to consider the more general setting where there are not necessarily Dirac states. However, it can be seen that as the number of vertices approaches the limit $N \to \infty$ then the states with energies closest to ϵ_D approach the Dirac states, and the restriction is unnecessary for large N.

For finite lattices without eigenenergies at the Dirac point we must use an avoided crossing around an alternative state close to the Dirac point. One would expect the algorithm still to work at these energies as they still lie within the conical dispersion regime of the spectrum, which is the critical feature of the search. Figure 3.6 shows the spectrum of the search Hamiltonian as a function of γ for a 10×10 cell torus. The spectrum is rather different to that shown in Figure 3.3. Due to there necessarily being an eigenenergy with $E = 0$ at $\gamma = 1$ because a single site has been disconnected from the rest of the lattice with on-site energy $\epsilon_D = 0$, there is an exact crossing at $\gamma = 1$. Therefore, the critical point must shift and we have to perform a sweep of γ values to find the avoided
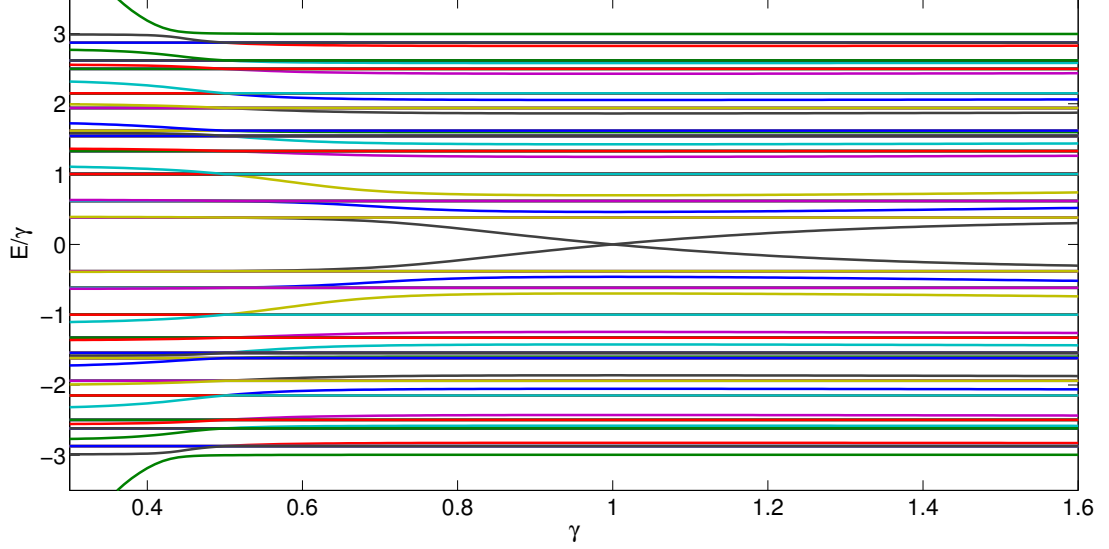
Figure 3.6: Numerically calculated spectrum of $H = -\gamma A + \sqrt{3}\,|\alpha_0, \beta_0\rangle^A \langle\ell| + \sqrt{3}\,|\ell\rangle \langle\alpha_0, \beta_0|^A$ as a function of γ for a 10×10 cell torus
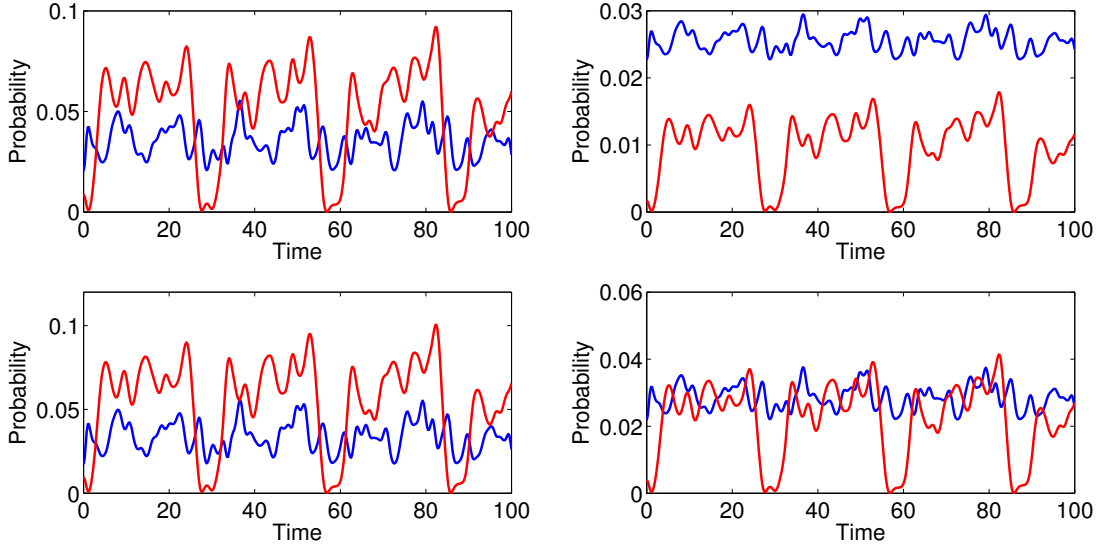
Figure 3.7: Numerically calculated search on a 10×10 cell graphene lattice using the avoided crossing with $\gamma < 1$. Shown are searches using four different random superpositions of the unperturbed degenerate eigenstates of the adjacency matrix with $E = 0.382$. Plotted is the sum of the probabilities to be found on the neighbour vertices (red) and the probability to be found at the marked vertex (blue).
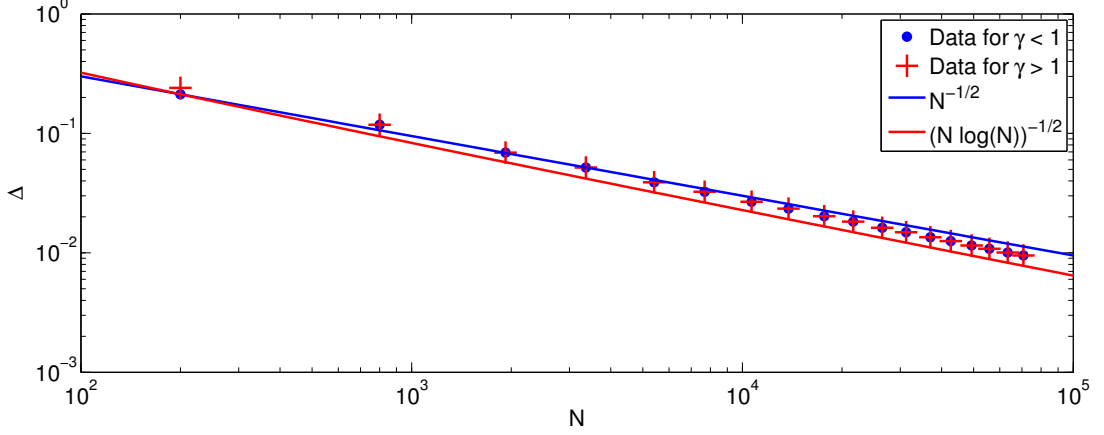
Figure 3.8: Numerically calculated avoided crossing gap Δ (dots) and curves $c_1/\sqrt{N}$ & $c_2/\sqrt{N \ln N}$ for comparison, as a function of number vertices N. The avoided crossings used are around the first excited energy above the Dirac energy $E = 0$.

crossing. In Figure 3.6 there are two avoided crossing around the states closest to the Dirac energy $E = 0$ at $\gamma \approx 0.7$ and $\gamma \approx 1.3$ which we can use to create a search. As the size of the lattice increases, the value of γ at which both avoided crossing gaps is narrowest approaches $\gamma = 1$ as the eigenstates approach the Dirac states.

Constructing an optimal starting state for non-Dirac state searches is more difficult as the form of the eigenstates changes as the lattice grows due to the quantised momenta values changing, whereas the Dirac states remain the same as they are always positioned at the $\underline{K}$-points. However, similar to the Dirac state searches, in an experiment it is more likely that a random superposition of the degenerate eigenstates is excited and so it is on these random superpositions that we focus. Figure 3.7 shows four searches initialised in such random superpositions of the degenerate unperturbed eigenstates, each with different amplitudes. The search behaviour is somewhat different to the case discussed in the previous sections. While the success probability does have a regular period, it does not have a well-defined peak on the neighbour vertices and reaches a sort-of plateau. As the critical value of γ is not $\gamma = 1$, the marked site does take part in the dynamics, leading to some oscillation of probability amplitude between the marked site and the neighbouring vertices. The success probability of measuring a neighbouring

vertex for the searches shown is, on average, an order of magnitude larger than the average probability measuring a random vertex which is 0.5%.

Figure 3.8 shows that the scaling of the energy gap for non-Dirac state searches is similar to the scaling of the energy gap for Dirac state searches, shown in Figure 3.5, but lies somewhere between $\mathcal{O}\left(1/\sqrt{N}\right)$ and $\mathcal{O}\left(1/\sqrt{N\ln N}\right)$.

3.4.3   Zigzag dimension torus

We have so far assumed a specific geometry for the unit cell of the torus, shown in Figure 3.1. However, it is well known that the properties of carbon nanotubes are dependent on the geometry of the tube and how the underlying graphene lattice is closed into a tube [79]. It is then possible that how one closes the graphene lattice into a torus could perhaps alter the effectiveness of the search and modify the dynamics in some way. Thus, we change from the previous setup, which we will call a 'chiral' torus, to the unit cell shown in Figure 3.9, which we will call a 'zigzag' torus (borrowing the terms from the language of carbon nanotubes).

An $M \times N$ zigzag lattice with periodic boundary conditions remains invariant under the translations $\underline{R} = M\underline{a}_1$ and also $\underline{R} = -\frac{N}{2}\underline{a}_1 + N\underline{a}_2$. These periodic boundary conditions lead to the quantised momenta

$$k_x = \frac{2\pi p}{M} \qquad k_y = \frac{4\pi q}{\sqrt{3}N} \, , \tag{3.107}$$

where $p\,(q) \in \{0, 1, \ldots M\,(N) - 1\}$. The condition for the eigenenergies of the torus to coincide with the Dirac energy then changes; M must be a factor of 3 and N must be a factor of 2.

Figure 3.10 shows the spectrum of the search Hamiltonian from Equation (3.33) applied to a 12×8 zigzag torus as a function of γ. The spectrum does not appear particularly different to that of the previous torus, shown in Figure 3.3, and we see the expected eigenenergies at the Dirac energy $E = 0$ with two perturber states entering the spectrum and interacting via an avoided crossing at $\gamma = 1$.

As the form of the Hamiltonian does not change, neither does the form of the Dirac states with energy $E = 0$. Thus, the reduced analysis of the previous chiral torus holds and the optimal starting states remain the same as that found in
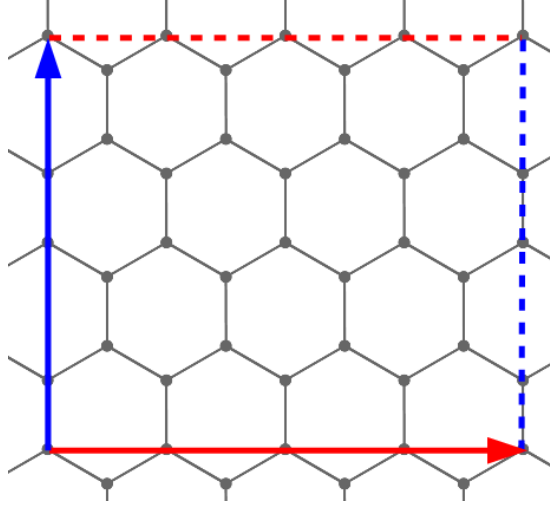
Figure 3.9: An example of a 4×4 zigzag torus cell. Border lines with the same colour are equivalent.

Equation (3.42). The evolution of the system under the full search Hamiltonian, using the optimal search starting state is displayed in Figure 3.11. The search behaviour is very similar to that of the chiral torus, however with a slight decrease in the success probability for a comparable number of sites in the lattice.

As none of the salient points to the scaling change with a re-drawing of the boundaries (e.g. the scaling of the first excited state above the Dirac energy and the conical nature of the spectrum around the Dirac energies), the success of the search does not change and it appears that the method of closing the graphene lattice into a torus has no marked effect on the search dynamics. This is confirmed by the scaling of the avoided crossing gap, shown in Figure 3.12.
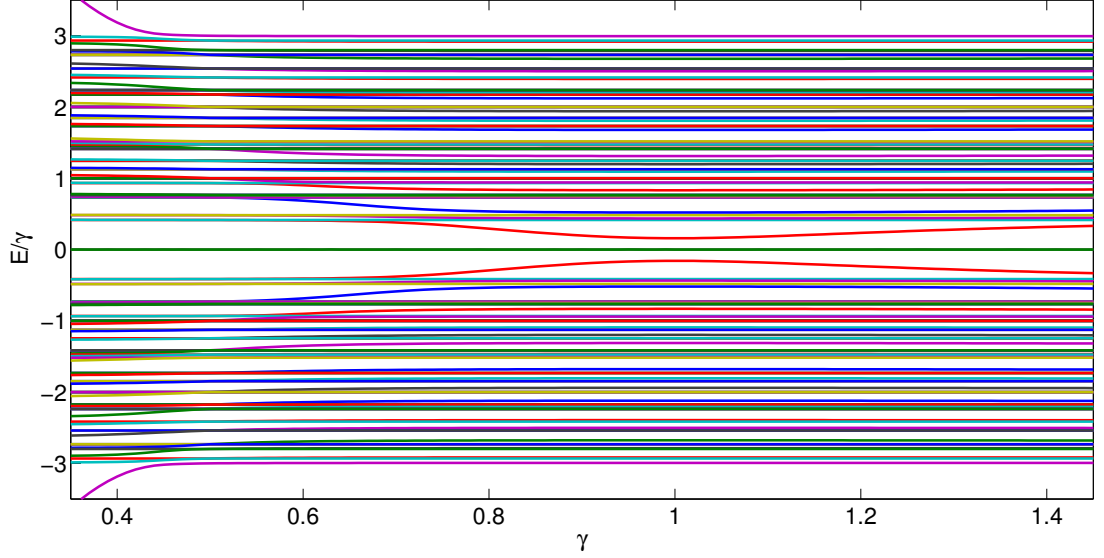
Figure 3.10: Numerically calculated spectrum of $H = -\gamma A + \sqrt{3}\,|\alpha_0, \beta_0\rangle^A \langle \ell| + \sqrt{3}\,|\ell\rangle \langle \alpha_0, \beta_0|^A$ as a function of γ for a 12×8 cell zigzag torus
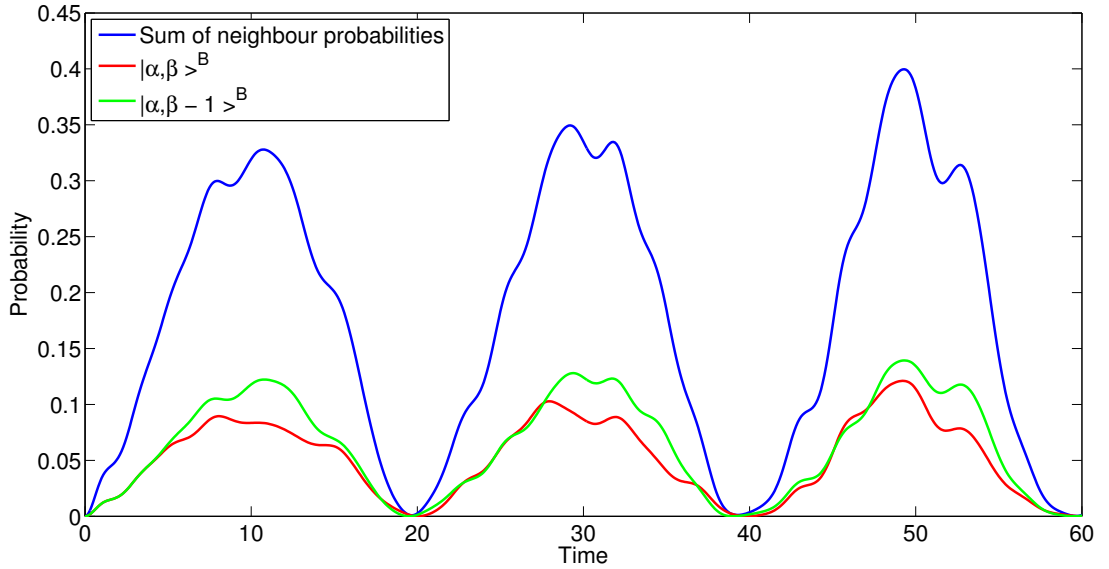
Figure 3.11: Numerically calculated search on a 12×8 cell graphene lattice using optimal starting state $|start\rangle$. The behaviour at $(\alpha, \beta - 1)^B$ and $(\alpha + 1, \beta - 1)^B$ is the same so only one is shown.
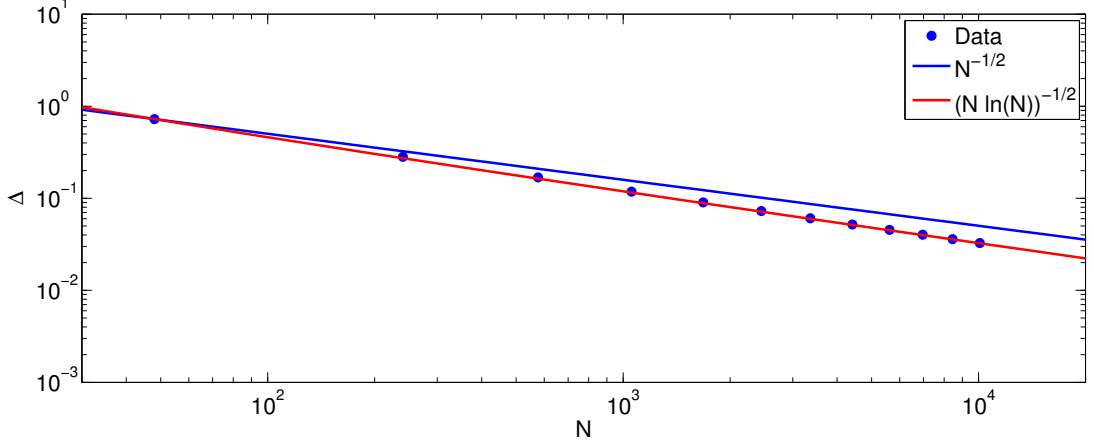
Figure 3.12: Numerically calculated avoided crossing gap Δ (dots) and curves $c_1/\sqrt{N}$ & $c_2/\sqrt{N \ln N}$ for comparison, as a function of number vertices N. The avoided crossings used are around the first excited energy above the Dirac energy $E = 0$.

3.5 Quantum communication

It was shown in [84] that DTQW search algorithms can be modified to create a communication protocol with the addition of another perturbation to a different vertex on the lattice. The same is true for the CTQW search algorithm described in this chapter but with slight differences due to the exact setup that we use. Explicitly, the model uses the same setup described in Section 3.2, that is, we use the unperturbed walk Hamiltonian

$$H_o = -A\,, \tag{3.108}$$

and the 3-bond perturbation matrix for a perturbation to an A-type sublattice vertex $(\alpha_s, \beta_s)^A$

$$W_s = \sqrt{3}\,|\alpha_s, \beta_s\rangle^A \langle \ell_s| + \sqrt{3}\,|\ell_s\rangle \langle \alpha_s, \beta_s|^A\,, \tag{3.109}$$

where $|\ell_s\rangle \equiv \frac{1}{\sqrt{3}}\left(|\alpha_s, \beta_s\rangle^B + |\alpha_s, \beta_s - 1\rangle^B + |\alpha_s + 1, \beta_s - 1\rangle^B\right)$ lives on the nearest-neighbours of $(\alpha_s, \beta_s)^A$. We also retain the original torus cell and periodic boundary conditions shown in Figure 3.1, assuming that the torus dimensions are such
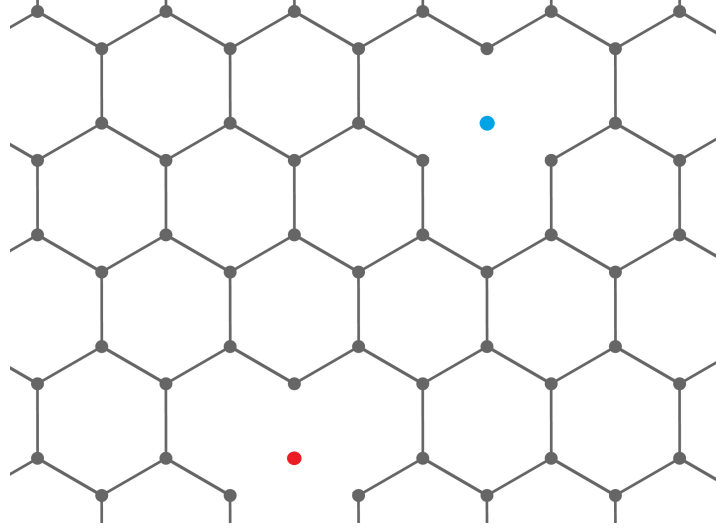
Figure 3.13: An example of the communication setup between two perturbations on the A sublattice. The blue and red sites have zero-strength hopping potential to their nearest-neighbours.

that there are eigenenergies coinciding with the Dirac energy. The communication Hamiltonian for signal transfer between vertices $(\alpha_s, \beta_s)^A$ and $(\alpha_t, \beta_t)^A$ is then

$$H = -A + W_s + W_t \,, \tag{3.110}$$

so that two sites are disconnected from the rest of the torus, illustrated in Figure 3.13, and the subscript s indicates the source vertex and t indicates the target vertex. By preparing the system in a state localised on the nearest-neighbours of the source vertex and allowing the system to evolve under the communication Hamiltonian, it will at some time evolve into a state localised on the nearest-neighbours of the other marked vertex, the target vertex.

However, it was shown previously that the behaviour of the quantum search and the search starting state depends on the location of the vertex being searched for and which sublattice it is on. Consequently, we identify different cases of signal transport and treat these separately. We break these different cases down into communication between vertices which share the same optimal search starting state, those which do not share the same optimal starting state but are on the same sublattice, and those which are on different sublattices.

3.5.1 Communication between equivalent sites

In our first case, we assume that there are two perturbations on the graphene lattice located at the points $(\alpha_s, \beta_s)^A$ & $(\alpha_t, \beta_t)^A$, chosen such that $e^{i\frac{2\pi}{3}(\alpha_s + 2\beta_s)} = e^{i\frac{2\pi}{3}(\alpha_t + 2\beta_t)}$. The equality of the two phases means a search for either vertex, using our search algorithm, would use the same optimal starting state, given in Equation (3.42).

To understand the system dynamics, we now reduce the communication Hamiltonian in Equation (3.110) in the same way as shown in Section 3.2. The basis we use consists of the Dirac states, the localised states $|\alpha_s, \beta_s\rangle^A$ & $|\alpha_t, \beta_t\rangle^A$, and the neighbour states $|\ell_s\rangle$ and $|\ell_t\rangle$. As both of the perturbed sites are on the A sublattice, we already know that $W_{s/t} |\underline{K}\rangle^B = W_{s/t} |\underline{K}'\rangle^B = 0$ and so, the Dirac states which lie only on the B sublattice do not interact with the system at all. Also, as the perturbations disconnect the basis states $|\alpha_t, \beta_t\rangle^A$ & $|\alpha_t, \beta_t\rangle^A$ from the underlying lattice, they too do not take part in the dynamics.

Thus, the basis we use to reduce the full Hamiltonian consists of $\{|\underline{K}\rangle^A, |\underline{K}'\rangle^A, |\ell_s\rangle, |\ell_t\rangle\}$, and leads to the reduced Hamiltonian

$$\tilde{H} = \sqrt{\frac{6}{N}} \begin{pmatrix} 0 & 0 & e^{i\frac{2\pi}{3}(\alpha+2\beta)} & e^{i\frac{2\pi}{3}(\alpha+2\beta)} \\ 0 & 0 & e^{i\frac{2\pi}{3}(2\alpha+\beta)} & e^{i\frac{2\pi}{3}(2\alpha+\beta)} \\ e^{-i\frac{2\pi}{3}(\alpha+2\beta)} & e^{-i\frac{2\pi}{3}(2\alpha+\beta)} & 0 & 0 \\ e^{-i\frac{2\pi}{3}(\alpha+2\beta)} & e^{-i\frac{2\pi}{3}(2\alpha+\beta)} & 0 & 0 \end{pmatrix}, \qquad (3.111)$$

where we have dropped the subscripts indicating source and target vertices, as the choice of positions, by definition, means that the phases for both are equal. Diagonalising this reduced Hamiltonian, we find it has eigenvalues $\lambda_2^{\pm} = \pm 2\sqrt{\frac{6}{N}}$ and $\lambda_0^{1,2} = 0$ with eigenvectors

$$|\tilde{\psi}_{\pm 2}\rangle = \frac{1}{2} \left(e^{i\frac{2\pi}{3}(\alpha+2\beta)} |\underline{K}\rangle^A + e^{i\frac{2\pi}{3}(2\alpha+\beta)} |\underline{K}'\rangle^A \pm |\ell_s\rangle \pm |\ell_t\rangle \right) \qquad (3.112)$$

$$|\tilde{\psi}_0^1\rangle = \frac{1}{\sqrt{2}} \left(e^{i\frac{2\pi}{3}(\alpha+2\beta)} |\underline{K}\rangle^A - e^{i\frac{2\pi}{3}(2\alpha+\beta)} |\underline{K}'\rangle^A \right) \qquad (3.113)$$

$$|\tilde{\psi}_0^2\rangle = \frac{1}{\sqrt{2}} \left(|\ell_s\rangle - |\ell_t\rangle \right). \qquad (3.114)$$

Using these eigenstates, we may rewrite the source neighbour state as

$$|\ell_s\rangle = \frac{1}{2}\left(|\tilde{\psi}_2\rangle - |\tilde{\psi}_{-2}\rangle\right) + \frac{1}{\sqrt{2}}|\tilde{\psi}_0^2\rangle \ . \tag{3.115}$$

Placing the system in the source state $|\ell_s\rangle$ and allowing the system to evolve under the reduced Hamiltonian, one finds

$$|\psi(t)\rangle = e^{-i\tilde{H}t}|\ell_s\rangle \tag{3.116}$$

$$= \frac{1}{2}\left(e^{-i\lambda_2^+ t}|\tilde{\psi}_2\rangle - e^{-i\lambda_2^- t}|\tilde{\psi}_{-2}\rangle\right) + \frac{1}{\sqrt{2}}|\tilde{\psi}_0^2\rangle \tag{3.117}$$

$$= \frac{-i}{2}e^{i\frac{2\pi}{3}(\alpha+2\beta)}\sin\left(\lambda_2^+ t\right)\left(|\underline{K}\rangle^A + e^{i\frac{2\pi}{3}(\alpha-\beta)}|\underline{K'}\rangle^A\right)$$
$$+ \frac{1}{2}\left(\cos\left(\lambda_2^+ t\right) + 1\right)|\ell_s\rangle + \frac{1}{2}\left(\cos\left(\lambda_2^+ t\right) - 1\right)|\ell_t\rangle \ . \tag{3.118}$$

We note that the term in the brackets involving only the Dirac states $|\underline{K}\rangle^A$ and $|\underline{K'}\rangle^A$ is actually the state $|start\rangle$ defined in Equation (3.42), the optimal search starting state for both vertices. We can now see that the system oscillates between the states localised on the neighbours of the perturbed vertices, $|\ell_s\rangle$ & $|\ell_t\rangle$, in a time $T = \frac{\pi}{2}\sqrt{\frac{N}{6}}$, via their optimal search starting state.

Figure 3.14 shows the system allowed to evolve under the full communication Hamiltonian from Equation (3.110). The initial state used for the time evolution shown in Figure 3.14 is the true localised state, that is, we run the quantum search with a single perturbation located at vertex $(\alpha_s, \beta_s)^A$ until it reaches maximum success probability, and then apply the second perturbation to the vertex $(\alpha_t, \beta_t)^A$. The figure confirms the behaviour expected from the reduced model calculation.

The communication mechanism essentially works in the same way as the quantum search algorithm, as it can be viewed as one marked vertex 'finding' another. The initial localised source state decays back towards the search starting state, and the system then searches for the target state.
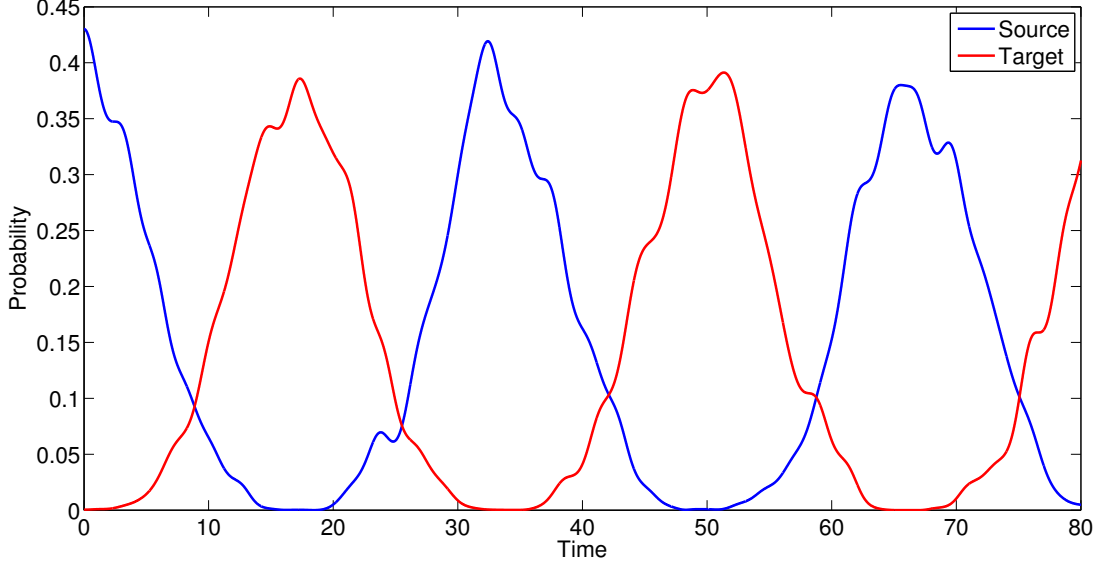
Figure 3.14: Numerically calculated signal transfer on a 12×12 cell graphene lattice between equivalent vertices, using the communication Hamiltonian in Equation (3.110). The system is initialised in $|\ell_s\rangle$ and localises on $|\ell_t\rangle$. Only the sum of probabilities to be found on the neighbour vertices is shown.

3.5.2 Communication between non-equivalent sites

We can carry out the same analysis for non-equivalent sites on the same sublattice, that is, those vertices on the same sublattice which do not share an optimal search starting state. However, the analysis does become slightly more complicated. This is due to interference effects since the two perturbation sites cannot interact via the same optimal search starting state as the system transitions from being in one localised state to another.

We continue to assume that both perturbations are located on the same sublattice, namely the A sublattice, but we now put in place the restriction $e^{i\frac{2\pi}{3}(\alpha_s + 2\beta_s)} \neq e^{i\frac{2\pi}{3}(\alpha_t + 2\beta_t)}$. As both perturbations remain on the same sublattice, we use the same basis to reduce the full Hamiltonian, specifically $\{|\underline{K}\rangle^A, |\underline{K}'\rangle^A, |\ell_s\rangle, |\ell_t\rangle\}$. We rewrite the position of the target vertex in terms of the source

vertex, so that $\alpha_t = \alpha_s + x$ and $\beta_t = \beta_s + y$. This gives the reduced Hamiltonian

$$
\tilde{H} = \sqrt{\frac{6}{N}} \begin{pmatrix} 0 & 0 & e^{i\frac{2\pi}{3}(\alpha_s+2\beta_s)} & e^{i\frac{2\pi}{3}(\alpha_s+2\beta_s+x+2y)} \\ 0 & 0 & e^{i\frac{2\pi}{3}(2\alpha_s+\beta_s)} & e^{i\frac{2\pi}{3}(2\alpha_s+\beta_s+2x+y)} \\ e^{-i\frac{2\pi}{3}(\alpha_s+2\beta_s)} & e^{-i\frac{2\pi}{3}(2\alpha_s+\beta_s)} & 0 & 0 \\ e^{-i\frac{2\pi}{3}(\alpha_s+2\beta_s+x+2y)} & e^{-i\frac{2\pi}{3}(2\alpha_s+\beta_s+2x+y)} & 0 & 0 \end{pmatrix} .
$$

$$(3.119)$$

This reduced Hamiltonian has eigenvalues $\lambda_{\sqrt{3}}^{\pm} = \pm\sqrt{3}\sqrt{\frac{6}{N}}$ & $\lambda_1^{\pm} = \pm\sqrt{\frac{6}{N}}$ with eigenvectors

$$
|\tilde{\psi}_{\pm\sqrt{3}}\rangle = \frac{e^{i\frac{2\pi}{3}(\alpha_s+2\beta_s)}}{2\sqrt{3}} \left(e^{i\frac{2\pi}{3}(x+2y)} - 1 \right) |\underline{K}\rangle^A + \frac{e^{i\frac{2\pi}{3}(2\alpha_s+\beta_s)}}{2\sqrt{3}} \left(e^{-i\frac{2\pi}{3}(x+2y)} - 1 \right) |\underline{K'}\rangle^A
$$
$$
\mp \frac{1}{2} |\ell_s\rangle \pm \frac{1}{2} |\ell_t\rangle \tag{3.120}
$$

$$
|\tilde{\psi}_{\pm 1}\rangle = \mp \frac{e^{i\frac{2\pi}{3}(\alpha_s+2\beta_s)}}{2} \left(e^{i\frac{2\pi}{3}(x+2y)} + 1 \right) |\underline{K}\rangle^A \pm \frac{e^{i\frac{2\pi}{3}(2\alpha_s+\beta_s)}e^{i\frac{2\pi}{3}(x+2y)}}{2} |\underline{K'}\rangle^A
$$
$$
- \frac{1}{2} |\ell_s\rangle - \frac{1}{2} |\ell_t\rangle . \tag{3.121}
$$

Once again, in order to calculate the time-evolution of the communication protocol, we express the basis state $|\ell_s\rangle$ in terms of the reduced Hamiltonian eigenvectors

$$
|\ell_s\rangle = \frac{1}{2} \left(-|\tilde{\psi}_{\sqrt{3}}\rangle + |\tilde{\psi}_{-\sqrt{3}}\rangle - |\tilde{\psi}_1\rangle - |\tilde{\psi}_{-1}\rangle \right) . \tag{3.122}
$$

Preparing the system in the localised state $|\ell_s\rangle$ and evolving under the reduced Hamiltonian from Equation (3.119), we obtain

$$
|\psi(t)\rangle = e^{-i\tilde{H}t} |\ell_s\rangle \tag{3.123}
$$
$$
= \frac{1}{2} \left(-e^{-i\lambda_{\sqrt{3}}^+ t} |\tilde{\psi}_{\sqrt{3}}\rangle + e^{-i\lambda_{\sqrt{3}}^- t} |\tilde{\psi}_{-\sqrt{3}}\rangle - e^{-i\lambda_1^+ t} |\tilde{\psi}_1\rangle - e^{-i\lambda_1^- t} |\tilde{\psi}_{-1}\rangle \right) \tag{3.124}
$$
$$
= \frac{i\, e^{i\frac{2\pi}{3}(\alpha_s+2\beta_s)}}{2} \left[\frac{1}{\sqrt{3}} \left(e^{i\frac{2\pi}{3}(x+2y)} - 1 \right) \sin\left(\lambda_{\sqrt{3}}^+ t\right) - \left(e^{i\frac{2\pi}{3}(x+2y)} + 1 \right) \sin\left(\lambda_1^+ t\right) \right] |\underline{K}\rangle^A
$$
$$
+ \frac{i\, e^{i\frac{2\pi}{3}(2\alpha_s+\beta_s)}}{2} \left[\frac{1}{\sqrt{3}} \left(e^{-i\frac{2\pi}{3}(x+2y)} - 1 \right) \sin\left(\lambda_{\sqrt{3}}^+ t\right) + e^{i\frac{2\pi}{3}(x+2y)} \sin\left(\lambda_1^+ t\right) \right] |\underline{K'}\rangle^A
$$
$$
+ \frac{1}{2} \left[\cos\left(\lambda_{\sqrt{3}}^+ t\right) + \cos\left(\lambda_1^+ t\right) \right] |\ell_s\rangle - \frac{1}{2} \left[\cos\left(\lambda_{\sqrt{3}}^+ t\right) - \cos\left(\lambda_1^+ t\right) \right] |\ell_t\rangle . \tag{3.125}
$$

Our only concern in the above, unwieldy expression are the prefactors of $|\ell_s\rangle$ & $|\ell_t\rangle$ as we are only interested in the transfer of probability amplitude between the two
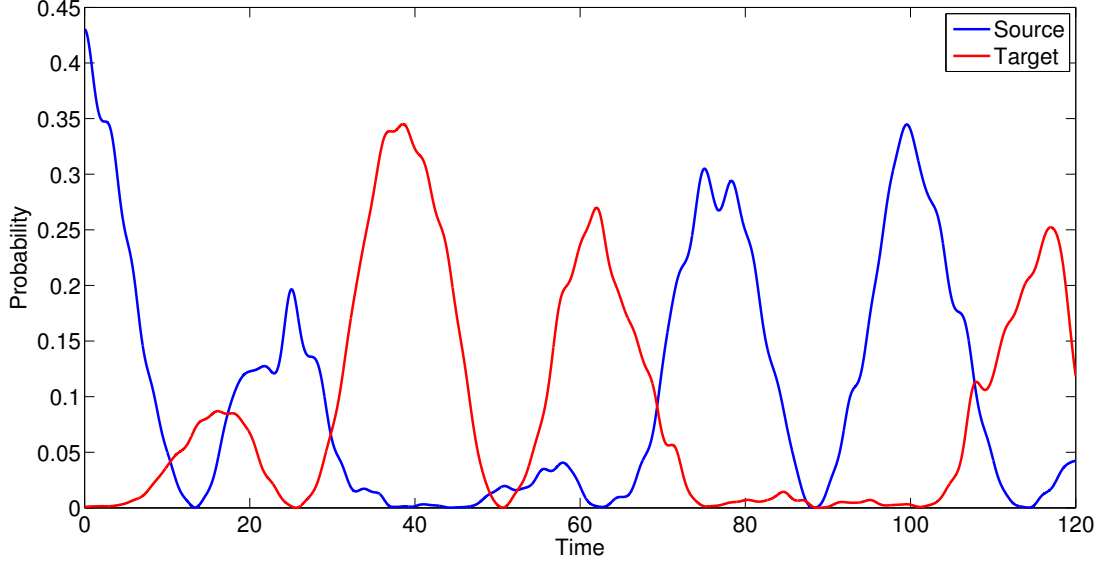
Figure 3.15: Numerically calculated signal transfer on a 12×12 cell graphene lattice between non-equivalent vertices, using the communication Hamiltonian in Equation (3.110). The system is initialised in $|\ell_s\rangle$ and localises on $|\ell_t\rangle$. Only the sum of probabilities to be found on the neighbour vertices is shown.
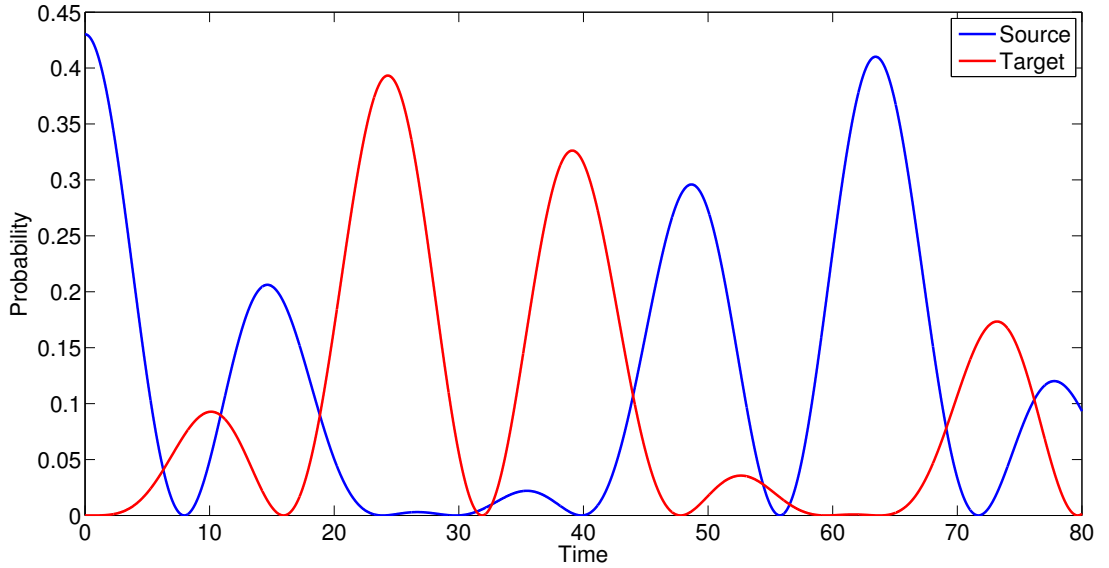
Figure 3.16: Plot of the analytically calculated signal transfer behaviour between non-equivalent vertices from Equation (3.125), for a 12×12 cell graphene lattice with $N = 288$ vertices. The probability has been scaled so that the source probability at $t = 0$ matches that shown in Figure 3.15 at $t = 0$.

perturbed vertices. These prefactors do not depend on the coordinates of the source and target vertices and, therefore, the behaviour of the system is the same for transport between all non-equivalent vertices on the same sublattice.

Figure 3.15 shows the system evolved under the full communication Hamiltonian. Again, the initial state is the true localised state on the nearest-neighbours of the source vertex, obtained by running the search algorithm using one marked vertex until it reaches its peak success probability. Unlike the transport between equivalent vertices, shown in Figure 3.14, where the signal pattern of the communication is periodic, the behaviour of transport between non-equivalent vertices is erratic with uneven peaks of probability at the two perturbations involved in the protocol. However, there are still significant probability peaks with around $65\% - 80\%$ state reconstruction.

The transport behaviour from Equation (3.125), calculated using the reduced Hamiltonian, is shown in Figure 3.16. The probability at time $t = 0$ has been scaled to match that shown in Figure 3.15. Our calculated behaviour has the same signal pattern as the numerically calculated behaviour from the full Hamiltonian, although over a shorter time scale so that the behaviour from $t = 0$ to $t \approx 75$ in Figure 3.16 matches the whole time-evolution shown in Figure 3.15. As our reduced model only makes use of the Dirac states and the perturber states we lose the contribution to the time-evolution from the rest of the spectrum. It is through this neglect of the rest of spectrum that we lose the logarithmic correction obtained for the quantum search in Section 3.3, and so our time-evolution of our calculated behaviour does not match the time-evolution obtained under the full Hamiltonian. Other numerics also show that signal transfer between all non-equivalent vertices displays the same behaviour.

The erratic nature of the signal pattern arises as the perturbed vertices do not share the same optimal starting state. As mentioned previously, the communication protocol is essentially the search mechanism in reverse, where one vertex 'finds' another. The behaviour then emerges from the interference between the two separate search mechanisms which interact due to the non-zero inner product of the three possible optimal search starting states for vertices on the A sublattice.

3.5.3 Communication between different sublattices

Signal transfer between perturbations on different sublattices is much more complex than the previous two cases. The reduced model cannot be used here because, as we have seen in earlier reduced model calculations, perturbations on one sublattice do not

interact with states which live on the other. Thus, when attempting to reduce the communication Hamiltonian as in the two preceding subsections, it decouples into two non-interacting quantum search Hamiltonians, one on the A sublattice and another on the B sublattice.

Consequently, we focus only on numerical simulations of transport between sublattices, examples of the time-evolution of such communication systems are shown in Figures 3.17 & 3.18 with further examples given in Appendix B. All the figures in this subsection, including those in Appendix B, use the same source state but use target states located on different vertices. In the same manner as described in the previous two subsections, the source state is obtained by running the quantum search with one perturbation until it reaches its peak success probability. The numerical results show that the transport takes place over a much longer timescale. We also find in the numerics that the localised states live mainly on one sublattice, and so these longer timescales can be attributed by the weak nature of the interaction between localised states on different sublattices.

The signal pattern shown in the figures is a superposition of two underlying system dynamics. This is seen in the beating pattern found in Figures 3.17 & 3.18, composed of a shorter period oscillation between successive recurrences at the same source/target sites and a longer period oscillation between maximum success probability at the source/target sites.

The shorter period oscillation is of the same order as the period between success times in the quantum search algorithm. There the system oscillates between the optimal starting state which lives on one sublattice and the nearest-neighbours of the marked vertex which are on the other sublattice. In this transport case, in contrast to probability amplitude simply oscillating between the sublattices, some amplitude remains behind on the other sublattice rather than oscillate back. This reduces the amplitude which can be used for each recurrence back to the initial state. This continues until the recurrence probability at the target perturbation reaches the same success probability as the initial state, and the behaviour then reverses. The numerical results also show there are only a finite number of different transport behaviours which are repeated across the lattice, but with no discernible pattern indicating which signal pattern will develop for transport between any two particular vertices. This behaviour remained true as the system size was increased.
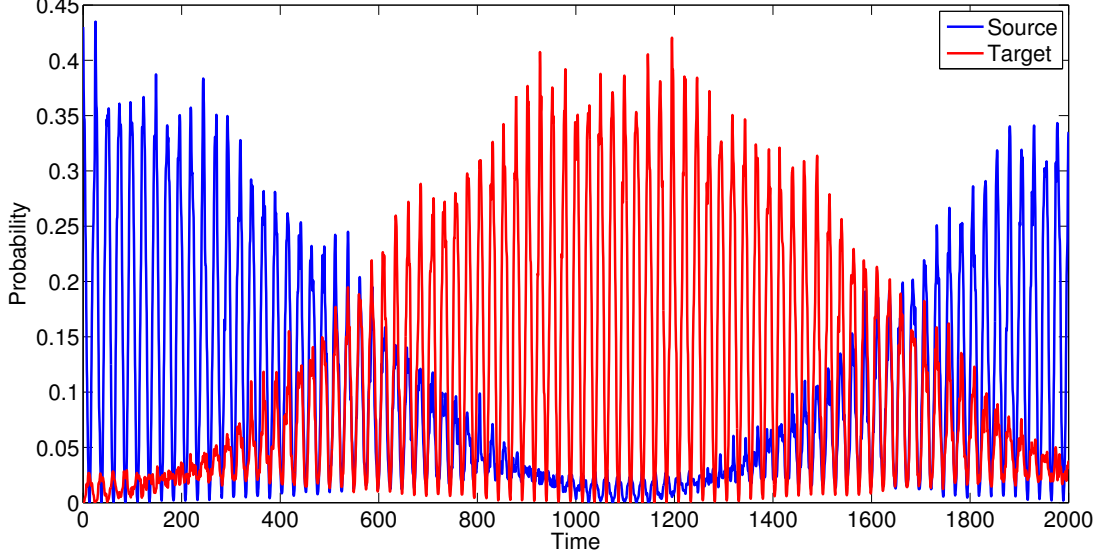
Figure 3.17: Numerically calculated signal transfer on a 12×12 cell graphene lattice between vertices on different sublattices, using the communication Hamiltonian in Equation (3.110). The system is initialised in $|\ell_s\rangle$ and localises on $|\ell_t\rangle$. Only the sum of probabilities to be found on the neighbour vertices is shown.
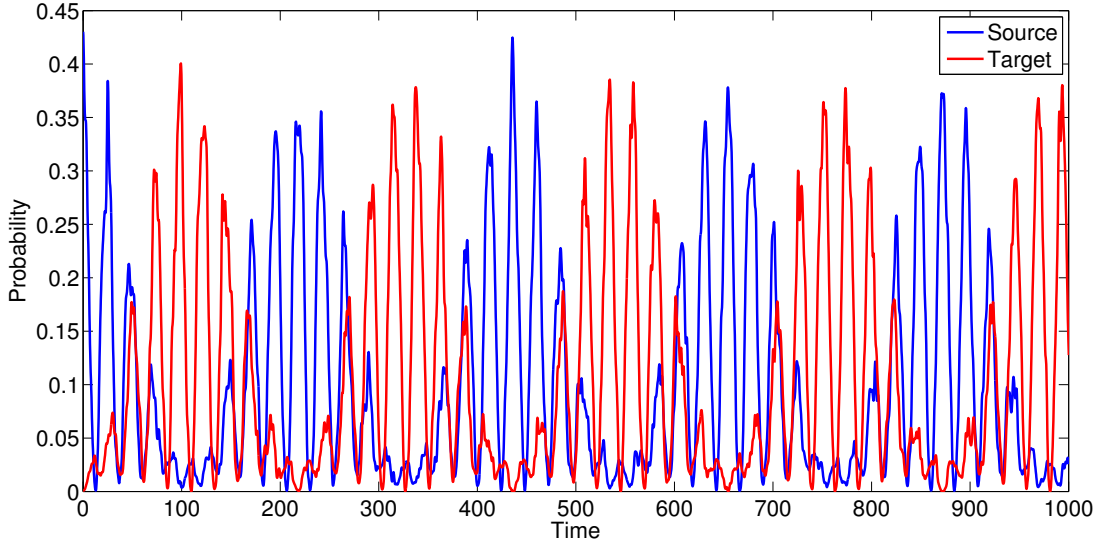
Figure 3.18: Another example of numerically calculated signal transfer on a 12×12 cell graphene lattice between vertices on different sublattices, using the communication Hamiltonian in Equation (3.110). The system is initialised in $|\ell_s\rangle$ and localises on a different target state $|\ell_t\rangle$ to the one used in Figure 3.17. Only the sum of probabilities to be found on the neighbour vertices is shown.

4

Searches using alternative perturbations and other graphene nanostructures

In this chapter, we review alternative perturbations for constructing searches and signal transfer protocols, as well as quantum walks on different graphene structures, namely carbon nanotubes and graphene sheets.

We will start this chapter by considering alternative methods of marking a vertex on a torus, such as modifying the hopping potentials in a different way, or the coupling of additional sites to the lattice. These searches will be analysed using the reduced Hamiltonian method first described in Chapter 3. We will then discuss the effect of these perturbations on quantum walks over other graphene structures mentioned, both in terms of searches or communication setups.

4.1   Search using single-bond perturbations

In the quantum search and communication systems we have discussed so far, we have only used perturbations where the bond strength of a vertex to all three of its nearest-neighbours is changed equally. However, this is only one possible way of introducing a perturbation through its bond strengths. In this section, we will describe a quantum search using a different perturbation type.

An alternative way of marking a vertex, compared to the triple-bond perturbation,
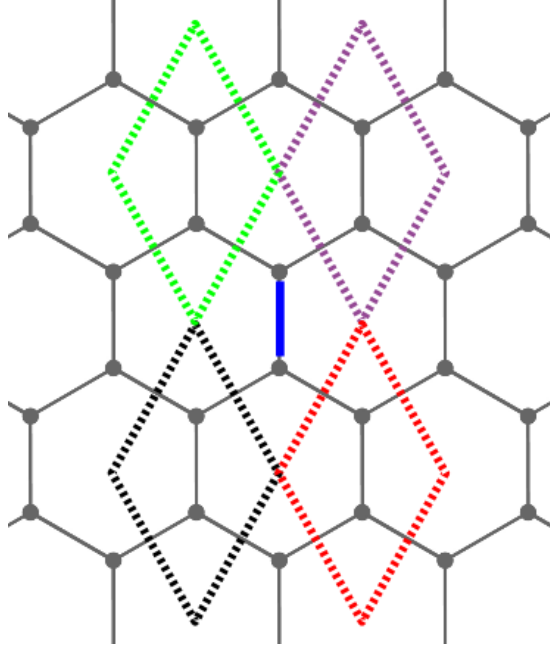
Figure 4.1: Example of single-bond perturbation (blue bond) from Equation (4.1) applied to a single cell. The colour of the surrounding cells chosen to match later figures showing walk dynamics.

is to modify the hopping potential between only one of a site's nearest-neighbours and the site itself. The perturbation matrix for this type of vertex marking is

$$W = |\alpha_0, \beta_0\rangle^A \langle\alpha_0, \beta_0|^B + |\alpha_0, \beta_0\rangle^B \langle\alpha_0, \beta_0|^A , \qquad (4.1)$$

with the simple eigenstates

$$|W_g\rangle = \frac{1}{\sqrt{2}} \left(|\alpha_0, \beta_0\rangle^A - |\alpha_0, \beta_0\rangle^B \right) \qquad (4.2)$$

$$|W_e\rangle = \frac{1}{\sqrt{2}} \left(|\alpha_0, \beta_0\rangle^A + |\alpha_0, \beta_0\rangle^B \right) \qquad (4.3)$$

and their associated eigenenergies $\lambda_{g/e} = \mp 1$.

The precise search Hamiltonian we use is

$$H = -\gamma A + W = -\gamma A + |\alpha_0, \beta_0\rangle^A \langle\alpha_0, \beta_0|^B + |\alpha_0, \beta_0\rangle^B \langle\alpha_0, \beta_0|^A , \qquad (4.4)$$

where γ is a free parameter. We assume the same torus cell as described previously, shown in Figure 3.1, and that there exist eigenstates whose eigenenergies coincide with

the Dirac energy.

This perturbation we have used is also a rank-2 matrix, same as the triple-bond perturbation matrix used in Chapter 3, and so again there are two perturber states. It also leaves the spectral symmetry of the Hamiltonian unchanged around $E = 0$ so there is a perturber state in both the positive and negative regions of the spectrum. We have chosen the perturbation such that it modifies the hopping potential between two vertices in the same cell, an example is given in Figure 4.1. As the perturbation matrix remains unchanged under permutations of the A and B sublattices, it marks both vertices in the cell in the same way. Therefore, it could be viewed as a perturbation marking out a particular cell, rather than marking the vertices themselves.

As we are now using a different perturbation to that used in Chapter 3, the avoided crossing used to generate search behaviour is not necessarily at $\gamma = 1$ (i.e. when the hopping potential between the marked vertices is zero) but most likely has another critical value and, therefore, we must search through the spectrum of H for an avoided crossing to use. Figure 4.2 shows the spectrum of Equation (4.4) as a function of γ for a 12×12 cell torus. Inspecting the region around the Dirac energy ($E = 0$), we see that two states (green curves) diverge away from the Dirac states and two states (red curves) approach. This continues until $\gamma \approx \frac{1}{3}$ where there is an exact crossing between the red and green curves, and this trend then reverses. Observing this behaviour, it would appear, at first guess, the critical value of γ relevant for the dynamics is $\gamma = \frac{1}{3}$ even though it does not look to be a conventional avoided crossing interaction.

In an effort to make this picture clearer, we attempt to understand this interaction by reducing the spectrum to only relevant eigenstates which would take part in the search dynamics by considering the symmetry classes of the lattice. In particular, we focus on those permutations of the lattice which leave the perturbation potential unchanged.

Specifically, the two permutation operations we initially choose are reflections about the vertical axis along the perturbed bond, labelled P_y, and reflections about the horizontal axis through the mid-point of the perturbed bond, labelled P_x. Both of these operators commute with the Hamiltonian and the perturbation matrix, leaving the spectrum unchanged. When considering the action of P_x on the two perturbed vertices, we find $P_x |\alpha_0, \beta_0\rangle^A = |\alpha_0, \beta_0\rangle^B$ and $P_x |\alpha_0, \beta_0\rangle^B = |\alpha_0, \beta_0\rangle^A$. It is clear from applying P_x to the perturber states in Equation (4.2) & (4.3) that the negative energy state $P_x |W_g\rangle = -|W_g\rangle$ and so is odd, and the positive energy state $P_x |W_e\rangle = |W_e\rangle$ and is even. Under the action of P_y both perturber states remain unchanged and are,
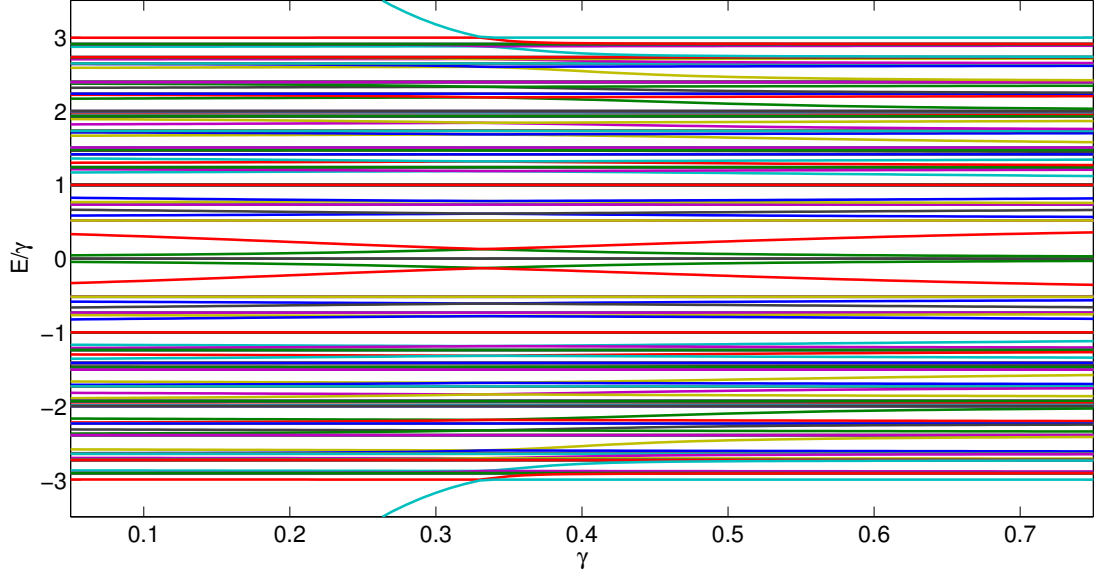
Figure 4.2: Numerically calculated spectrum of $H = -\gamma A + |\alpha_0, \beta_0\rangle^A \langle \alpha_0, \beta_0|^B + |\alpha_0, \beta_0\rangle^B \langle \alpha_0, \beta_0|^A$ as a function of γ for a 12×12 cell torus.
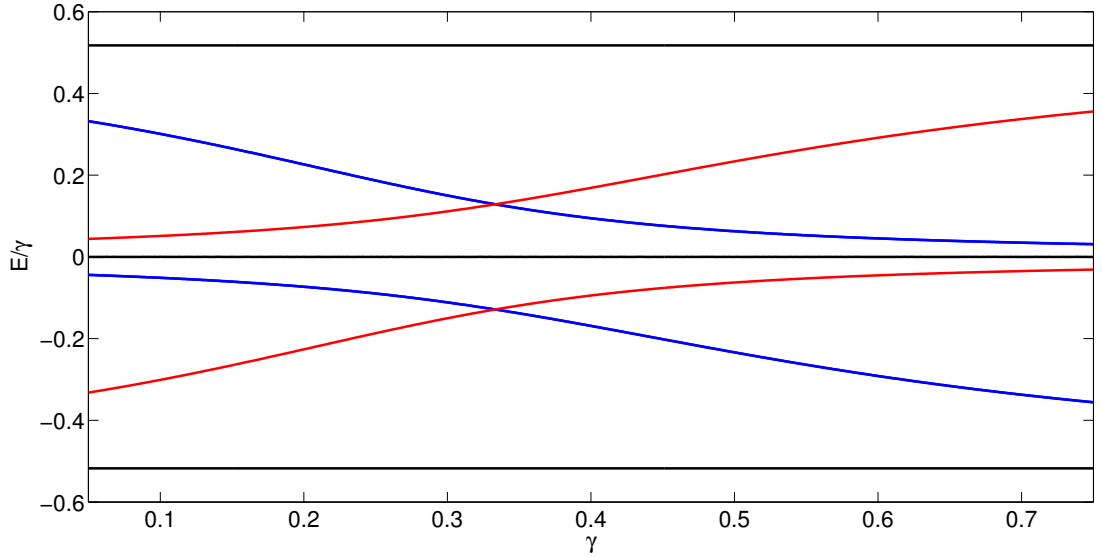
Figure 4.3: Numerically calculated spectrum of $H = -\gamma A + |\alpha_0, \beta_0\rangle^A \langle \alpha_0, \beta_0|^B + |\alpha_0, \beta_0\rangle^B \langle \alpha_0, \beta_0|^A$ as a function of γ for a 12×12 cell torus, focused on the avoided crossing around $E = 0$. The curves have been coloured depending on the states parity with respect to the P_x operator: even (blue), odd (red), undefined (black).

therefore, even with respect to P_y.

In a similar way to the unperturbed eigenstates discussed in SubSection 3.3.1, those states in the spectrum of the search Hamiltonian which remain degenerate as γ is changed do not 'feel' the perturbation and do not need to be included when considering the search dynamics. Being able to neglect these states, our next step is to classify those states which are perturbed as odd or even with respect to the reflection operators P_x & P_y.

Figure 4.3 shows a smaller region of the spectrum after we classify these states in terms of their parities. We restrict our attention to those states closest to the Dirac energy and colour the states depending on whether they are odd (red) or even (blue) with respect to P_x (degenerate states which are superpositions of both parities are coloured black). We have not coloured states dependent on their P_y parity as they are all even. It becomes apparent when the spectrum is deconstructed in this way, the interesting region of the spectrum around $\gamma = \frac{1}{3}$ is two different avoided crossings superimposed, one composed of states with even P_x parity and the other of states with odd parity. The minimum energy gap for both these sets of curves, which is the critical point necessary for the search, is $\gamma = \frac{1}{3}$, the point at which the two avoided crossing curves cross each other.

The parities of the states shown in Figure 4.3 agree with those which would be expected after considering the parities of the perturbers states. The blue avoided crossing in Figure 4.3 where the states decrease in energy with increasing γ is influenced by the positive energy perturber state $|W_e\rangle$. Therefore, as it is a superposition including $|W_e\rangle$, which is even with respect to P_x, the blue curves are even with respect to P_x. A similar argument is true for the red avoided crossing when considering the negative energy perturber state $|W_g\rangle$.

This analysis in terms of symmetries can be performed with other symmetries, and, in fact, the reflection operators P_x and P_y only exist for tori where the underlying torus cell has equal numbers of cells in each direction, and so the use of other symmetries is required to understand tori with different dimensions. For other tori, a similar deconstruction of the spectrum may be carried out using a rotation symmetry and the rotation operator C_2. The rotation operator C_2 is a rotation by π around the mid-point of the perturbed bond. Such a rotation applied to the eigenstates of the perturbation matrix W leads to $C_2 |W_g\rangle = -|W_g\rangle$ and $C_2 |W_e\rangle = |W_e\rangle$. This results in the same transformation as an application of P_x, allowing us to again classify states as having

an even or odd parity.

Having now established that the search dynamics are generated through avoided crossings and established the critical value is $\gamma = \frac{1}{3}$, to actually create a search we must first construct a starting state which has the optimal chance of succeeding. To find this initial state, we numerically reduce the search Hamiltonian, setting $\gamma = \frac{1}{3}$, using a basis formed from the states which we suspect of being involved in the search dynamics. The basis we use includes the Dirac states and also the two eigenstates of the single-bond perturbation matrix, that is, we use $\{ |\underline{K}\rangle^A , |\underline{K}'\rangle^A , |\underline{K}\rangle^B , |\underline{K}'\rangle^B , |W_g\rangle ,$ $|W_e\rangle \}$. We then numerically diagonalise this reduced Hamiltonian, which we label $\tilde{H}$, and we find three distinct pairs of eigenvalues: $\lambda_0^{1,2} = 0, \lambda_a^\pm = \pm a \ \& \ \lambda_b^\pm = \pm b$. Those eigenvectors corresponding to $\lambda_0^{1,2}$ are constructed using only the Dirac states and have no component from the perturber states, and so do not take part in any search dynamics.

The other eigenstates of $\tilde{H}$, however, do have components from both the Dirac states and the perturber states, and it is from these states we construct our starting state. We do this by keeping only the phases of the eigenstates corresponding to the Dirac states and then renormalising the resulting vector, i.e if the normalised eigenstate of $\tilde{H}$ is

$$|\tilde{\psi}\rangle = \alpha_1 |\underline{K}\rangle^A + \alpha_2 |\underline{K}'\rangle^A + \alpha_3 |\underline{K}\rangle^B + \alpha_4 |\underline{K}'\rangle^B + \beta_1 |W_g\rangle + \beta_2 |W_e\rangle , \qquad (4.5)$$

then we would only keep those state with an α_i prefactor and construct our starting state as

$$|start\rangle = \frac{1}{\sqrt{\sum_{i=1}^4 |\alpha_i|^2}} \left(\alpha_1 |\underline{K}\rangle^A + \alpha_2 |\underline{K}'\rangle^A + \alpha_3 |\underline{K}\rangle^B + \alpha_4 |\underline{K}'\rangle^B \right) . \qquad (4.6)$$

We repeat this process in turn for each of the four eigenstates of $\tilde{H}$. When comparing the starting states we have constructed we find that they reduce to two different starting states, as the two starting states created from the $\lambda_a^\pm$-eigenvectors are the same as the two from the $\lambda_b^\pm$-eigenvectors. Considering the two unique starting states in the same way, we find one starting state has even parity, and the other has odd parity, with respect to the reflection operator P_x. This explains why we have two different starting states, one for each avoided crossing system, identified by its reflection symmetry.

The system evolution under the search Hamiltonian using one of the numerically found optimal states is shown in Figures 4.4 & 4.5. We show the search behaviour

for only one of the initial states as it is the same for both optimal starting states. Figure 4.4 plots the probability of being found in the marked and neighbouring cells whereas Figure 4.5 plots the probability of being found in the marked vertices and their direct nearest-neighbours.

In Figure 4.5 the behaviour on the two marked vertices is the same and the nearest-neighbours of the marked vertices also have the same behaviour as each other. It is clear from the figures there is a significant localisation on the marked vertices or their nearest-neighbours, with the probability of being found on either of the marked vertices peaking at around $16 - 18\%$. From Figure 4.5 we can also see that the probability of being found on each of the marked vertices nearest-neighbours peaks at around 8%, resulting in a total probability of being found on the marked vertices and their nearest-neighbours of approximately 48%.

It can also be seen when comparing Figures 4.4 & 4.5 that the probability of being found on one of the nearest-neighbours and the probability of being found in the neighbouring cells is very similar. This indicates that there is a significant drop-off in probability amplitude away from the perturbed site. The success probability fluctuates even as it peaks, as the probability amplitude oscillates between the marked vertices and their nearest-neighbours. This is due to the probability amplitude being constrained in the local area by the increased hopping potential between the two marked vertices.

We numerically find that the critical value of γ remains at $\gamma = \frac{1}{3}$ and Figure 4.6 shows the scaling of the gap of the two avoided crossings at the critical value as the system size increases. As the search time is inversely proportional to the gap of the avoided crossing (described in SubSection 3.1), it also gives an estimate of the running time of the search. The scaling indicates a time till first localisation of $T = \mathcal{O}\left(\sqrt{N \ln N}\right)$ and is similar to the scaling of the quantum search in previous chapter, shown for various setups in Figures 3.5, 3.8 & 3.12.

We note that interpreting the single-bond perturbation as marking a single cell is similar to the quantum search by Childs & Goldstone in [21] where they used a modified Dirac Hamiltonian as the walk Hamiltonian. The two sublattices leading to a two-site basis fulfils the role played by the spin component of the Dirac Hamiltonian in their algorithm. Essentially, the spin degree of freedom in [21] augmented the Hilbert space to allow for a successful quantum search, whereas in a search on graphene this extra degree of freedom occurs naturally in terms of the two sublattices.
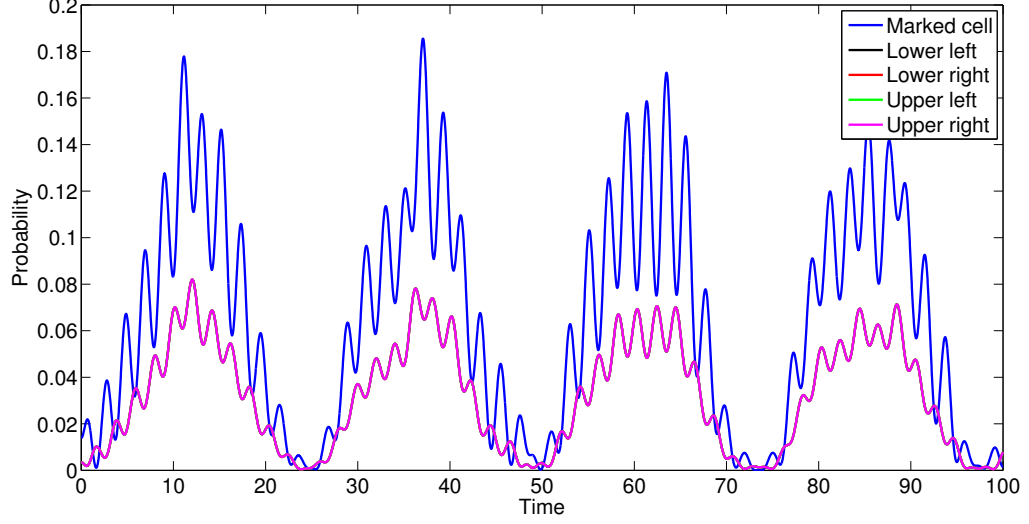
Figure 4.4: Numerically calculated search on a 12×12 cell graphene lattice using optimal starting state evolved under $H = -\gamma A + |\alpha_0, \beta_0\rangle^A \langle\alpha_0, \beta_0|^B + |\alpha_0, \beta_0\rangle^B \langle\alpha_0, \beta_0|^A$. Plotted are the probabilities to be found in the marked and nearest-neighbour cells using the line colours in Figure 4.1. The behaviour at each of the nearest-neighbour cells is the same, so only the behaviour at one can be seen.
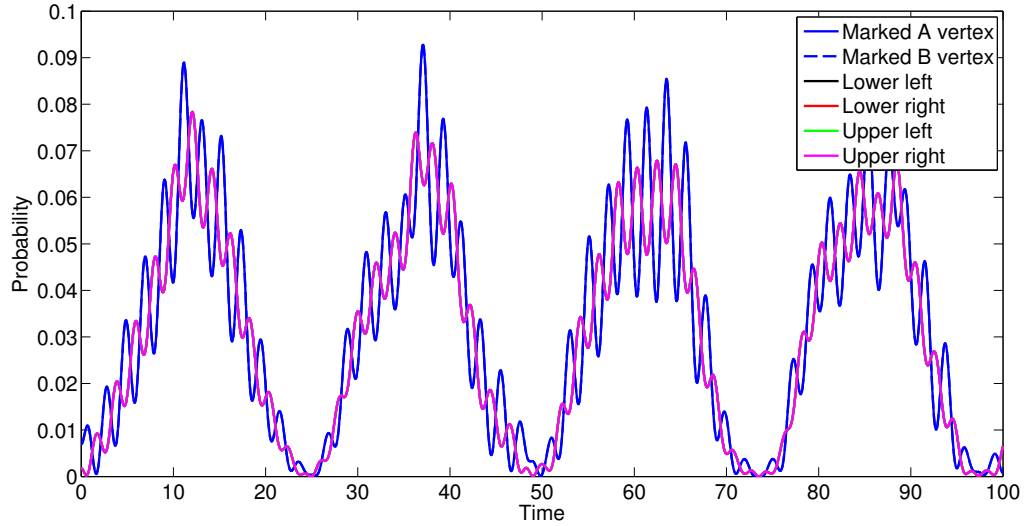
Figure 4.5: Numerically calculated search on a 12×12 cell graphene lattice using optimal starting state evolved under $H = -\gamma A + |\alpha_0, \beta_0\rangle^A \langle\alpha_0, \beta_0|^B + |\alpha_0, \beta_0\rangle^B \langle\alpha_0, \beta_0|^A$. Plotted are the probabilities to be found at the marked vertices and their direct nearest-neighbours using the line colours in Figure 4.1. The behaviour at each of the nearest-neighbour vertices is the same, so only the behaviour at one can be seen.
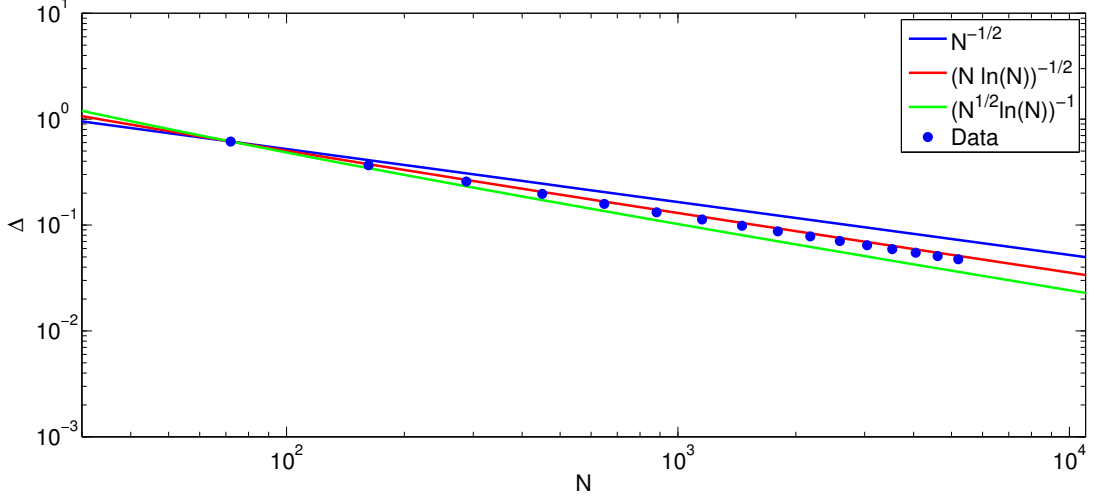
Figure 4.6: Numerically calculated avoided crossing gap (dots) between states nearest $E = 0$ at $\gamma = \frac{1}{3}$ in the spectrum of the search Hamiltonian in Equation (4.4). Also shown are the curves $c_1/\sqrt{N}$, $c_2/\sqrt{N \ln N}$ & $c_3/\left(\sqrt{N} \ln N\right)$ for comparison, as a function of number vertices N.

4.2 Additional sites

4.2.1 Search using single additional vertex

In this section, rather than mark vertices by a change of hopping potential, we will discuss perturbing a graphene lattice with the addition of extra vertices. Our reason for so far using hopping potential perturbations to mark a vertex instead of altering its on-site energy is that only by changing the hopping potential could we force a perturbation to interact with the conical region of the spectrum. However, this is based upon the assumption that we wish to only work with the lattice itself. Ridding ourselves of this restriction, it may be possible to create a perturbation which interacts with the conical region of the spectrum with the inclusion of an additional site and fine-tune the interaction by modifying its on-site energy.

Our perturbation matrix for the coupling of an additional vertex to a single A-type site is

$$W\left(\gamma\right) = -\left|\alpha_0, \beta_0\right\rangle^A \left\langle site\right| - \left|site\right\rangle \left\langle \alpha_0, \beta_0\right|^A + \gamma \left|site\right\rangle \left\langle site\right|, \qquad (4.7)$$

where $\left|site\right\rangle$ is the additional vertex and γ is a free parameter. This matrix can be split into two parts. The first part consists of the two terms involving both $\left|site\right\rangle$ & $\left|\alpha_0, \beta_0\right\rangle^A$.
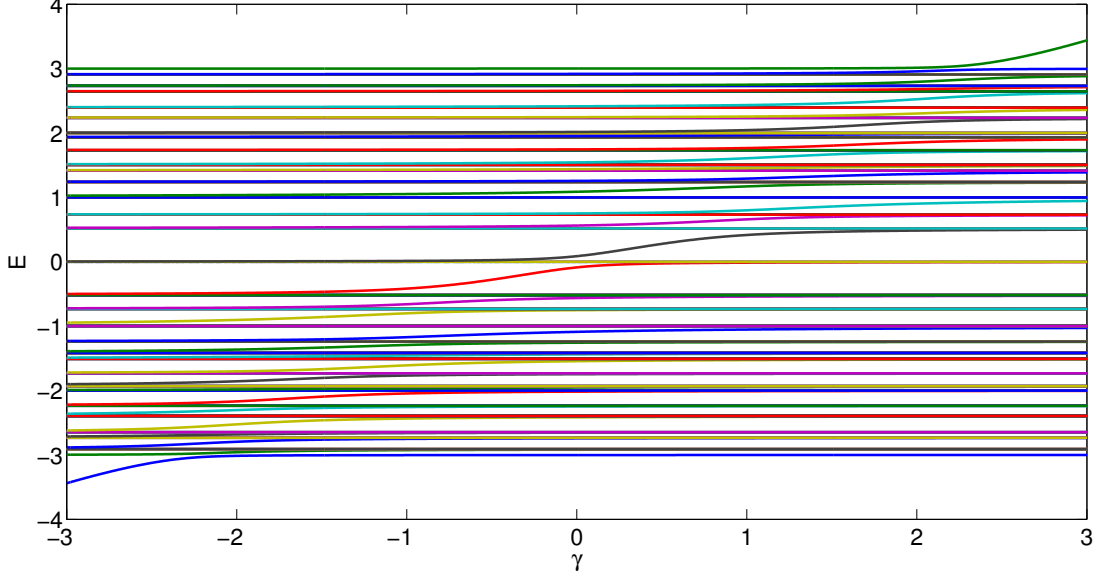
Figure 4.7: Numerically calculated spectrum of search Hamiltonian from Equation (4.9) as a function of γ for a 12×12 cell torus.

These are the hopping potential terms binding the additional vertex to the graphene lattice and the sign of these terms has been chosen to match the unperturbed walk Hamiltonian $H_o = -A$. The second part, $\gamma |site\rangle \langle site|$, is the entry corresponding to the on-site energy and the free parameter γ allows us to fine-tune this property.

Our search Hamiltonian using this perturbation follows as

$$H = H_o + W(\gamma) \tag{4.8}$$

$$= -A - |\alpha_0, \beta_0\rangle^A \langle site| - |site\rangle \langle \alpha_0, \beta_0|^A + \gamma |site\rangle \langle site| . \tag{4.9}$$

In constructing the adjacency matrix, we have assumed the same torus cell as used in the previous section and Chapter 3, shown in Figure 3.1, and that there are eigenstates whose eigenenergies coincide with the Dirac energy.

We must now search through the spectrum of the search Hamiltonian as γ is varied for an avoided crossing which we can use to construct some type of search. In Figure 4.7 we show the spectrum as a function of γ. We can see a clear avoided crossing around the Dirac states with energy $E = 0$ at $\gamma = 0$, that is, when the on-site energy of the additional vertex matches that of the vertices in the underlying lattice.
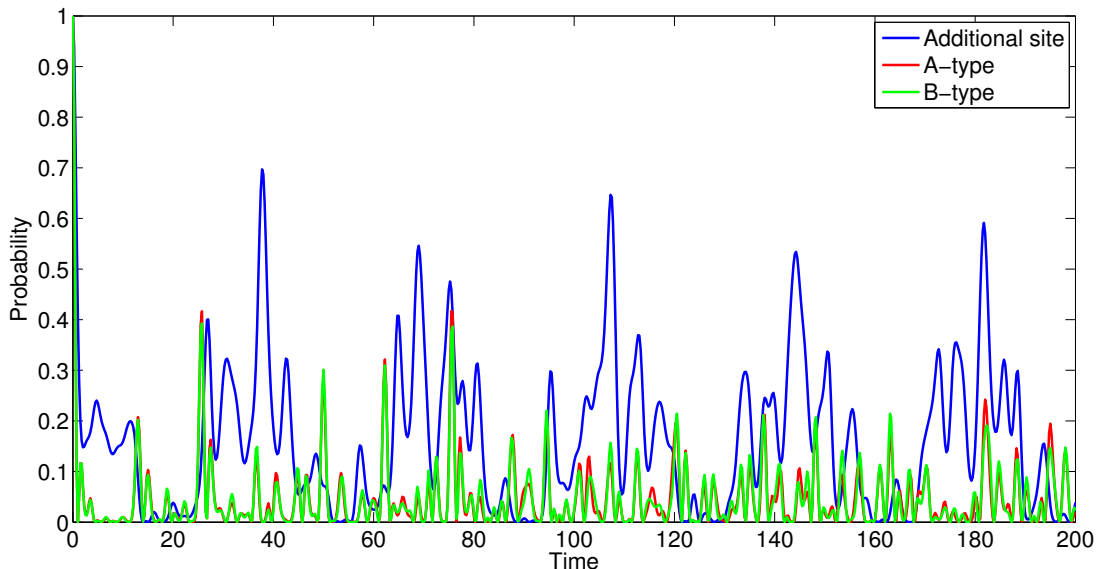
Figure 4.8: Time-evolution of different initial localised states, evolved under the Hamiltonian in Equation (4.10) on a 12×12 cell torus. The different initial states are localised on the additional vertex, a random site on the A- and the B-sublattice.

Thus, using our critical point, the search Hamiltonian reduces to

$$H = -A - |\alpha_0, \beta_0\rangle^A \langle site| - |site\rangle \langle \alpha_0, \beta_0|^A \ , \tag{4.10}$$

which is simply the adjacency matrix of the whole lattice, including the additional site. At this stage, it seems that merely the addition of an extra site is enough to create the necessary environment for search behaviour.

As an indicator of the transport properties of the lattice, and the difference in system behaviour at the additional site, we compare the dissipation and revival probabilities of different initially localised states. The time-evolution of various states initially localised to a single vertex are shown in Figure 4.8. It compares the time-evolution of an initial state localised on the additional vertex to the behaviour at two randomly chosen vertices on the underlying lattice, on both A and B sublattices. We can see that the two curves for the two vertices on the underlying lattice (red and green curves) very closely mimic each other. This should be expected as, before the introduction of a very localised and relatively weak perturbation, all vertices on the lattice are equivalent, as are the two sublattices. Therefore, we take this behaviour as typical for localised states anywhere on the original lattice (this is borne out by further numerics not shown). We see in

Figure 4.8 that for vertices on the underlying lattice there are occasional significant recurrences of around $35 - 40\%$ but overall the signal is fairly unstructured and has revival probabilities of roughly $10 - 15\%$. This is in contrast to the behaviour at the additional site where the maximum revival probability is between $55 - 70\%$ and, although slightly erratic, there is a definite period between successive occurences of period $T \approx 35$.

This difference in the transport of dynamics and improvement in the localisation and dissipation of an initially localised state compared to those on the basic lattice are a good indicator we can use this system to construct a search algorithm. To this end, we construct a reduced Hamiltonian to solve for the dynamics and derive our initial search state. We restrict the states we consider to the Dirac states and the additional site $|site\rangle$, that is, those involved in the avoided crossing.

We find, using Equation (4.10), $H |\underline{K}\rangle^B = H |\underline{K}'\rangle^B = 0$. This is clear from the observation that the Dirac states are 0-eigenvectors of $-A$, by construction they lie only on the B sublattice so $^A\langle \alpha_0, \beta_0 | \underline{K}/\underline{K}' \rangle^B = 0$, and as the additional site is only coupled to the A sublattice $\langle site | \underline{K}/\underline{K}' \rangle^B = 0$. We also note that $H |site\rangle = |\alpha_0, \beta_0\rangle^A$, as $-A |site\rangle = 0$.

Thus, our reduced system involves only three states, namely $\{|\underline{K}\rangle^A, |\underline{K}'\rangle^A, |site\rangle\}$. Reducing the full Hamiltonian from Equation (4.10) in this basis results in the reduced Hamltonian

$$\tilde{H} = \sqrt{\frac{2}{N}} \begin{pmatrix} 0 & 0 & e^{-i\frac{2\pi}{3}(\alpha_0 + 2\beta_0)} \\ 0 & 0 & e^{-i\frac{2\pi}{3}(2\alpha_0 + \beta_0)} \\ e^{i\frac{2\pi}{3}(\alpha_0 + 2\beta_0)} & e^{i\frac{2\pi}{3}(\alpha_0 + 2\beta_0)} & 0 \end{pmatrix}. \tag{4.11}$$

This reduced Hamiltonian is in fact the same reduced Hamiltonian, up to a constant factor, we found for the triple-bond perturbation search in Equation (3.38) from Section 3.2. The only difference between the two systems are the eigenvalues which for this system are $\lambda_{\pm\sqrt{2}} = \pm\sqrt{2}\sqrt{\frac{2}{N}}$ and $\lambda_0 = 0$.

In Section 3.2, it was shown the system there oscillates from the delocalised state into the localised state in a time $T = \frac{\pi}{4}\sqrt{\frac{N}{3}}$. As the only differences between the two systems are the nature of the localised states and the eigenvalues, the only difference in behaviour between the two systems is exactly which state the system localises to and the time taken. Thus, using the same starting state, found in Equation (3.42), we find that the system here rotates from a superposition of the Dirac states to a state localised on the additional site in a time $T = \frac{\pi}{4}\sqrt{N}$.

As it is essentially the same dynamics, the same analysis of the potential starting states from Section 3.2 remains true for this system. Therefore, there are overall six possible starting states, three for an additional site coupled to each sublattice. We also know that a random superposition of the Dirac states will reduce the success probability, on average, by a factor of $\frac{1}{4}$. See pages 50 & 63 for more details.

Figure 4.9 shows the additional site system prepared in its optimal search starting state allowed to evolve under the full Hamiltonian in Equation (4.10). It confirms the search behaviour that we expected using our reduced model and there is strong localisation of around $50 - 60\%$ probability for the system to be measured on the additional site. As the additional vertex is coupled to only one of the underlying lattice vertices, a search for the marked vertex can be completed with one additional classical step. Again, similar to the triple-bond perturbation search in Chapter 3, we have effectively searched for a vertex by localising on a nearest-neighbour instead of directly on the marked vertex.

As the search time is inversely proportional to the energy gap at the avoided crossing, by considering the scaling of the gap we can learn about the scaling of the search time. Figure 4.10 shows the scaling of the energy gap, demonstrating that the time taken for first localisation is approximately $T = \mathcal{O}\left(\sqrt{N \ln\left(N\right)}\right)$. This is comparable to the types of searches described in Chapter 3 and Section 4.1.
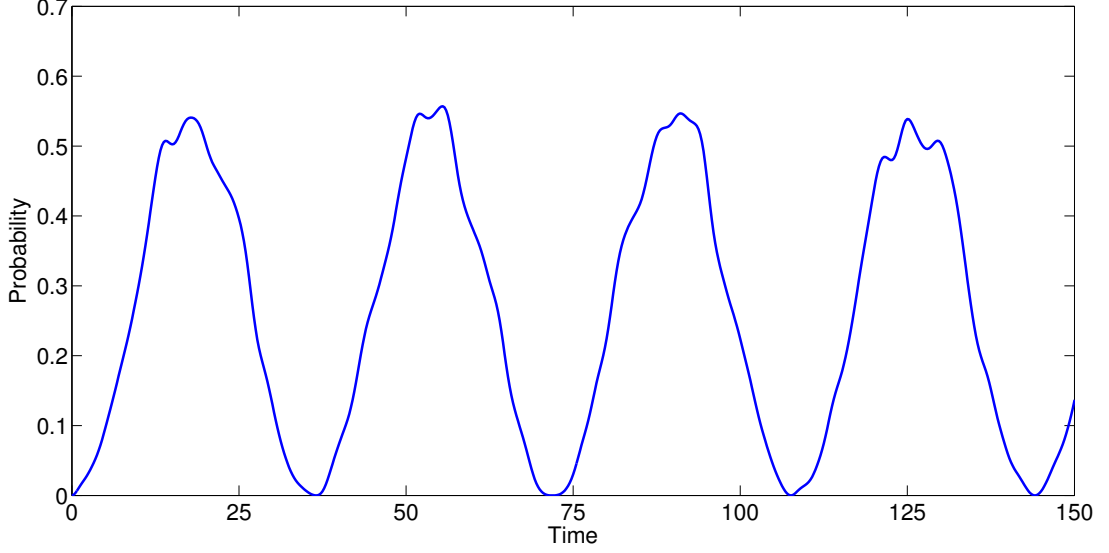
Figure 4.9: Numerically evolved search on a a 12×12 cell graphene torus using optimal search starting state, and evolved under the Hamiltonian from Equation (4.10). Plotted is the probability at the additional vertex only.
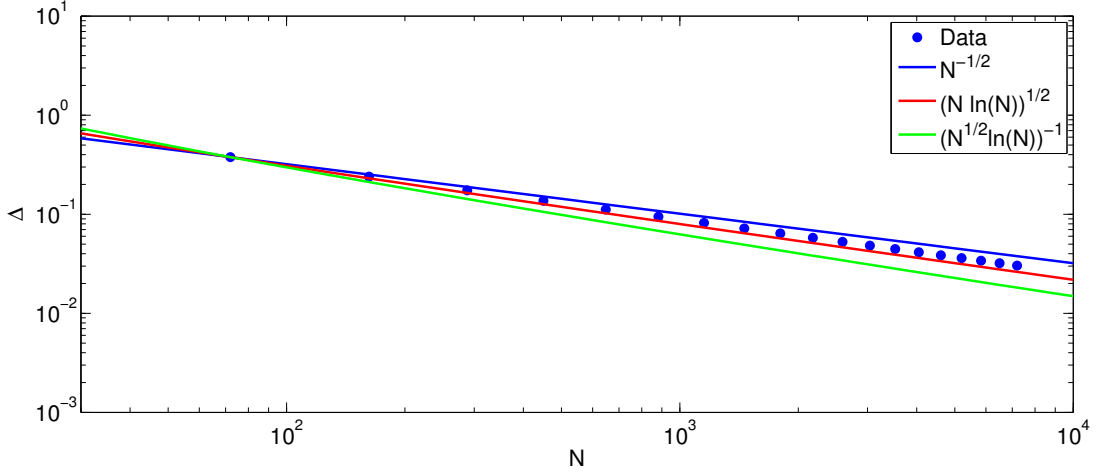
Figure 4.10: Numerically calculated avoided crossing gap (dots) between states nearest $E = 0$ at $\gamma = 0$ for the search Hamiltonian in Equation (4.10). Also shown are the curves $c_1/\sqrt{N}$, $c_2/\sqrt{N \ln N}$ & $c_3/\left(\sqrt{N} \ln N\right)$ for comparison, as a function of number vertices N.

4.2.2 Communication using additional vertices

As the search dynamics of additional sites bound to a single site of the graphene lattice are the same as introducing a triple-bond perturbation, one may assume that other aspects of the triple-bond perturbation remain true. Namely, we attempt to construct a communication protocol using additional sites in the same way as triple-bond perturbations. That is, we construct the communication Hamiltonian

$$H = -A - |\alpha_s, \beta_s\rangle^A \langle site_s| - |site_s\rangle \langle \alpha_s, \beta_s|^A - |\alpha_t, \beta_t\rangle^A \langle site_t| - |site_t\rangle \langle \alpha_t, \beta_t|^A \ , \ (4.12)$$

for signal transfer between additional sites coupled to A-type sites $(\alpha_s, \beta_s)^A$ and $(\alpha_t, \beta_t)^A$.

Indeed, we find that signal transfer in this setup is possible and the resulting dynamics are the same as in Section 3.5 for the triple-bond perturbation. However, we include the figures here for completeness. In contrast to Section 3.5, the initial state for the communication is localised only on the additional vertex and is not the extended localised state found by running the search algorithm with only one perturbation.
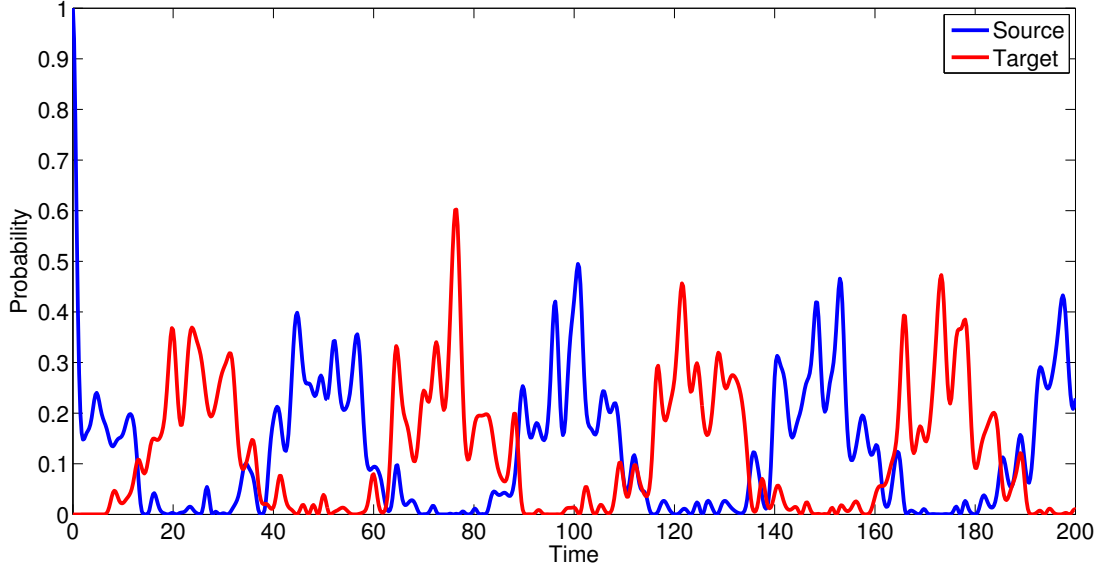
Figure 4.11: Numerically calculated signal transfer on a 12×12 cell graphene lattice between additional vertices coupled to equivalent vertices, time-evolved under the communication Hamiltonian in Equation (4.12).
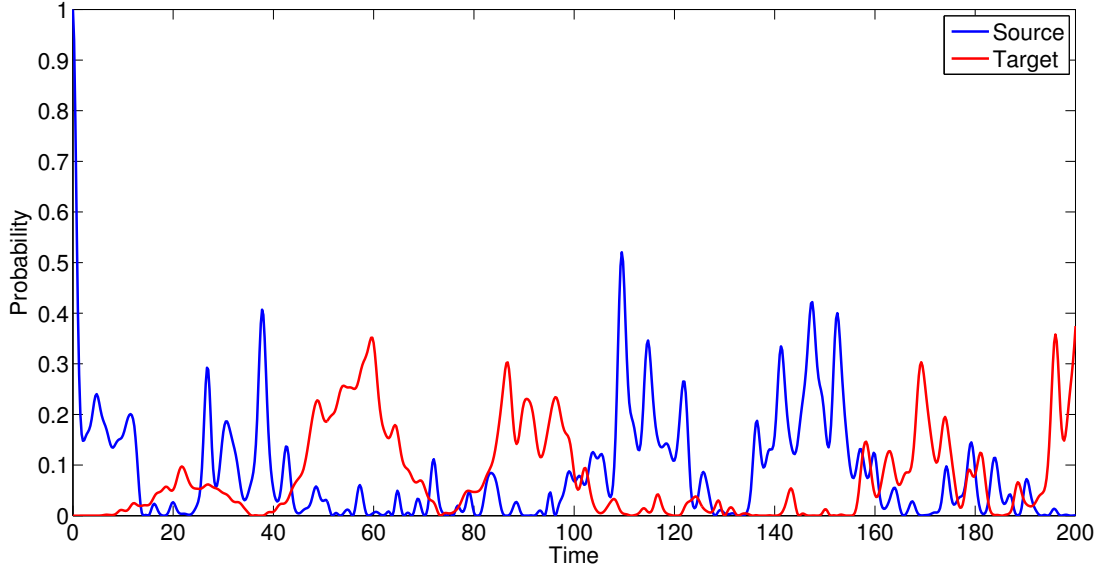
Figure 4.12: Numerically calculated signal transfer on a 12×12 cell graphene lattice between additional vertices coupled to non-equivalent vertices, time-evolved under the communication Hamiltonian in Equation (4.12).
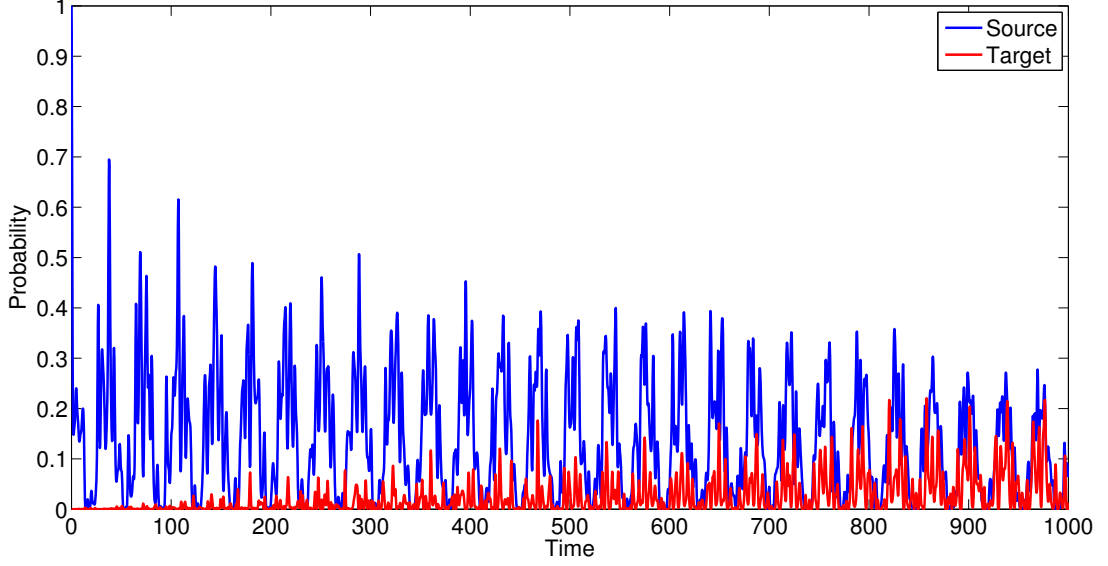
Figure 4.13: Numerically calculated signal transfer on a 12×12 cell graphene lattice between additional vertices coupled to vertices on different sublattices, time-evolved under the communication Hamiltonian in Equation (4.12).
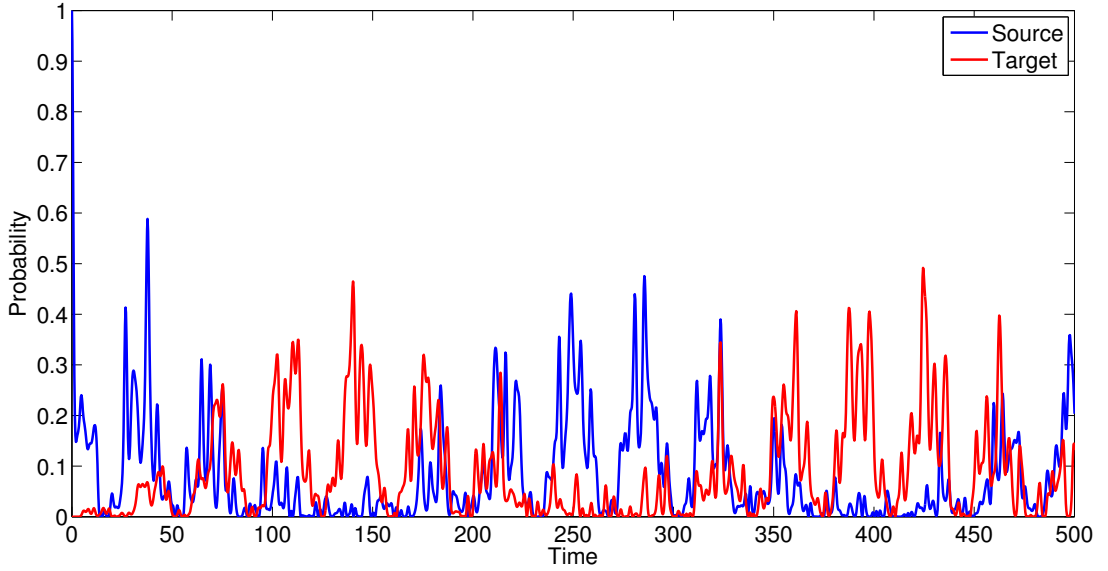
Figure 4.14: Numerically calculated signal transfer on a 12×12 cell graphene lattice between additional vertices coupled to vertices on different sublattices, time-evolved under the communication Hamiltonian in Equation (4.12). This system uses a different target site to Figure 4.13.

4.2.3 Additional configurations

The perturbation we have used in the previous two subsections was only linked to a single vertex on the lattice. However, in this subsection we inspect alternative arrangements for coupling additional sites to our lattice. We borrow some ideas for the setups we use from perturbations to physical graphene lattices involving additional atoms [85] and construct generally similar lattice configurations.

4.2.3.1 Bridge setup

The first alternative system we construct is the bridge setup where an additional vertex is placed in between the two vertices and above the connecting bond which make-up a single cell, the setup is shown in Figure 4.15. The Hamiltonian for a search using such a perturbation is

$$H = H_o + W\left(\gamma\right) \tag{4.13}$$
$$= -A - \left(|\alpha_0, \beta_0\rangle^A + |\alpha_0, \beta_0\rangle^B\right)\langle site| - |site\rangle\left(\langle\alpha_0, \beta_0|^A + \langle\alpha_0, \beta_0|^B\right)$$
$$+ \gamma\,|site\rangle\langle site|\,. \tag{4.14}$$

We use the same unperturbed search Hamiltonian as previously, that is, $H_o = -A$, and our focus is on fine-tuning the on-site energy of $|site\rangle$ using the parameter γ.

Figure 4.16 shows the spectrum of the search Hamiltonian as a function of γ for a 12×12 cell torus. Unlike the previous case of the single additional site coupling to only one vertex on the lattice, the avoided crossing in the spectrum does not occur when $\gamma = 0$ but rather takes a different critical value, in this particular case $\gamma = 0.676$. This critical value of γ scales as N grows larger and we find from our numerical results that this critical parameter tends asymptotically towards $\gamma_c = \frac{2}{3}$. This non-zero value of γ means that the additional vertex has a different on-site energy to all the lattice vertices.

We again first look at the dissipation and revival probability of states initially localised on a single vertex as an indicator of the transport dynamics and how they differ with the introduction an extra site. Figure 4.17 shows the time-evolution of the bridge setup, evolved under the Hamiltonian in Equation (4.14) with $\gamma = 0.676$, for three different initial states: one localised on the additional vertex, one on a randomly chosen A-type vertex and another on a randomly chosen B-type vertex. It can be seen from the figure that the behaviour at the two randomly chosen A- & B-type vertices is
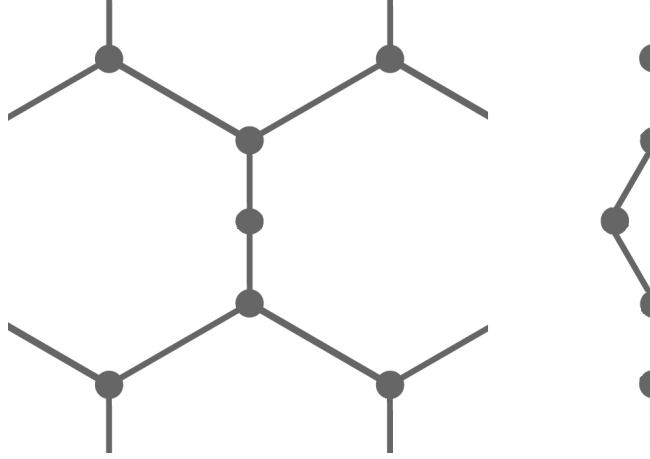
Figure 4.15: Example of additional vertex bridge setup. The left picture shows the lattice from above with the additional site being the middle vertex in the central bond. The figure on the right is the perturbation seen along the plane of the lattice.
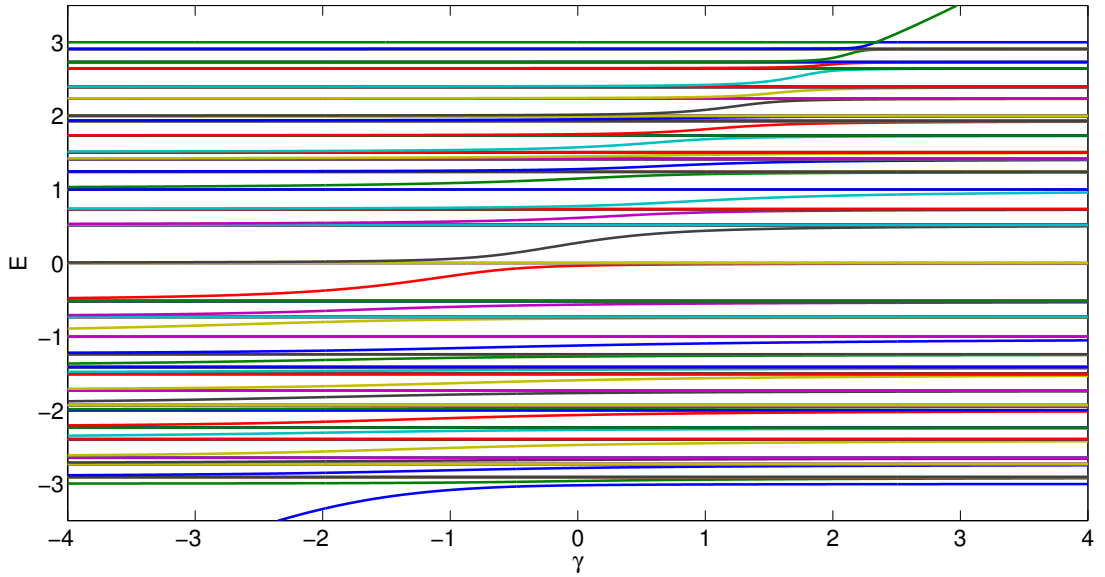
Figure 4.16: Numerically calculated spectrum of search Hamiltonian from Equation (4.14) as a function of γ for a 12×12 cell torus.
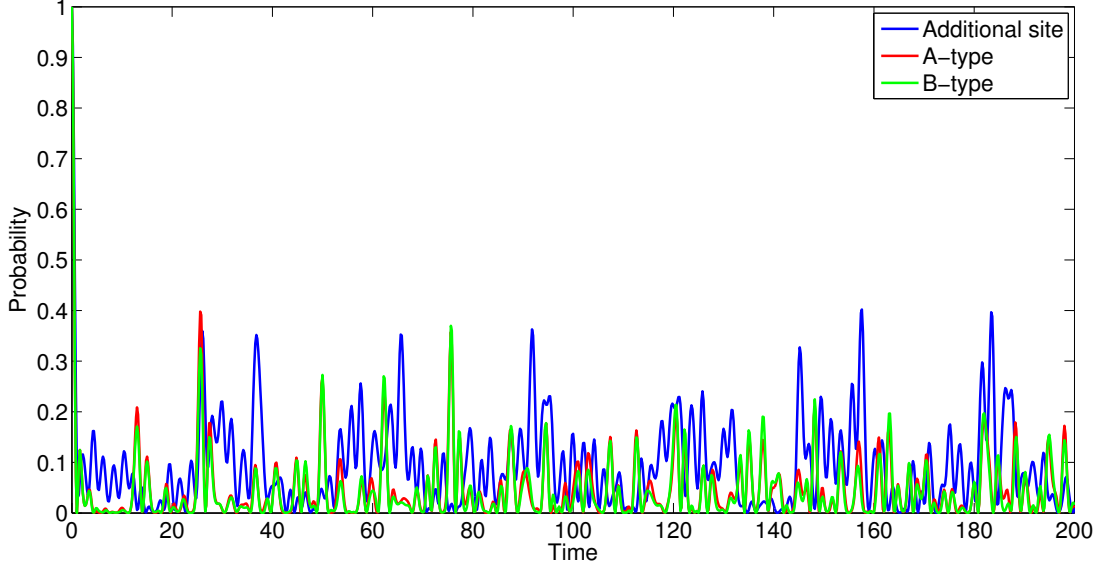
Figure 4.17: Time-evolution of different initial localised states, evolved under the Hamiltonian in Equation (4.14) on a 12×12 cell torus. The different initial states are localised on the additional vertex, a random site on the A- and the B-sublattice.
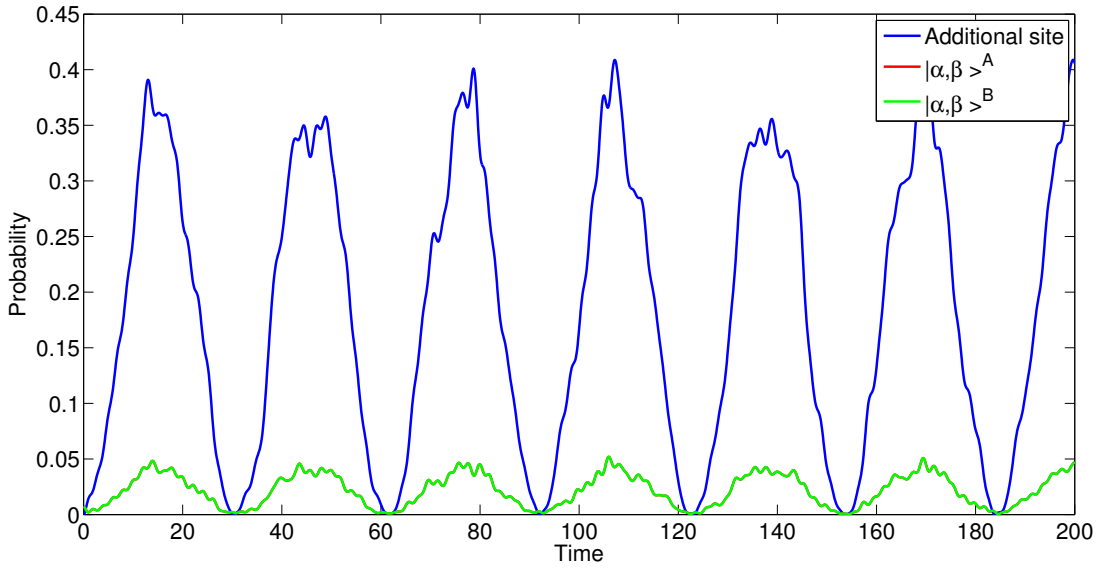
Figure 4.18: Numerically evolved search on a a 12×12 cell graphene torus using optimal search starting state, and evolved under the Hamiltonian from Equation (4.14). The behaviour at the two nearest-neighbours is the same so only one of the curves can be seen.

99
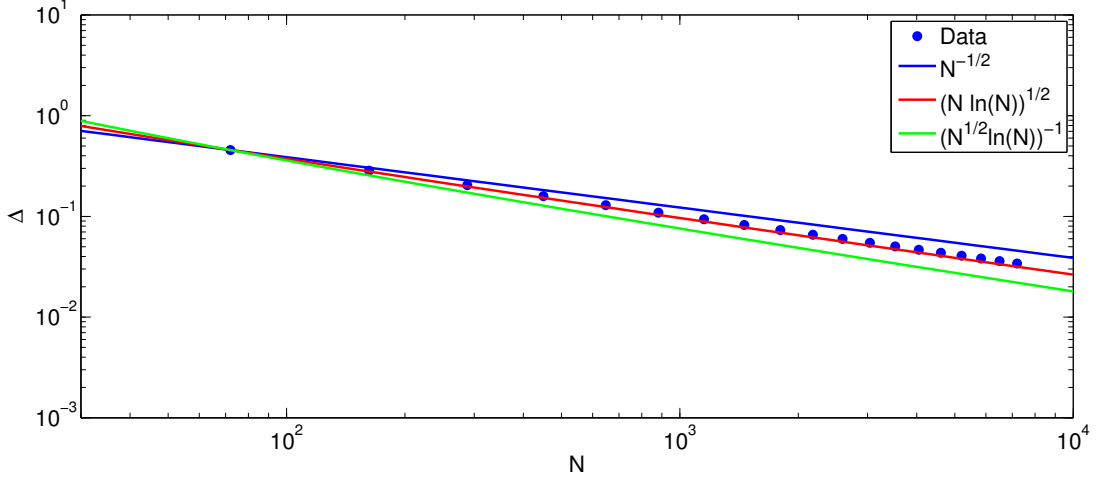
Figure 4.19: Numerically calculated avoided crossing gap (dots) between states nearest to $E = 0$ for the search Hamiltonian in Equation (4.14). Also shown are the curves $c_1/\sqrt{N}$, $c_2/\sqrt{N \ln N}$ & $c_3/\left(\sqrt{N} \ln N\right)$ for comparison, as a function of number vertices N.

almost identical and may be taken as typical behaviour of a state initially localised on a vertex on the underlying lattice. There are occasional significant peaks in probability but these are very narrow peaks and overall the revival probability is around 10% or lower. However, the revival probability peaks at the additional vertex tend to be around 20% or greater, with broader, more sustained peaks in localisation at the additional site, indications that we can create a search protocol using this type of perturbation.

By following the procedure described on page 85 and numerically reducing the search Hamiltonian in Equation (4.14) using a basis consisting of the Dirac states and also the eigenstates of the perturbation matrix, we can construct an optimal initial starting state. Doing this we find three identical starting states, constructed using equal weighted contributions from Dirac states on both sublattices. This is to be expected as the perturbation interacts with both sublattices in the same manner and, therefore, should be viewed as a perturbation of a single cell rather than of a particular vertex, in the same way as the single-bond perturbation in the previous section.

Allowing the bridge system to evolve after being placed in its optimal search starting state, we find the search behaviour shown in Figure 4.18. We find strong localisation on the additional site of around $35 - 40\%$ with a period similar to that of the peaks in the revival probability in Figure 4.17. There is also some localisation on the nearest-neighbours of the additional vertex of around 5% each; the time-evolution at each

nearest-neighbour is the same. This means that for a search of a cell, at least for a 12×12 cell lattice, there is almost 50% probability of localising on the cell or its nearest-neighbour, that is, the additional vertex.

4.2.3.2 Additional site coupled to nearest-neighbours

Here we inspect another alternative arrangement, shown in Figure 4.20, where there is an additional vertex directly above a lattice site which couples not only to the site it is directly above but to that sites nearest-neighbours also.

The search Hamiltonian for such a system is

$$H = H_o + W \tag{4.15}$$

$$= -A - \left(|\alpha_0, \beta_0\rangle^A + |\alpha_0, \beta_0\rangle^B + |\alpha_0, \beta_0 - 1\rangle^B + |\alpha_0 + 1, \beta_0 - 1\rangle^B \right) \langle site| \tag{4.16}$$

$$- |site\rangle \left(\langle \alpha_0, \beta_0|^A + \langle \alpha_0, \beta_0|^B + \langle \alpha_0, \beta_0 - 1|^B + \langle \alpha_0 + 1, \beta_0 - 1|^B \right) + \gamma |site\rangle \langle site| \,,$$

where A is the adjacency matrix of the underlying lattice, $|site\rangle$ is the basis state associated with the additional vertex, and γ is a free-parameter describing the on-site energy of the additional vertex. Thus, we assume that the binding of the additional site to the rest of the lattice is the same as the interaction strength between all lattice vertices.

We follow the procedure of inspecting the spectrum of this search Hamiltonian as a function of γ around the Dirac states for an avoided crossing which can be used for a search protocol. In Figure 4.21 we find our avoided crossing located around the Dirac states for $\gamma = -1.997$. In fact, we see that the perturber state entering the spectrum from the region of lower energy interacts very strongly with the spectrum, forcing an avoided crossing in the centre of the spectrum even when the perturber state is still rather isolated from the main body of the spectrum. Similar to the bridge setup, we find that the critical value of γ at which the avoided crossing occurs scales with N and tends towards $\gamma_c = -2$ as N grows larger.

Such a strong interacting perturber state implies that the states forming the avoided crossing will have a large component from the perturber state. This in turn implies that a system initialised on the additional vertex and allowed to evolve in time will remain very strongly localised. In fact, this is what we see in the revival probability shown in Figure 4.22. We find a distinctive beating pattern where there is a longer period oscillation between localised & delocalised states of around $T \approx 45$, and then a
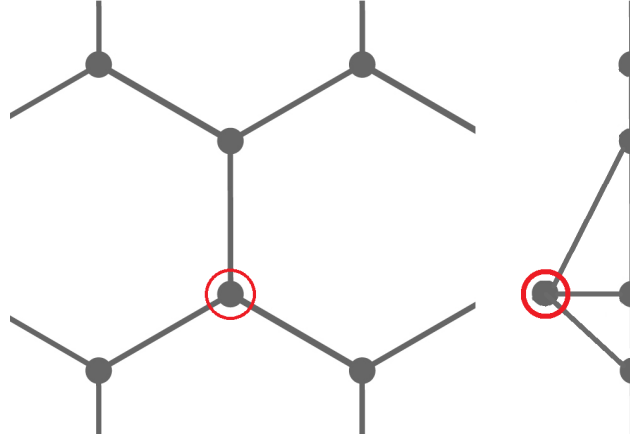
Figure 4.20: Example of the additional site perturbation setup described by the Hamiltonian in Equation (4.16), where the red circle shows the position of the perturbation. The left picture shows the lattice from above with the additional site placed directly above a lattice site while also coupled to that lattice sites nearest-neighbours. The figure on the right is the perturbation seen along the plane of the lattice.
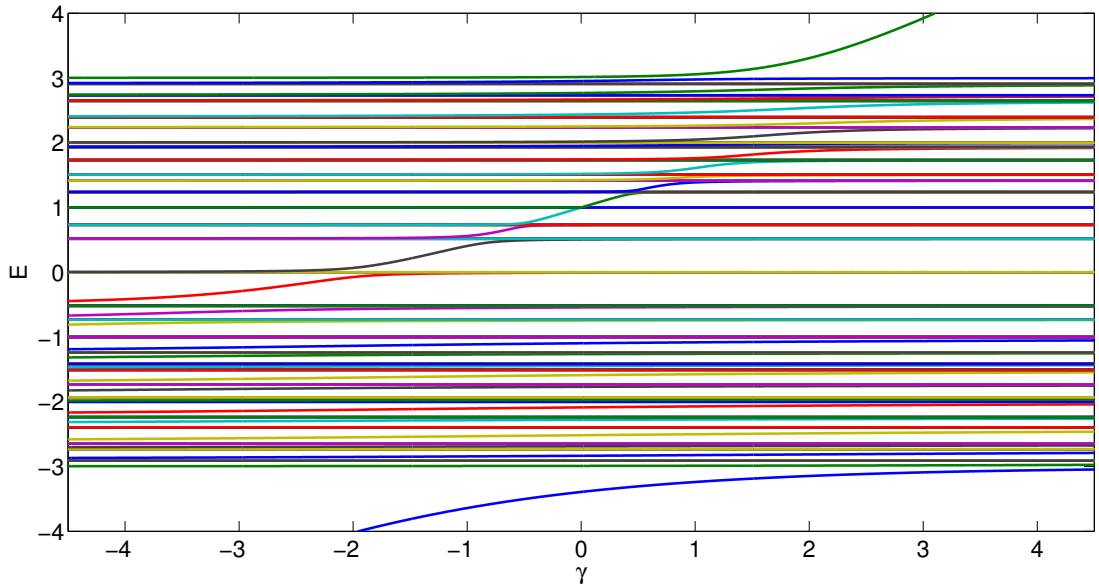

Figure 4.21: Numerically calculated spectrum of search Hamiltonian from Equation (4.16) as a function of γ for a 12×12 cell torus.
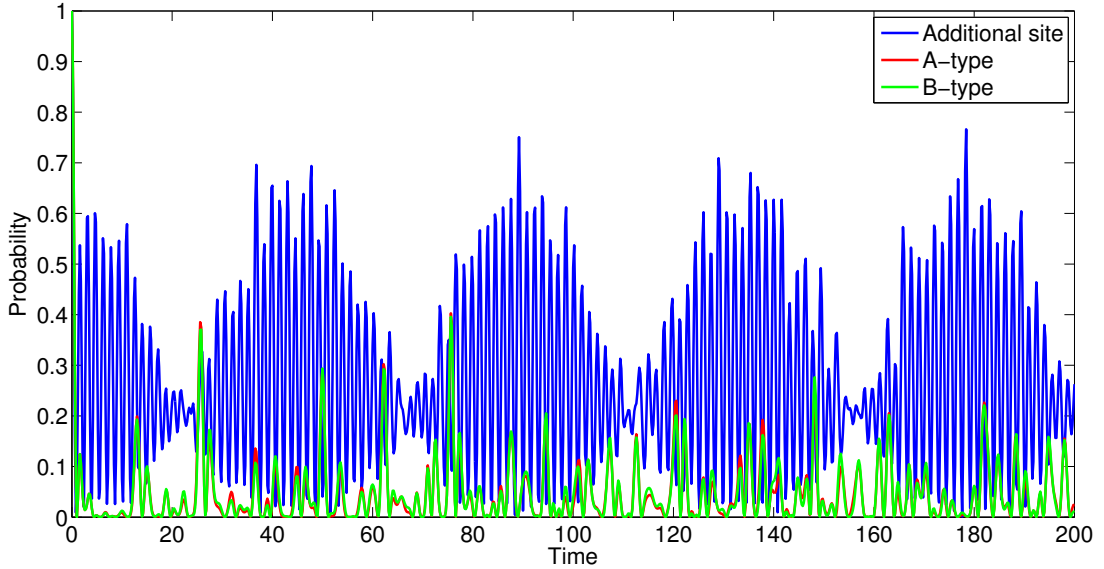
Figure 4.22: Time-evolution of different initial localised states, evolved under the Hamiltonian in Equation (4.16) on a 12×12 cell torus. The different initial states are localised on the additional vertex, a random site on the A- and the B-sublattice.

much shorter period oscillation. Further investigation reveals that the shorter period oscillation comes from a fluctuation between the additional vertex and the other basis states forming the perturber state. This beating pattern can, therefore, be simplified further as the longer period oscillation between the localised perturber state & a delocalised lattice state, and the shorter oscillation between the internal components of the perturber state. The peak of each revival of probability at the additional site is $65 - 80\%$. Both of these properties, the regular nature of the signal pattern and the high recurrence probability, indicate that a successful search can be created.

Again we numerically solve for the optimal starting state, reducing the full search Hamiltonian in Equation (4.16) using a basis formed of the Dirac states and the eigenstates of the perturbation matrix. The time-evolution of the system when initialised in the optimal search starting state is plotted in Figure 4.23. We find strong localisation on the additional site and also on the vertex it is placed directly above. This is not surprising as they are highly interconnected since they share nearest-neighbours and are coupled to each other. Overall, for the 12×12 cell torus we look at we find the combined success probability at a peak for both the additional site and the vertex it is placed above is approximately 70%, with a 10% probability of being found on the nearest-neighbours as well. We also find the time taken for the success probabil-

103
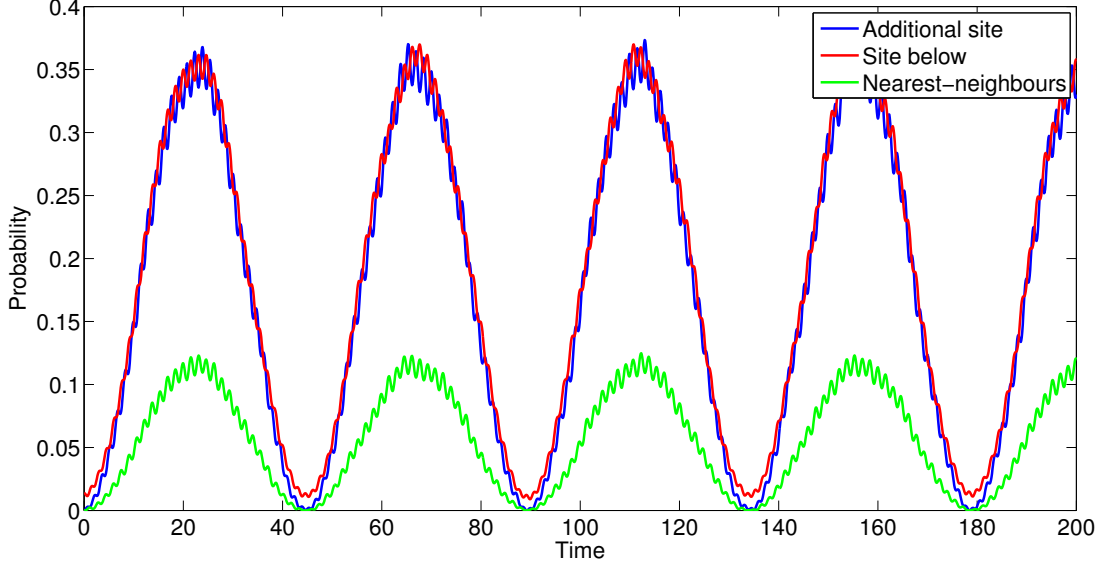
Figure 4.23: Numerically evolved search on a 12×12 cell graphene torus using optimal search starting state, and evolved under the Hamiltonian from Equation (4.16). The nearest-neighbours curve (green) is the sum of the probabilities to be found on the nearest-neighbours.
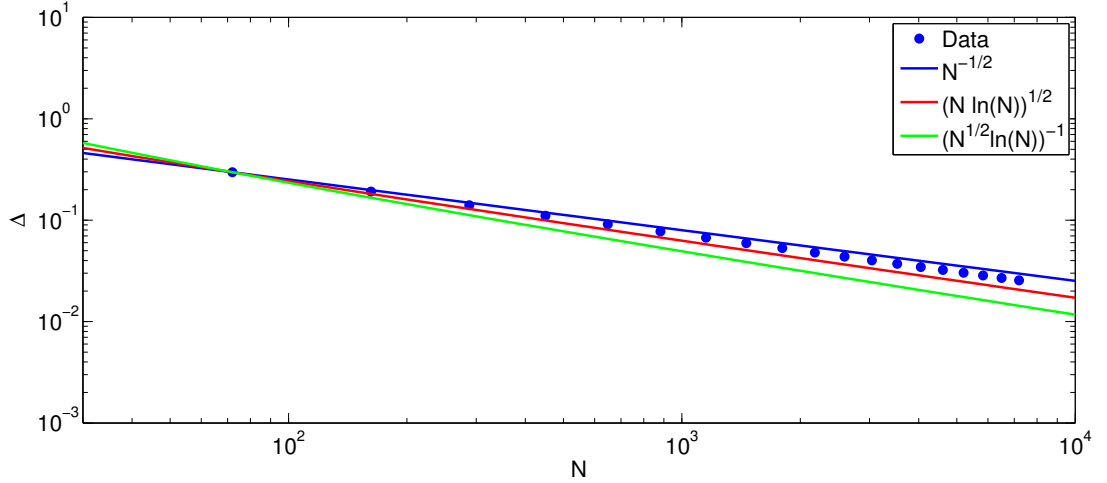
Figure 4.24: Numerically calculated avoided crossing gap (dots) between states nearest to $E = 0$ for the search Hamiltonian in Equation (4.16). Also shown are the curves $c_1/\sqrt{N}$, $c_2/\sqrt{N \ln N}$ & $c_3/\left(\sqrt{N} \ln N\right)$ for comparison, as a function of number vertices N.

ity to peak in Figure 4.23 closely matches the period in the recurrence probability in Figure 4.22.

The scaling of the avoided crossing gap is displayed in Figure 4.24. The figure implies that the time taken for the first search localisation is comparable to the previous searches in this chapter and also in Chapter 3. However, the straight line fit does not exactly capture the asymptotic behaviour but it can be seen that there is some logarithmic correction to the $\mathcal{O}\left(\sqrt{N}\right)$ behaviour.

4.3   Armchair nanotube

In order to understand the effect of relaxing the period boundary conditions we now change the lattices we search from graphene tori to carbon nanotubes [79, 86]. There are three types of carbon nanotubes, classified by how the graphene sheet is closed into a tube, which are: armchair, zigzag, and chiral. The electronic band nature of these is well understood for the idealised case of nanotubes of infinite length, see for example [79]. It has been shown that, unlike the other two types of nanotube, the band structure of armchair nanotubes always allows for an energy at the Dirac energy regardless of the nanotube diameter, and so it is on these types of nanotubes that we focus.

However, in the finite case, which we are interested in as we only wish to search across a finite number of sites, this band structure of the nanotube becomes discrete and the length of the nanotube must be carefully chosen so that an eigenstate of the system remains at the Dirac energy. An example of a finite armchair nanotube is shown in Figure 4.25. We choose the finite length of the nanotube to be along the horizontal axis and we close the underlying graphene lattice into a nanotube along the vertical axis, that is, the nanotube is periodic along the vertical axis.

In Appendix C we give a more detailed treatment of the nature of the eigenstates and the spectra of finite armchair nanotubes, and so we will only give a shortened discussion of the relevant properties here. We denote the basis states by $|m, A/B, l\rangle$, where m indicates the mth A/B-type vertex in the horizontal direction in the lth cell. The nanotube is composed from N_y cells along the vertical axis with the translation vector $\underline{R}_y = -\underline{a}_1 + \underline{a}_2 = \sqrt{3}\underline{j}$ between successive cells, where $\underline{a}_1, \underline{a}_2$ are the graphene lattice basis vectors and $\underline{j}$ is the unit basis vector in the y-direction. Along the vertical axis, the component of the eigenstates in this direction are Bloch states leading to the
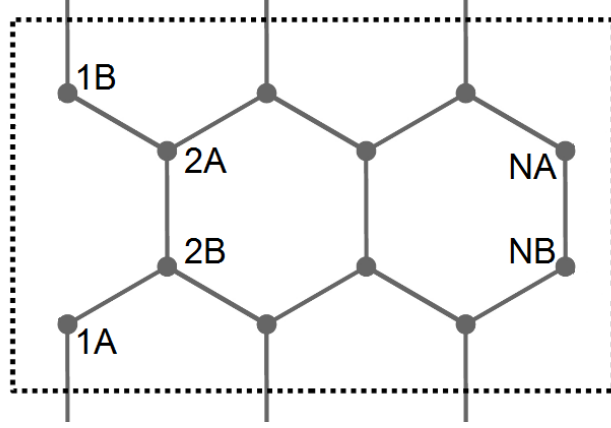
Figure 4.25: Example of nanotube cell. The nanotube is periodic along the vertical axis. In the horizontal direction the cell is finite with a width of N_x sites.

condition on the y-component of the momenta

$$k_y = \frac{2\pi q}{\sqrt{3}N_y}, \qquad q \in \{0, 1, \dots N_y - 1\}. \tag{4.17}$$

As the nanotube has a finite length with Dirichlet boundary conditions at the edges, one finds that the horizontal component of the amplitudes of eigenstates have the general form $\psi_{m,l} = A_l \sin(k_x m)$, where we have incorporated any phases and normalisation factors into A_l and m denotes the vertex coordinate along the horizontal component. That is, the eigenstates of the finite nanotube are standing waves along the length of the nanotube, a result first described in [87]. The allowed wavelengths of these standing waves leads to the allowed values of the x-component of the momenta

$$k_x = \frac{\pi p}{N_x + 1}, \qquad p \in \{1, 2, \dots N_x\}. \tag{4.18}$$

Using the Bloch nature of the eigenstates in the y-direction and the standing wave description in the x-direction we arrive at the energy relation

$$E = \epsilon_D \pm t \sqrt{1 + 4\cos^2(k_x) + 4\cos(k_x)\cos\left(\frac{\sqrt{3}k_y}{2}\right)}. \tag{4.19}$$

Due to the discretisation of the momenta, $(k_x, k_y) = \left(\frac{2\pi}{3}, 0\right)$ is the only potential point where this energy relation becomes equal to the Dirac energy ϵ_D. By matching Equation (4.18) to the Dirac point we find that there are only Dirac energies when

$N_x = 3r - 1$, where r is an integer.

As there is only one potential Dirac point for finite armchair nanotubes, it follows that there are only two Dirac states (one from the bonding and the anti-bonding regions of the spectrum). As we have $k_y = 0$ at the Dirac point, the Bloch wave around the circumference of the nanotube is simply a uniform superposition. Another important feature of the Dirac states on the nanotube is the existence of nodal points where the amplitude of the eigenstate is 0. These nodal points occur at every third site along the horizontal axis.

We proceed by considering the triple-bond perturbation used in Chapter 3 and the additional site perturbation from Section 4.2, both at the edges of the nanotube and in the bulk. Also of interest here is how the sinusoidal nature of the eigenstates along the length of the nanotube, induced by its finite length, modifies the nature of the search. In particular we are interested in how the nodal points in the Dirac states, which do not arise in the Bloch states on the graphene torus, affect any searches. Although other eigenstates will have zero amplitude at certain vertices, it is understood that when we refer to nodal points we are only considering the zeros of the Dirac states.

4.3.1 Triple-bond perturbation

In our new coordinate system our triple-bond perturbation matrix, first found in Chapter 3, becomes

$$W = |m, A, l\rangle \left(\langle m + 1, B, l| + \langle m - 1, B, l| + \langle m, B, l| \right) + h.c. . \tag{4.20}$$

with eigenstates $|W_\pm\rangle = \frac{1}{\sqrt{6}} \left(\langle m + 1, B, l| + \langle m - 1, B, l| \pm \sqrt{3} |m, A, l\rangle + \langle m, B, l| \right)$ and eigenvalues $\lambda_\pm = \pm\sqrt{3}$. We have assumed here that we are perturbing an A-type vertex on an even x-coordinate, so that the perturbed site and its nearest-neighbours remain within one nanotube cell. While it is easy to re-write this perturbation matrix for other sites we restrict ourselves to this form for simplicity.

The Hamiltonian for our search is then

$$H = -\gamma A + W \,, \tag{4.21}$$

where A is the adjacency matrix of the nanotube and γ is a free parameter (we do not give the full expression for the adjacency matrix as it is rather cumbersome, however, it can be found in Appendix C).

In pursuit of an avoided crossing which can be used to create a search, we inspect the spectrum of the Hamiltonian as the parameter γ is changed. We look at several spectra as we move the location of the perturbed site from being close to the edge across the length of the nanotube taking into account sites in the bulk and also those sites which are nodal points with respect to the Dirac states. Throughout this section, the dimensions of the nanotube we choose are $(N_x, N_y) = (32, 5)$. Our choice of dimensions ensures that there exist states at the Dirac energy and that the total number of sites $(N = 320)$ is similar to the number of sites in searches in previous sections, for ease of comparison.

We find that the spectra for perturbations near the edge and in the bulk have very minor differences in the exact values of the calculated eigenenergies but the general features remain the same, and so we only show one plot of the spectrum in Figure 4.26. We restrict our view of the spectrum to the region of interest as there are far fewer degenerate eigenenergies than in the graphene torus spectrum, making the rest of the spectrum very dense. There is a very distinct avoided crossing around the Dirac energy at $\gamma = 1$, corresponding to complete isolation of the perturbed vertex from the rest of the lattice. This is exactly the same as we observed for the triple-bond perturbation on the torus.

The spectrum of the search Hamiltonian at a nodal point in Figure 4.27, however, is markedly different, displaying an exact crossing at the Dirac energy. Therefore, at these nodal points on the nanotubes, which are every third vertex, there is no mechanism in the spectrum which we can use to form a search protocol. It is perhaps not surprising that we do not find an avoided crossing in this situation as the effective removal of the perturbed vertex will not perturb the Dirac state in any way, given that the Dirac state has zero amplitude at this vertex already.

Using the same procedure as previously used in this chapter, we reduce the search Hamiltonian numerically in a basis consisting of the two Dirac states and two superpositions of the eigenvectors of the perturbation matrix. The two superpositions we use are $|\ell\rangle = \frac{1}{\sqrt{2}}(|W_+\rangle + |W_-\rangle)$ and $|m, A, l\rangle = \frac{1}{\sqrt{2}}(|W_+\rangle - |W_-\rangle)$, the former superposition living only on the neighbours of the perturbed vertex and the latter resulting in the basis state corresponding to the perturbed vertex. We find in the eigensystem of the reduced Hamiltonian that there are two eigenstates which live exclusively on $|\ell\rangle$ or the Dirac states, and there are two eigenstates which have contributions from both $|\ell\rangle$ and the Dirac states. It is from the second two eigenstates which we form the search starting state, which is a weighted superposition of the Dirac states. This weighted
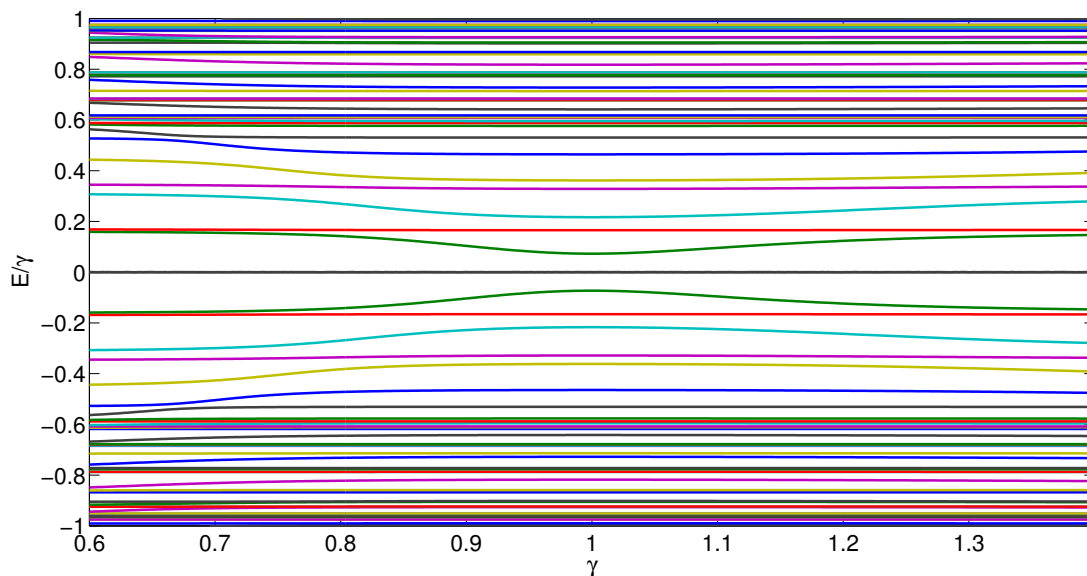
Figure 4.26: Numerically calculated spectrum of search Hamiltonian from Equation (4.21) as a function of γ for a finite armchair nanotube with dimensions $(N_x, N_y) = (32, 5)$. Spectra for perturbations at the edges and in the bulk are almost identical, shown here is the spectrum for a perturbation in the bulk.
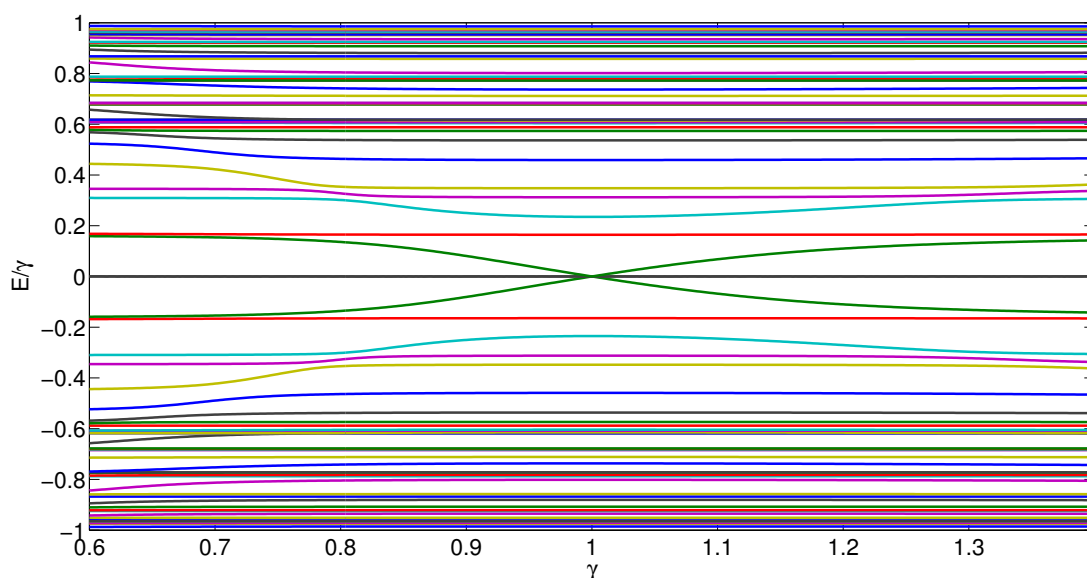

Figure 4.27: Numerically calculated spectrum of search Hamiltonian from Equation (4.21) as a function of γ for a finite armchair nanotube with dimensions $(N_x, N_y) = (32, 5)$, where the perturbation has been placed on a nodal point of the Dirac states.

superposition of the Dirac states we obtain is actually a uniform superposition over one sublattice, the same sublattice as the perturbed vertex, excluding the nodal points which remain with zero amplitude.

Figures 4.28 & 4.29 show two searches time-evolved using the initial search starting state we obtained from our reduced Hamiltonian procedure: the first figure is for a perturbation placed close to the edge and the other when the perturbation is positioned in the bulk. Comparing these figures to the three-bond perturbation search on the torus in Chapter 3 (see for example either Figure 3.4 or Figure 3.11), we see that there is a marked difference in behaviour and success probability induced by the relaxing of the periodic boundary conditions along one axis.

For the search using a perturbation located near the edge, shown in Figure 4.28, we see a reduction in success probability to localise on the nearest-neighbours of the perturbed vertex of around a factor of 2-3 when compared to the search on the torus. Another effect of the boundary so close to the perturbation is to cause the behaviour at each of the neighbouring vertices to be significantly different. However, searches in the bulk, shown for one bulk site in Figure 4.29, display behaviour closer to searches on a graphene torus in that the behaviour at each of the nearest-neighbours is roughly the same. The success probability is also closer to a search on a torus for a similar number of sites but is still lower. One property which the edge & bulk perturbation searches share is that the maximum probability at each peak in success probability fluctuates significantly. We propose that this effect is due to the reflection of probability amplitude from the edges of the nanotube. This is supported by the changes in the interference pattern in the signal as the perturbation is moved across the lattice.

Our next consideration is the scaling of the energy gap of the avoided crossing with system size, as this determines the scaling of the time taken for the first localisation of the search protocol. We check two different cases of scaling behaviour: keeping the diameter of the nanotube constant while increasing its length (which is closer to physical nanotubes which tend to have a much longer length than diameter), and the alternative case of increasing both the diameter and length together. Figure 4.30 shows the scaling of the energy gap of avoided crossing as the length of the nanotube is increased for both edge and bulk perturbations. Unfortunately, we find that the scaling of the energy gap in this case the scaling is close to $\Delta = \mathcal{O}\left(N^{-1}\right)$ which implies that the quantum search on a nanotube scales no better than the classical search. However, this is because a carbon nanotube is essentially a 1-dimensional object (as seen by the 1-dimensional quantum confinement of finite nanotubes [87]) and, therefore, we would expect the
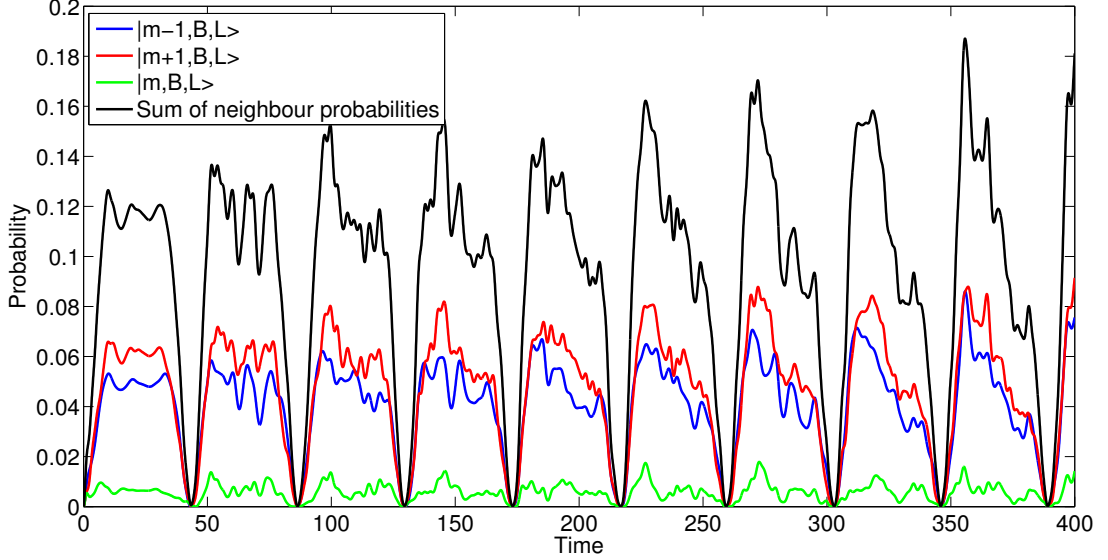
Figure 4.28: Numerically evolved search on a finite armchair nanotube with dimensions $(N_x, N_y) = (32, 5)$ and evolved under the Hamiltonian from Equation (4.21). The perturbation is placed near the edge of the nanotube and the search begins in the optimal search starting state.
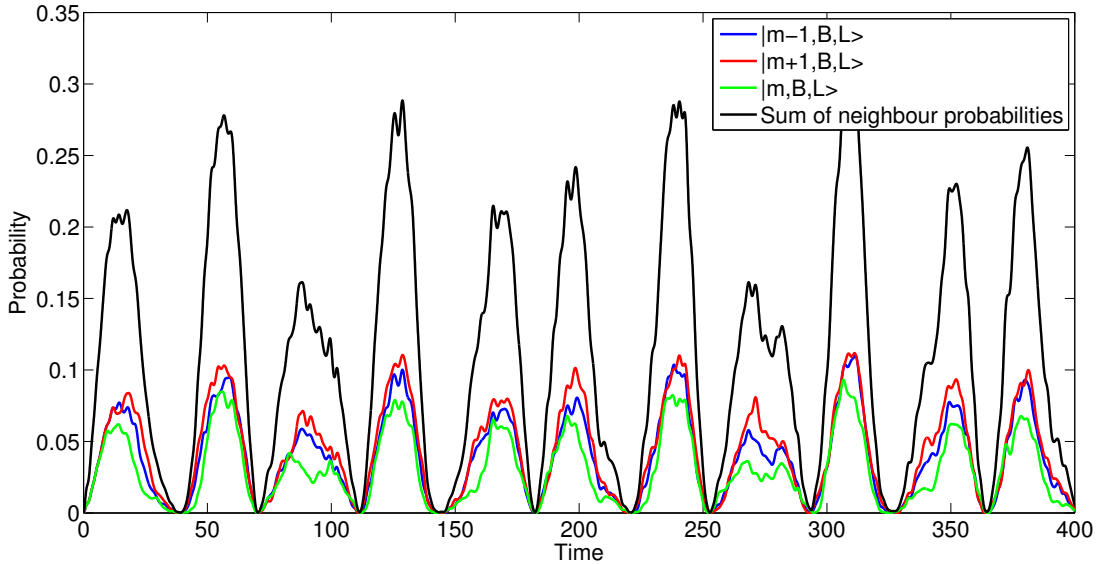

Figure 4.29: Numerically evolved search on a finite armchair nanotube with dimensions $(N_x, N_y) = (32, 5)$ and evolved under the Hamiltonian from Equation (4.21). The perturbation is placed in the bulk of the nanotube and the search begins in the optimal search starting state.

eigenenergy spacing to scale as $E_{n+1} - E_n = \mathcal{O}\left(N_y^{-1}\right)$. This is, indeed, what has been described in other theoretical analyses [86]. However, if we assume that the dimensions of the nanotube are increased in diameter and length, it can no longer be treated as a 1-dimensional object and must be treated as a 2-dimensional structure. In this case, we return to the scaling that we found for previous searches on the tori, as displayed for the nanotube in Figure 4.31.
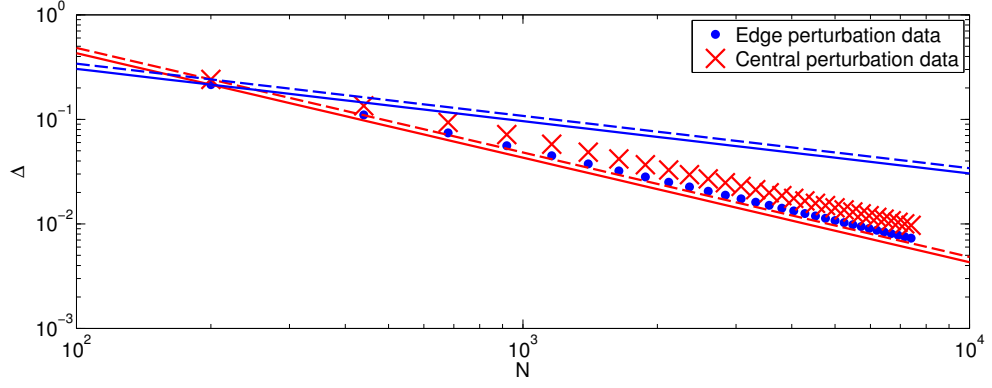
Figure 4.30: Numerically calculated avoided crossing gap between states nearest to $E = 0$ for the search Hamiltonian in Equation (4.21) as the length of the nanotube is increased. Also shown are the curves $c_1/\sqrt{N}$ (blue curves) and c_2/N (red curves) for comparison, as a function of the number of vertices N. Dashed curves correspond to fits to the central perturbation, solid curves correspond to fits to the edge perturbation.
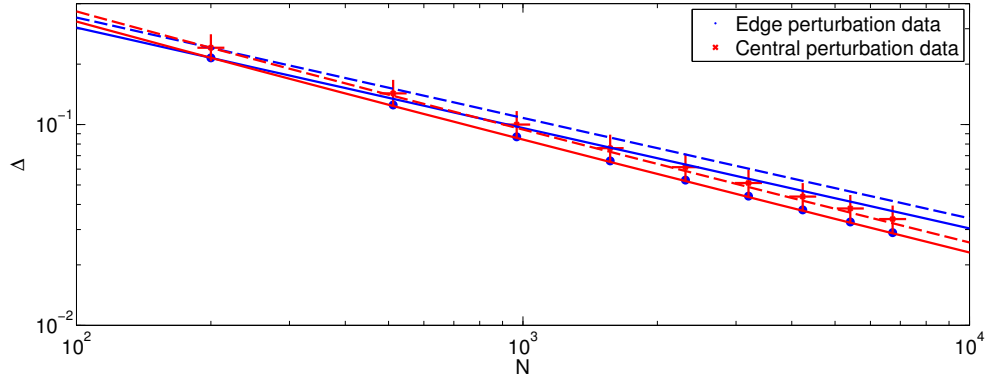
Figure 4.31: Numerically calculated avoided crossing gap between states nearest to $E = 0$ for the search Hamiltonian in Equation (4.21) as the diameter and length of the nanotube are increased. Also shown are the curves $c_1/\sqrt{N}$ (blue curves) and $c_2/\sqrt{N \ln(N)}$ (red curves) for comparison, as a function of the number of vertices N. Dashed curves correspond to fits to the central perturbation, solid curves correspond to fits to the edge perturbation.

4.3.2 Additional site perturbation

As well as checking the effect of boundaries on the triple-bond perturbation, we investigate the effect of a boundary on perturbations constructed from additional sites. In this subsection we use only additional sites coupled to a single vertex, as we first looked at for the graphene torus in Section 4.2. The perturbation matrix we use is

$$W\left(\gamma\right) = -\left|site\right\rangle\left\langle m, A, l\right| - \left|m, A, l\right\rangle\left\langle site\right| + \gamma\left|site\right\rangle\left\langle site\right|, \tag{4.22}$$

where γ is a free parameter determining the on-site energy of the additional site $\left|site\right\rangle$, leading to the search Hamiltonian

$$H = -A + W\left(\gamma\right) \tag{4.23}$$

$$= -A - \left|site\right\rangle\left\langle m, A, l\right| - \left|m, A, l\right\rangle\left\langle site\right| + \gamma\left|site\right\rangle\left\langle site\right|. \tag{4.24}$$

Figure 4.32 shows the spectrum of the search Hamiltonian as we vary γ searching for an avoided crossing which we can employ for our search. We show only one figure for both perturbations at the edge and the bulk as we find no difference in the general features of the spectrum. We again find, in the same way as additional sites coupled to the graphene torus in Section 4.2, an avoided crossing occurs around the Dirac energy at $\gamma = 0$, that is, when the on-site energy of the additional site matches that of all other vertices in the nanotube. Similar to the triple-bond perturbation at a nodal point in the Dirac states, we find that the spectrum for additional sites coupled to a nodal vertex, shown in Figure 4.33, does not contain an avoided crossing we can use.

We first calculate the revival probability (i.e. the probability for an initially localised state to return) for states localised on the additional sites and compare them to the revival probability for randomly chosen vertices on both the A and B sublattices. We find a slight difference in the revival behaviour at the edge (Figure 4.35) when compared to a bulk perturbation (Figure 4.34). It can be seen that interference effects at the nanotube edge disrupts the periodicity and the well-defined peaks for the 2nd & 3rd revivals in the behaviour of the edge perturbation. There is also a minor difference in the period between revivals between the two perturbation locations, which we would expect to result in different search times.

We find that the revival probability for a perturbation localised on a nodal point, shown in Figure 4.36 has a shorter period and a marginally higher success probability. Inspecting the perturbed and unperturbed eigenstates, we find that the additional site
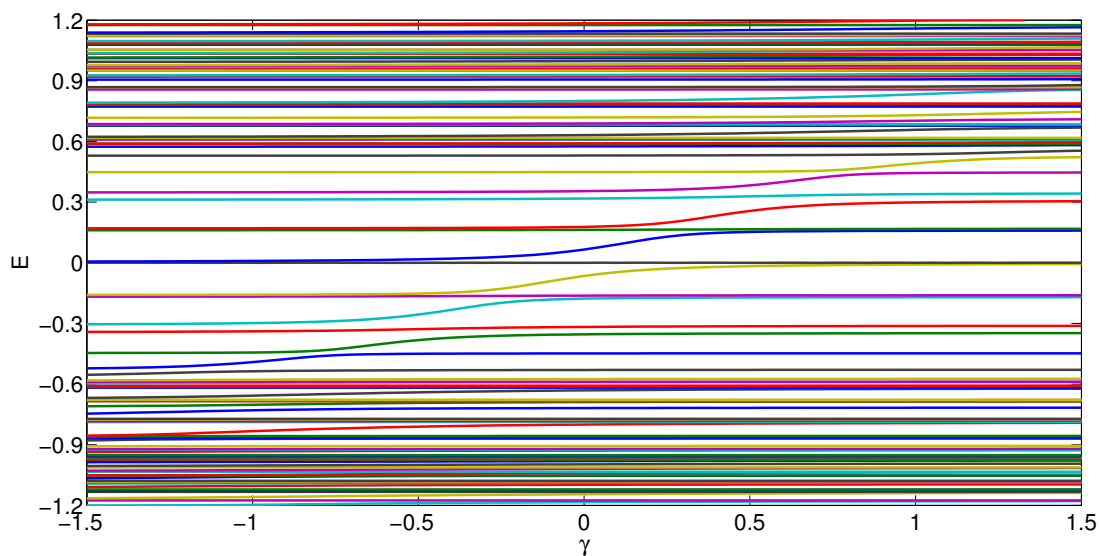
Figure 4.32: Numerically calculated spectrum of search Hamiltonian from Equation (4.24) as a function of γ for a finite armchair nanotube with dimensions $(N_x, N_y) = (32, 5)$. Spectra for perturbations at the edges and in the bulk are almost identical, shown here is the spectrum for a perturbation in the bulk.
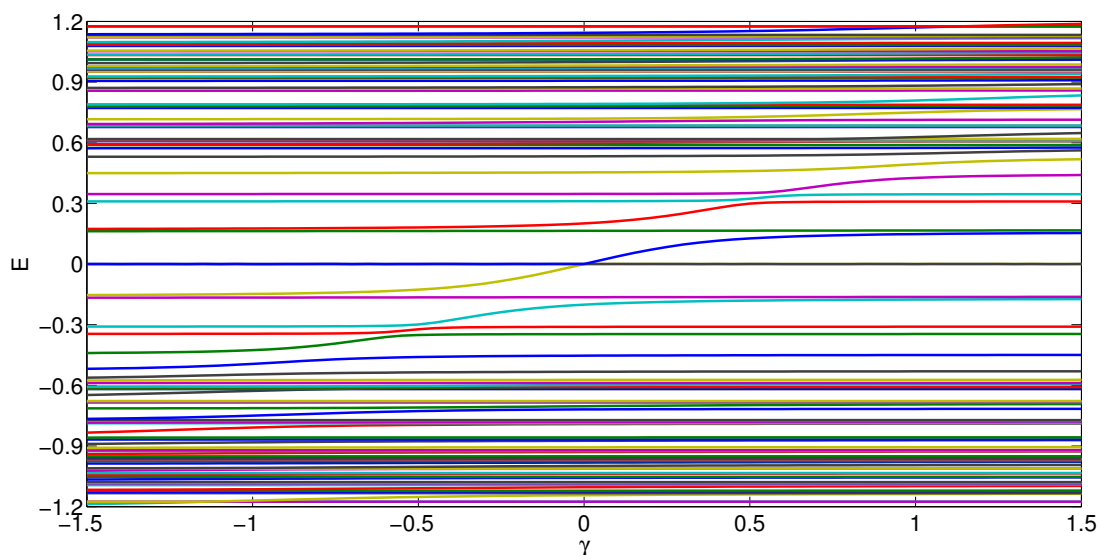

Figure 4.33: Numerically calculated spectrum of search Hamiltonian from Equation (4.24) as a function of γ for a finite armchair nanotube with dimensions $(N_x, N_y) = (32, 5)$, where the perturbation has been placed on a nodal point of the Dirac states.
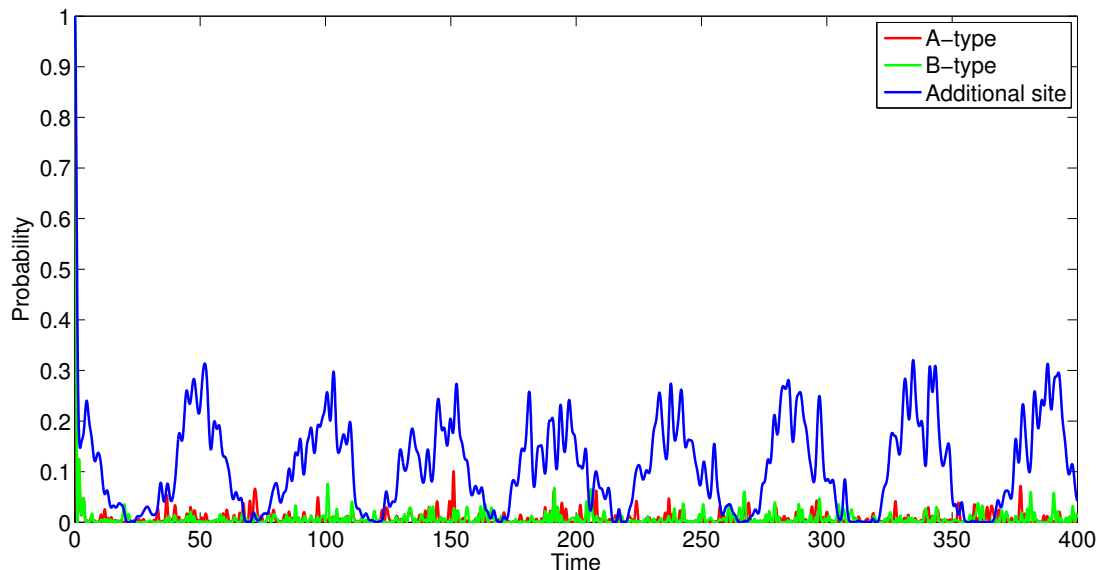
Figure 4.34: Time-evolution of different initial localised states, evolved under the Hamiltonian in Equation (4.24) on a finite armchair nanotube with dimensions $(N_x, N_y) = (32, 5)$ with a perturbation in the bulk. The different initial states are localised on the additional vertex, a random site on the A- and the B-sublattice.
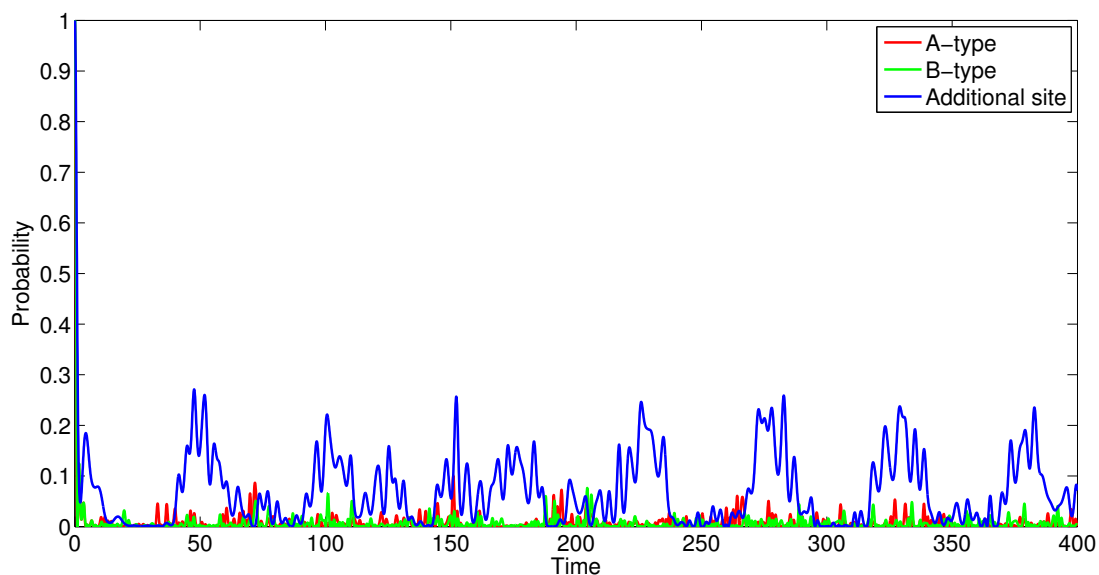

Figure 4.35: Time-evolution of different initial localised states, evolved under the Hamiltonian in Equation (4.24) on a finite armchair nanotube with dimensions $(N_x, N_y) = (32, 5)$ with a perturbation at the edge. The different initial states are localised on the additional vertex, a random site on the A- and the B-sublattice.
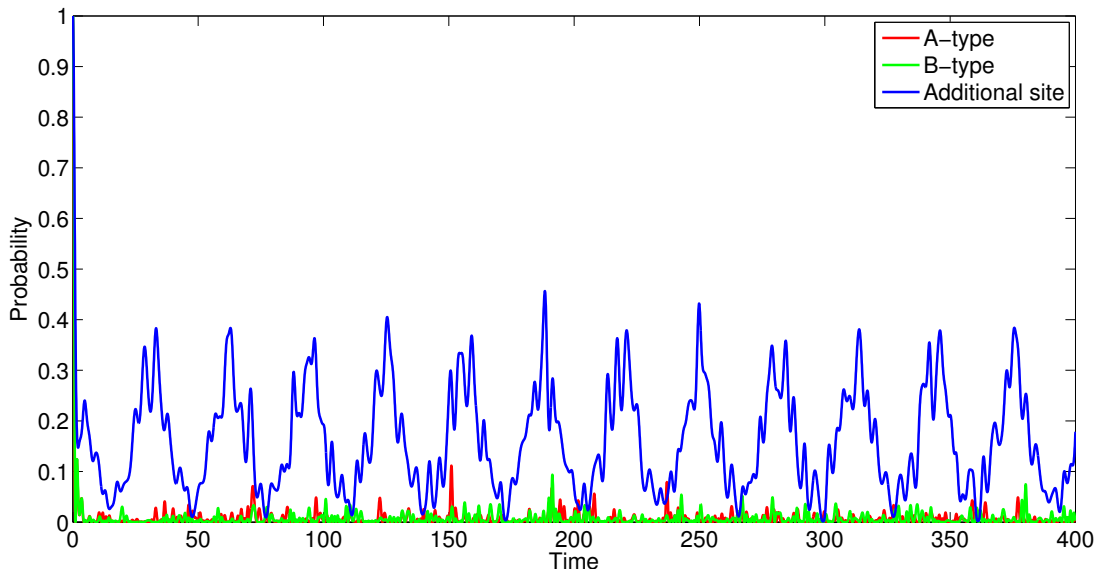
Figure 4.36: Time-evolution of different initial localised states, evolved under the Hamiltonian in Equation (4.24) on a finite armchair nanotube with dimensions $(N_x, N_y) = (32, 5)$ with a perturbation on a nodal point. The different initial states are localised on the additional vertex, a random site on the A- and the B-sublattice.

in this case couples to the eigenstates nearest and next-nearest in energy to the Dirac energy, that is four states in total rather than a single Dirac state. We note that the nearest and next-nearest eigenstates are almost degenerate in energy and that the coupling of the additional site to these states is almost equal in strength.

We proceed by reducing the search Hamiltonian from Equation 4.24 in a basis constructed using the two Dirac states and the basis vector corresponding to the additional site. Through this method we find the same search starting states as in the previous subsection for the triple-bond perturbations. This sharing of optimal search starting states for both types of perturbation was also discovered in searches on the graphene torus and so the introduction of boundaries does not affect the relationship between different perturbation types.

The numerically evolved searches for the additional site perturbation are shown in Figures 4.37 & 4.38, for perturbations in the bulk and the edge respectively. In the figures we plot the probability to be found at the additional site and also the probability to be found at the lattice site it is coupled to. However, we find that the probability to be found at the lattice site rarely increases above $p_{lattice} = 1/N = 3.125 \times 10^{-3}$, which we take to be the average probability of being found at any particular vertex on

117
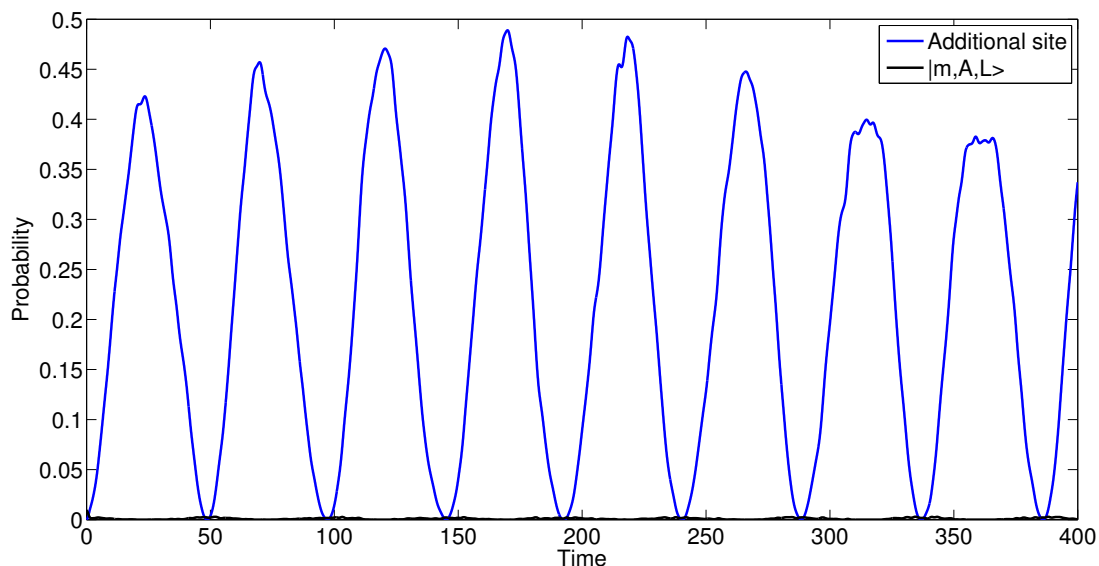
Figure 4.37: Numerically evolved search on a finite armchair nanotube with dimensions $(N_x, N_y) = (32, 5)$ and evolved under the Hamiltonian from Equation (4.24). The perturbation is placed in the bulk of the nanotube and the search begins in the optimal search starting state.
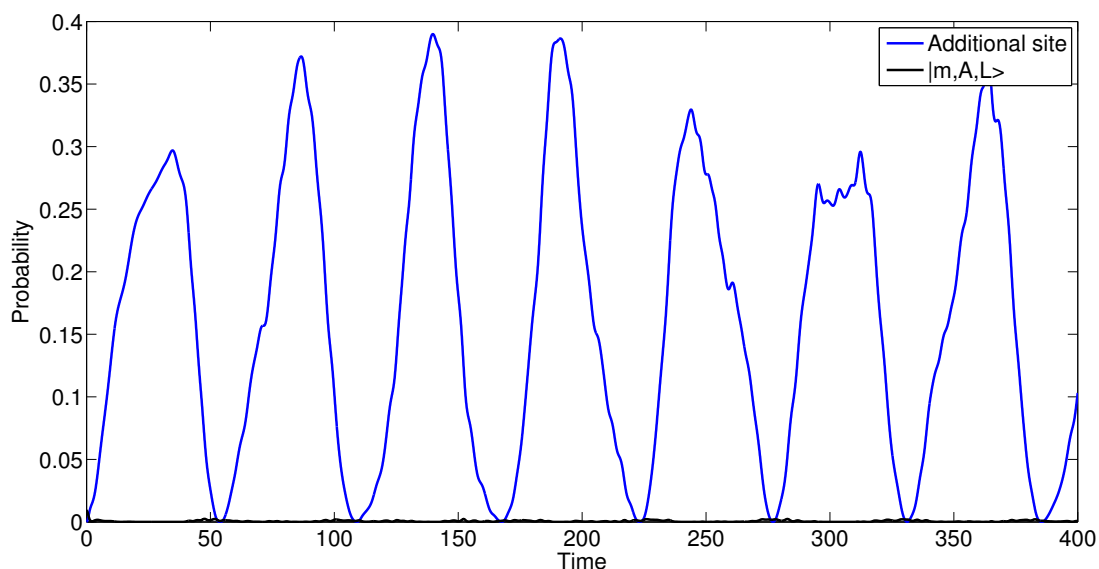
Figure 4.38: Numerically evolved search on a finite armchair nanotube with dimensions $(N_x, N_y) = (32, 5)$ and evolved under the Hamiltonian from Equation (4.24). The perturbation is placed at the edge of the nanotube and the search begins in the optimal search starting state.
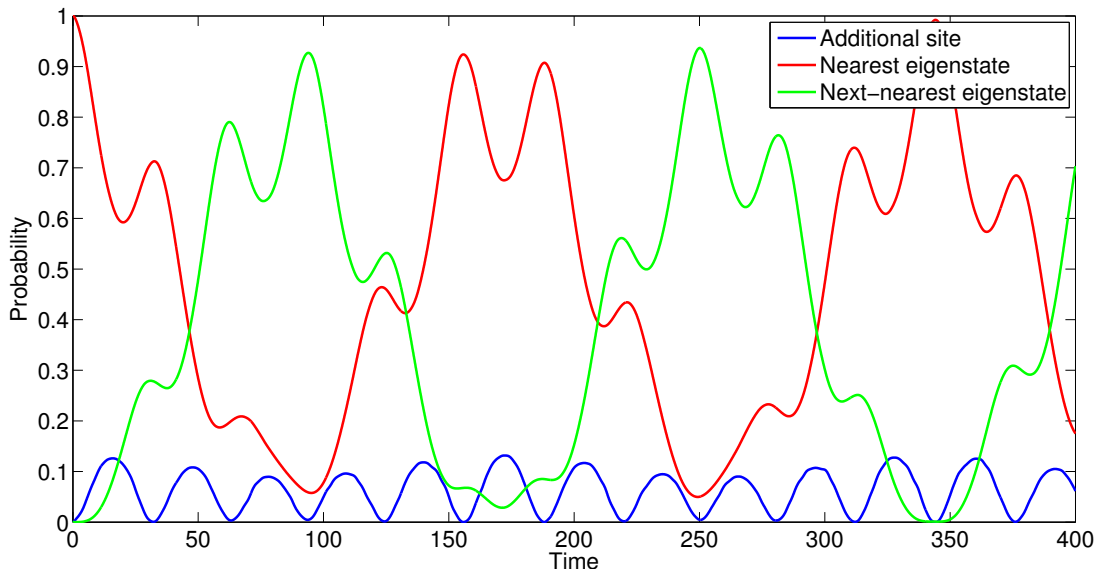
Figure 4.39: Numerically evolved search on a finite armchair nanotube with dimensions $(N_x, N_y) = (32, 5)$ and evolved under the Hamiltonian from Equation (4.24). The perturbation is placed at the edge of the nanotube and the search begins in the optimal search starting state.

the lattice. We find that there is around a 25% decrease in success probability when comparing the search at the edge to the search in the bulk. There is also a difference in the period of successive peaks of success probability between the two searches, matching the behaviour shown in the revival probability plot. However, the overall pattern of the search signature remains between the two cases.

We note that, although the revival probability for the additional site coupled to a nodal vertex has significant revivals, we cannot search for these vertices using the Dirac states. As the Dirac states have zero amplitude at these nodal points, when acted upon by the perturbation matrix results in $W(0)|Dirac\rangle = 0$ and so the Dirac states do not couple to the perturbation. However, it is possible that one would be able to create a search using the states nearest the Dirac point and in Figure 4.39 we set $\gamma = 0$ and attempt to run a search using the unperturbed eigenstate nearest in eigenenergy below the Dirac energy. We find that the system actually oscillates between the nearest and next-nearest unperturbed eigenstates using the additional site as a coupling mechanism. This is similar to the way the triple-bond communication protocol between equivalent sites on the torus in Section 3.5 operates by coupling perturbations via the same search starting state. In this case, the unperturbed eigenstates play

the role of the source/target states, rather than the additional site being one of the source/target states as we would wish in a search protocol.

One may expect that alternative values of the perturbation parameter γ would allow us to search at the nodal points and, in fact, we find two avoided crossings around these states with energies $E \approx 0.15$ in the spectrum in Figure 4.33 for $\gamma \approx 0.25$. Using either of these crossings and placing the system in either of the nearly degenerate unperturbed eigenstates, we find a similar behaviour to that found in Figure 4.39 but with shorter periods between localisations. Inspecting the behaviour over much longer timescales, however, we find an additional beating pattern arising from the slightly different coupling of the additional site to the unperturbed eigenstates. This results in the peak probability to be found in either unperturbed eigenstate decaying to around 50% as the peaks begin to occur in syncrony before becoming out of sync and the peak probability to be found in either unperturbed eigenstate increases again. We stress that the probability to be found at the additional site does not increase during this process, only the probability to be found in either of the unperturbed eigenstates. We do not attempt to take this analysis further because, as we have seen in a similar case for the search on the torus in Chapter 3, the critical value of γ will scale, and the exact form of these eigenstates changes, with the size of the lattice.

We also consider the transport properties of the additional site across the lattice. The different cases are split into communication between perturbations coupled to the same sublattice, different sublattices, and nodal points. Again, we also further split these cases into perturbations in the bulk and at the nanotube edge.

Figure 4.40 shows the communication protocol between two perturbations coupled to the A sublattice in the bulk. One can see that the signal has a very regular pattern with significant localisation at each vertex, two orders of magnitude larger than the average probability of being found at any lattice vertex $p_{lattice} = 1/N$. The communication signal between all sites in the bulk on the same sublattice behaves in the same way, unlike the communication protocol on the graphene torus where there are two different signal patterns. This is due to the way the communication works by interacting via the search starting state (which are the same as in SubSection 4.3.1). As already pointed out, the search starting state for all perturbations on the same sublattice is the same and they are actually a uniform superposition on a single sublattice (bar the nodal points). Thus, all the perturbations couple in the same way and, as there is only one optimal starting state, there are no other states to interfere in the communication system.
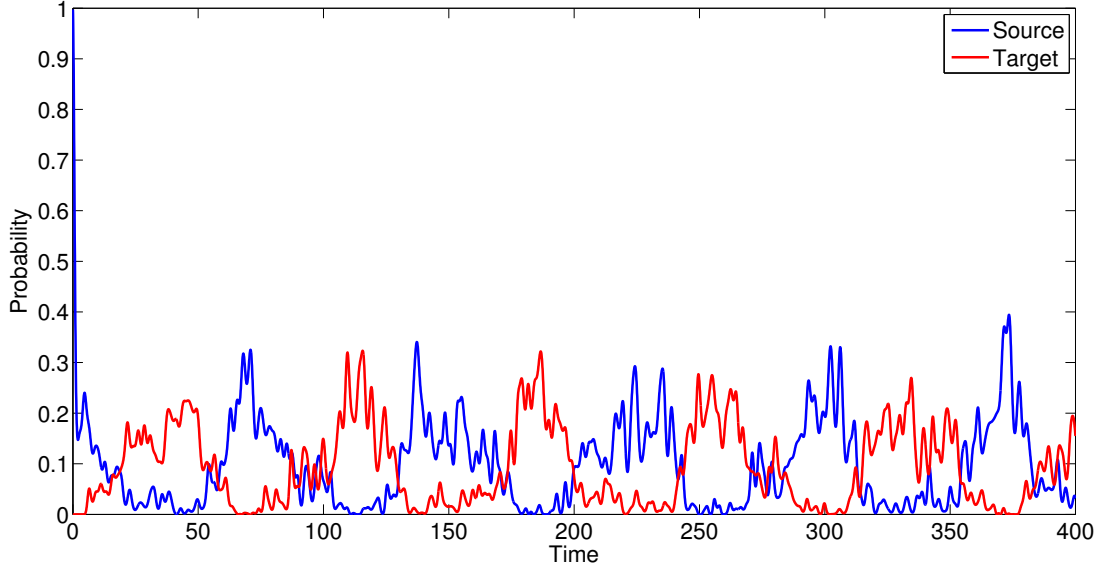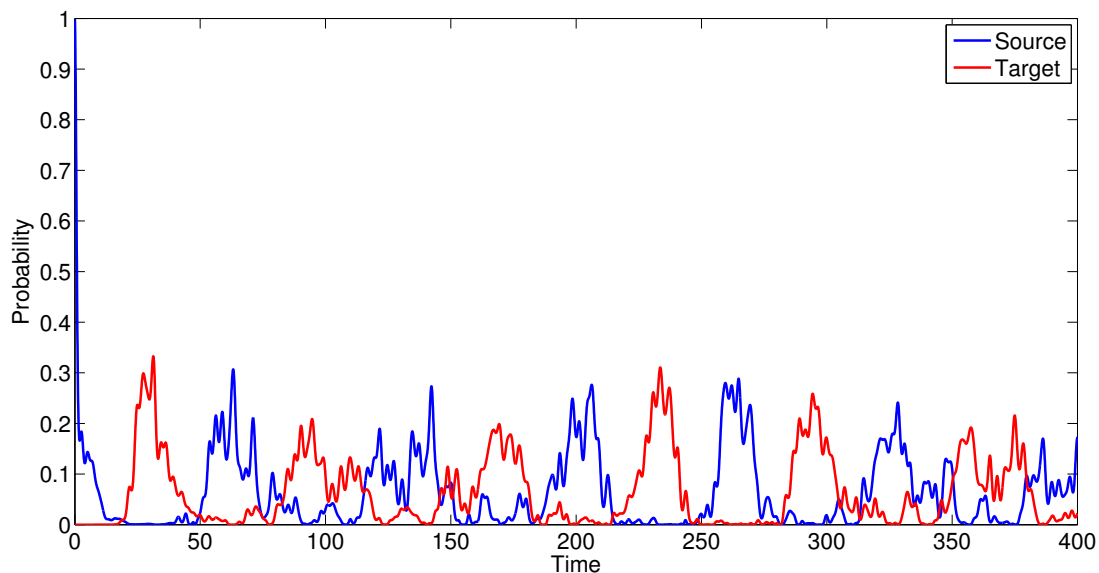
Figure 4.40: Numerically calculated signal transfer on a finite armchair nanotube with dimensions $(N_x, N_y) = (32, 5)$ between two perturbations coupled to A-type vertices in the bulk.
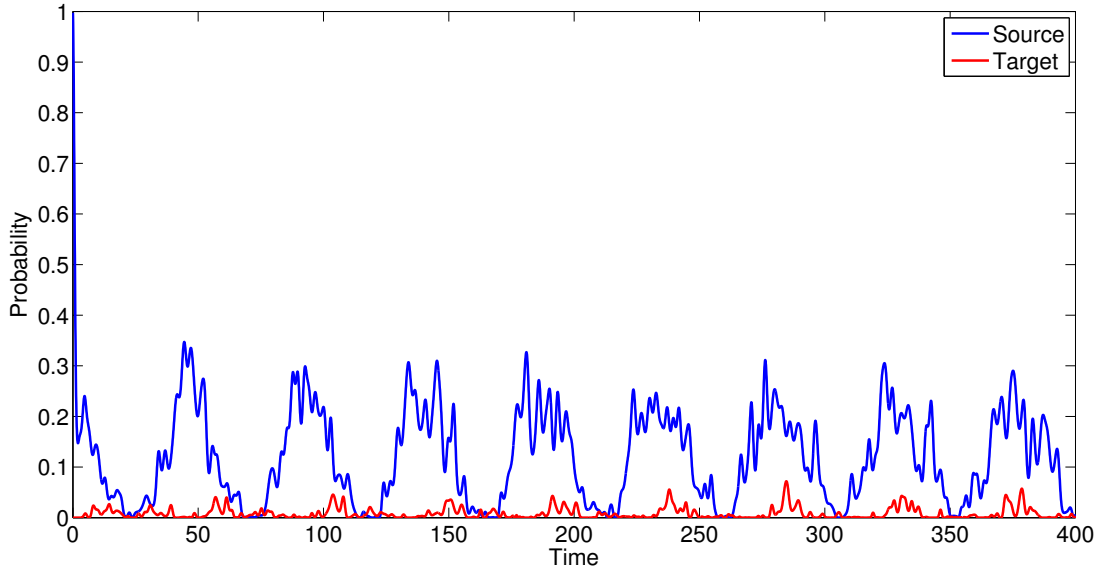

Figure 4.41: Numerically calculated signal transfer on a finite armchair nanotube with dimensions $(N_x, N_y) = (32, 5)$ between two perturbations coupled to A-type vertices in the bulk. The target vertex is a nodal point of the Dirac states.
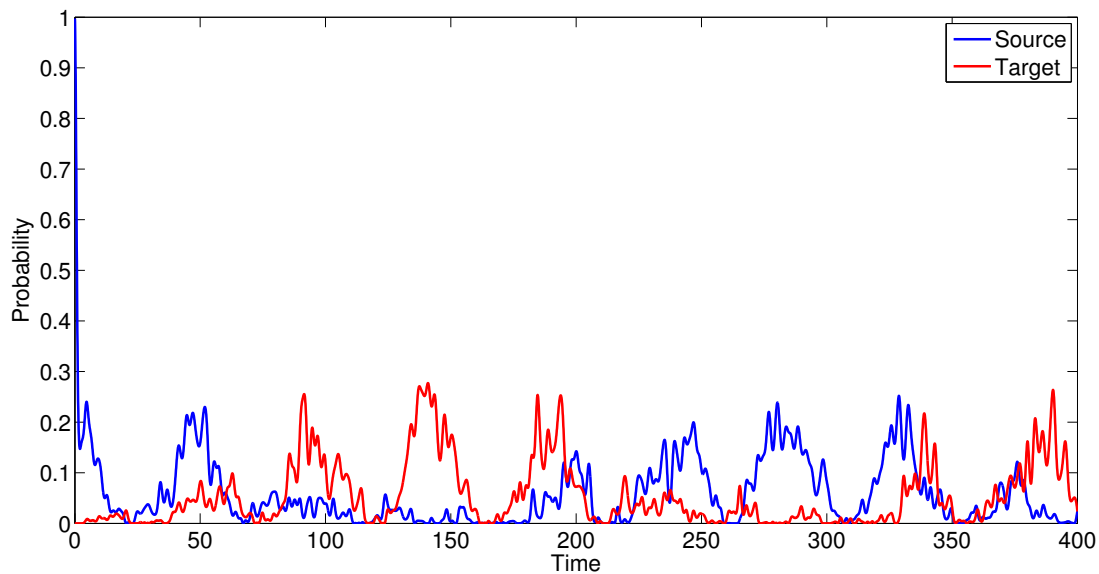
Figure 4.42: Numerically calculated signal transfer on a finite armchair nanotube with dimensions $(N_x, N_y) = (32, 5)$ between two perturbations coupled to different sublattices in the bulk.

Figure 4.43: Numerically calculated signal transfer on a finite armchair nanotube with dimensions $(N_x, N_y) = (32, 5)$ between two perturbations coupled to A-type vertices in on the edges of the nanotube.

Signal transfer to perturbations coupled to a nodal point is not possible, as can be seen in Figure 4.41. Again, this is because of the way the nodal point interacts with the Dirac state, or rather the fact that it does not interact. Thus, there is no state for the two perturbations to couple via and, consequently, there is no reliable signal transfer between them. We also find that there is much faster signal propagation between the sublattices when compared to transport on the graphene torus. Figure 4.42 shows the communication protocol between the two sublattices and we find a very similar signal pattern between all A- and B-type vertices. Again, we explain this in terms of the optimal search starting states and, as they are both uniform superpositions over A and B sublattices, all perturbations on each sublattice interact with the starting states in the same way.

For perturbations located at the edge there are some differences in the transport case. Our results show that there is only a minor change in transport between perturbations coupled to the same sublattice, displayed in Figure 4.43, where there is a slightly greater variation in peak success probability, which we ascribe to reflection effects at the boundary. However, for communication between two perturbations located at opposite edges and coupled to different sublattices, we find that there is no localisation at the target vertex. Rather, at the target vertex the success probability does not rise above the noise level when compared to other vertices. We do not show this case here, as it is very similar to the revival probability at a single additional site figures shown previously.

4.4   Graphene sheets

We finish this chapter with a short study of searches and signal transport on graphene sheets without periodic boundary conditions in any direction. As we have seen in the case of the finite armchair nanotube, the imposition of Dirichlet boundary conditions at an edge generates eigenstates with a sinusoidal nature. One complication caused by this is that, when considering either of the search or communication protocols on graphene sheets, there is a lack of eigenstates at the Dirac energy due to the inability to equate the quantised momenta with the necessary points in $\underline{k}$-space. Rather, instead of Dirac states, there are so called 'edge states' very close to the Dirac energy for the bearded and zigzag edged lattice types [88, 89], shown in Figure 4.44. As their name suggests, these edge states primarily live on the zigzag and bearded edges with negligible amplitude in the bulk of the sheet.
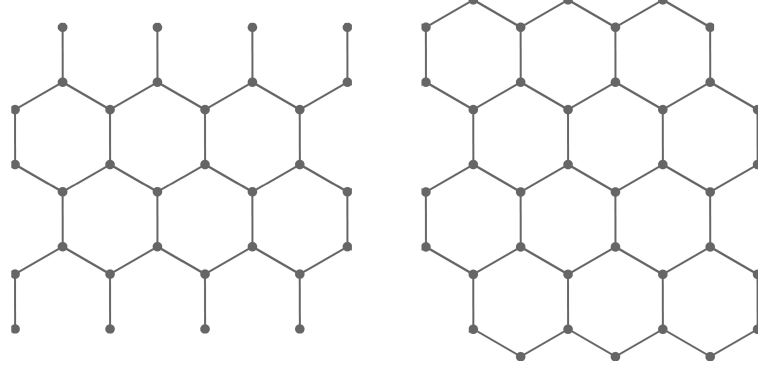
Figure 4.44: Examples of two finite graphene sheets, with dimensions in terms of primitive cells which we label $(N_x, N_y) = (4, 4)$. Along the vertical axis of both sheets are armchair edges. Left) The horizontal boundaries are formed by bearded edges. Right) The horizontal boundaries are formed by zigzag edges.

Throughout this section we choose the dimensions, in terms of primitive cells, of the graphene sheet to be $(N_x, N_y) = (10, 10)$ which means that a bearded edge sheet consists of $N = 200$ sites and a zigzag sheet is formed of $N = 218$ sites. On these lattices we initially focus on the triple-bond perturbation used in Chapter 3, positioned at a vertex centrally located in the bulk of a graphene sheet. That is, we choose our search Hamiltonian, for a perturbed A-type site, to be

$$H = -\gamma A + |\alpha_o, \beta_o\rangle^A \left(\langle \alpha_o, \beta_o - 1|^B + \langle \alpha_o + 1, \beta_o - 1|^B + \langle \alpha_o, \beta_o|^B \right) + h.c. \,. \quad (4.25)$$

We inspect the spectra of the search Hamiltonian as a function of γ on both lattices in Figure 4.45 & 4.46. Both spectra have very few degenerate states, if any, making the spectra very condensed, so we show only the region of interest. There are clear avoided crossings in both figures around the Dirac energy $E = 0$ at $\gamma = 1$, as the perturber states interact with several eigenstates with eigenenergies close to the Dirac energy. We find there are more edge states in the bearded edge lattice with energies very near $E = 0$ but the first couple of energies beyond this are very similar (those near $E = \pm 0.2$ and $E = \pm 0.4$).

The eigenstates near the Dirac energy are all non-degenerate. Therefore, it is not possible for us to set-up a superposition of degenerate eigenstates which is optimal for searching. For this reason we do not perform the reduced Hamiltonian analysis which has been carried out for previous searches. Rather, our initial search starting state must be a single eigenstate of the unperturbed Hamiltonian $H_o = -A$.
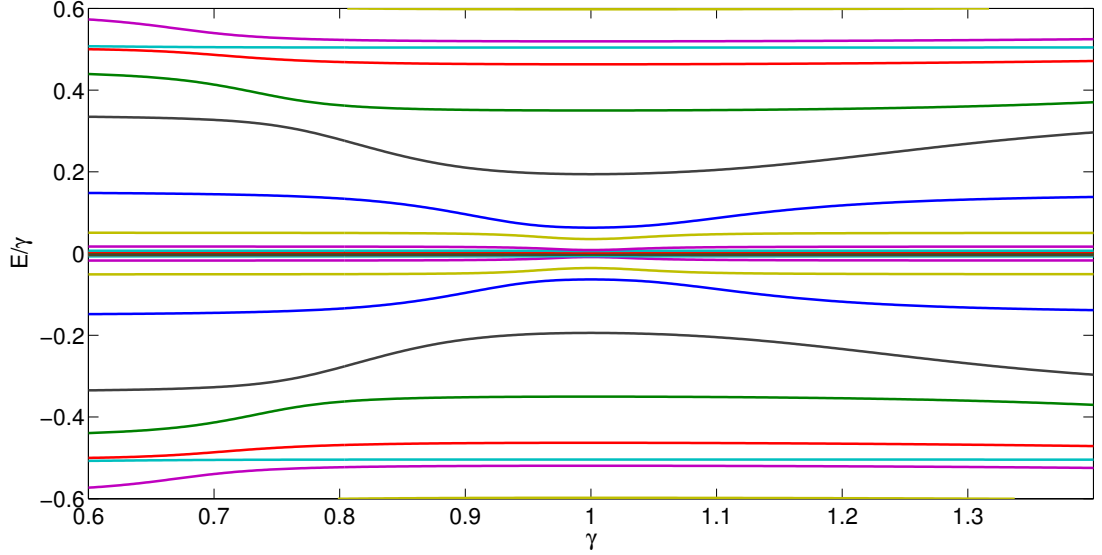
Figure 4.45: Numerically calculated spectrum of search Hamiltonian from Equation (4.25) as function of γ for a bearded edge graphene sheet with dimensions $(N_x, N_y) = (10, 10)$. The perturbation used is located in the centre of the graphene sheet.
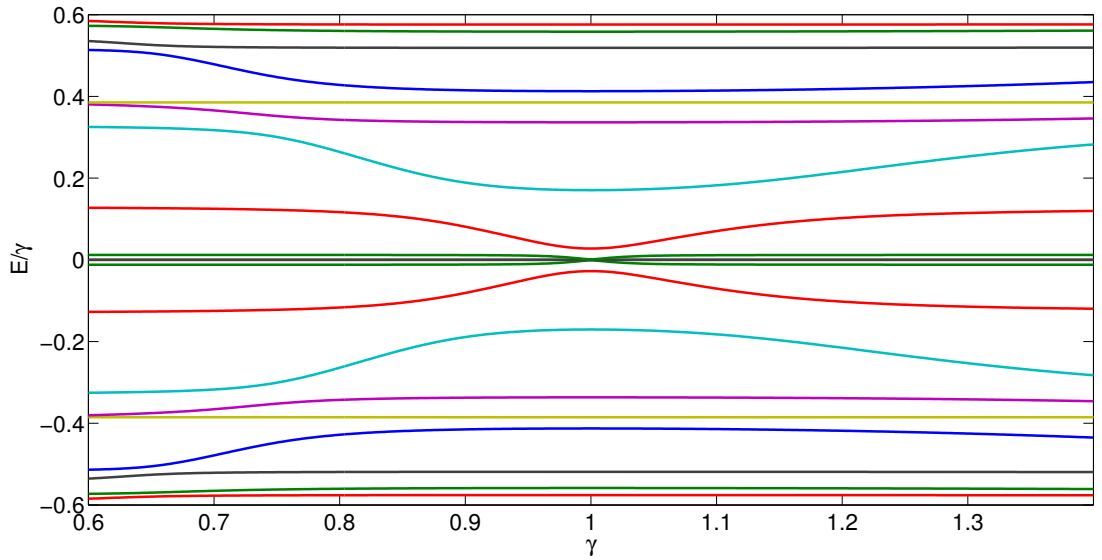
Figure 4.46: Numerically calculated spectrum of search Hamiltonian from Equation (4.25) as function of γ for a zigzag edge graphene sheet with dimensions $(N_x, N_y) = (10, 10)$. The perturbation used is located in the centre of the graphene sheet.
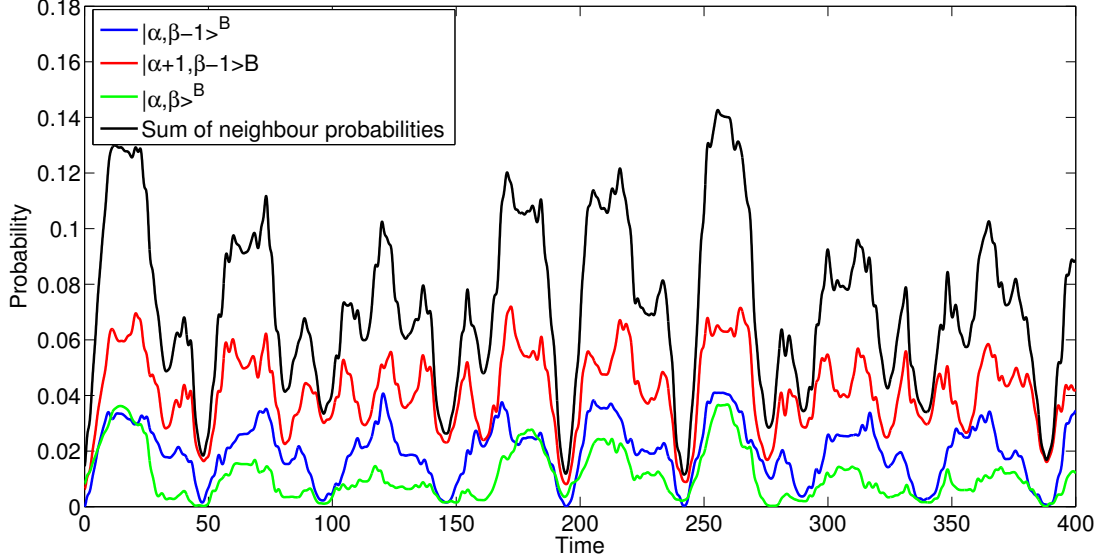
Figure 4.47: Numerically evolved search on a bearded edge graphene sheet with dimensions $(N_x, N_y) = (10, 10)$ and evolved under the Hamiltonian from Equation (4.26). The perturbation used here is placed in the centre of the graphene sheet and the search begins in the unperturbed eigenstate with eigenenergy $E = 0.1495$.
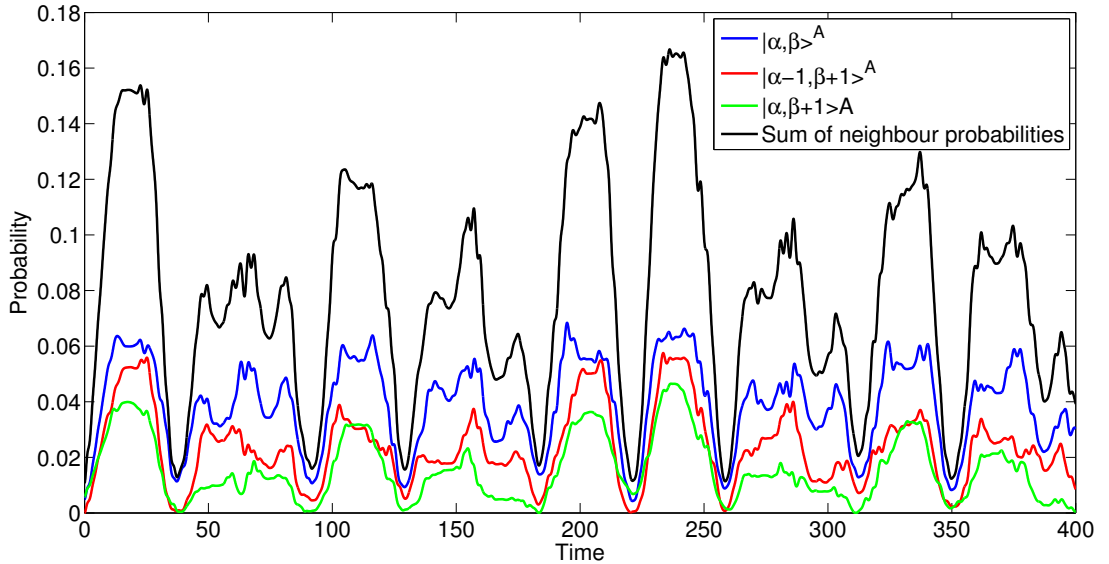
Figure 4.48: Numerically evolved search on a zigzag edge graphene sheet with dimensions $(N_x, N_y) = (10, 10)$ and evolved under the Hamiltonian from Equation (4.26). The perturbation used here is placed in the centre of the graphene sheet and the search begins in the unperturbed eigenstate with eigenenergy $E = 0.1365$.

Setting $\gamma = 1$, our search Hamiltonian is then

$$H = -A + |\alpha_o, \beta_o\rangle^A \left(\langle \alpha_o, \beta_o - 1|^B + \langle \alpha_o + 1, \beta_o - 1|^B + \langle \alpha_o, \beta_o|^B \right) + h.c. \,. \quad (4.26)$$

We find, by running searches using the unperturbed eigenstates as initial states, the edge states do not play a role in the search dynamics with no significant localisation on the neighbour sites above $p_{lattice} = 1/N \approx 0.005$, the average probability to be found at any site on the lattice. However, using the first non-edge state as our initial state does yield localisation around two orders of magnitude greater than $p_{lattice} = 0.005$. Searches evolved using these non-edge states are shown in Figures 4.47 & 4.48, for the bearded and zigzag lattices respectively. While the peaks in success probability have differing maxima as the system evolves, the signal pattern has a very definite period and the maxima in success probability is consistently an order of magnitude above $p_{lattice}$.

We see from Figures 4.47 & 4.48 there is no clear difference between the searches on the two lattices and, for searches in the bulk at least, the imposition of non-periodic boundary conditions at all edges does not destroy the search effect which we have created. However, as we move the perturbation to other parts of the lattices differences begin to appear and we find certain regions are unable to be searched.

In the bearded edge lattice type it is observed that searches cannot be performed very near the bearded edge, using either edge states or states that are spread across the whole lattice, as the probability to be found at or near the perturbed vertex fails to rise above the noise level. We find the search effect only begins to reappear as we move away from the bearded edge boundary, further into the lattice than the edge states penetrate.

The same is not true for the zigzag edge lattice; however, we find that the fewer edge states in that system do not penetrate as deeply into the lattice and theorise that the lack of interaction with the edge states allows the search to work. It appears, therefore, that already localised states are unusable as far as search dynamics are concerned.

A possible explanation of this behaviour is that the edge states can be viewed as a kind-of one-dimensional system and, as we saw from the scaling argument towards the end of SubSection 4.3.1, one-dimensional systems imply an energy spacing between successive energy levels of $E_{n+1} - E_n = \mathcal{O}\left(N^{-1}\right)$. Thus, the perturber state interacts with many states in a dense part of the spectrum and the search fails.

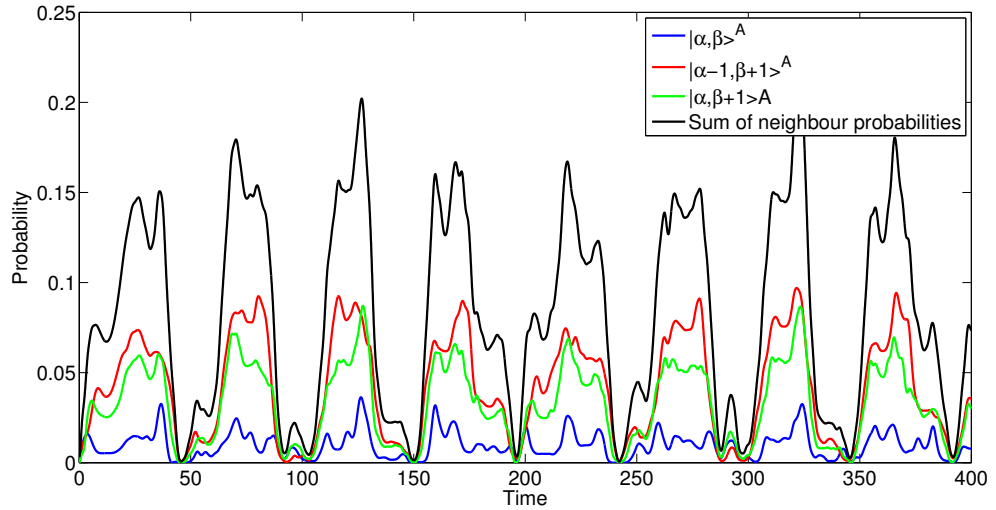When considering searches with perturbations placed elsewhere in the lattice, away
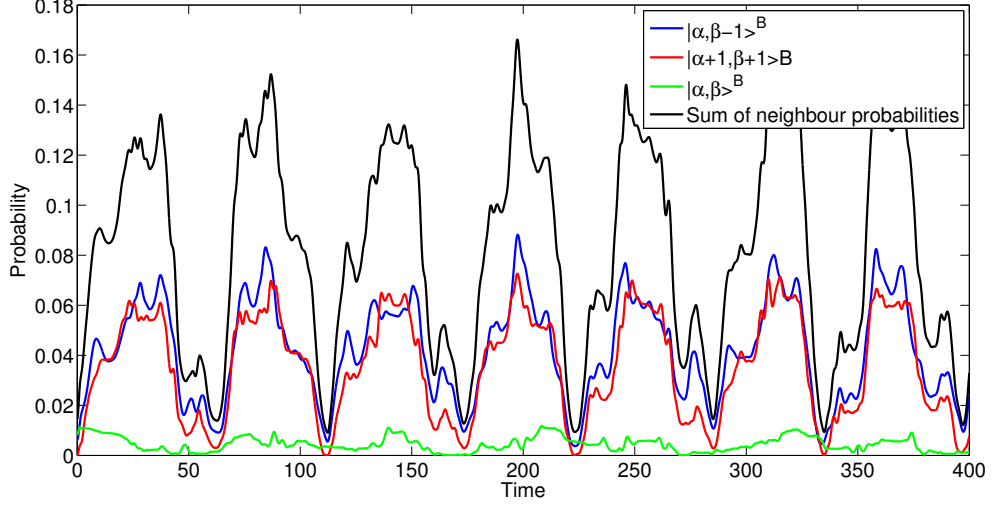
Figure 4.49: Numerically evolved search on a zigzag edge graphene sheet with dimensions $(N_x, N_y) = (10, 10)$ and evolved under the Hamiltonian from Equation (4.26). The perturbation used here is placed half way along the left armchair edge. The search begins in the unperturbed eigenstate with eigenenergy $E = 0.1495$.

from the bearded and zigzag edges, we find similar results to those found for the nanotube case. There we found some variation in the search behaviour with perturbation position but the search remains effective. We find the same for both lattices here, but with an observable increase in variation with position and an increase in success probability as we move towards the centre of the lattice. We show a couple of different searches at different positions for both lattices in Figures 4.49-4.52 to display the variation.
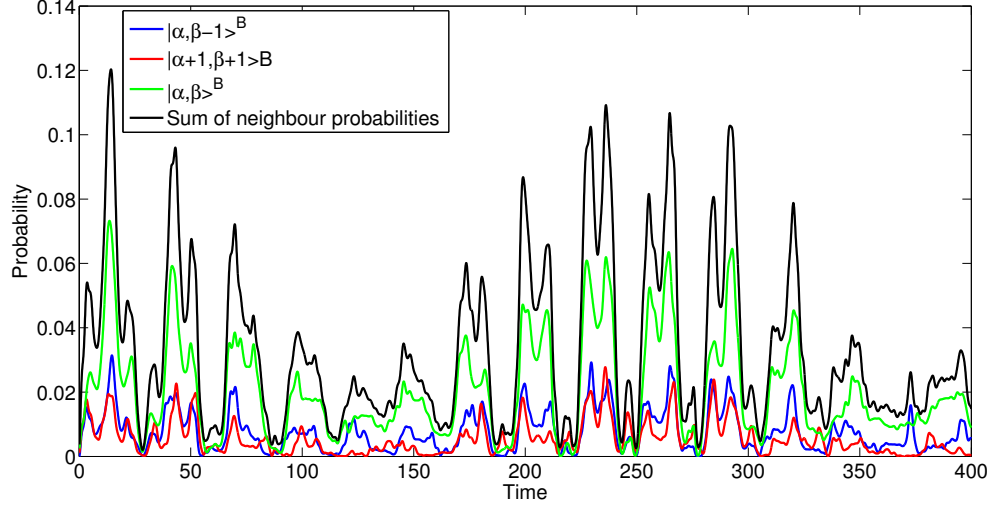
Figure 4.50: Numerically evolved search on a zigzag edge graphene sheet with dimensions $(N_x, N_y) = (10, 10)$ and evolved under the Hamiltonian from Equation (4.26). The perturbation used here is placed in the centre of horizontal axis and a third of the way up the vertical axis. The search begins in the unperturbed eigenstate with eigenenergy $E = 0.1495$.

Figure 4.51: Numerically evolved search on a zigzag edge graphene sheet with dimensions $(N_x, N_y) = (10, 10)$ and evolved under the Hamiltonian from Equation (4.26). The perturbation used here is placed in the bottom left corner of the graphene sheet and the search begins in the unperturbed eigenstate with eigenenergy $E = 0.1365$.
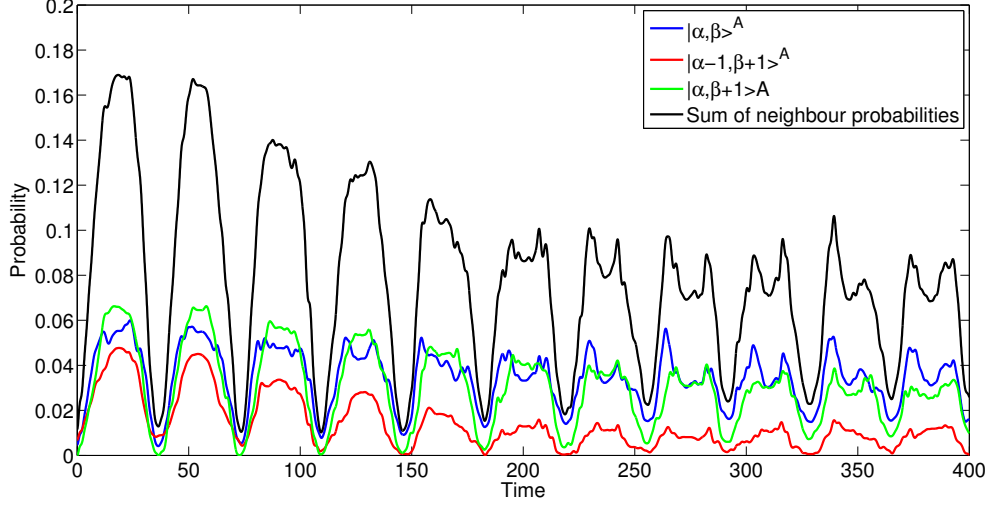
Figure 4.52: Numerically evolved search on a zigzag edge graphene sheet with dimensions $(N_x, N_y) = (10, 10)$ and evolved under the Hamiltonian from Equation (4.26). The perturbation used here is placed two sites left of the perturbation used in Figure 4.48. The search begins in the unperturbed eigenstate with eigenenergy $E = 0.1365$.

For these graphene sheets, we also consider the issue of signal transport between additional sites coupled to vertices on the edges of the lattices, first considered in Section 4.2. We do not consider the case of communication involving two triple-bond perturbations due to the more complex search behaviour and resulting localised state. Instead we focus on the simpler localised states constructed using a single additional site. The additional sites are coupled to the underlying lattice using the perturbation matrix

$$W_{s/t} = - |\alpha, \beta\rangle \langle s/t| - |s/t\rangle \langle \alpha, \beta| \, , \tag{4.27}$$

where the index s or t signify the source or target perturbations respectively and sign of the entries has been chosen to match the coupling used in the unperturbed walk Hamiltonian $H_o = -A$.

We proceed by coupling the additional sites to points on the vertical armchair edges of the graphene sheets rather than the zigzag or bearded edges. As we have already seen in the triple-bond case, the perturbations near these boundaries do not couple very strongly into the dominant eigenstates at these points, the edge states. Therefore, with the lack of an eigenstate to couple via, we would not expect communication between additional sites on the zigzag or bearded edges to be possible. This is indeed what we

130

find when attempting to establish a communication protocol between these points; the success probability at the target vertex fails to reliably increase above the noise level with any discernible period.

The positioning of the additional sites at the armchair edges of the zigzag lattice, seen in Figures 4.53 & 4.54, is more successful than for the bearded lattice case. We find only two different signal patterns, those between A-type perturbations in Figure 4.53 and those between different sublattices in Figure 4.54. There are minor differences in the behaviours as we approach the zigzag edge but the basic structure of the signal remains the same, and is not affected by the positioning of the perturbations at the inner or outer part of the armchair edge.

We find that attempting to implement a communication protocol on the bearded edge lattice is not as fruitful. The signal pattern is more consistent as the target perturbation is moved from being coupled to the same sublattice to a different sublattice to the source perturbation, but does not reach the same success probability as the zigzag edge case. A typical example of the signal transfer for this case is shown in Figure 4.55.
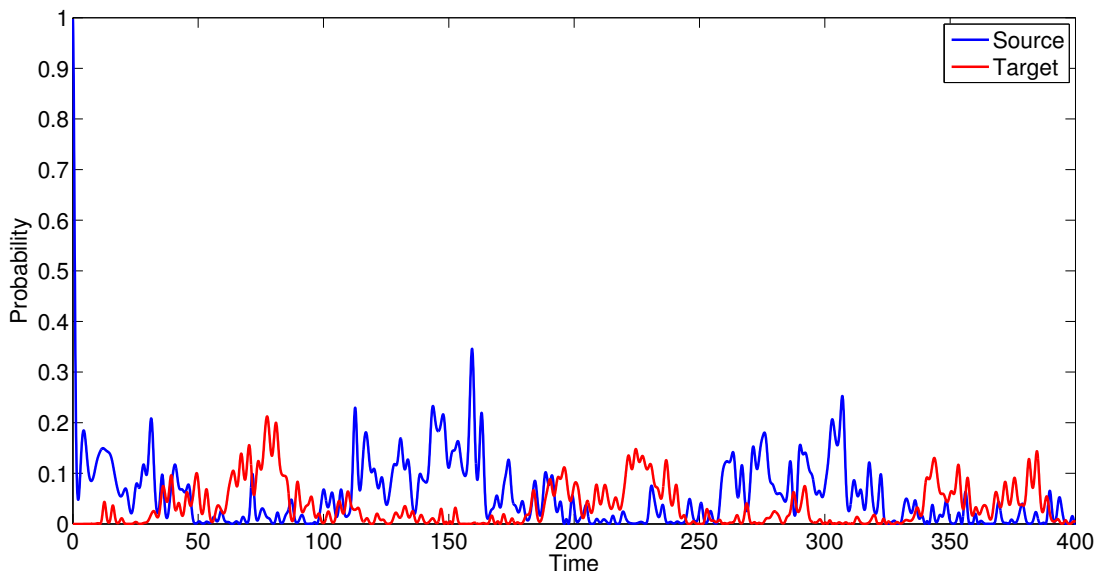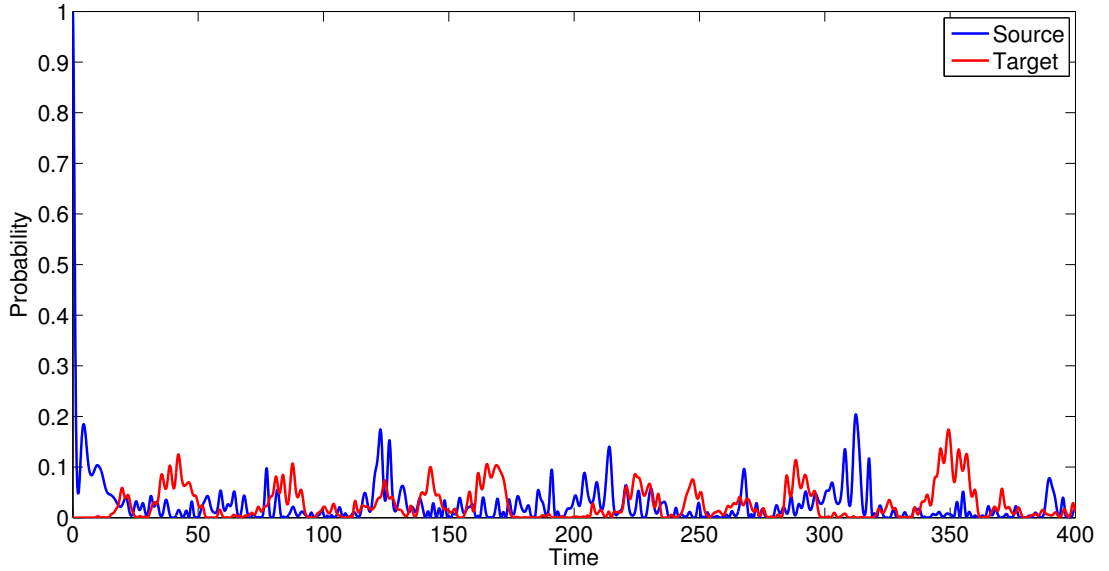

Figure 4.53: Numerically calculated signal transfer on a zigzag edge graphene sheet with dimensions $(N_x, N_y) = (10, 10)$ between two A-type perturbations coupled to opposite armchair edges.
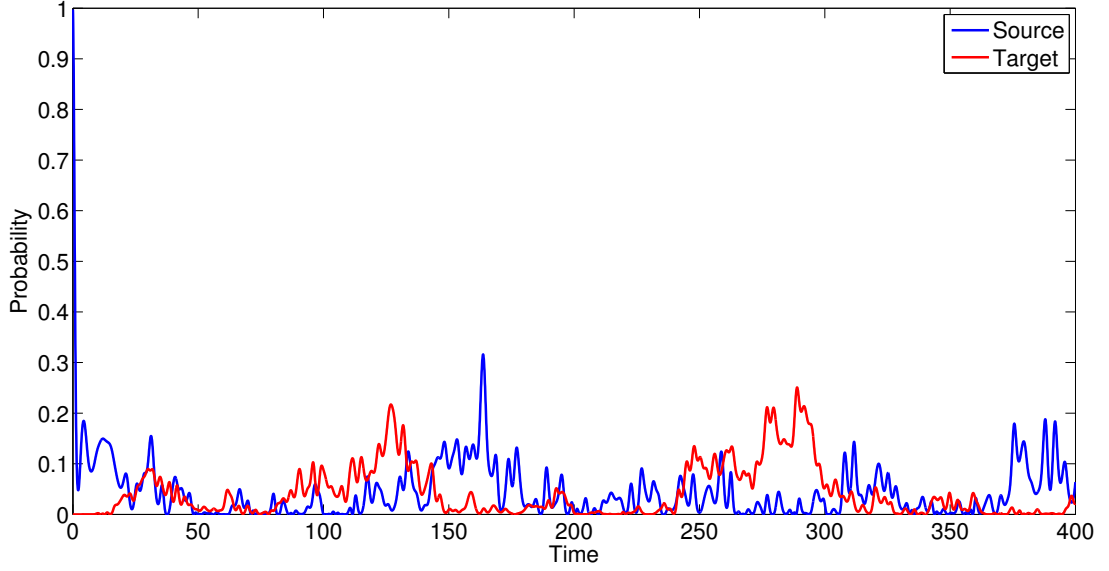
Figure 4.54: Numerically calculated signal transfer on a zigzag edge graphene sheet with dimensions $(N_x, N_y) = (10, 10)$ between two perturbations coupled to different sublattices on opposite armchair edges.

Figure 4.55: Numerically calculated signal transfer on a bearded edge graphene sheet with dimensions $(N_x, N_y) = (10, 10)$ between two A-type perturbations coupled to opposite armchair edges.

5

Microwave experiment modelling

In this chapter we describe the theoretical modelling of a microwave resonator experiment, designed by a group based at the Université de Nice Sophie-Anitpolis [90, 91, 92]. This group had carried out work on microwave analogues of graphene and, when learning of our work on searches on graphene, decided to attempt to demonstrate these effects in their experiments, and also further utilise the phenomena in more novel applications as well. This chapter contains numerical work done to support their experiments and also some possible directions for the future.

In these experiments, dielectric discs placed in a honeycomb lattice formation in a microwave resonator act as an analogue for graphene. By virtue of the nature of the interactions between the discs, the spectra of these microwave resonator setups have similar features to the electronic band structure of graphene. As a result, these microwave analogues offer a cost-effective and technically simpler alternative to experimenting directly with graphene. In this chapter we will give a short explanation of the experimental setup used and detail the theoretical model we apply. We shall then describe some benchmark simulations where we model features of the unperturbed lattice, and conclude this chapter with demonstrations of search and transport behaviour in the microwave experiment setup. We stress that figures relating to physical experiments presented in this chapter are from [92] and are not the author's work.

5.1   Experiment description

The use of microwave resonators as analogues for quantum mechanical systems has been established since the 1990's, especially in the investigation of quantum chaos in billiard systems, see for example the seminal paper [93] or reviews of the field in [94, 95]. The use of microwave systems to investigate what are quantum phenomena is enabled through the equivalence of the spatial Helmholtz equation governing the electromagnetic waves in the resonator and the time-independent Schrödinger equation in two dimensions. This allows one to investigate 'particle in a box' behaviour through classical means. For investigations into quantum chaos, specific shapes of microwave cavities (billiards) are constructed and microwaves are transmitted into the *empty* cavity. Through measuring the reflection spectrum important properties for quantum chaos can be analysed, for example the spectral statistics of eigenfrequencies or nodal patterns of wavefunctions, and comparisons with predictions from quantum theory can be made.

It was demonstrated in [90] that by including dielectric discs within the microwave cavity one creates a closed scattering system, allowing one to form microwave systems analogous to materials or structures without any connecting leads, such as an isolated graphene sheet. In their setup resonances of the system correspond to wavefunctions which are strongly contained within in each dielectric disc and which decay rapidly in the surrounding air. Thus, the analogy with materials arises as we consider the dielectric discs as corresponding to atomic sites in the material with electrons strongly bound to each atom. By arranging the discs in the characteristic hexagonal lattice structure of graphene one is able to probe features of the carbon structure which may be difficult to access using other techniques.

This agreement between microwave analogues and graphene was demonstrated in [90], where it was shown for such a honeycomb lattice arrangement that the spectrum of eigenfrequencies contains a Dirac point and also that for zigzag edges there exist edge states, both typical features of graphene lattices. In a different publication [91] the same group were also able to analyse the nature of the interactions between discs and their interaction strength, demonstrating the tight-binding nature of the couplings. A student from the same group, using a similar setup which we describe shortly, in his Masters thesis [92] was able to demonstrate switching or searching behaviour in the dynamics of such microwave systems, and it was from this thesis which we will later take our benchmark scenarios for our model.

A simple diagram of the experimental apparatus used in [92] is shown in Figure 5.1.
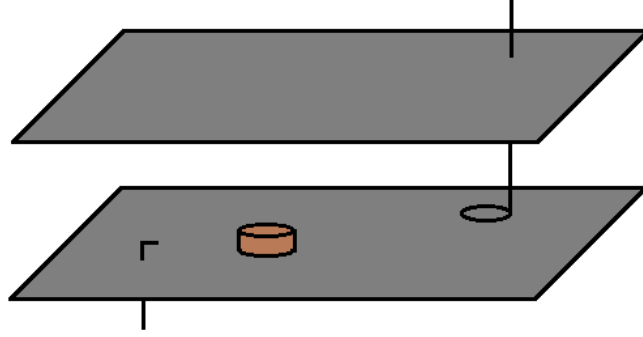
Figure 5.1: Example of experimental apparatus used in [92]. It consists of two parallel metallic surfaces with a kink antenna protruding from the lower plate and a loop antenna descending from the upper plate. The lower plate is fixed but the upper plate can be moved to allow measurements at different locations. Also shown is one of the dielectric discs with a high refractive index ($n_d = 6$).

The microwave resonator consists of two parallel metallic plates, on which are placed the dielectric discs. In the lower plate is a kink antenna and in the upper plate there is a loop antenna, both of which are capable of exciting the system. The dielectric discs have a high index of refraction ($n_d = 6$) which is important for creating the tight-binding behaviour. In [90] it was found that by exciting the system containing a single disc, there is a single resonance peak corresponding to an isolated wavefunction centered on the disc and decaying exponentially outside the disc. It is due to the high index of refraction of the dielectric discs that one can excite resonances of the system which do not form standing waves outside of the discs. It was also demonstrated that with each inclusion of an additional disc, there is a single additional well-localised state. Thus, the system is constructed from a collection of bound states, localised on the dielectric discs, which have a weak evanescent interaction with their neighbours due to the exponential decay of the wavefunctions outside of the discs, exactly like the tight-binding model so frequently used in condensed matter physics.

The arrangement of discs we wish to model, as used in [92], is shown in Figure 5.2. The setup has only armchair edges because, as discussed in Section 4.4, other edge types have states which live almost exclusively at the edge and have energies very near the Dirac point. Only using armchair edges completely removes any possibility of a perturbation coupling to an edge state.

In the experiments the two quantities which are measured are the transmission coefficient S_{12}, which is the signal received by the loop antenna transmitted from the
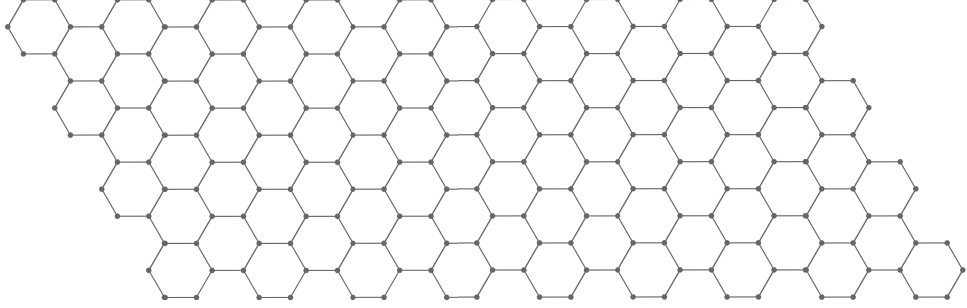
Figure 5.2: Layout of dielectric discs from the experimental setup in [92]. The grid only has armchair edges to remove the influence of edge states on any dynamics.

kink antenna, and the reflection coefficient from the loop antenna S_{22}. By using two antennae it is possible to not only determine the amplitude of S_{12} but also the phase, allowing for a full description of the eigenstates of the system. The two measured quantities offer different information. In [90], the authors explain that when measuring the reflection coefficient S_{22} what is actually measured is the total current through the loop antenna, which is $T = 1 - |S_{22}|^2$. In [90] it is detailed how this quantity is related to the density of states (DoS) or, more specifically, the local density of states (LDoS) $\mathcal{L}(r, \nu)$ and they show

$$\mathcal{L}(r, \nu) \propto 1 - |S_{22}(r, \nu)|^2, \tag{5.1}$$

where r denotes the position of the loop antenna and ν indicates the frequency being measured. By making a measurement of the reflection coefficient S_{22} from the loop antenna over each disc in the setup and averaging one can then find the DoS. This can then be used to determine the resonances or eigenfrequencies of the system. When perturbations are added to the system these can be identified by an additional resonance in the DoS, or more specifically, a splitting of one of the unperturbed resonances into two resonances. In terms of the energy levels of a perturbed quantum system, this splitting would equate to an avoided crossing involving the perturbed state and an unperturbed eigenstate, as described in Section 3.1.

In addition to measuring the reflected signal from the loop antenna S_{22}, it is also possible to measure the phase and amplitude of the transmitted signal from the kink antenna to the loop antenna S_{12}. This involves measuring a signal from the kink antenna at each disc using the loop antenna. One then has a spatially resolved picture of the resonances of the system. To investigate any dynamics in this system one must transform this data about the resonances or eigenfrequencies into some information in

the time domain. In [92] this is achieved by taking the Fourier transform of S_{12} over a relevant set of frequencies. For example, to analyse the effect of a perturber on the dynamics, one would take the Fourier transform of S_{12} only over a frequency interval which includes the split frequencies mentioned in the previous paragraph.

The nature of the evanescent couplings in the microwave analogue of graphene was investigated in [91]. It was demonstrated that the couplings between discs extends further than just between nearest-neighbour, and higher-order couplings are important as well. They showed that also considering the additional next- and next-next-nearest-neighbour interactions in theoretical models of the lattice system is sufficient to capture the features of the spectrum not found in the simpler nearest-neighbour tight-binding model. It was also demonstrated that the strength of the couplings between discs can be controlled by increasing the distance between them and how these different interaction strengths affect the DoS.
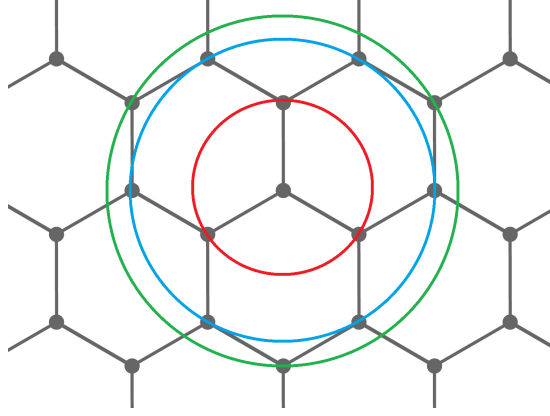
Figure 5.3: Diagram of tight-binding couplings between discs. The sites intersected by a coloured circle are coupled with the central disc in the following way : red - nearest-neighbour, blue - next-nearest-neighbour, green - next-next-nearest-neighbour.

5.2 Numerical approach & initial benchmarks

To simulate the experimental setup described and the arrangement of discs displayed in Figure 5.2, we need to make significant changes to the models and programs used to create the numerical results in the previous two chapters. The first, and most obvious, change is in the physical interpretation of the tight-binding model. We must now interpret the diagonal entries of the Hamiltonian matrix as the resonances of an individual disc and the off-diagonal entries describing couplings between discs are now due to the constructive interference of overlapping, exponentially-decaying localised wavefunctions. Thus, the coupling terms are now positive unlike the negative terms in the adjacency matrix previously. The Hamiltonian can now been written as

$$H = \nu_o \mathbb{1} + t_1 A + t_2 A' + t_3 A'', \tag{5.2}$$

where the ν_o is the resonant eigenfrequency of a single disc, and t_1, t_2 & t_3 are the nearest, next-nearest & next-next-nearest neighbour interaction strengths. We also denote by A the adjacency matrix and A' & A'' are matrices describing which discs are next-nearest & next-next-nearest neighbours.

The experiment which we model from [92] has a nearest-neighbour separation between discs of $d = 10$mm and the resonance of each of the discs is measured to be $\nu_o = 6.647$GHz. We apply this value for the single disc resonance to our own model

and use the information on the dependence of the coupling parameters on disc separation from [91] to set the nearest-neighbour couplings in our model. Consequently, we set the nearest-neighbour coupling to $t_1 = 0.078$GHz and, after advice from the experimental group in Nice, the higher-order couplings to $t_2 = 0.1t_1$ & $t_3 = 0.05t_1$. These higher-order parameters are comparable to those detailed for lattices of various dimensions in [91].

Our first step in assessing the veracity of our theoretical model is by comparing our numerically calculated eigenfrequencies with the resonances measured in the experimental setup we are attempting to describe. We diagonalise our Hamiltonian and plot the eigenfrequencies along with the experimentally measured data supplied by the author of [92], both the LDoS and the transmission spectrum averaged over all the discs, in Figure 5.4. On comparison, we see that the general features of the spectra agree, that is, the asymmetry in the spectra and a reduction in states around the Dirac point at $\nu_D = 6.62$GHz. In particular we note the first eigenfrequencies either side of the Dirac point, as these are the critically important states for any search or transport dynamics. There is also a general agreement in the DoS in Figure 5.5.

It is apparent that the theoretical and experimental resonances do not match exactly. As the nearest-neighbour coupling t_1 has been experimentally verified, attempts were made to improve the agreement between the two spectra by modifying the higher-order couplings. However, while improvements were made in the agreement for the two eigenfrequencies around the Dirac points, this came at the cost of severely removing any agreement with the widths of the bands and, consequently, the DoS. In light of this, we keep the original parameters discussed and accept the general, qualitative description which our model provides.

Our next step is the propagation of an initially localised pulse through the lattice. In Figure 5.6 we show the experimental data for the pulse propagation. Also shown in the figure is the location of the kink antenna from which the pulse originates. It is clear from the figure that the signal diffuses outwards from the antenna and decays rapidly. It is explained in [92], due to the nature of the antenna used in the experiment, the pulse is not exactly a spherical wave as one may have expected, but rather the pulse spreads more rapidly towards the lower part of the setup. The spreading of the pulse is also affected by the initial state which is not localised to simply a single disc as the antenna couples to several discs. The decay in the system originates from the losses within the dielectric discs and from signal escaping at the edges of the microwave system into the environment.
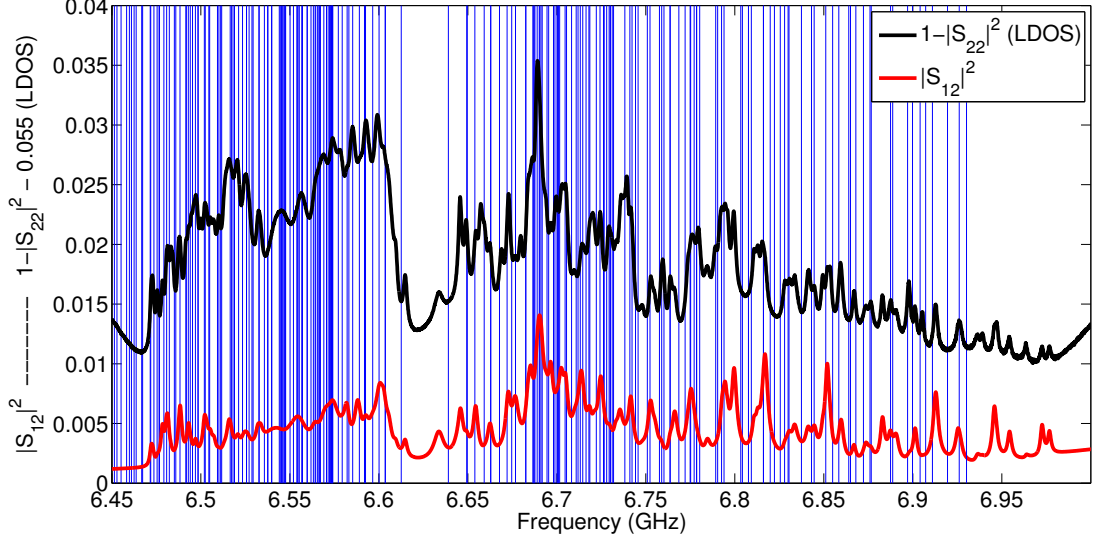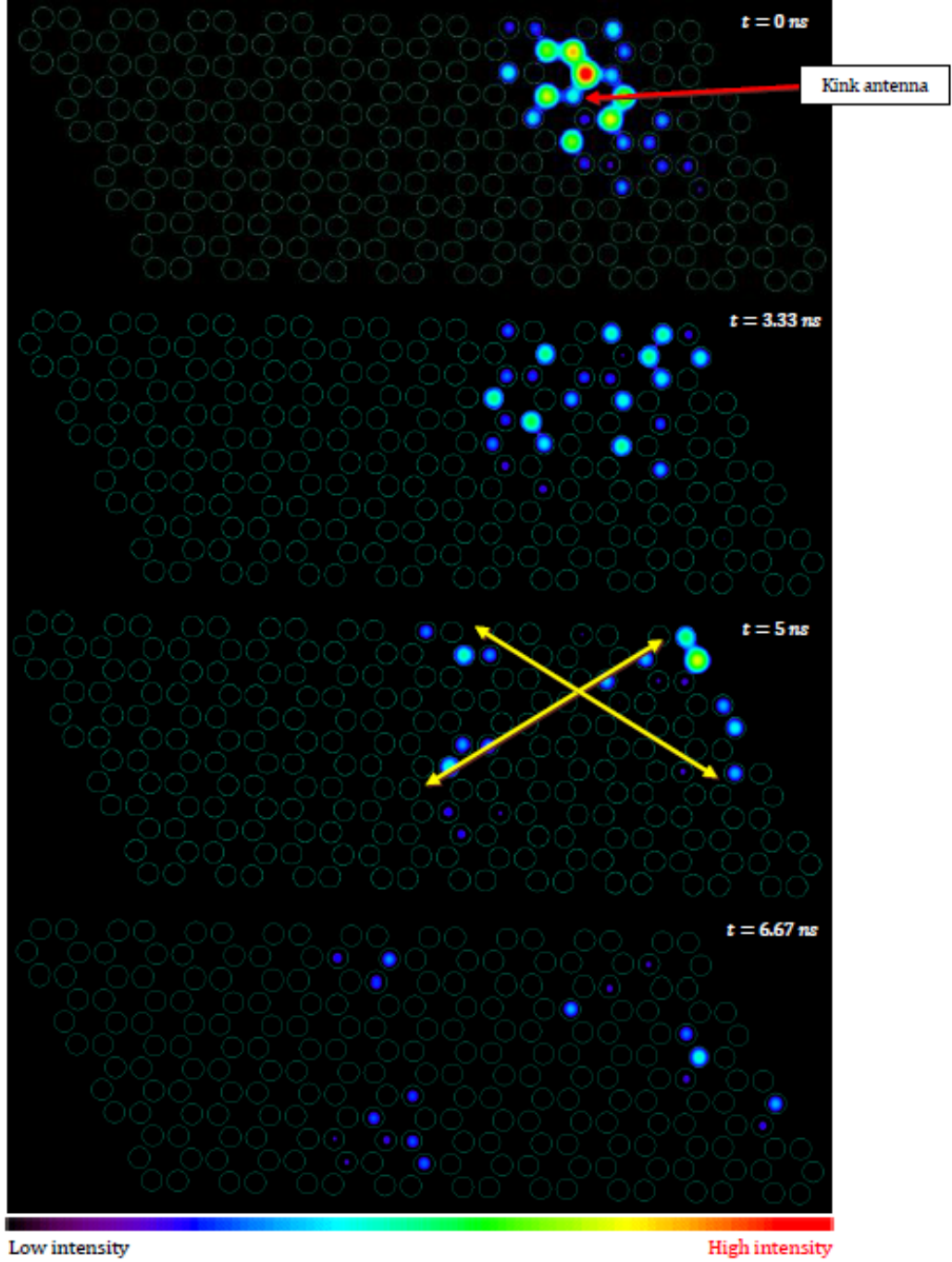
Figure 5.4: Plot of the experimentally measured reflection coefficient S_{22} and transmission coefficient S_{12} data, provided by the author of [92]. Also plotted as the blue vertical lines are the eigenfrequencies of the Hamiltonian matrix described in Equation 5.2.
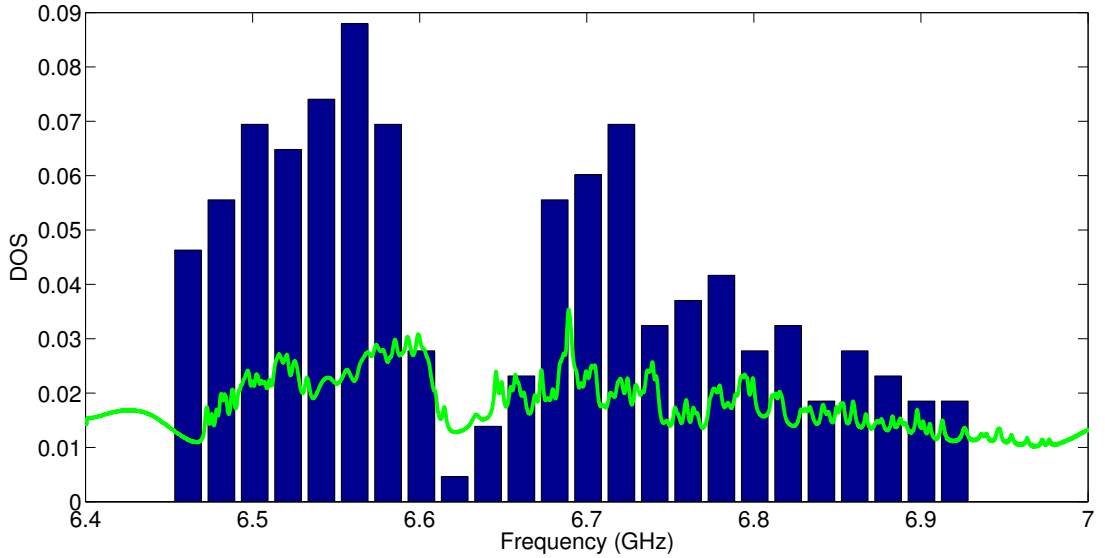
Figure 5.5: Normalised density of states for the eigenfrequencies of the Hamiltonian matrix in Equation 5.2. Also shown as the green curve is $1 - |S_{22}|^2 - 0.055$, provided by the author of [92], which is proportional to the LDOS, averaged across the whole lattice.

Figure 5.6: Experimentally measured time-evolution of an initially localised pulse propagating throughout the microwave setup, obtained from [92]. The figure is broken up into four different intensity plots of the lattice at different moments in time.

We attempt to recreate the time-evolution of a localised pulse in order to compare the dynamics and the timescales for the dispersion. In our theoretical model we prepare the system in a localised state using only the seven most intense points of the initial pulse, where we set the red point in Figure 5.6 to an intensity of 0.4 and the other six points which correspond to the yellow/green discs to an intensity of 0.1 .

Figure 5.7 shows the intensity with time of the initially most intense point and its nearest-neighbours. We see that the initial pulse decays rapidly into the rest of the bulk with some small revivals over a timescale of the same order as found in the experiment. Figures 5.8-5.10 show the continued time-evolution over the whole lattice, at the times displayed in Figure 5.6 and also two further points in time. These figures confirm that the pulse continues out into the rest of the setup and that the distances covered for the timescales shown are similar when compared to the experiment.

There are differences between the experimental and theoretical results as we do not include any damping or losses in the model. Therefore, we see greater reflection at the edges and there are points of significant intensity further away from the origin of the pulse than in the experimental results, as in the experiment one finds that the signal has decayed at these points. Losses in the experiment occur at the edges of the lattice where signal propagates out into the environment and there are also losses within the dielectric discs. The difficulty incorporating these effects into our theoretical model arose from attempting to balance the two dissipative effects. Only applying one type of losses into the model did not capture the damping behaviour and, therefore, we decide not to apply any dissipative terms in the model.
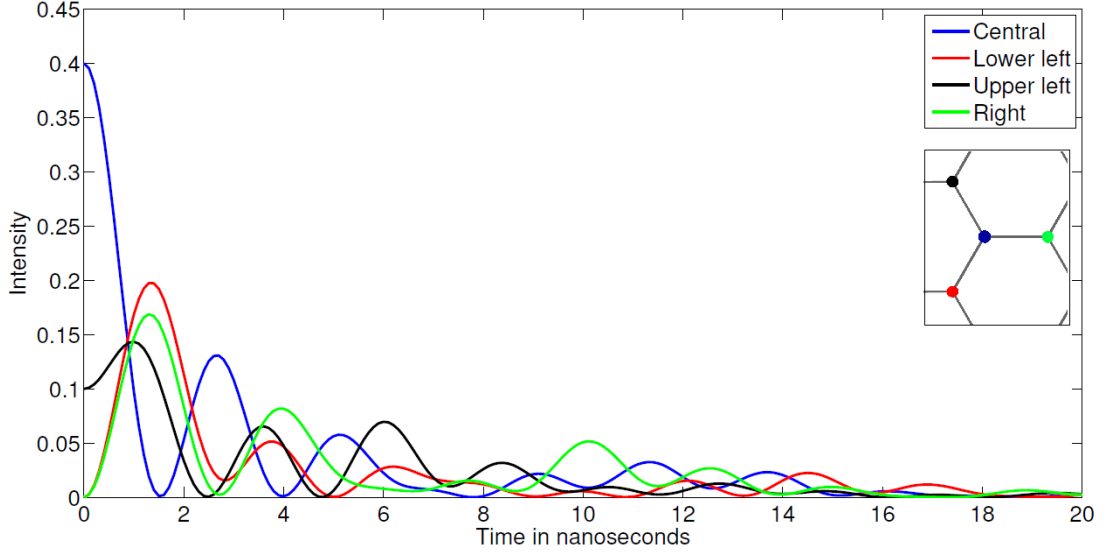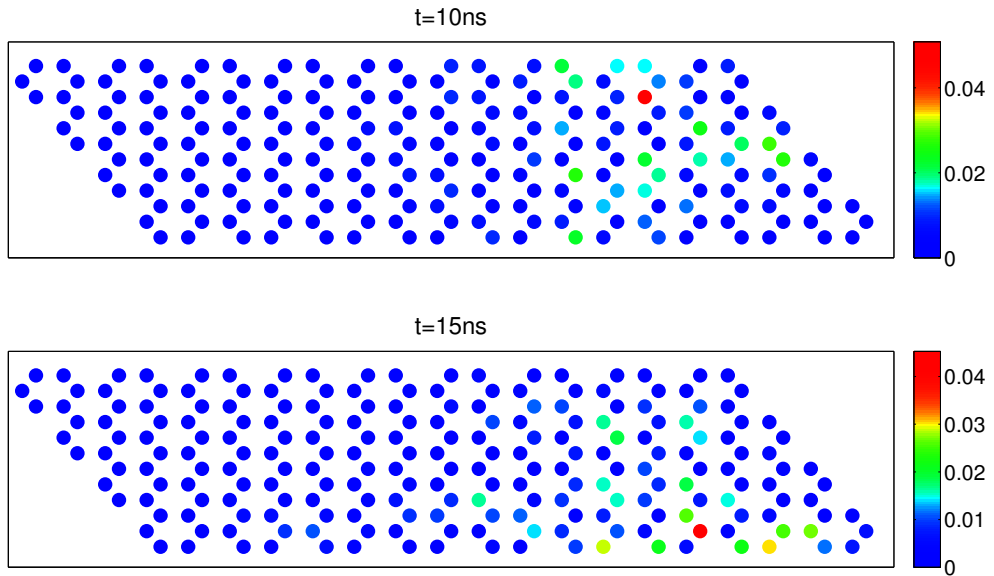
Figure 5.7: Numerically calculated time-evolution for the most intense point of the initial pulse shown in the Figure 5.6 and its nearest-neighbours. The inset shows which colours correspond to which points.
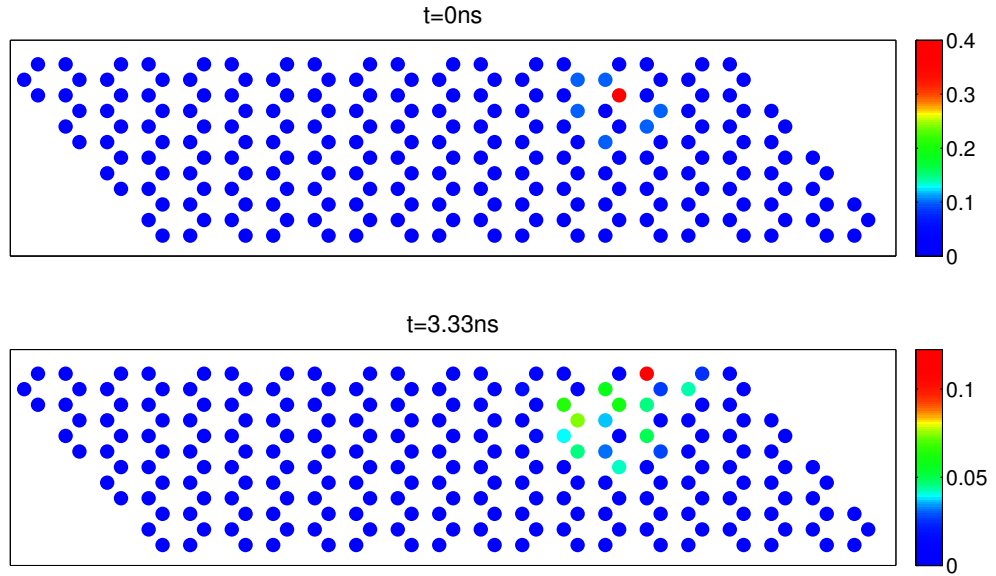

Figure 5.8: Numerically calculated time-evolution of an initially localised pulse propagating throughout the lattice. The figure is broken up into two different intensity plots of the lattice at different moments in time.
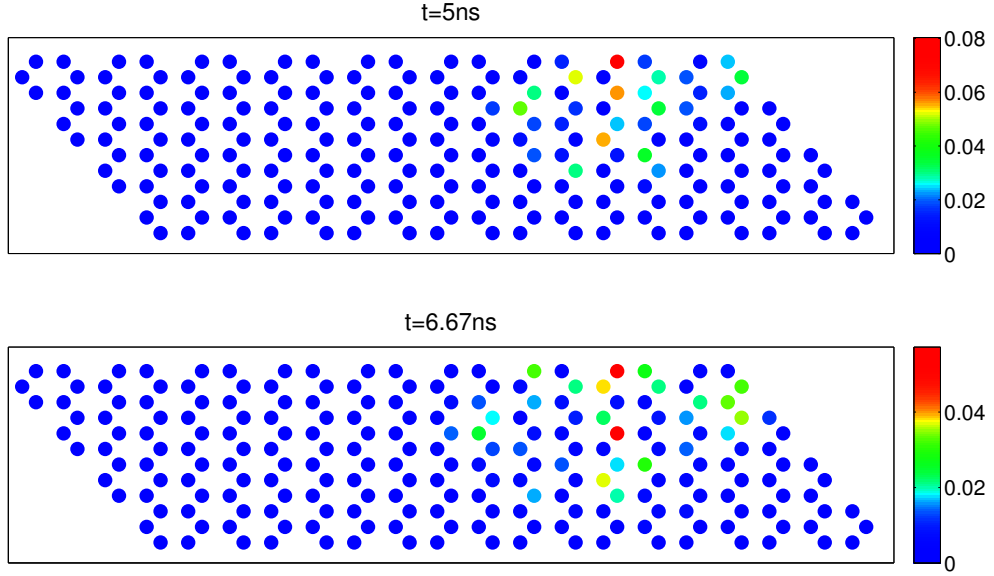
Figure 5.9: Numerically calculated time-evolution of an initially localised pulse propagating throughout the lattice. The figure is broken up into two different intensity plots of the lattice at different moments in time.

Figure 5.10: Numerically calculated time-evolution of an initially localised pulse propagating throughout the lattice. The figure is broken up into two different intensity plots of the lattice at different moments in time.
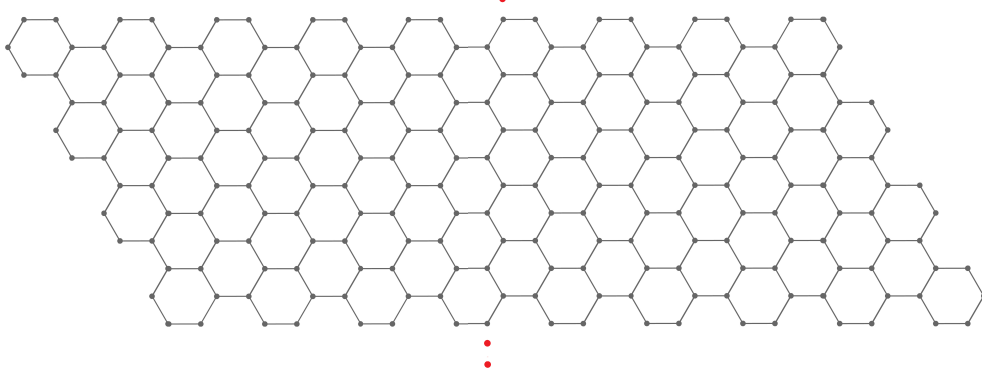
Figure 5.11: Layout of dielectric discs from the experimental setup including the perturber discs, as used in [92].

5.3 Switching behaviour

In [92] a switching protocol was demonstrated, an effect closely related to the search dynamics which have been described throughout this thesis. In this switching setup there are two perturbers, where one is tuned to the first eigenstate above the Dirac point and the other is tuned to the first eigenstate below the Dirac point. The aim is to then force the system to localise on a particular perturbation depending on how the setup is excited.

The positions of the perturbers in relation to the lattice are shown in Figure 5.11. The experimental setup uses two different types of perturber: a single disc and a dimer setup composed of two discs. For the first perturber, a single disc was found whose individual resonance matches the eigenfrequency of the state above the Dirac point. For the second perturber, the distance between the discs forming the dimer is adjusted, and, therefore, the coupling between the discs is also adjusted, such that one of the internal resonances of the dimer matches the eigenfrequency of the state below the Dirac point. The advantage of this dimer setup is that one can tune the perturber into an eigenfrequency of ones choosing.

The experiment used various different discs with different single disc resonances and also various different distances, and, consequently, couplings, between discs. The discs arranged in the lattice structure use the same coupling parameters as described in the previous section, that is, $(\nu_o, t_1, t_2, t_3) = (6.647\text{GHz}, 0.078\text{GHz}, 0.1t_1, 0.05t_1)$. However, as stated, the two perturbers are tuned into the specific eigenfrequencies of this particular system. As the spectrum in the theoretical model does not exactly

match that of the experimental setup, we do not use the same parameters described in [92] but instead follow the same method of tuning the perturber discs to unperturbed eigenstates.

The distance of the two perturbers to the lattice is larger than the separation between discs in the lattice itself, $d = 12$mm rather than $d = 10$mm, and so the coupling of the perturbers to the lattice is lower (we take the coupling values from [91]). The resonance of the single disc perturber is tuned to the unperturbed eigenfrequency above the Dirac point that we find in our theoretical method, so we choose our parameters to be $(\nu_o, t_{1'}, t_{2'}, t_{3'}) = (6.639\text{GHz}, 0.4\text{GHz}, 0.1t_{1'}, 0.05t_{1'})$. For the dimer perturber, we keep the experimental single disc resonances which are used but we adjust the interaction between the two dimer discs, t_d, to so that the internal resonance of the dimer matches the eigenfrequency below the Dirac point. Therefore, the parameters we choose for the dimer are $(\nu_o, t_{1'}, t_{2'}, t_{3'}, t_d) = (6.7\text{GHz}, 0.4\text{GHz}, 0.1t_{1'}, 0.05t_{1'}, 0.0874\text{GHz})$.

Also important is the nature of the eigenstates near the Dirac point. The form of these states is important as the dynamics will be dependent on how the perturber discs couple to the target eigenstates. For example, as we have seen in Section 4.3, the coupling of a perturber to a nodal point of an eigenstate prevents any search dynamics.

Figure 5.12 displays the measured eigenstates nearest the Dirac point from the experiment. The distribution of the wavefunction intensity is not evenly spread over the lattice. This asymmetry in the lattice is due to the position of the antenna (the arrow to the right in Figure 5.12). As we do not have this feature in our tight-binding model, the eigenstates we obtain, shown in Figures 5.13, are essentially distributed across the whole lattice. However, the pattern of very high intensity points matches well and the most important points, that is those points corresponding to the red arrows in Figure 5.12, also match. It is essential that these sites have high intensity because it is at these points that the kink antenna injects signal into the system and where the perturbers couple to the lattice, and the high intensity of these points ensures the interactions with these states.

We note the existence of low intensity horizontal striations in the theoretical eigenstates which are not found in the experimental results. We believe we obtain these due to the 'hard' Dirichlet boundary conditions at the edges of the lattice, which forces a sinusoidal pattern across the lattice, whereas the experimental apparatus has losses at the boundary.

We evolve the system using two different starting states. For the first run, we prepare the system in the unperturbed eigenstate above the Dirac point and allow it to
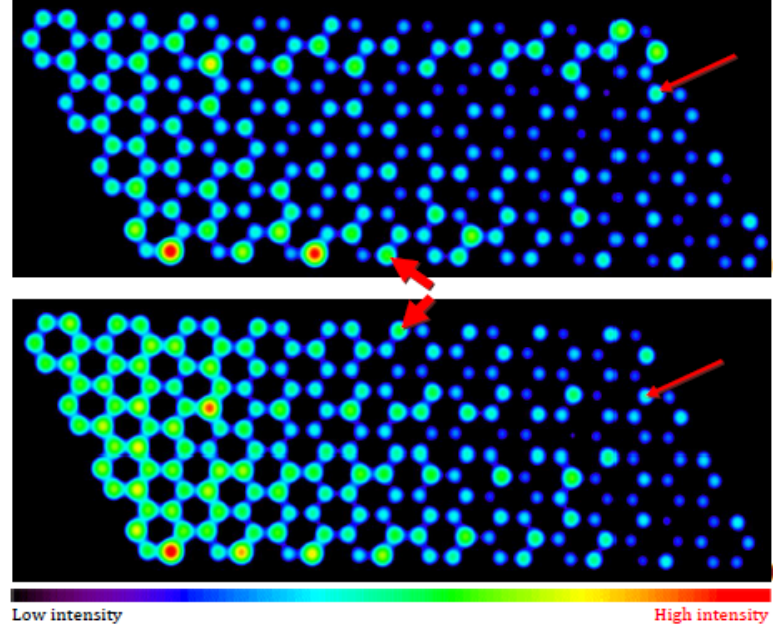
Figure 5.12: Intensity plot of the wavefunctions around the Dirac point, taken from [92]. The upper plot displays the lower eigenfrequency state, the lower plot shows the higher eigenfrequency state. The arrow on the right marks the position of the kink antenna, whereas the arrows in the centre of the figures denote the position of the dimer and single disc perturbations.
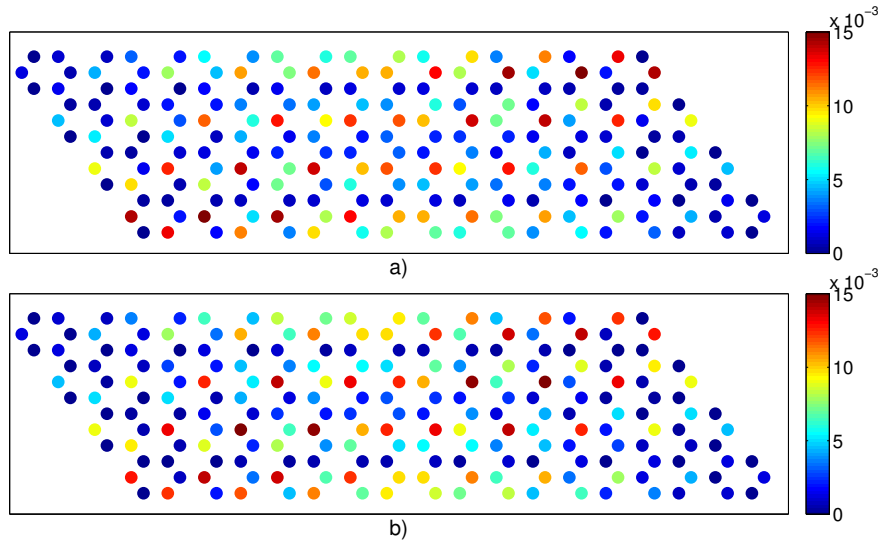
Figure 5.13: Numerically calculated wavefunctions around the Dirac point. Subplot a) displays the lower eigenfrequency state, subplot b) shows the higher eigenfrequency state.

evolve in time, this is shown in Figure 5.15. In the experiment shown in Figure 5.14, the kink antenna excites the system using the associated unperturbed eigenfrequency. Figures 5.16 & 5.17 show the experimental & theoretical results for the same procedure using the unperturbed eigenfrequency below the Dirac point.

We see for both perturbers and in both the experiment & theoretical results, the system successfully localises on the perturbers and then oscillates back to the bulk eigenstate. In the experimental results shown in Figures 5.14 & 5.16, it is found that the time taken for the initial localisation on the perturbers in both cases is similar. However, the important timescale is the beating time, that is, the time taken to decay from a localised state back into the bulk. In the experiment this beating time is longer for the single perturber case than the dimer perturber case. This is in contrast to our theoretical results in Figures 5.15 & 5.17, where the time for oscillations between localisation and bulk state is longer for the dimer perturbation than the single perturber case. We show the beating times for both sets of results in the table below for ease of comparison:

	Single disc	Dimer
Experiment results	292ns	89ns
Theoretical results	70ns	120ns

The qualitative description of the dynamics agrees between the experimental and theoretical results, as does the general order of the beating times for the dimer case. However, exactly why the disagreement between the experiment and the theory is so large for the single perturber remains unclear but there are indications that the cause may be due to the coupling of the perturbers to the unperturbed lattice. By reducing the strength of the coupling of the single perturber to the unperturbed lattice one can improve the agreement of the timescales, as seen in Figure 5.18. In constructing our theoretical model we have assumed that the coupling strength between two discs with different disc resonances is the same as between two discs which have the same single disc resonance. However, this may not be the case leading to the discrepancy we see in the localisation times.

An alternative possible explanation to the discrepancy could be the method of simulation itself. As mentioned previously, the time-evolution of the experiment is found by taking the Fourier transform over a frequency range containing the two split resonances in each of the switching dynamics. This essentially neglects the interaction of all other states in the spectrum, unlike our method of preparing the system in one of
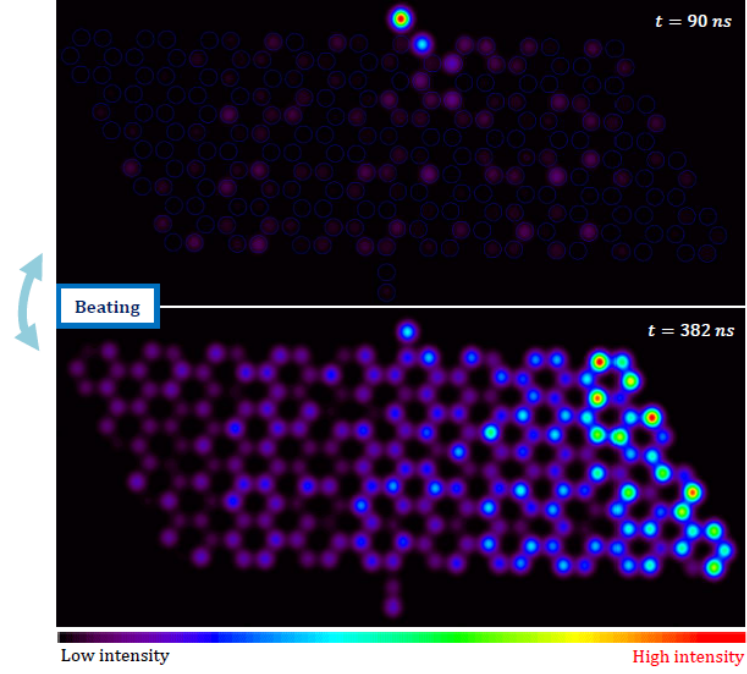
Figure 5.14: Switching behaviour for the single disc perturber measured in the experiment, obtained from [92].
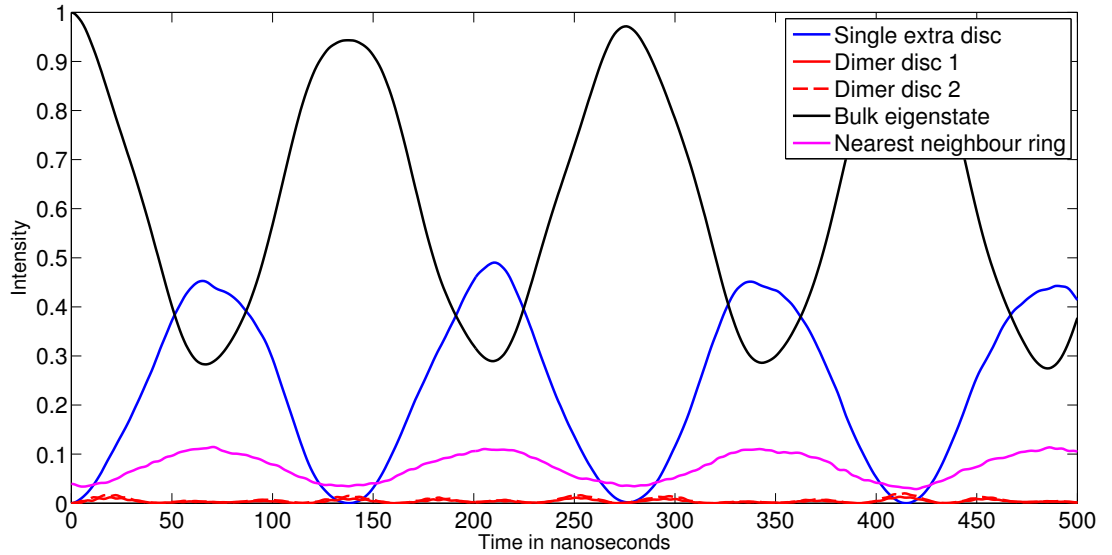
Figure 5.15: Numerically calculated time-evolution of the system using the first unperturbed eigenstate above the Dirac point as the initial state.
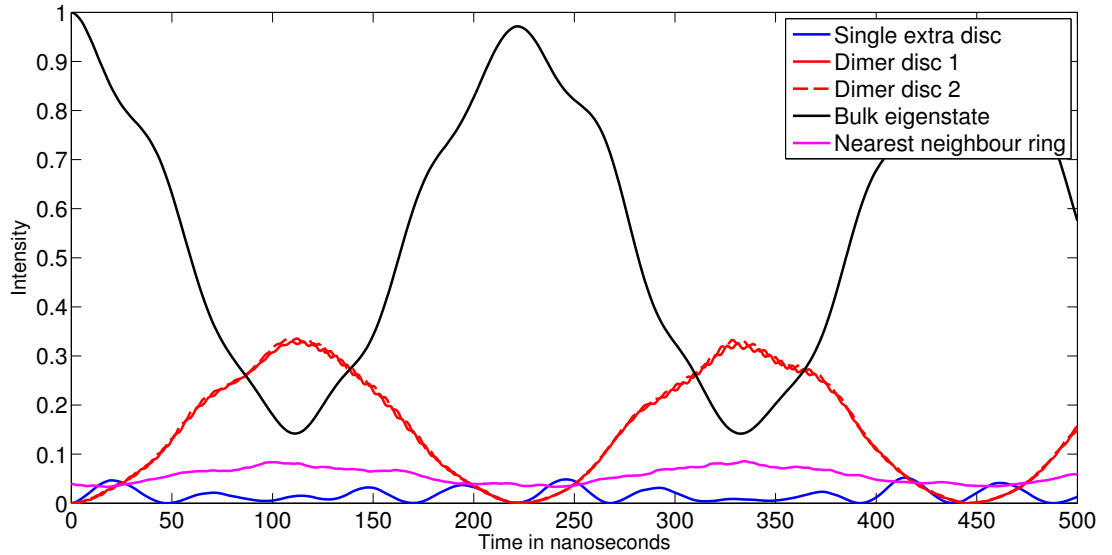
149
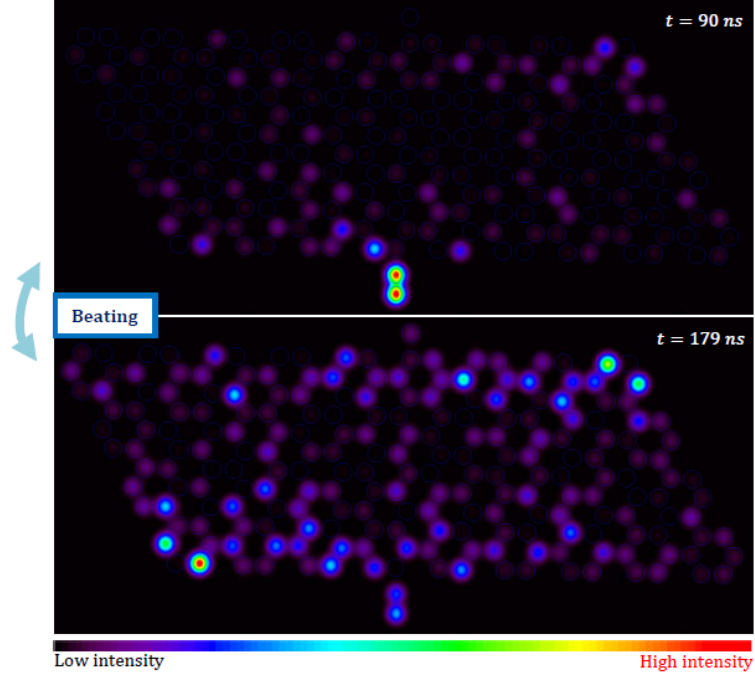
Figure 5.16: Switching behaviour for the dimer perturber measured in the experiment, obtained from [92].

Figure 5.17: Numerically calculated time-evolution of the system using the first unperturbed eigenstate below the Dirac point as the initial state.
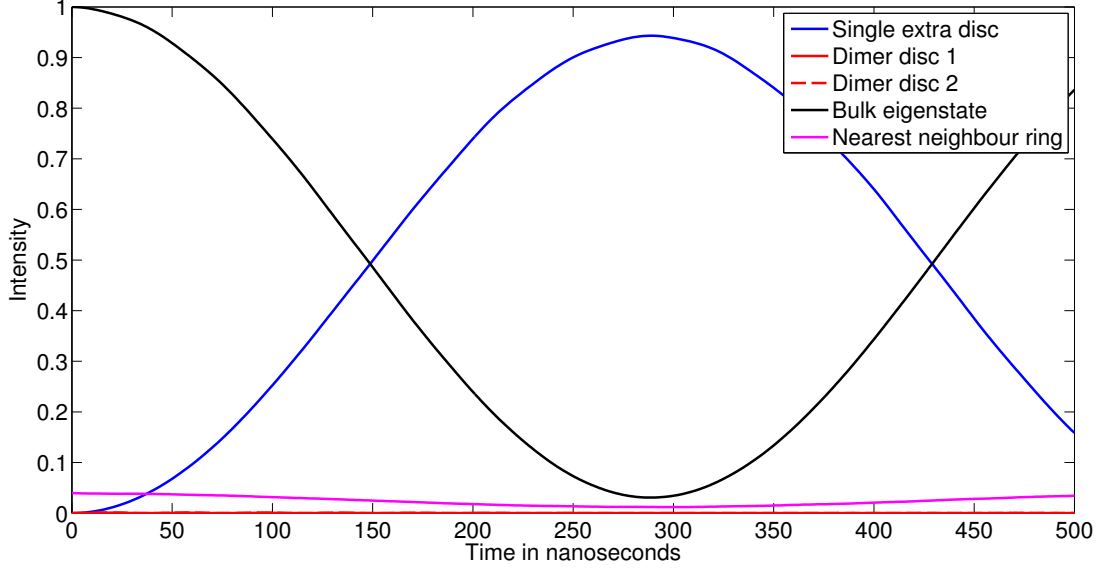
Figure 5.18: Numerically calculated time-evolution of the system using the first unperturbed eigenstate above the Dirac point as the initial state. This system uses a perturbation coupling strength which is 0.23 times the coupling strength used in Figures 5.15 & 5.17.

the unperturbed eigenstates and allowing it to evolve under the perturbed Hamiltonian. In order to simulate the experimental method we use as a starting state for our time-evolution superpositions of the two perturbed eigenstates involved in each of the switching dynamics, thereby neglecting interactions from other states in the spectrum. That is, we use an equal superposition of the two perturbed eigenstates below the Dirac point for the dimer case and an equal superposition of the two perturbed eigenstates above the Dirac point for the single perturber case.

We show our theoretical results for these two cases in Figures 5.19 & 5.20. The agreement is not improved and the behaviour is extremely similar to that described in the previous paragraph. We assume, therefore, that we are missing some element in our theoretical model and suppose that this feature is either a misunderstanding of the perturber coupling strengths or possibly the damping and losses which occur in the physical system.

Figure 5.19: Numerically calculated time-evolution of the system using the first perturbed eigenstate above the Dirac point as the initial state.
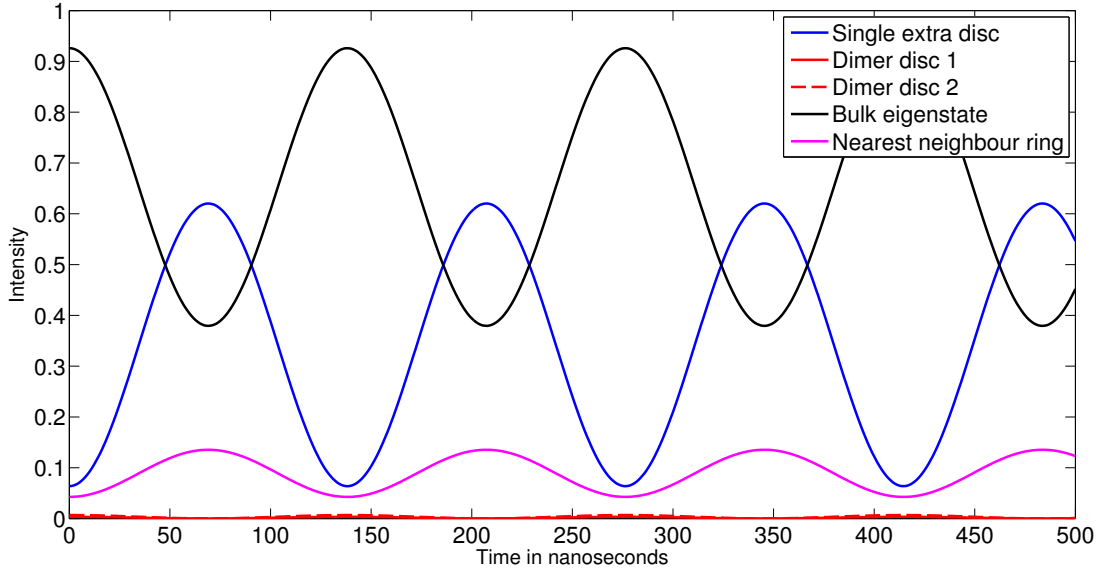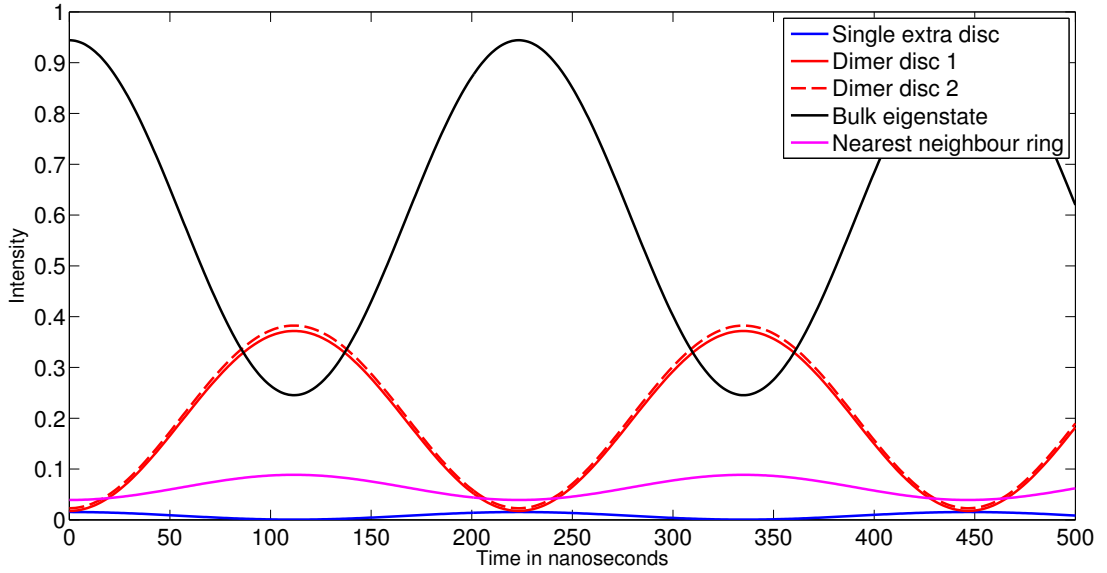

Figure 5.20: Numerically calculated time-evolution of the system using the first perturbed eigenstate below the Dirac point as the initial state.
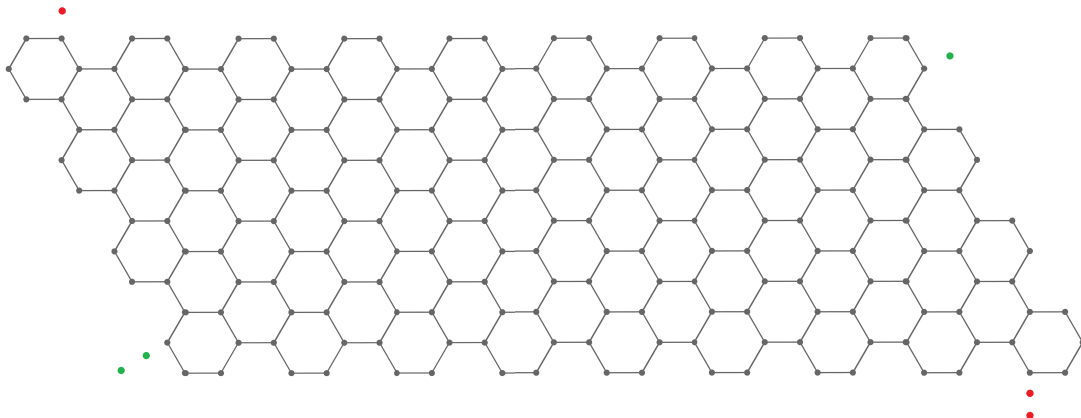
Figure 5.21: Alternative arrangements of perturber discs (coloured dots) alongside the original lattice of dielectric discs. Only one set of coloured discs is used at any one time.

5.4 Further simulation results

In this section we move from attempting to replicate experimental results presented in [92] to modelling potential alternative setups. We focus in particular on different positions of the perturbers, and, as an extension to this, channeling amplitude from one perturber to another.

5.4.1 Alternative switching arrangements

Our investigation of the effect of different perturber positions on the switching behaviour focuses on two setups, shown in Figure 5.21. In both of the setups we attempt to couple the perturbers to the same eigenstates as previously, shown in Figures 5.12 & 5.13, and keep the same single disc resonances and couplings. The first setup we choose places the perturbers near low intensity regions of the eigenstates we attempt to couple to, they are placed at the red points in Figure 5.21. In the second setup we choose positions where the perturbers are near to isolated points of high intensity, that is, at the green points in Figure 5.21. The choice of perturbation locations allows us to check how the system's behaviour relies on the coupling of the perturbers to their nearest-neighbours and also the neighbourhood around the nearest-neighbours.

We stress that when we model the dynamics of these systems only one pair of perturbers is coupled to the lattice, only either the red positioned perturbers or the green positioned perturbers.

The time-evolution for the perturbers coupled to low intensity regions is shown in Figures 5.22 & 5.23, that is, for the red points in Figure 5.21. As previously, when searching for the single perturber case we prepare the system in the first eigenstate above the Dirac point and when searching for the dimer perturber we prepare the system in the first eigenstate below the Dirac point. In both cases the system successfully localises on the perturber discs. However, when comparing these results with those of our models of the experimental setup in Figures 5.15 & 5.17, we see that the localisation intensities for both types of perturbation are reduced by a factor of roughly one half and the time taken for the first localisation takes approximately twice as long.

Figures 5.24 & 5.25 display the time-evolution for the perturbers placed near an isolated point of high intensity in the target eigenstates, the green points in Figure 5.21. For each perturber, we prepare the system in the necessary unperturbed eigenstate and allow it to evolve under the perturbed Hamiltonian. In these cases, our results are much closer to those of the original experimental setup in Figures 5.15 & 5.17 than the first alternative arrangement. The localisation intensities are very similar but we find that our new arrangement takes less time to reach peak localisation.

Thus, we find that we can modify the timescale not only by modifying the coupling strength of the perturbers to the lattice but also by where we couple to the lattice. Our results demonstrate that positioning a perturber so that it couples to a high intensity region, as in the previous section, leads to a faster and more successful search. This is perhaps not surprising, as the interaction between the target eigenstate and a perturber placed near a region of low intensity will be reduced, leading to the increased time taken to localise on the perturbation. However, we also find that placing a perturber by an isolated high intensity point results in faster localisation than placing it by a region of high intensity points, as in the original experimental setup. We suggest that, in the isolated high intensity point case, this is due to less interference effects near the perturber as the signal propagates, so that less amplitude destructively interferes and more amplitude makes its way to the perturber.

Interestingly, this improvement in localisation time with a reduction of highly intense points near to the perturbations may explain the dynamics of another alternative arrangement not shown here. In this setup the perturber discs were placed within the 'armchair' cavity at the edge, such that it was the same distance away from the four discs which form the 'armchair'. Placing a perturbation at one of these points means that it interacts with more discs than a perturbations outside the edge. For example, the previous perturbations would only interact with one lattice disc with
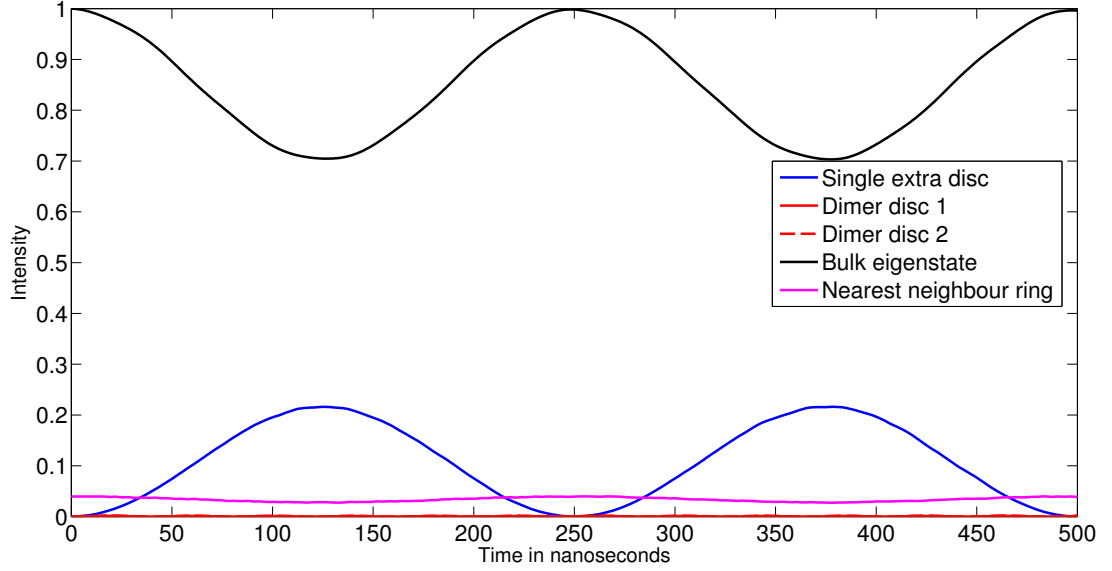
Figure 5.22: Numerically calculated time-evolution of the system using the first unperturbed eigenstate above the Dirac point as the initial state, where the perturbers are placed at the red points in Figure 5.21.
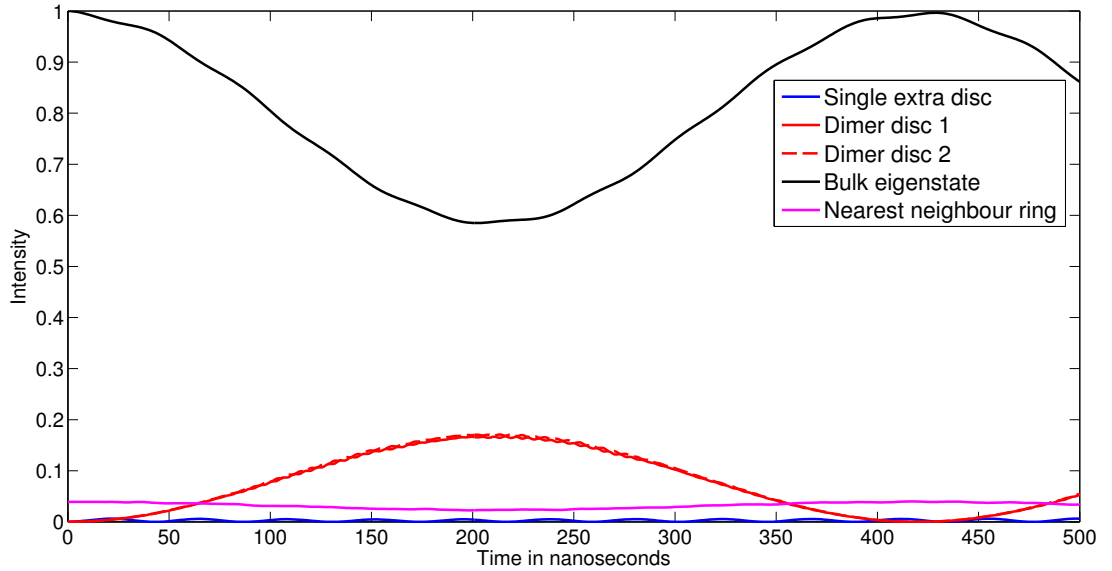
Figure 5.23: Numerically calculated time-evolution of the system using the first unperturbed eigenstate below the Dirac point as the initial state, where the perturbers are placed at the red points in Figure 5.21.

Figure 5.24: Numerically calculated time-evolution of the system using the first unperturbed eigenstate above the Dirac point as the initial state, where the perturbers are placed at the green points in Figure 5.21.
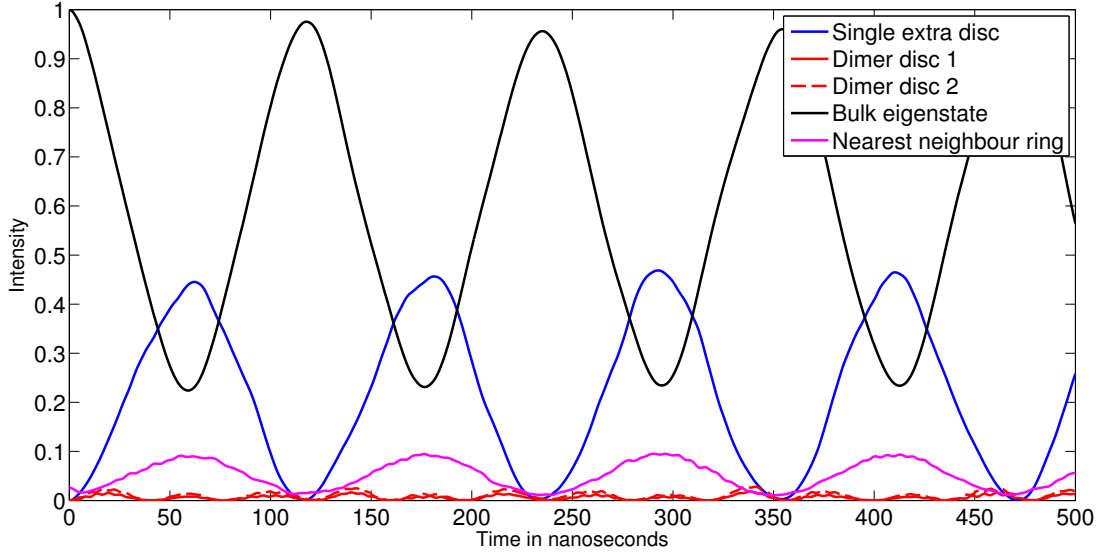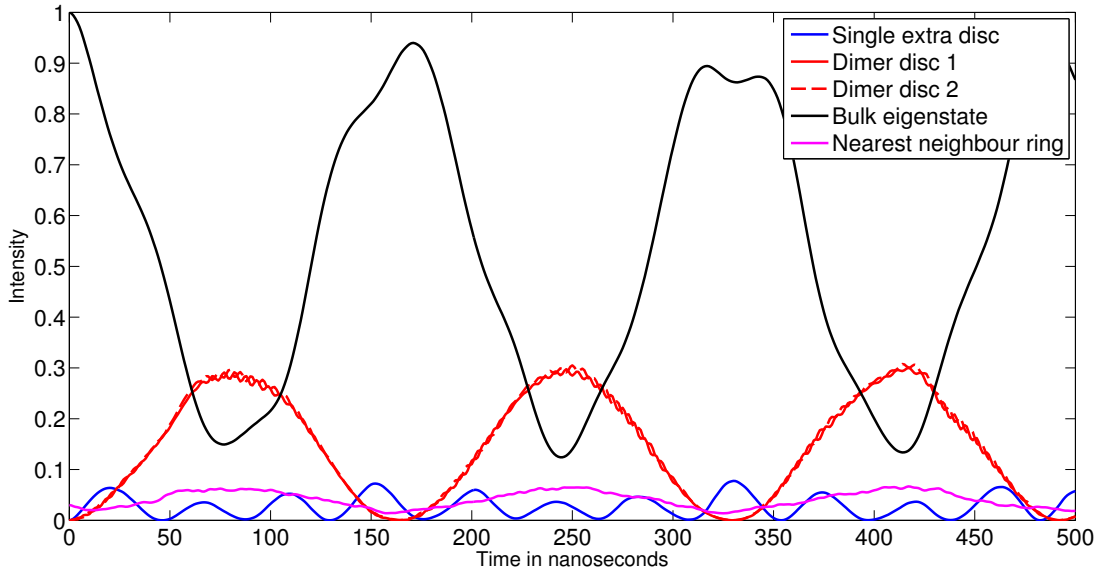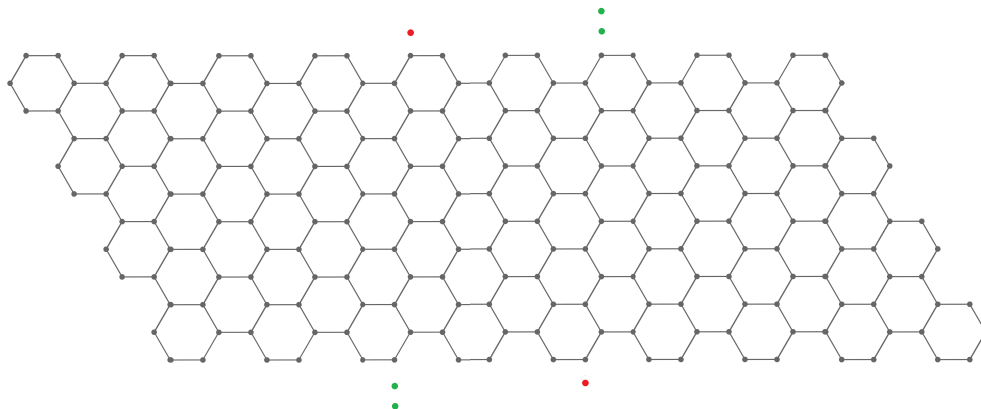

Figure 5.25: Numerically calculated time-evolution of the system using the first unperturbed eigenstate below the Dirac point as the initial state, where the perturbers are placed at the green points in Figure 5.21.

Figure 5.26: Setup of perturber discs (coloured dots) alongside the original lattice of dielectric discs for directed transport protocol. Both sets of coloured discs are coupled to the lattice at the same time.

nearest-neighbour t_1 coupling whereas an inner perturbation would interact with four lattice discs at this coupling strength. Using these types of perturbation arrangements it proved difficult to force the system to localise with significant probability in a short timescale. Again, we believe that the nature of the coupling to many discs creates much destructive interference, destroying any localisation effect.

5.4.2 Channelling between perturbations

We now turn to transport between perturbers coupled to the same eigenstate. Our aim is to transfer signal between two perturbations and then change to transferring signal between two different perturbations. In what follows, we only attempt to communicate between two perturbers of the same type, that is, either between two dimers or between two single disc perturbers.

We first check that it is possible for transport to occur between just two perturbers coupled to the same eigenstate before attempting to couple four perturbers to the lattice. The location of the perturbers for our initial checks are the same as in the experimental setup, shown in Figure 5.2. We couple two dimer perturbations to the first eigenstate below the Dirac point and in a different model there are two single perturber discs coupled to the eigenstate above the Dirac point. The system is then prepared in a state localised on one perturber and allowed to evolve in time. The initial state localised on the dimer is the antisymmetric equal superposition. Our results are shown in Figures 5.27 & 5.28. We see that one can successfully transfer signal from one

perturber to another, coupling the two via the bulk eigenstate. The localisation effect is stronger for the dimer case than it is for the single perturber case but the localised intensity for both cases is greater than 0.5. We also note preparing the system in one of the bulk eigenstates to which the perturbations are coupled, one can search for both of the perturbations which are coupled to that eigenstate at the same time, with the localised intensity split evenly between the two.

Having established that a transfer protocol is possible, we now investigate the addition of four perturbers to the original lattice, two single disc perturbers and two dimer perturbers, in the positions shown in Figure 5.26. Our aim is to transfer signal only between perturbers of the same type, which are coupled to the same eigenstate, by preparing the system in a localised state on one of the perturbers and allowing the system to evolve in time.

Figures 5.29 & 5.30 show the results and we find that directed transport between two specific perturbers can be achieved. When focusing on the first localisation at the target perturber, one finds for the dimer perturber case the localisation intensity and the time taken for localisation are comparable to the situation where there were only two dimers coupled to the lattice. For the single disc perturbers, though, we find a reduction of around $25-30\%$ in the intensity at the target perturbation and an increase of approximately 40% in the length of time taken for this localisation on comparison with when there were only two single disc perturbers coupled to the lattice. However, the intensity at the target perturber is still significant and the timescale is comparable with the transport between the dimers.

The increase in the length of time taken for localisation on the single perturbers is consistent with our previous results where we manipulate the localisation time by moving the perturbers; the perturbers have been moved to regions of lower intensity of the coupled eigenstates and, thus, we expect the localisation time to increase.

It is important to note that there is only an increase in intensity at the two desired perturbers in each case, the perturbations of the other type remain uninvolved in the dynamics. Within this setup we see that we can excite specific multiple perturbations using a single bulk state and also target individual perturbations across the lattice. Both of these results imply that one may be able channel signal from one perturbation to several others which are coupled to the same eigenstate, where one input controls many outputs. Due to the variability in behaviour of this system with perturbation position we do not attempt it here, as differing localisation times are likely to introduce interference which will affect the dynamics.
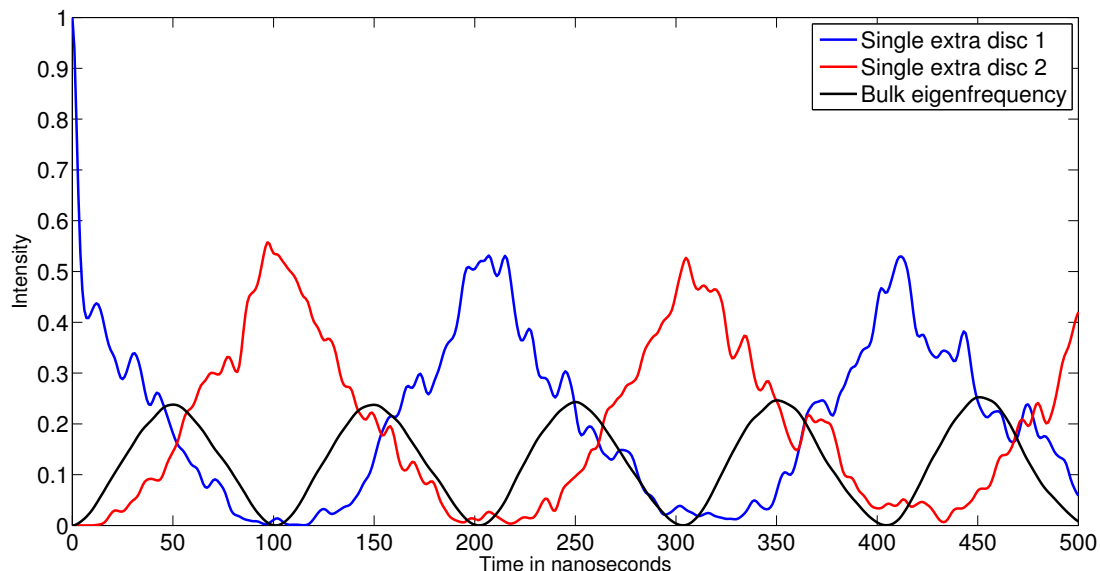
Figure 5.27: Numerically calculated time-evolution of the lattice with two single discs coupled to the lattice. The system is prepared in a state localised on one of the extra discs.
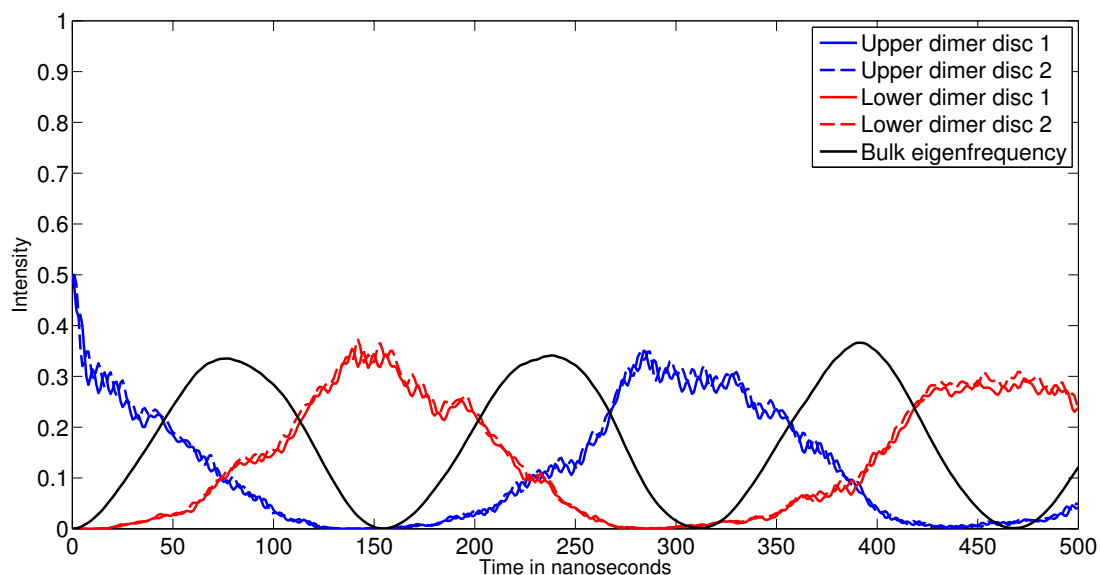
Figure 5.28: Numerically calculated time-evolution of the lattice with two dimers coupled to the lattice. The system is prepared in a state localised on one of the dimers.
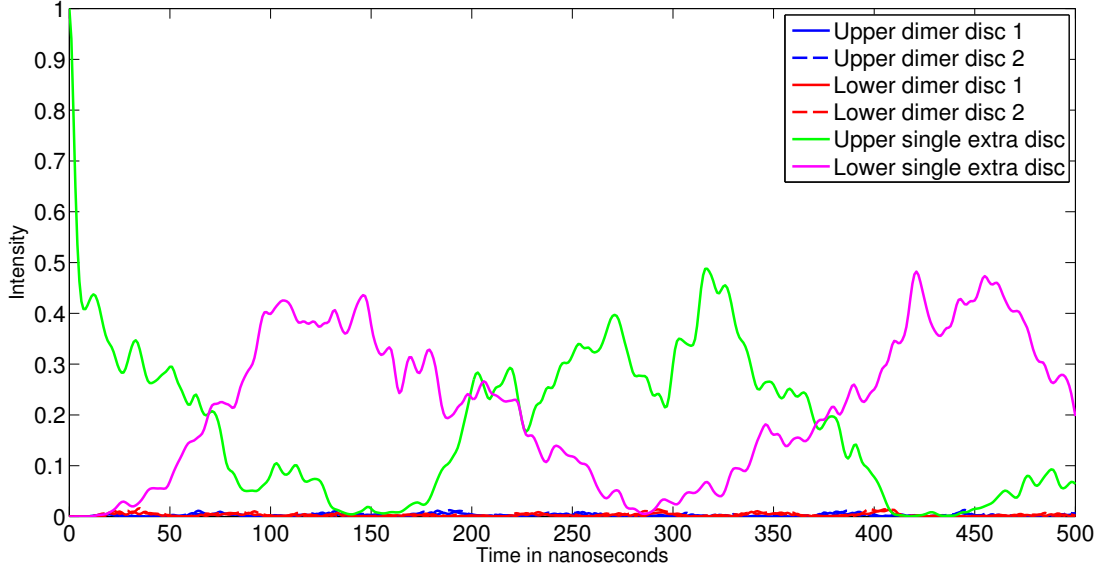
Figure 5.29: Numerically calculated time-evolution of the system shown in Figure 5.26. The system is prepared in a state localised on the one of the single disc perturbations.
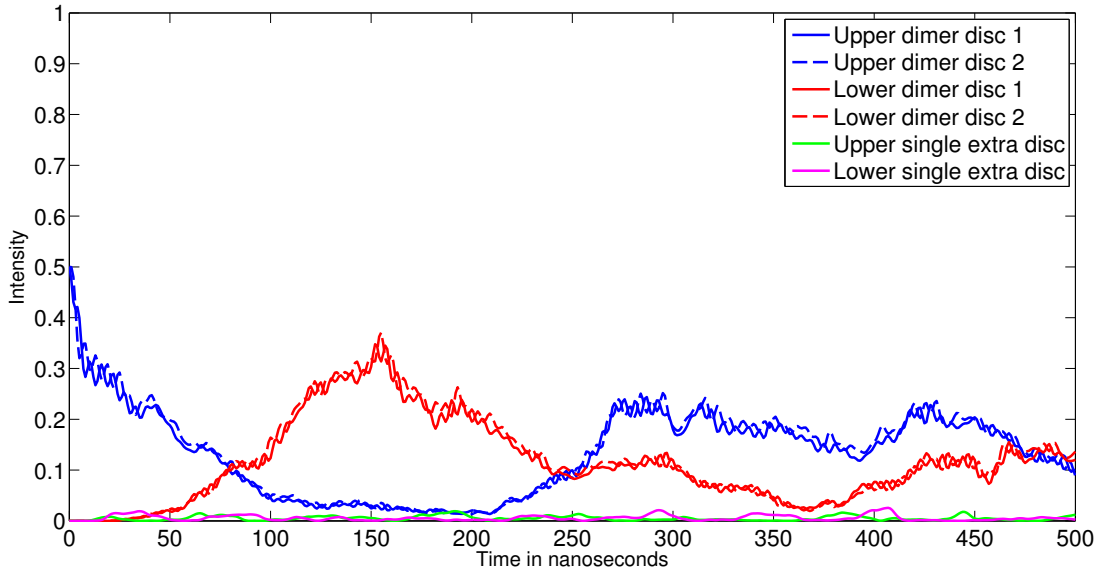
Figure 5.30: Numerically calculated time-evolution of the system shown in Figure 5.26. The system is prepared in a state localised on the one of the dimers.

5.4.3 Lattice scaling

We complete this section by considering the effect of increasing the size of the lattice. As described in Section 3.1, the timescale for the dynamics we are interested in is inversely proportional to the spectral gap between the two perturbed eigenstates involved. Therefore, inspecting how this spectral gap scales as the lattice is increased gives a good indication of the timescales involved for any searching/switching dynamics on the lattice.

We return to the experimental setup in Section 5.2, where there is just one single disc perturber and one dimer perturber. The initial parameters for the perturbers which used for the original lattice consisting of 216 discs are $(\nu_o, t_{1'}, t_{2'}, t_{3'}) = (6.639\text{GHz}, 0.4\text{GHz}, 0.1t_{1'}, 0.05t_{1'})$ for the single disc perturber and $(\nu_o, t_{1'}, t_{2'}, t_{3'}, t_d) = (6.7\text{GHz}, 0.4\text{GHz}, 0.1t_{1'}, 0.05t_{1'}, 0.0874\text{GHz})$ for the dimer disc perturber.

However, these parameters, in particular the single disc perturber resonance ν_o and the internal dimer coupling t_d, are chosen for this specific lattice so that they couple with the desired eigenstates. As the lattice is increased the eigenfrequencies will change and, therefore, the perturbers will no longer be efficiently coupled to the states either side of the Dirac point. Consequently, as the lattice is increased we modify the necessary parameters so that the perturbers couple to the new eigenstates. Namely, for each lattice size, we change the single disc perturber resonance ν_o to match the eigenfrequency above the Dirac point and the internal dimer coupling t_d is chosen such that the lower dimer resonance matches the eigenfrequency below the Dirac point.

As the lattice is increased we numerically calculate the spectrum of the unperturbed Hamiltonian (that is, with no perturbations), modify the parameters of the perturbers and then calculate the spectrum of the perturbed Hamiltonian where the perturbations have been added. In Figure 5.31 the spectral gap between the two perturbed eigenstates above (corresponding to the single perturber) and also for the two below the Dirac point (corresponding to the dimer perturber) are plotted. Also plotted are the best-fitting $N^{-\frac{1}{2}}$ and $(N \ln N)^{-\frac{1}{2}}$ curves.

Both types of fit have coefficients of determination R^2 above 0.998, implying they are good fits to the data, however, inspecting the plots visually it appears the $N^{-\frac{1}{2}}$ fit is a slightly better fit for smaller N. This may seem at first glance to imply that we have found a way of removing logarithmic corrections to the running time for a two-dimensional lattice but one must keep in mind that it is the asymptotic behaviour which we are interested in, where it is difficult to see a difference, and we are most likely missing corrective terms to our fits. However, it is clear the resonance splitting has a
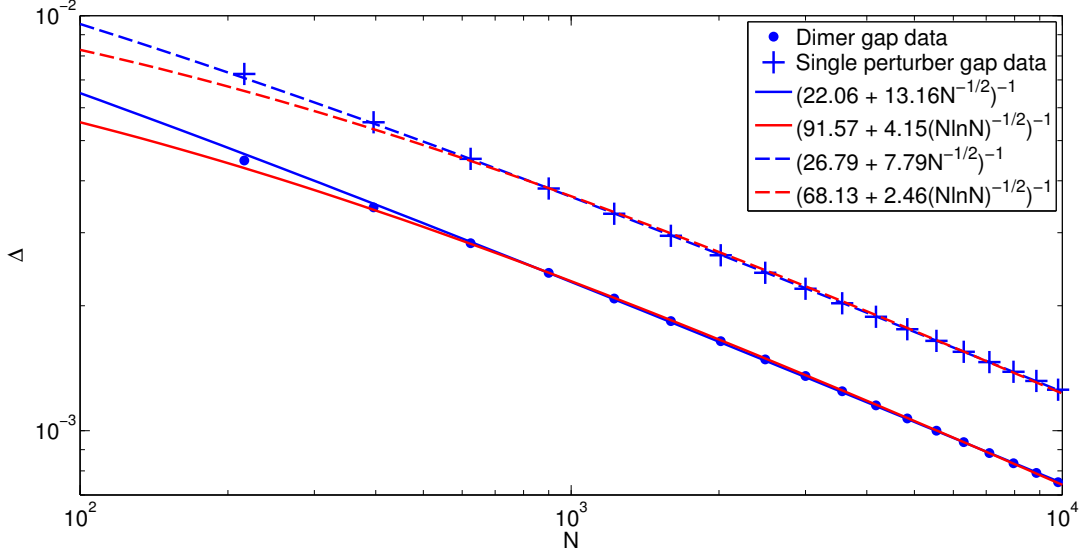
Figure 5.31: Numerically calculated spectral gap between the two eigenfrequencies below the Dirac point and also the two eigenfrequencies above the Dirac point. Also included are the best-fit $N^{-\frac{1}{2}}$ and $(N \ln N)^{-\frac{1}{2}}$ curves for comparison with the data.

leading-order of $\mathcal{O}\left(N^{-\frac{1}{2}}\right)$, implying the timescales of the dynamics and any search using this system will succeed faster than the classical time $T = \mathcal{O}(N)$.

6

Conclusions

We have developed a new continuous-time quantum walk search algorithm on a two-dimensional lattice, namely a graphene lattice. The running time and success probability of the algorithm are calculated. By modifying the search algorithm one can construct a communication protocol where signal is transferred between two perturbations on the lattice. Alternative methods of creating search algorithms on graphene lattices have been considered, as well as the development of search algorithms on different carbon structures. We also numerically model a set of microwave resonator experiments which study setups analogous to graphene and present some possible extensions to these experiments.

Our search mechanism is constructed by an avoided crossing involving a localised perturber state and an eigenstate of the unperturbed graphene Hamiltonian. The search dynamics then arises from oscillations between the two eigenstates of the search Hamiltonian which are a superposition of the localised perturber state and unperturbed eigenstates. The critical feature of our quantum walk search on graphene is the conical dispersion relation in the electronic spectrum of graphene. It is this feature which prevents the perturber state interacting with many unperturbed eigenstates and keeps the avoided crossing isolated in the spectrum.

We find that the by marking a state through changing its coupling strength to its nearest neighbours one can force a localised perturber state to interact with states in the conical regime of the spectrum. Through setting the nearest-neighbour coupling of a particular vertex on a graphene torus to zero, effectively removing it from the lattice, one can create a search algorithm which evolves from a superposition of the unperturbed eigenstates which lie at the Dirac energy to a state localised on the target

vertex's nearest-neighbours. We first describe this behaviour by modelling the system in a 3×3 reduced Hamiltonian matrix before further analysing the search behaviour by analysing the full search Hamiltonian spectrum using similar methods to those found in [20]. This leads to us finding that the algorithm succeeds in a time $T = \mathcal{O}\left(\sqrt{N \ln N}\right)$ with probability $\mathcal{O}\left(1/\ln N\right)$.

We find that the search mechanism persists when random superpositions of the Dirac states or even other states from the conical regime of the spectrum are used as initial states. By introducing another perturbation of the same type, we find also that one can transfer signal between the neighbours of the two perturbed sites in a time of the same order as the search time. Crucial to both the search and the communication are different phases within the eigenstates which the perturbations are coupled to as these can modify the behaviour. For graphene tori where there exist Dirac eigenstates, there are six different choices of optimal superpositions of the Dirac eigenstates for initial starting states, three for perturbations to each sublattice, due to the repetition of phases within the Dirac states. When transferring signal across the lattice, we also characterise several different communication behaviours depending on whether the source and target perturbations are on different sublattices and also whether they share an optimal starting state.

We have also demonstrated that other perturbation types may be used to create search protocols, for example, changing only the coupling from a marked vertex to one nearest-neighbour. A search using this type of perturbation may be viewed as marking a primitive cell of the graphene lattice since both vertices involved are perturbed in the same way. If one loses the restriction of working with only the underlying lattice, it has been demonstrated searches can be developed using an additional vertex placed atop the lattice, coupled to one or more vertices of the underlying lattice. Communication using one of these additional vertex setups has also been shown to be possible, demonstrating similar behaviour to that found for communication cases involving three-bond perturbations.

While most of the cases we consider take place on graphene tori, it has been shown that placing perturbations on different carbon structures, namely armchair nanotubes and graphene sheets, does not destroy the effects but does introduce some subtleties into the behaviour. The proximity of a perturbation to an armchair edge of one of these structures does affect the signal pattern of search behaviour but the localisation effect does remain. Negative effects do arise when the perturbation is positioned on a nodal point of an armchair nanotube or near a non-armchair edge of a graphene sheet

and searches at these sites are not possible.

Some numerical modelling of a set of experimental results for a microwave analogue of graphene are also included, where we adapt previous models to include next-nearest and next-next-nearest neighbours. This model successfully replicates the qualitative features of the spectra of the experiment as well as the propagation of a pulse across the lattice. The numerical results also include modelling of switching behaviour where two different perturbations are coupled to different eigenstates, resulting in localisation on one of the perturbers only when a certain eigenfrequency is excited. Using our theoretical model, different perturbation setups were compared which showed that the position of the perturbers in relation to the high or low intensity regions of the eigenstates we couple to has a significant effect on the search dynamics. Further numerics demonstrated directed transport between different perturbers coupled to the microwave lattice should be possible and that the scaling of the resonance splitting, inversely proportional to the timescale for search dynamics, implies a speed-up over classical search dynamics will remain as the system size is increased.

Several aspects of this work could be continued further. For example, a more detailed theoretical treatment of the single-bond perturbation search and its relation to the Dirac Hamiltonian search in [21] would be interesting to pursue. As well as the single-bond perturbation search, further theoretical analysis of the communication protocol, specifically classification of different behaviours in signal transfer between sublattices, would be useful. One potential application is the transport of signals or current at a single atomic level and it is for this reason further analysis of the communication would be interesting to pursue.

Related to this is the directed transport between perturbers in the microwave experiment setup and it would be interesting to drive both of these arrangements with continuous-signal to simulate the application of current to the lattices. The introduction of spin to these systems would be a further development to these signal transfer cases, as the transport of qubits across graphene lattices would be an intriguing development.

As described in Chapter 2, research into quantum walk search algorithms has mostly involved walks across regular lattices. It would be a useful line of research to investigate the propagation of walks across generic or random graphs, due to the possibility of establishing the relationship of the valency of vertices or the role of symmetry on the dispersion time of walks. While it almost certainly true that most physical implementations of quantum walks would occur in crystalline, and therefore regular, structures, from an information theory point of view being able to search databases or networks

which develop naturally without such structure would advantageous.

Possibly related to this is the transport of energy in biological organisms where photosynthetic systems appear to utilise quantum mechanical wave interference effects for exciton transfer [96, 97]. It would be interesting to see whether ideas and techniques used in quantum searches could help explain the behaviour of these biological systems. While there is some debate over whether the organisms already considered, namely light-harvesting bacteria, truly utilise quantum behaviour, analysis of more complex plant forms may provide further insight into the use of quantum mechanics in biology and, conversely, could offer new ideas on how quantum walks on disordered networks could be used effectively.

Recently, Childs & Ge [98] published work with similar ideas to those found here. In their paper they develop a general approach for constructing lattice Hamiltonians in $d \geq 2$ dimensions which have Dirac points in their spectra. This is achieved by generating lattices with multiple sites per cell, such as graphene lattices. Through developing their general approach they detail criteria to determine whether an on-site perturbation to a vertex or a complete decoupling of the vertex from a particular lattice type is a more effective method of marking. It would be interesting to see if these criteria could be extended to include other perturbation types, as mentioned in Chapter 4, and check whether they are more effective than other methods of marking a vertex or if any successful marking of a vertex results in the same search time and success probability.

It also remains to be seen whether searches on two-dimensional lattices can lose their logarithmic factor in the running time and achieve the optimal search time $T = \mathcal{O}\left(\sqrt{N}\right)$ obtained by Grover's search algorithm. In light of the explanation of both continuous- and discrete-time quantum walk search algorithms given at the start of Chapter 3 and previous results described in Chapter 2, we do not believe this would be possible, at least not in any physical system, unless one could employ a search Hamiltonian with a sub-linear dispersion relation.

Appendix A

Derivation of further I_{2n} estimates

Here we derive the leading order behaviour of the sums I_2 and I_{2n} described in Equation (3.63) in SubSection 3.3.2, and compare our calculated behaviour with the numerically evaluated summations.

We start from the I_{2n} sum written in terms of the momenta quantum numbers p, q

$$I_{2n} = \frac{2\sqrt{3}N^{n-1}}{(8\pi^2)^n} \left[\sideset{}{'}\sum_{(p,q)\in L} \frac{1}{(p^2+q^2-pq)^n} + \sideset{}{'}\sum_{(p,q)\in L'} \frac{1}{(p^2+q^2-pq)^n} \right] + \mathcal{O}(1) , \quad \text{(A.1)}$$

where the region of summation L is spanned by

$$\begin{aligned} p &\in \{-\frac{\sqrt{N}}{3}, -\frac{\sqrt{N}}{3}+1, \ldots \frac{2\sqrt{N}}{3}-1\} \\ q &\in \{-\frac{2\sqrt{N}}{3}, -\frac{2\sqrt{N}}{3}+1, \ldots \frac{\sqrt{N}}{3}-1\}, \end{aligned} \quad \text{(A.2)}$$

and L' by

$$\begin{aligned} p &\in \{-\frac{2\sqrt{N}}{3}, -\frac{2\sqrt{N}}{3}+1, \ldots \frac{\sqrt{N}}{3}-1\} \\ q &\in \{-\frac{\sqrt{N}}{3}, -\frac{\sqrt{N}}{3}+1, \ldots \frac{2\sqrt{N}}{3}-1\}. \end{aligned} \quad \text{(A.3)}$$

It can be seen from both of these regions that the maximum absolute value of p or q is

$\frac{2\sqrt{N}}{3}$. We then deform the region of summation for both sums so that the maximum is the same in both p and q so that we deal with just the one summation

$$I_{2n} = \frac{4\sqrt{3}}{(8\pi^2)^n} N^{n-1} \sum_{(p,q)=-\frac{2\sqrt{N}}{3}}^{\frac{2\sqrt{N}}{3}} \frac{1}{(p^2 + q^2 - pq)^n} + \mathcal{O}(1). \tag{A.4}$$

By making use of the Poisson summation formula

$$\sum_{x=n}^{N} f(x) = \sum_{k=-\infty}^{\infty} \int_{n}^{N} f(x') e^{i2\pi x' k} dx', \tag{A.5}$$

the summation can be transformed into an integral over the same region. As well as applying the Poisson summation formula, we make the conversion to polar coordinates $(p,q) \to (r,\theta)$, so that $p \equiv r\cos\theta$ and $q \equiv r\sin\theta$.

Through deforming the area of the original summation and the conversion to polar coordinates, we induce an error from an overestimate (underestimate) at the lower (upper) boundary. However, our new limits depend in the same way as the original summation limits on N and so we must capture the same asymptotic behaviour, creating only an $\mathcal{O}(1)$ error.

These approximations and transformations result in

$$I_{2n} \approx \frac{4\sqrt{3}}{(8\pi^2)^n} N^{n-1} \sum_{k_1,k_2=-\infty}^{\infty} \int_0^{2\pi} \int_1^{\frac{2\sqrt{N}}{3}} \frac{e^{i2\pi(k_1\cos\theta + k_2\sin\theta)r}}{r^{2n}\left(1 - \frac{1}{2}\sin 2\theta\right)^n} r\, dr\, d\theta. \tag{A.6}$$

We proceed by rescaling the radial coordinate integral and changing variables to $\rho \equiv \frac{r}{\sqrt{N}}$

$$I_{2n} \approx \frac{4\sqrt{3}}{(8\pi^2)^n} \sum_{k_1,k_2=-\infty}^{\infty} \int_0^{2\pi} \int_{\frac{1}{\sqrt{N}}}^{\frac{2}{3}} \frac{e^{i2\pi(k_1\cos\theta + k_2\sin\theta)\rho\sqrt{N}}}{\rho^{2n-1}\left(1 - \frac{1}{2}\sin 2\theta\right)^n} d\rho\, d\theta, \tag{A.7}$$

thereby changing the limits of integration and removing the factor of N^{n-1} in front of the summation over the Poisson indices.

We then calculate the leading order behaviour for each I_{2n}, that is, the single term where $k_1 = k_2 = 0$, and split the I_{2n} sums into the cases where $n = 1$ and $n > 1$.

Focusing on the $n = 1$ or I_2 case, we obtain

$$I_2 \approx \frac{4\sqrt{3}}{8\pi^2} \int_0^{2\pi} \frac{d\theta}{1 - \frac{1}{2}\sin 2\theta} \int_{\frac{1}{\sqrt{N}}}^{\frac{2}{3}} \frac{d\rho}{\rho} \tag{A.8}$$

$$= \frac{4\sqrt{3}}{8\pi^2} \frac{4\pi}{\sqrt{3}} \left[\ln \rho \right]_{\frac{1}{\sqrt{N}}}^{\frac{2}{3}} \tag{A.9}$$

$$= \frac{2}{\pi} \left(\frac{1}{2} \ln N + \ln \left(\frac{2}{3} \right) \right) \tag{A.10}$$

$$= \mathcal{O} \left(\ln N \right) . \tag{A.11}$$

For the $n > 1$ cases we find

$$I_{2n} \approx \frac{4\sqrt{3}}{(8\pi^2)^n} \int_0^{2\pi} \frac{d\theta}{\left(1 - \frac{1}{2} \sin 2\theta \right)^n} \int_{\frac{1}{\sqrt{N}}}^{\frac{2}{3}} \rho^{1-2n} d\rho \tag{A.12}$$

$$= \frac{4\sqrt{3}}{(8\pi^2)^n} J_n \left[\frac{1}{2 - 2n} \rho^{2-2n} \right]_{\frac{1}{\sqrt{N}}}^{\frac{2}{3}} \tag{A.13}$$

$$= \frac{4\sqrt{3}}{(8\pi^2)^n} J_n \frac{1}{2n - 2} \left(N^{n-1} - \left(\frac{2}{3} \right)^{2-2n} \right) \tag{A.14}$$

$$= \mathcal{O} \left(N^{n-1} \right) \tag{A.15}$$

where the function J_n is the angular coordinate integral which does not depend on N and, therefore, will just be some finite number.

In Figure A.1 we show the numerically calculated I_{2n} functions for $n = 1, 2, 3$ and we also plot the leading order behaviour we have just calculated. We see that the general form of the data points and the theoretical curves is similar, however, there is some difference in the exact values. We show in Figure A.2 the same numerically calculated I_{2n} functions along with the best-fit curves and the residuals between the data and the fit. The coefficient of determination R^2 for all of the best-fit curves is greater than 0.9998, implying that they are a good match for the data. The leading-order prefactors we obtain through our best-fit curves and also from the calculations in Equations A.10 & A.14 are shown in the tables below, as well as the error when comparing the two sets of prefactors:

	Best-fit	Theoretical	Absolute error	Percentage error
I_2	0.3245	0.3183	6.2×10^{-3}	1.9%
I_4	0.0086	0.0054	3.2×10^{-3}	37.5%
I_6	8.97×10^{-5}	5.11×10^{-5}	3.86×10^{-5}	43%

We see from the table that the calculated prefactors and those obtained through numerical fitting procedures are of the same order and, looking at the absolute error,

the discrepancy is not large. The percentage error demonstrates that the agreement with the calculated prefactors becomes worse as we look at I_{2n} with larger n values but the prefactors do retain the correct order.

The agreement may be improved with the inclusion of next-leading order terms to the calculated behaviour, which would require the evaluation of the rest of the Poisson summation in Equation A.7, as we may have assumed the wrong model for the best-fit procedure. An incorrect assumption for the best-fit procedure would lead to a comparison of two different models. For example, it may not be the case that the I_6 summation is of the form $ax^2 + bx + c$ but rather $ax^2 + c$, which would lead to the best-fit and calculated leading-order prefactors not agreeing. This line of thinking would also explain the much smaller percentage error for the I_2 summation than the other two summations if we have the correct model for the I_2 summation and not the other two. However, we are only interested in the leading-order behaviour and, from inspecting Figure A.1, it can be seen that our calculated behaviour matches the growth of the I_{2n} summations.
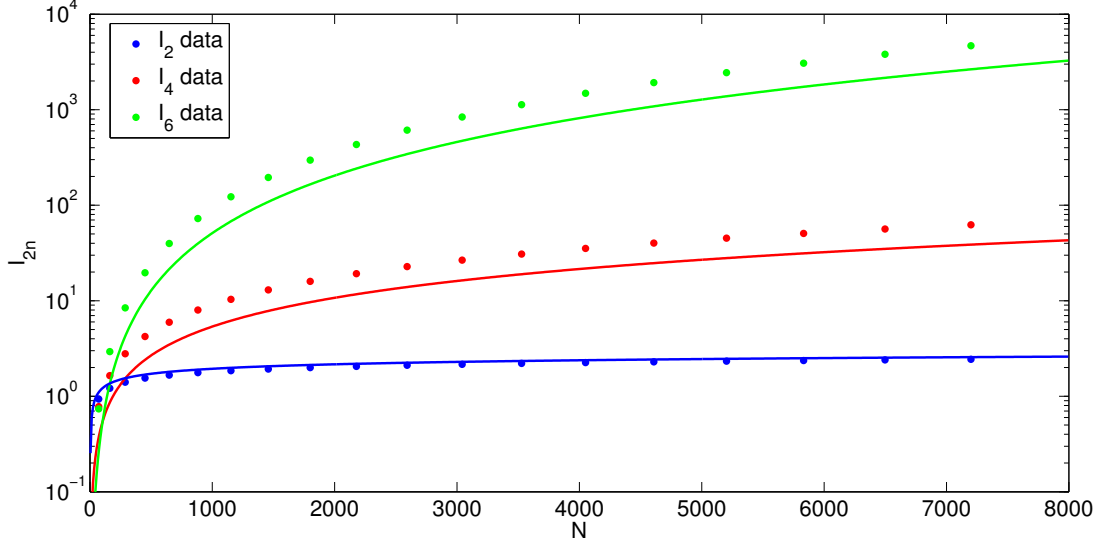
Figure A.1: Plot of the numerically calculated I_{2n} functions for $n = 1, 2, 3$. Also included is the leading order behaviour taken from Equations A.10 & A.14.
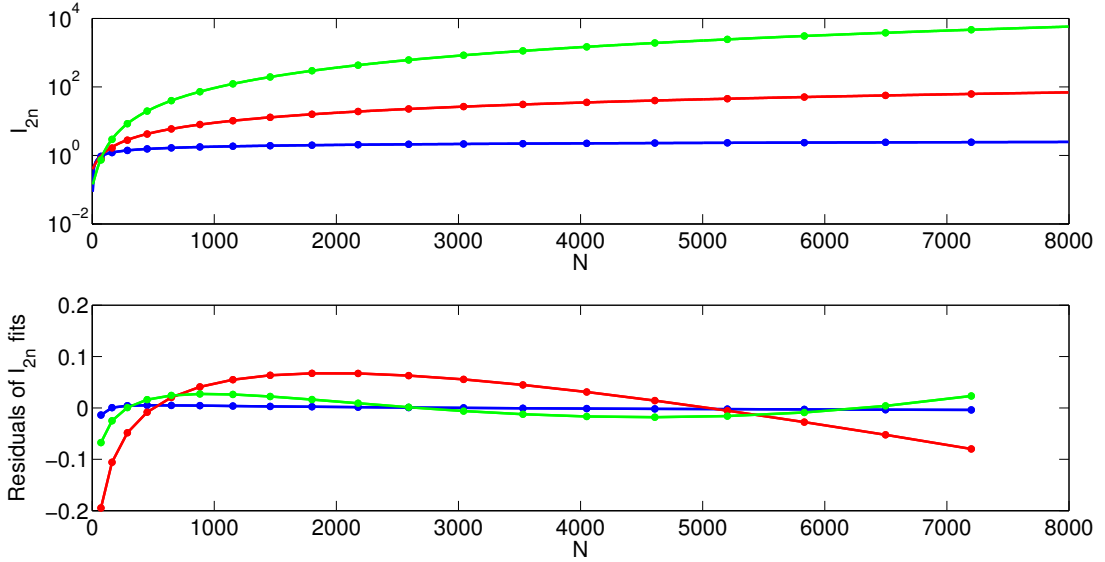
Figure A.2: Plots of the numerically calculated I_2, I_4 & I_6 functions and the best-fit curves including the residuals. The blue curves and points correspond to the I_2 data and the best-fit curve $y = 0.3245 \ln N - 0.4330$. The red curves and points correspond to the I_4 data and the best-fit curve $y = 0.0086N + 0.3521$. The green curves and points correspond to the I_2 data and the best-fit curve $y = 8.97 \times 10^{-5} x^2 + 0.0030x + 0.1255$.

Appendix B

Further examples of communication between different sublattices

This appendix includes additional examples of signal transfer between perturbations on different sublattices, as described in SubSection 3.5.3. All of these examples share the same source state but have different target vertices. Only included are the distinct transport behaviours found on a 12×12 cell torus. Figures B.3 & B.3 look very similar but do, in fact, have slightly different periods.
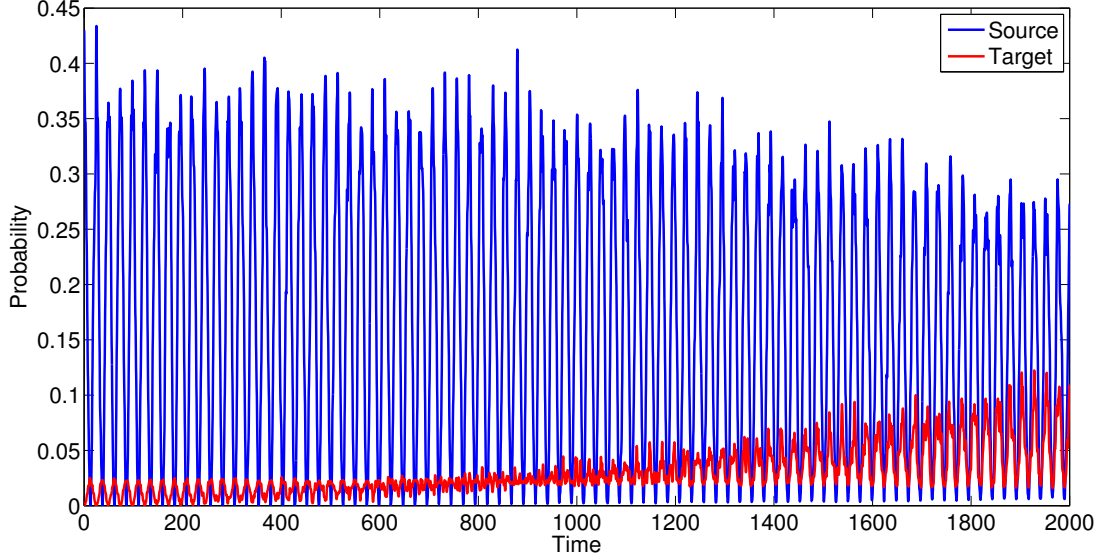
Figure B.1: Numerically calculated signal transfer on a 12×12 cell graphene lattice between vertices on different sublattices, using the communication Hamiltonian in Equation (3.110). The system is initialised in $|\ell_s\rangle$ and localises on $|\ell_t\rangle$. Only the sum of probabilities to be found on the neighbour vertices is shown.
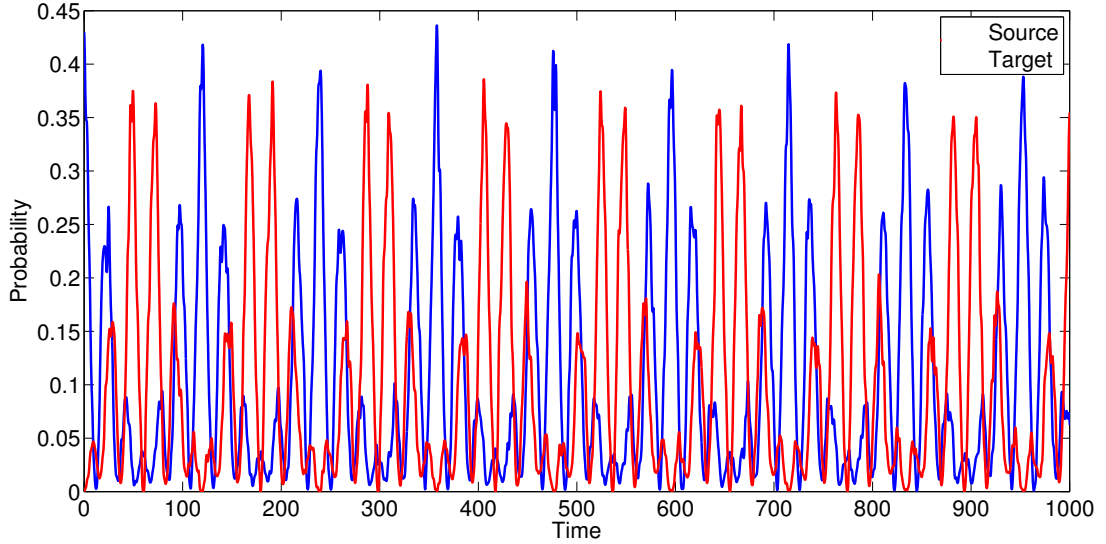
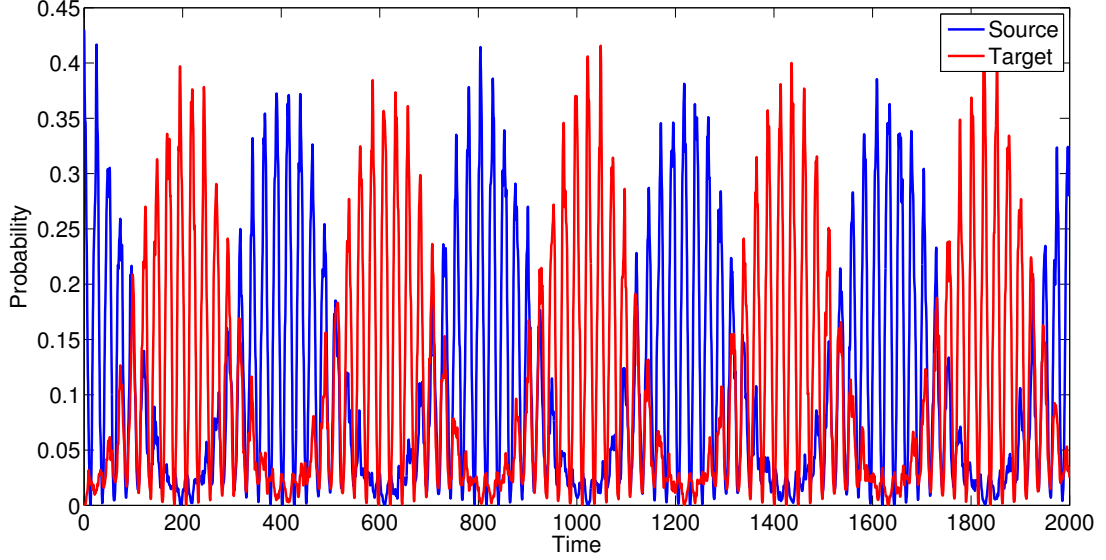**Figure B.2:** Numerically calculated signal transfer on a 12×12 cell graphene lattice between vertices on different sublattices, using the communication Hamiltonian in Equation (3.110). The system is initialised in $|\ell_s\rangle$ and localises on $|\ell_t\rangle$. Only the sum of probabilities to be found on the neighbour vertices is shown.

173

Figure B.3: Numerically calculated signal transfer on a 12×12 cell graphene lattice between vertices on different sublattices, using the communication Hamiltonian in Equation (3.110). The system is initialised in $|\ell_s\rangle$ and localises on $|\ell_t\rangle$. Only the sum of probabilities to be found on the neighbour vertices is shown.
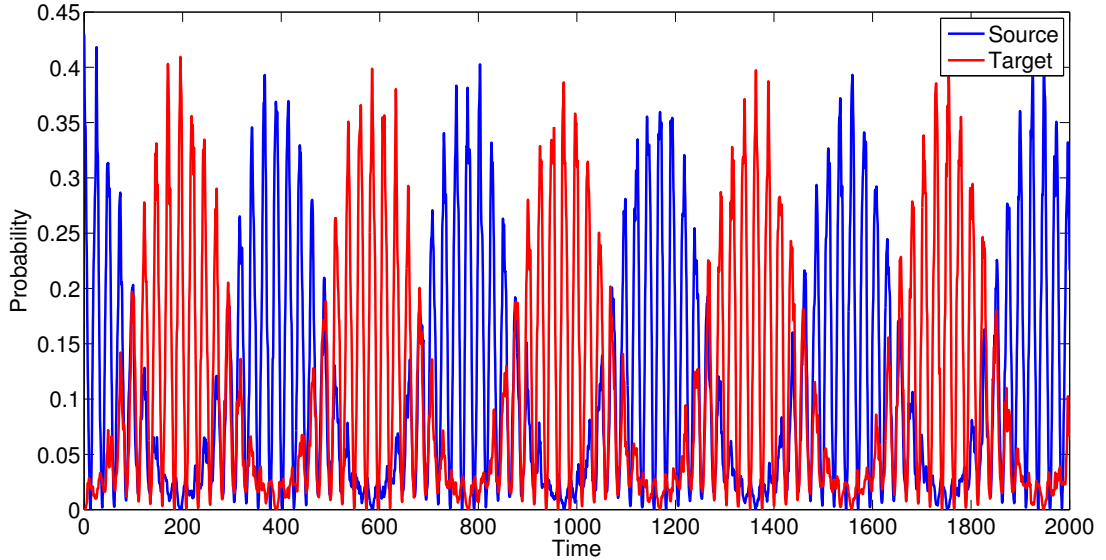

Figure B.4: Numerically calculated signal transfer on a 12×12 cell graphene lattice between vertices on different sublattices, using the communication Hamiltonian in Equation (3.110). The system is initialised in $|\ell_s\rangle$ and localises on $|\ell_t\rangle$. Only the sum of probabilities to be found on the neighbour vertices is shown.

Appendix C

Spectral properties of finite armchair nanotubes

Following the method found in [88] where the electronic states of graphene nanoribbons are discussed, we derive the spectrum of finite armchair nanotubes. In what follows we assume the same spatial and reciprocal lattice vectors as found in Section 2.6. We also set, for convenience, the lattice constant to $a = 1$ and the on-site energy of each vertex to $\epsilon_D = 0$.

The nanotube cell presented in Figure 4.25 is of the armchair type. The armchair edge runs along the vertical axis and the nanotube has periodic boundary conditions in this axis with period N_y nanotube cells. In the horizontal direction the nanotube has length N_x sites, with Dirichlet boundary conditions being imposed at both ends.

The tight-binding Hamiltonian for the armchair nanotube with the labelling shown in Figure 4.25 is

$$
\begin{aligned}
H = t \sum_{l=1}^{N_y} \Bigg[&\sum_{m=1}^{N_x} \left(|m, A, l\rangle \langle m \pm 1, B, l| + |m, B, l\rangle \langle m \pm 1, A, l| \right) \\
&+ \sum_{m \in odd}^{N_x} \left(|m, A, l\rangle \langle m, B, l-1| + |m, B, l\rangle \langle m, A, l+1| \right) \\
&+ \sum_{m \in even}^{N_x} \left(|m, A, l\rangle \langle m, B, l| + |m, B, l\rangle \langle m, A, l| \right) \Bigg] .
\end{aligned}
\tag{C.1}
$$
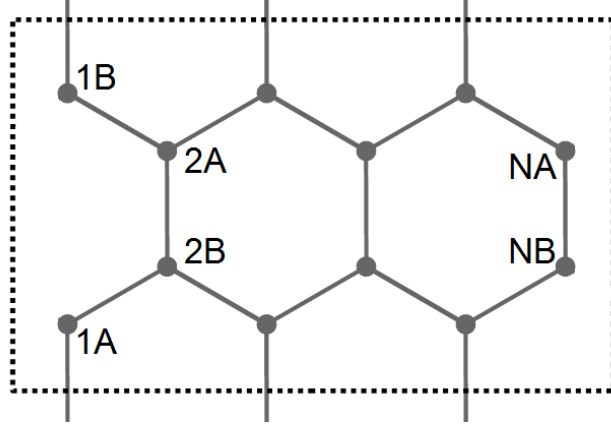
Figure C.1: Example of nanotube cell. The nanotube is periodic in the vertical y-direction. In the horizontal direction the cell is finite with a width of N_x sites.

Our wavefunction for this system is

$$|\psi\rangle = \sum_{m,l=1}^{N_x,N_y} \left[\psi_{m,l}^A \, |m, A, l\rangle + \psi_{m,l}^B \, |m, B, l\rangle \right] , \qquad (C.2)$$

where $\psi_{m,l}^{A/B}$ is the complex amplitude at the mth A/B-type vertex in the horizontal direction in the lth nanotube cell.

It is possible to see from Figure 4.25 that the translation vector between successive nanotube cells is $\underline{R}_y = -\underline{a}_1 + 2\underline{a}_2 = \sqrt{3}\underline{j}$. The periodic boundary condition along the vertical axis implies the the condition on the wavefunction amplitude $\psi_{m,l}^{A/B} = \psi_{m,l+N_y}^{A/B}$. Therefore, the vertical component of wavefunction must be a Bloch state and the phase difference between successive cells must be $e^{ik_y\sqrt{3}}$. The periodic boundary condition can then be expressed as $e^{ik_y\sqrt{3}N_l} = 1$ leading to the quantised momenta

$$k_y = \frac{2\pi q}{\sqrt{3}N_l}, \qquad q \in \{0, 1, \dots N_l - 1\} . \qquad (C.3)$$

Using this information about the vertical component of the wavefunction amplitudes, we now identify in the nanotube cell different substructures and relative phases which we must include in the wavefunction description. To this end we split the wavefunction into different terms dependent upon the position along the horizontal axis,

176

$$|\psi\rangle = \sum_{l=1}^{N_y} e^{ik_y\sqrt{3}l} \left[\sum_{m\in odd}^{N_x} \left(a_m |m,A,l\rangle + e^{i\frac{2k_y}{\sqrt{3}}} b_m |m,B,l\rangle \right) \right.$$
$$\left. + \sum_{m\in even}^{N_x} \left(e^{i\frac{\sqrt{3}k_y}{2}} a_m |m,A,l\rangle + e^{i\frac{k_y}{2\sqrt{3}}} b_m |m,B,l\rangle \right) \right]. \tag{C.4}$$

By applying the above wavefunction to the tight-binding Hamiltonian in Equation (C.1), we find the following equations of motion describing the amplitudes a_m, b_m

$$Ea_m = t \left(e^{-i\frac{k_y}{2\sqrt{3}}} (b_{m+1} + b_{m-1}) + e^{-i\frac{2k_y}{\sqrt{3}}} b_m \right) \tag{C.5}$$

$$Eb_m = t \left(e^{i\frac{k_y}{2\sqrt{3}}} (a_{m+1} + a_{m-1}) + e^{i\frac{2k_y}{\sqrt{3}}} a_m \right). \tag{C.6}$$

Considering the amplitudes at the boundaries of the nanotube cell we find

$$Ea_1 = t \left(e^{-\frac{k_y}{2\sqrt{3}}} b_2 + e^{-i\frac{2k_y}{\sqrt{3}}} b_1 \right) \tag{C.7}$$

$$Ea_{N_x} = t \left(e^{-\frac{k_y}{2\sqrt{3}}} b_{N_x-1} + e^{-i\frac{2k_y}{\sqrt{3}}} b_{N_x} \right) \tag{C.8}$$

$$Eb_1 = t \left(e^{i\frac{k_y}{2\sqrt{3}}} a_2 + e^{i\frac{2k_y}{\sqrt{3}}} a_1 \right) \tag{C.9}$$

$$Eb_{N_x} = t \left(e^{i\frac{k_y}{2\sqrt{3}}} a_{N_x-1} + e^{i\frac{2k_y}{\sqrt{3}}} a_{N_x} \right). \tag{C.10}$$

Inherent in these equations of motion for the boundary amplitudes is the assumption

$$a_0 = b_0 = a_{N_x+1} = b_{N_x+1} = 0, \tag{C.11}$$

that is, if there were additional vertices to either side of the nanotube cell in the horizontal direction they would have zero amplitude.

After viewing the equations governing the amplitudes at the horizontal boundary we assume the ansatz

$$a_m = Ae^{ik_x m} + Be^{-ik_x m} \tag{C.12}$$

$$b_m = Ce^{ik_x m} + De^{-ik_x m}. \tag{C.13}$$

Applying the boundary conditions to the ansatz we obtain the following

$$a_0 = A + B = 0 \tag{C.14}$$

$$b_0 = C + D = 0 \tag{C.15}$$

$$a_{N_x+1} = A\left(e^{ik_x(N_x+1)} - e^{-ik_x(N_x+1)}\right) = 2Ai\sin\left(k_x\left(N_x+1\right)\right) \tag{C.16}$$

$$b_{N_x+1} = C\left(e^{ik_x(N+x+1)} - e^{-ik_x(N_x+1)}\right) = 2Ci\sin\left(k_x\left(N_x+1\right)\right), \tag{C.17}$$

and using the fact $a_{N+1} = b_{N+1} = 0$ we obtain the second part of the quantised momenta

$$k_x = \frac{\pi p}{N_x + 1}, \qquad p \in \{1, 2, \dots N_x\}. \tag{C.18}$$

We have now reduced the form of the horizontal amplitudes a_m, b_m to

$$a_m = A\sin\left(k_x\right), \qquad b_m = C\sin\left(k_x m\right), \tag{C.19}$$

where we have incorporated the factors of $2i$ into A, C. Inserting these expressions for the amplitudes into the equations of motion in Equation C.5 & C.6 we find the matrix

$$\begin{pmatrix} E & -t\left(2e^{-i\frac{k_y}{2\sqrt{3}}}\cos\left(k_x\right) + e^{-i\frac{2k_y}{\sqrt{3}}}\right) \\ -t\left(2e^{i\frac{k_y}{2\sqrt{3}}}\cos\left(k_x\right) + e^{i\frac{2k_y}{\sqrt{3}}}\right) & E \end{pmatrix} \begin{pmatrix} A \\ C \end{pmatrix} = 0, \tag{C.20}$$

governing the coefficients A & C. Taking the determinant of this 2×2 matrix gives us the energy relation

$$E = \pm t\sqrt{1 + 4\cos^2\left(k_x\right) + 4\cos\left(k_x\right)\cos\left(\frac{\sqrt{3}k_y}{2}\right)}. \tag{C.21}$$

We also find that the horizontal component of the wavefunction amplitudes take the form

$$a_m = \frac{N_c}{\sqrt{2}}\sin\left(k_x m\right), \qquad b_m = \pm\frac{N_c}{\sqrt{2}}\frac{f^*}{|f|}\sin\left(k_x m\right), \tag{C.22}$$

where N_c is a normalisation constant and $f = 2e^{-i\frac{k_y}{2\sqrt{3}}}\cos\left(k_x\right) + e^{-i\frac{2k_y}{\sqrt{3}}}$.

The energy relation in Equation (C.21) has energies which lie at the Dirac energy $\epsilon_D = 0$ at the points

$$\underline{K} = \frac{2\pi}{3}\underline{i}, \qquad \underline{K'} = \frac{\pi}{3}\underline{i} + \frac{2\pi}{\sqrt{3}}\underline{j}. \tag{C.23}$$

However, the allowed values of k_y mean $k_y \neq \frac{2\pi}{\sqrt{3}}$ so only the $\underline{K}$-point is allowed, reducing the number of eigenstates at the Dirac point from four to two. Comparing the $\underline{K}$-point with the allowed values of k_x we find $\frac{p}{N_x+1} = \frac{2}{3}$, that is, there are only eigenenergies which coincide with the Dirac energy when $N_x + 1$ is some integer multiple of 3. At this eigenenergy the horizontal amplitudes reduce to

$$a_m = \frac{N_c}{\sqrt{2}} \sin\left(k_x m\right), \quad b_m = \pm\frac{N_c}{\sqrt{2}} \sin\left(k_x m\right) . \tag{C.24}$$

An important feature of these amplitudes, with respect to quantum searches using eigenstates constructed from these amplitudes, is the existence of nodal points when $k_x m$ is an integer multiple of π, occurring whenever m is some integer multiple of 3.

References

[1] I. Foulger, S. Gnutzmann, and G. Tanner. Quantum search on graphene lattices. *Phys. Rev. Lett.*, 112:070504, Feb 2014. v

[2] D. Deutsch. Quantum theory, the church-turing principle and the universal quantum computer. *Proc. R. Soc. Lond. A*, 400:97–117, July 1985. 2

[3] D. Deutsch. Rapid solution of problems by quantum computation. *Proc. R. Soc. Lond. A*, 439:553–558, December 1992. 2

[4] R. Cleve, A. Ekert, C. Macchiavello, and M. Mosca. Quantum algorithms revisited. *Proc. R. Soc. Lond. A*, 454:339–354, January 1998. 2

[5] P. W. Shor. Algorithms for quantum computation: discrete logarithms and factoring. *Foundations of Computer Science, IEEE Annual Symposium on*, 0:124–134, 1994. 2

[6] L. K. Grover. A fast quantum mechanical algorithm for database search. In *Proceedings of the twenty-eighth annual ACM symposium on Theory of computing*, STOC '96, pages 212–219, New York, NY, USA, 1996. ACM. 2, 7

[7] L. K. Grover. Quantum mechanics helps in searching for a needle in a haystack. *Phys. Rev. Lett.*, 79:325–328, Jul 1997. 2, 7

[8] Y. Aharonov, L. Davidovich, and N. Zagury. Quantum random walks. *Phys. Rev. A*, 48:1687–1690, Aug 1993. 2, 6

[9] N. Shenvi, J. Kempe, and K. B. Whaley. Quantum random-walk search algorithm. *Phys. Rev. A*, 67:052307, May 2003. 2, 24, 25, 26

[10] A. Ambainis, J. Kempe, and A. Rivosh. Coins make quantum walks faster. In *Proceedings of the sixteenth annual ACM-SIAM symposium on Discrete algorithms*,

SODA '05, pages 1099–1108, Philadelphia, PA, USA, 2005. Society for Industrial and Applied Mathematics. 2, 3, 25, 26, 27, 41, 42

[11] A. M. Childs. Universal computation by quantum walk. *Phys. Rev. Lett.*, 102:180501, May 2009. 3

[12] N. B. Lovett, S. Cooper, M. Everitt, M. Trevers, and V. Kendon. Universal quantum computation using the discrete-time quantum walk. *Phys. Rev. A*, 81:042330, Apr 2010. 3

[13] M. Karski, L. Förster, J. Choi, A. Steffen, W. Alt, D. Meschede, and A. Widera. Quantum walk in position space with single optically trapped atoms. *Science*, 325(5937):174–177, 2009. 3, 28

[14] H. Schmitz, R. Matjeschk, Ch. Schneider, J. Glueckert, M. Enderlein, T. Huber, and T. Schaetz. Quantum walk of a trapped ion in phase space. *Phys. Rev. Lett.*, 103:090504, Aug 2009. 3, 28

[15] H. B. Perets, Y. Lahini, F. Pozzi, M. Sorel, R. Morandotti, and Y. Silberberg. Realization of quantum walks with negligible decoherence in waveguide lattices. *Phys. Rev. Lett.*, 100:170506, May 2008. 3, 29

[16] C. M. Chandrashekar. Implementing the one-dimensional quantum (hadamard) walk using a bose-einstein condensate. *Phys. Rev. A*, 74:032307, Sep 2006. 3

[17] O. Mandel, M. Greiner, A. Widera, T. Rom, T. W. Hänsch, and I. Bloch. Coherent transport of neutral atoms in spin-dependent optical lattice potentials. *Phys. Rev. Lett.*, 91:010407, Jul 2003. 3

[18] K. S. Novoselov, V. I. Fal'ko, L. Colombo, P. R. Gellert, M. G. Schwab, and K. Kim. A roadmap for graphene. *Nature*, 490:192–200, 2012. 3

[19] A. K. Geim and K. S. Novoselov. The rise of graphene. *Nature Materials*, 6:183–191, 2007. 3

[20] A. M. Childs and J. Goldstone. Spatial search by quantum walk. *Phys. Rev. A*, 70:022314, Aug 2004. 3, 4, 26, 35, 37, 38, 44, 46, 51, 164

[21] A. M. Childs and J. Goldstone. Spatial search and the dirac equation. *Phys. Rev. A*, 70:042312, Oct 2004. 3, 4, 27, 35, 51, 86, 165

[22] S. Karlin and H. M. Taylor. *A First Course in Stochastic Processes.* 2nd Edition. Academic Press, 1975. 6, 18

[23] J. Kempe. Quantum random walks: An introductory overview. *Contemporary Physics*, 44(4):307–327, 2003. 6

[24] R. Portugal. *Quantum Walks and Search Algorithms.* Springer, 2013. 6, 18

[25] S. E. Venegas-Andraca. Quantum walks: a comprehensive review. *Quantum Information Processing*, 11(5):1015–1106, 2012. 6

[26] R. P. Feynman and A.R. Hibbs. *Quantum Mechanics and Path Integrals.* McGraw-Hill Book Company, 1965. 6

[27] D. A. Meyer. From quantum cellular automata to quantum lattice gases. *Journal of Statistical Physics*, 85(5-6):551–574, 1996. 6, 13

[28] D. Aharonov, A. Ambainis, J. Kempe, and U. Vazirani. Quantum walks on graphs. In *Proceedings of the thirty-third annual ACM symposium on Theory of computing*, STOC '01, pages 50–59, New York, NY, USA, 2001. ACM. 6, 22, 23

[29] A. Ambainis, E. Bach, A. Nayak, A. Vishwanath, and J. Watrous. One-dimensional quantum walks. In *Proceedings of the thirty-third annual ACM symposium on Theory of computing*, STOC '01, pages 37–49, New York, NY, USA, 2001. ACM. 6, 16

[30] E. Farhi and S. Gutmann. Quantum computation and decision trees. *Phys. Rev. A*, 58:915–928, Aug 1998. 6, 19, 23

[31] C. H. Bennett, E. Bernstein, G. Brassard, and U. Vazirani. Strengths and weaknesses of quantum computing. In *SIAM J. Comput*, pages 1510–1523. Society for Industrial and Applied Mathematics, 1997. 7

[32] M. Boyer, G. Brassard, P. Høyer, and A. Tapp. Tight bounds on quantum searching. *arXiv:quant-ph/9605034v1*, 1996. 8

[33] R. J. Wilson and J. J. Watkins. *Graphs: An Introductory Approach.* John Wiley & Sons, Inc, 1990. 9

[34] C. Kittel. *Introduction to Solid State Physics.* John Wiley & Sons, 8th edition, 2004. 11

[35] N. Konno. Quantum random walks in one dimension. *Quantum Information Processing*, 1(5):345–354, 2002. 16

[36] B. Tregenna, W. Flanagan, R. Maile, and V. Kendon. Controlling discrete quantum walks: coins and initial states. *New Journal of Physics*, 5(1):83, 2003. 16

[37] D. ben Avraham, E. M. Bollt, and C. Tamon. One-dimensional continuous-time quantum walks. In HenryO. Everitt, editor, *Experimental Aspects of Quantum Computing*, pages 295–308. Springer US, 2005. 20

[38] V. Kendon and B. Tregenna. Decoherence can be useful in quantum walks. *Phys. Rev. A*, 67:042315, Apr 2003. 21

[39] V. Kendon. Decoherence in quantum walks - a review. *Mathematical Structures in Computer Science*, 17(6):1169–1220, Dec 2007. 21

[40] F. L. Marquezino, R. Portugal, and G. Abal. Mixing times in quantum walks on two-dimensional grids. *Phys. Rev. A*, 82:042341, Oct 2010. 23

[41] C. Moore and A. Russell. Quantum walks on the hypercube. In *Proceedings of the 6th International Workshop on Randomization and Approximation Techniques*, RANDOM '02, pages 164–178, London, UK, UK, 2002. Springer-Verlag. 23

[42] J. Kempe. Discrete quantum walks hit exponentially faster. *Probability Theory and Related Fields*, 133:215–235, 2005. 10.1007/s00440-004-0423-2. 23

[43] F. Magniez, A. Nayak, P. C. Richter, and M. Santha. On the hitting times of quantum versus random walks. In *Proceedings of the Twentieth Annual ACM-SIAM Symposium on Discrete Algorithms*, SODA '09, pages 86–95, Philadelphia, PA, USA, 2009. Society for Industrial and Applied Mathematics. 23

[44] R. A. M. Santos and R. Portugal. Quantum hitting time on the complete graph. *International Journal of Quantum Information*, 08(05):881–894, 2010. 23

[45] A. M. Childs, E. Farhi, and S. Gutmann. An example of the difference between quantum and classical random walks. *Quantum Information Processing*, 1(1/2):35–43, April 2002. 23

[46] H. Krovi and T. A. Brun. Quantum walks with infinite hitting times. *Phys. Rev. A*, 74:042334, Oct 2006. 23

[47] A. M. Childs, R. Cleve, E. Deotto, E. Farhi, S. Gutmann, and D. A. Spielman. Exponential algorithmic speedup by a quantum walk. In *Proceedings of the thirty-fifth annual ACM symposium on Theory of computing*, STOC '03, pages 59–68, New York, NY, USA, 2003. ACM. 23

[48] A. Ambainis. Quantum walk algorithms for element distinctness. In *In: 45th Annual IEEE Symposium on Foundations of Computer Science, OCT 17-19, 2004. IEEE Computer Society Press, Los Alamitos, CA*, pages 22–31, 2004. 23

[49] F. Magniez, M. Santha, and M. Szegedy. Quantum algorithms for the triangle problem. In *Proceedings of the Sixteenth Annual ACM-SIAM Symposium on Discrete Algorithms*, SODA '05, pages 1109–1117, Philadelphia, PA, USA, 2005. Society for Industrial and Applied Mathematics. 23

[50] H. Buhrman and R. Špalek. Quantum verification of matrix products. In *Proceedings of the Seventeenth Annual ACM-SIAM Symposium on Discrete Algorithm*, SODA '06, pages 880–889, New York, NY, USA, 2006. ACM. 23

[51] F. Magniez and A. Nayak. Quantum complexity of testing group commutativity. In L. Caires, G. F. Italiano, L. Monteiro, C. Palamidessi, and M. Yung, editors, *Automata, Languages and Programming*, volume 3580 of *Lecture Notes in Computer Science*, pages 1312–1324. Springer Berlin Heidelberg, 2005. 23

[52] P. Benioff. *Quantum Computation and Information: AMS Special Session Quantum Computation and Information, Washington, D.C., January 19-21, 2000*. American Mathematical Society, Boston, MA, USA, 2002. arXiv:quant-ph/0003006. 25

[53] S. Aaronson and A. Ambainis. Quantum search of spatial regions. In *Proceedings of the 44th Annual IEEE Symposium on Foundations of Computer Science*, FOCS '03, pages 200–, Washington, DC, USA, 2003. IEEE Computer Society. 25

[54] G. Brassard, P. Hyer, M. Mosca, and A. Tapp. *Quantum Computation and Information: AMS Special Session Quantum Computation and Information, Washington, D.C., January 19-21, 2000*. American Mathematical Society, Boston, MA, USA, 2002. arXiv:quant-ph/0005055v1. 25

[55] L. K. Grover. Quantum computers can search rapidly by using almost any transformation. *Phys. Rev. Lett.*, 80:4329–4332, May 1998. 25

[56] B. Hein and G. Tanner. Quantum search algorithms on the hypercube. *J. Phys. A: Math. Theor.*, 42:085303, January 2009. 25, 36

[57] B. Hein and G. Tanner. Quantum search algorithms on a regular lattice. *Phys. Rev. A*, 82:012326, Jul 2010. 25

[58] V. Potoček, A. Gábris, T. Kiss, and I. Jex. Optimized quantum random-walk search algorithms on the hypercube. *Phys. Rev. A*, 79:012325, Jan 2009. 26, 27

[59] A. Ambainis, A. Backurs, N. Nahimovs, R. Ozols, and A. Rivosh. Search by quantum walks on two-dimensional grid without amplitude amplification. *arXiv:1112.3337v1*, 2011. 26

[60] A. Tulsi. Faster quantum-walk algorithm for the two-dimensional spatial search. *Phys. Rev. A*, 78:012310, Jul 2008. 26, 27

[61] G. Abal, R. Donangelo, F. L. Marquezino, and R. Portugal. Spatial search on a honeycomb network. *Mathematical. Structures in Comp. Sci.*, 20(6):999–1009, 2010. 26, 35, 41, 42

[62] E. Farhi and S. Gutmann. Analog analogue of a digital quantum computation. *Phys. Rev. A*, 57:2403–2406, Apr 1998. 27

[63] E. Agliari, A. Blumen, and O. Mülken. Quantum-walk approach to searching on fractal structures. *Phys. Rev. A*, 82:012305, Jul 2010. 27

[64] A. Patel and K. S. Raghunathan. Search on a fractal lattice using a quantum random walk. *Phys. Rev. A*, 86:012332, Jul 2012. 27

[65] H. Krovi, F. Magniez, M. Ozols, and J. Roland. Quantum walks can find a marked element on any graph. *arXiv:1002.2419v2*, 2014. 27

[66] N. B. Lovett, M. Everitt, M. Trevers, D. Mosby, D. Stockton, and V. Kendon. Spatial search using the discrete time quantum walk. *Natural Computing*, 11(1):23–35, 2012. 27

[67] D. Bouwmeester, I. Marzoli, G. P. Karman, W. Schleich, and J. P. Woerdman. Optical galton board. *Phys. Rev. A*, 61:013410, Dec 1999. 28

[68] P. H. Souto Ribeiro, S. P. Walborn, C. Raitz, L. Davidovich, and N. Zagury. Quantum random walks and wave-packet reshaping at the single-photon level. *Phys. Rev. A*, 78:012326, Jul 2008. 28

[69] M. A. Broome, A. Fedrizzi, B. P. Lanyon, I. Kassal, A. Aspuru-Guzik, and A. G. White. Discrete single-photon quantum walks with tunable decoherence. *Phys. Rev. Lett.*, 104:153602, Apr 2010. 28

[70] A. Schreiber, K. N. Cassemiro, V. Potoček, A. Gábris, P. J. Mosley, E. Andersson, I. Jex, and Ch. Silberhorn. Photons walking the line: A quantum walk with adjustable coin operations. *Phys. Rev. Lett.*, 104:050502, Feb 2010. 28

[71] F. Zähringer, G. Kirchmair, R. Gerritsma, E. Solano, R. Blatt, and C. F. Roos. Realization of a quantum walk with one and two trapped ions. *Phys. Rev. Lett.*, 104:100503, Mar 2010. 28

[72] L. Sansoni, F. Sciarrino, G. Vallone, P. Mataloni, A. Crespi, R. Ramponi, and R. Osellame. Two-particle bosonic-fermionic quantum walk via integrated photonics. *Phys. Rev. Lett.*, 108:010502, Jan 2012. 28

[73] J. Du, H. Li, X. Xu, M. Shi, J. Wu, X. Zhou, and R. Han. Experimental implementation of the quantum random-walk algorithm. *Phys. Rev. A*, 67:042316, Apr 2003. 28

[74] A. Peruzzo, M. Lobino, J. C. F. Matthews, N. Matsuda, A. Politi, K. Poulios, X.-Q. Zhou, Y. Lahini, N. Ismail, K. Wrhoff, Y. Bromberg, Y. Silberberg, M. G. Thompson, and J. L. OBrien. Quantum walks of correlated photons. *Science*, 329(5998):1500–1503, 2010. 29

[75] J. O. Owens, M. A. Broome, D. N. Biggerstaff, M. E. Goggin, A. Fedrizzi, T. Linjordet, M. Ams, G. D. Marshall, J. Twamley, M. J. Withford, and A. G. White. Two-photon quantum walks in an elliptical direct-write waveguide array. *New Journal of Physics*, 13(7):075003, 2011. 29

[76] Y.-C. Jeong, C. Di Franco, H.-T. Lim, M.S. Kim, and Y.-H. Kim. Experimental realization of a delayed-choice quantum walk. *Nature Communications*, 4(2471), 2013. 29

[77] C. Di Franco, M. Mc Gettrick, T. Machida, and Th. Busch. Alternate two-dimensional quantum walk with a single-qubit coin. *Phys. Rev. A*, 84:042337, Oct 2011. 29

[78] D. S. L. Abergel, V. Apalkov, J. Berashevich, K. Ziegler, and T. Chakraborty. Properties of graphene: a theoretical perspective. *Advances in Physics*, 59(4):261–482, 2010. 29, 34

[79] H.-S. P. Wong and D. Akinwande. *Carbon Nanotube and Graphene Device Physics.* Cambridge University Press, 2011. 29, 67, 105

[80] P. R. Wallace. The band theory of graphite. *Phys. Rev.*, 71:622–634, May 1947. 30

[81] A. H. Castro Neto, F. Guinea, N. M. R. Peres, K. S. Novoselov, and A. K. Geim. The electronic properties of graphene. *Rev. Mod. Phys.*, 81:109–162, Jan 2009. 34

[82] C. L. Siegel. *On Advanced Analytic Number Theory.* Tata Institute of Fundamental Research, 1961. 55, 56

[83] Z. Nan-Yue and K. S. Williams. On the epstein zeta function. *Tamkang Journal of Mathematics*, 26(2):165–176, 1995. 56

[84] B. Hein and G. Tanner. Wave communication across regular lattices. *Phys. Rev. Lett.*, 103:260501, Dec 2009. 70

[85] F. Banhart, J. Kotakoski, and A. V. Krasheninnikov. Structural defects in graphene. *ACS Nano*, 5(1):26–41, 2011. 97

[86] A. Javey and J. Kong. *Carbon Nanotube Electronics.* Springer, 2009. 105, 112

[87] A. Rubio, D. Sánchez-Portal, E. Artacho, P. Ordejón, and J. M. Soler. Electronic states in a finite carbon nanotube: A one-dimensional quantum box. *Phys. Rev. Lett.*, 82:3520–3523, Apr 1999. 106, 110

[88] K. Wakabayashi, K. Sasaki, T. Nakanishi, and T. Enoki. Electronic states of graphene nanoribbons and analytical solutions. *Science and Technology of Advanced Materials*, 11(5):054504, 2010. 123, 175

[89] W. Yao, S. A. Yang, and Q. Niu. Edge states in graphene: From gapped flat-band to gapless chiral modes. *Physical review letters*, 102(9):096801, 2009. 123

[90] U. Kuhl, S. Barkhofen, T. Tudorovskiy, H.-J. Stöckmann, T. Hossain, L. de Forges de Parny, and F. Mortessagne. Dirac point and edge states in a microwave realization of tight-binding graphene-like structures. *Phys. Rev. B*, 82:094308, Sep 2010. 133, 134, 135, 136

[91] M. Bellec, U. Kuhl, G. Montambaux, and F. Mortessagne. Tight-binding couplings in microwave artificial graphene. *Phys. Rev. B*, 88:115437, Sep 2013. 133, 134, 137, 139, 146

[92] J. Böhm. Quantum search algorithm and directed transport in microwave tight-binding systems. Master's thesis, Department of Physics, Philipps Universität Marburg, July 2013. 133, 134, 135, 136, 137, 138, 139, 140, 141, 145, 146, 147, 149, 150, 153

[93] H.-J. Stöckmann and J. Stein. quantum chaos in billiards studied by microwave absorption. *Phys. Rev. Lett.*, 64:2215–2218, May 1990. 134

[94] H.-J. Stöckmann. *Quantum Chaos: an introduction*. Cambridge University Press, 1999. 134

[95] F. Haake. *Quantum Signatures of Chaos*. Berlin - Springer, 2001. 134

[96] G. S. Engel, T. R. Calhoun, E. L. Read, T.-K. Ahn, T. Mancal, Y.-C. Cheng, R. E. Blankenship, and G. R. Fleming. Evidence for wavelike energy transfer through quantum coherence in photosynthetic systems. *Nature*, 446:782–786, 2007. 166

[97] N. Lambert, Y.-N. Chen, Y.-C. Cheng, C.-M. Li, G.-Y. Chen, and F. Nori. Quantum biology. *Nature Physics*, 9:10–18, 2012. 166

[98] A. M. Childs & Y. Ge. Spatial search by continuous-time quantum walks on crystal lattices. *arXiv:1403.2676*, 2014. 166